Modélisation avancée de la combustion turbulente diphasique en régime de forte dilution par les gaz brûlés

Nicolas Enjalbert

INSA de Rouen

THÈSE

présentée par :

Nicolas Enjalbert

pour l'obtention du titre de Docteur

Discipline : Energétique
Spécialité : Mécanique des Fluides
Formation doctorale : Sciences Physiques, Mathématiques et de l'Information pour l'Ingénieur
Laboratoire d'accueil : UMR 6614–CNRS–CORIA

Modélisation avancée de la combustion turbulente diphasique en régime de forte dilution par les gaz brûlés

soutenue le 16 décembre 2011

devant le Jury composé de :

Rapporteurs :	Michel Champion – Directeur de Recherche au CNRS
	César Dopazo – Professeur à l'Université de Saragosse
Examinateurs :	Emmanuel Fiani – Direction Production et Energies Durables ADEME
	Frédéric Grisch – Professeur à l'INSA de Rouen
	Bernard Labegorre – Expert Combustion Air Liquide
	Ronan Vicquelin – Maître de Conférences à l'Ecole Centrale Paris
Encadrants :	Pascale Domingo – Directrice de Recherche au CNRS
	Vincent Moureau – Chargé de Recherche au CNRS
	Luc Vervisch – Professeur à l'INSA de Rouen

Remerciements

Cette thèse fut une expérience totale. Il m'est difficile de songer à quelque événement survenu entre son initiation en février 2008 et son achèvement il y a quelques semaines sans y trouver l'empreinte, centrale ou périphérique, évidente ou en creux, du travail de doctorat.

Formuler mes remerciements est ainsi bien autre chose qu'un exercice convenu. Il s'agit de reconnaître la contribution de chacun à ces trois années de construction, chaque succès professionnel apportant les gratifications qui venaient justifier mon implication personnelle, chaque acte de soutien intime offrant l'énergie pour poursuivre l'effort d'endurance doctorale. Je m'attèle à cette tâche en dernier lieu, et clos ainsi temporellement autant que symboliquement ce chapitre de vie — acte empreint de nostalgie mais libératoire !

Je sais gré à MM. Champion et Dopazo d'avoir accepté d'être rapporteurs de ce manuscrit et d'avoir examiné avec tant d'attention mon travail. Merci en particulier au second d'avoir franchi la distance qui sépare Saragosse de Rouen pour participer à ma soutenance.

Ma sincère reconnaissance va à MM. Labegorre et Camy-Peyret. Ils m'ont proposé une thèse qui correspondait exactement à mes attentes, ouvert les portes du Centre de Recherche Claude-Delorme d'Air Liquide et de son groupe Modélisation, et ont grandement aidé au déroulement de ces trois années. Jean-Baptiste Mossa puis Alexandre Naudin m'ont accompagné et fait confiance, ce dernier notamment en fin de thèse ; je les en remercie vivement. Je remercie également M. Boukhalfa de m'avoir accueilli au sein du CORIA.

Je suis redevable à Luc Vervisch et Pascale Domingo, mes encadrants, de la confiance qu'ils m'ont accordée à tous égards, la liberté avec laquelle ils m'ont permis de travailler et la sérénité avec laquelle, grâce à leur expérience, j'ai pu avancer sur des chemins parfois peu balisés (FCCT !). À ceux-ci s'ajoute Vincent Moureau, qui a encadré la deuxième partie de mes travaux, et dont le talent et la présence ont été infiniment précieux durant le sprint des derniers mois au CORIA. Je remercie également Guillaume Ribert et Ghislain Lartigue pour leurs conseils, leurs coups de main avisés, et leur constante disponibilité.

C'est l'ensemble du laboratoire que je voudrais ensuite remercier, les nombreux services rendus, les agréables discussions extra-professionnelles ; je mentionne en particulier Isabelle Lebon, Valérie Thieury, Christophe Letailleur, qui resteront liés au souvenir de ces années.

Le CORIA m'est apparu, grâce à eux et grâce à mes aînés doctorants présents lors de mon arrivée, comme un lieu extrêmement accueillant. C'est l'impression la plus frappante de mes premières semaines. David, Subbu, Guillaume, Rina, Caroline,

Amélie, Grégory, Mathieu, Gautier, Alex (mentionné plus haut puisqu'il est ensuite devenu mon interlocuteur à l'Air Liquide), merci de m'avoir reçu ainsi, enjoués, généreux, m'éclairant sur la CAN, le système politique indien, Rouen — m'aidant à fuir la rue St-Nicolas, à éviter la rue du Trésor et à rejoindre la rue des Faulx — mais aussi sur Mac, william a.k.a. willy, Stanford, la TCAR, Lââm, les mystères de Virgin Radio, le McDo de Bois-Guillaume (ou était-ce Bihorel ? Mont-Saint-Aignan ?), et j'en passe.

Les générations se sont succédé, je suis doucement devenu un aîné aussi, et mon quotidien rouennais et doctorant s'est tissé autour des compagnons de route, co-galériens du RU, co-chercheurs et chercheurs de bugs, de brin, de réponses aux questions de la vie, de mojitos Place du Vieux, Praça da Figueira ou Hlavné Námestie : Danh, Éric, Jiesheng, Gilles, JP, Chloé, Marianne, Mechline, Joseph, Benoît, Mathias, Émilien, et les compères d'open space, les meilleurs ! Cindy, Suresh, François, Guillaume.

Tous, souvenirs, amis d'aujourd'hui et demain, je remercie cette thèse — le peut-on ? oui ! — d'avoir fait se croiser nos chemins.

Je réserve un mot particulier à Élise, la lumière que j'allais rencontrer en me lançant dans cette aventure. Contemplant ces trois ans, je crois que de nombreuses entraves ont été levées, Élise. Que l'avenir nous offre de voir, ensemble souvent, céder les suivantes !

Remontant la Seine, j'exprime toute ma reconnaissance à mes parents qui ont soutenu mon entreprise et si souvent offert leur hospitalité.

Plus loin encore de Rouen, je remercie enfin tous mes compagnons parisiens qui dans l'ombre d'Haussmann ont suivi et allégé mon périple doctoral, peuplé et nourri sa trame. De Charonne à Port-Royal, de la Flèche d'Or à l'Industrie, de l'étude de Gébé au Couvent de l'Assomption, à Pleyel ou à la Maroquinerie, à Fican, à la Tour du Bon, à Trégastel, à Épinal, autour d'un thé ou près de l'âtre, je ne suis rien sans vous.

Paris, le 25 février 2012

Contents

Introduction

The PhD work described in this thesis was carried out within the combustion modeling team at CORIA. It was funded jointly by the French Environment and Energy Management Agency (ADEME) and the Air Liquide group.

Its research objectives were defined within the framework of the SAFIR project (Simulation Avancée des Foyers Industriels avec Recycle), itself a part of a broader three-year technology partnership between the two aforementioned actors and the Total group: an industrial-scale pilot trial of carbon capture and storage (CCS). CCS is one of the methods explored by industrial actors to mitigate the contribution of fossil fuel combustion to global warming through carbon dioxide (CO_2) emissions. As a new technique, its economic viability and technical feasibility are still to be demonstrated; such is the role of this project.

Three approaches are available for capturing carbon dioxide from combustion processes: *pre-combustion*, which requires the transformation, before the combustion process, of the fuel (by gasification for coal, or reforming for natural gas) into a synthetic gas (composed mainly of CO and H_2), the conversion with steam of its carbon monoxide into CO_2, then extracted using a physical absorbent; *post-combustion*, in which CO_2 is separated from the exhaust gases downstream of the full combustion of the fuel with air, usually through chemical absorption by amines; and *oxy-combustion*, where the oxidizer used in the combustion process is oxygen rather than air, enabling the exhaust gases to be mainly composed of CO_2 and H_2O, carbon dioxide being then retrieved by compression that condensates the vapor into liquid water. Each of these approaches features advantages and drawbacks in terms of investment and operational costs, energy efficiency, operability, environmental impact and these are being evaluated in a number of recent works, by industrial and academic actors as well as international organisations [Kanniche 10, Finkenrath 11, Koornneef 12].

The option chosen in the present project is oxy-combustion. On a Total-run installation in the natural gas extraction site of Lacq, a Southern France locality, a 30-MW electricity production facility was revamped to accommodate the injection of CO_2 into deep ground layers (4,500 m). Air Liquide is involved in the overhaul to implement oxy-combustion burners [Cieutat 09]. Future applications of the process include oil extraction sites, where the fossil source would be heavy fuel oil.

Four burners of the Air Liquide technology REOXAL, of nominal power each 8 MW, were set up in the boiler. They are designed to be flexible for gaseous and liquid fuels, to enable, on a transient basis, combustion with air rather than oxygen, and to achieve flame stability even for difficult liquid fuels . An important feature of the burners is the external recirculation of part of the flue gases, injected like the oxidizer and fuel through a set of dedicated injectors at the flame base.

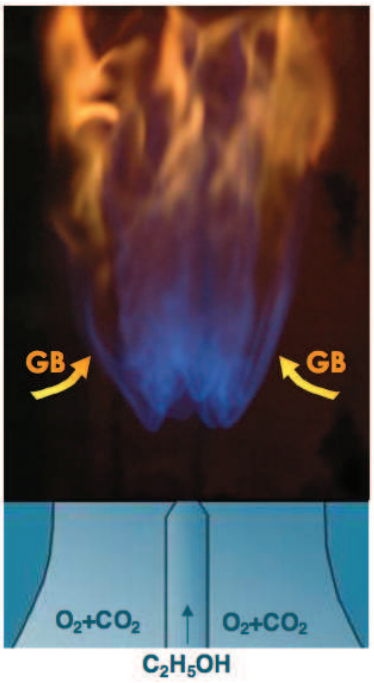

Figure 1: Target configuration of the SAFIR experiment: an ethanol spray within an O_2–CO_2 co-flow, with possible dilution of the flame by recirculating burnt gases. Reproduced from [Cessou 10].

Within this context, the SAFIR project aimed at developing solutions for the numerical simulation of such a process. Two objectives were outlined: i) accounting for the effects of dilution of the reactants by burnt gases; ii) exploring properties of two-phase combustion, and opening prospects for simulating high-viscosity, weakly volatile fuel oil combustion. The strategy, as far as the CORIA laboratory was concerned, was built around two tasks: a two-phase turbulent spray flame experiment conducted by the team of A. Cessou, D. Honoré and G. Cléon [Cessou 10]; and a modeling effort including the present work, aiming at developing a model toolbox for simulating the experiment.

What is naturally referred to as the SAFIR experiment is a 25-kW burner, comprising an ethanol spray that combusts within a co-flow of oxygen diluted with carbon dioxide, see Fig. 1. The apparatus is designed so as to allow different levels of dilution – from 0 % (pure oxygen) to 60 % in volume proportions – and different co-flow velocities, achieved through a system of removable insets with different exit diameters. The experiment is focused on studying the effect of dilution on the flame stabilization, its structure, the energy transfer and pollutant emissions. A large range of measurements is available, forming a robust basis for comparing experimental results with simulation, and aiming at collecting sufficient information on the problem's limit conditions.

On the numerical side, the contribution of this work is twofold:

- a Large-Eddy Simulation of the SAFIR spray flame has been carried out on an unstructured mesh, based on detailed flamelet chemistry and at a 250-µm spatial resolution, until then unattained for a two-phase turbulent reacting flow.

Significant features of the experiment, in particular the general flame structure and anchoring distance, have successfully been captured. This work may be seen as preliminary to numerous prospects: only one of the different dilution/velocity settings has been simulated and the ability of the computation to recover the flame response to these parameters must yet be demonstrated; indeed, it was decided to first tackle a case where no internal dilution occurs (the surrounding co-flow protects the flame base from the burnt gases that recirculate within the combustion chamber), and time did not allow to extend the simulation to other cases. Also, a number of improvements may be achieved on subgrid-scale droplet dispersion and combustion–evaporation interaction modeling.

- a new modeling approach for turbulent chemistry tabulation has been developed that takes into account the flow's mixing history and formally improves the description of multiple-parameter chemistry. At stake is the modeling of complex configurations, such as multiple-fluid problems (that require more than one mixture fraction) or those with heterogeneous dilution effects (calling for including such fields as the enthalpy into the chemical description). Named FCCT, for Flow-Controlled Chemistry Tabulation, this model attempts at combining the advantages of tabulated chemistry with the flexibility of transported pdf methods.
  FCCT was first validated on a turbulent jet flame in a vitiated co-flow [Cabra 05], a reference literature configuration that is a classical two-fluid problem and has been simulated in RANS and LES following numerous modeling approaches. The next step was to apply FCCT to a more complex problem. The chosen SAFIR flame was not in itself a candidate for complex parameterization: a single mixture fraction suffices to describe mixing (it is a two-fluid problem, one fuel and one oxidizer), and the flame dynamics are not impacted by heterogeneous dilution effects. Thus FCCT was not applied to the SAFIR case. However, in the REOXAL burner featuring external gas recirculation, which is the end application of SAFIR, the description of mixing requires two mixture fractions. Thus, steps were taken to assess the feasibility of applying FCCT to a REOXAL simulation.

This report is structured in three parts. Part I builds the theoretical and technical framework of LES in the single-phase and two-phase applications addressed by this work. In **Chapter 1**, the equations driving both phases and the model for their two-way interaction are presented. A discussion on multiple-fluid problems, one guiding thread of this manuscript, is given in its last section. Then, the numerical framework of the two solvers used for the simulations is detailed in **Chapter 2**. The technical contributions brought by the present work to allow for the modeling of complex spray injection and evaporation, as well as the study of the resulting statistics, are listed.

In Part II, the steps leading to the SAFIR spray flame simulation are discussed. **Chapter 3** is devoted to the spray injection numerical procedure: several approaches are followed to obtain relevant statistics compared with those collected in the experiment. The momentum two-way coupling and subgrid-scale dispersion model are

assessed. **Chapter 4** then deals with the reacting simulation. A review of statistical approaches in turbulent combustion modeling is given, that both applies to the SAFIR case and gives a framework for the subsequent description of FCCT. Final simulation results are presented, where two variance models have been used. Flame structure and thermochemical fields are compared with the experiment.

Part III is then devoted to the Flow-Controlled Chemistry Tabulation model. **Chapter 5** is the reproduction, with some additions, of a publication issued during the course of the present PhD [Enjalbert 11]. In it are presented the model's principles, its practical implementation, and its validation on the aforementioned literature jet flame. In **Chapter 6**, the flow structure and mixing patterns in a REOXAL oxy-burner configuration are studied and the adaptation of FCCT to this three-fluid application is discussed.

Part I

Principles and numerics of LES

Chapter 1

LES of single- and two-phase flows

The equations governing the behavior of single- and two-phase flows, as well as the models invoked in their simulation, are detailed in this chapter. Its contents give a common theoretical background underlying the rest of the present report. The first two sections are devoted to the descriptive framework and evolution laws of the carrier and dispersed phases. Their filtered counterparts are examined in a following section. Finally, some notions relative to the parameterization of mixing are given in a last paragraph.

Contents

1.1 Carrier phase conservation equations

1.1.1 Navier–Stokes

The reference situation of a compressible Newtonian fluid carrying no dispersed phase is first considered. The conservative form of the equations governing its dynamics, forming the Navier–Stokes system, reads as follows:

$$\frac{\partial \rho}{\partial t} + \underline{\nabla} \cdot (\rho \underline{u}) = 0 \tag{1.1}$$

$$\frac{\partial (\rho \underline{u})}{\partial t} + \underline{\nabla} \cdot (\rho \underline{u} \otimes \underline{u}) = -\underline{\nabla} p + \underline{\nabla} \cdot \underline{\underline{\tau}} + \rho \underline{f} \tag{1.2}$$

$$\frac{\partial (\rho e_t)}{\partial t} + \underline{\nabla} \cdot (\rho \underline{u} e_t) = -\underline{\nabla} \cdot (p \underline{u}) + \underline{\nabla} \cdot (\underline{\underline{\tau}} \cdot \underline{u}) + \underline{\nabla} \cdot (\lambda \underline{\nabla} T) + \rho \underline{f} \cdot \underline{u} + \dot{\mathcal{Q}} \tag{1.3}$$

where the formalism of Poinsot & Veynante [Poinsot 05] is used:

- $\underline{\underline{\tau}}$ is the viscous stress tensor, defined as

$$\underline{\underline{\tau}} = \mu \left(\underline{\underline{\nabla}}\, \underline{u} + {}^{\mathrm{T}}\underline{\underline{\nabla}}\, \underline{u} - \frac{2}{3} (\underline{\nabla} \cdot \underline{u})\, \underline{\underline{1}} \right) \tag{1.4}$$

  with μ the dynamic viscosity;
- $-\lambda \underline{\nabla} T$ is the heat diffusion term, which follows a Fourier law, with λ the heat conduction coefficient;
- e_t is the total energy, defined as the sum of internal energy and kinetic energy
- $\underline{f}$ is the resultant of the volume forces applied homogeneously to the gas (gravity, ...);
- $\dot{\mathcal{Q}}$ is the external heating rate, which can be positive (spark ignition, ...) or negative (heat loss at the walls or by radiation, ...).

Moreover, the fluid is assumed to obey the ideal gas law:

$$\frac{p}{\rho} = \frac{\mathcal{R} T}{W}\,, \tag{1.5}$$

where $\mathcal{R} = 8.315\,\mathrm{J/mol{\cdot}K}$ is the ideal gas constant and W the average molecular mass of the gas mixture.

1.1.2 Multi-species transport

Mass fractions

In the context of this work, the gas is a mixture of several species, indexed by $m = 1, \ldots, N_s$, whose composition is characterized by the mass fractions

$$Y_m = \frac{\rho_m}{\rho}\,, \tag{1.6}$$

so that $\sum_m Y_m = 1$. From them, the average molecular mass and heat capacity of the mixture are defined as

$$W = \left(\sum_m \frac{Y_m}{W_m} \right)^{-1}\,, \tag{1.7}$$

$$C_p = \sum_m C_{p,m}(T)\, Y_m \,, \tag{1.8}$$

where the dependency of C_p with T must be noted. The molar fraction of a species m is denoted by X_m and is related to the mass fractions through:

$$X_m = W \frac{Y_m}{W_m} \,. \tag{1.9}$$

The mass fraction Y_m is driven by the following conservation equation:

$$\frac{\partial(\rho Y_m)}{\partial t} + \underline{\nabla} \cdot (\rho \underline{u} Y_m) = \underline{\nabla} \cdot (\rho \mathcal{D}_m \underline{\nabla} Y_m) + \dot{\omega}_m \,, \tag{1.10}$$

where $\dot{\omega}_m$ is the production rate of the concerned species. In this equation, the diffusive term is written by assuming the diffusion of species m into the fluid obeys a binary diffusion law, and involves the diffusivity $\mathcal{D}_m = \lambda/(\rho C_p \mathrm{Le}_m)$ (see Section 1.1.4 of the book by Poinsot & Veynante [Poinsot 05]).

In the present work, a unique and constant Lewis $\mathrm{Le} = 1$ is assumed for all species. A single diffusivity coefficient $\mathcal{D}$ may be used. It is related to the dynamic viscosity by $\rho\mathcal{D} = \mu/\mathrm{Sc}$, where Sc is the Schmidt number, assumed here to be constant. This hypothesis leads to neglect differential diffusivity effects, which may affect flame front stability, but it is widely invoked for non-hydrogen hydrocarbon fuels and is here deemed acceptable.

Similarly, the heat diffusion coefficient is determined from the molecular viscosity as $\lambda = \mu C_p/\,\mathrm{Pr}$, where Pr is linked to Sc through:

$$\mathrm{Le} = \frac{\mathrm{Sc}}{\mathrm{Pr}} \,. \tag{1.11}$$

Molecular viscosity laws

Several laws may be adopted for the dynamic viscosity.

Sutherland law. The viscosity is expressed as a sole function of temperature, through

$$\mu(T) = \mu_0 \frac{T_0 + C}{T + C} \left(\frac{T}{T_0}\right)^{3/2} \,, \tag{1.12}$$

where three constants μ_0, T_0 and C are required inputs, such that μ_0 is the viscosity at the reference temperature T_0. A practical usage of this law is usually enabled by assuming that the viscosity properties are those of the main fluid, in most cases air.

Wilke's formula. An alternative that takes into account the dependency of the viscosity with composition is the semi-empirical law by Wilke [Wilke 50]:

$$\mu = \sum_{i=1}^{N_s} \frac{X_i \mu_i}{\sum_j X_j \phi_{ij}} \tag{1.13}$$

where the ϕ_{ij} coefficients are composition-independent and defined as

$$\phi_{ij} = \frac{\left[1 + \left(\frac{\mu_i}{\mu_j}\right)^{1/2} \left(\frac{W_j}{W_i}\right)^{1/4}\right]^{1/2}}{2\sqrt{2}\left(1 + \frac{W_i}{W_j}\right)^{1/2}} \,. \tag{1.14}$$

If $i = j$, $\phi_{ij} = 1$, however these coefficients are not symmetric, $\phi_{ij} \neq \phi_{ji}$. The viscosities μ_i of each species may be given a temperature dependency.

1.1.3 Energy quantities

In the Navier–Stokes system derived above, the energy conservation equation (1.3) was written on the total energy e_t, but it may often be more convenient to solve other quantities, that are equivalent but obey transport equations in which the rhs terms differ. A closer look is taken at them in this section, in particular at the pressure and viscous terms.

Total energy e_t. In the equation for the total energy e_t, the pressure and viscous terms represent the power of the external forces on the surface ∂V of a control volume V:

$$\int_{\partial V} \underline{u} \cdot \left(-p\,\underline{n} + \underline{\underline{\tau}} \cdot \underline{n}\right) \mathrm{d}S \,.$$

Observing that $\underline{u} \cdot (\underline{\underline{\tau}} \cdot \underline{n}) = (\underline{\underline{\tau}} \cdot \underline{u}) \cdot \underline{n}$, this surface integral may be rewritten as the volume integral of the divergence term $\underline{\nabla} \cdot (-p\,\underline{u} + \underline{\underline{\tau}} \cdot \underline{u})$, which is how the pressure and viscous forces terms read in Eq. (1.3).

Total enthalpy h_t. Writing an equation for the total enthalpy $h_t = e_t + p/\rho$ is then done with help from the continuity equation (1.1), enabling the relation

$$\frac{\partial(\rho h_t)}{\partial t} + \underline{\nabla} \cdot (\rho \underline{u} h_t) = \frac{\partial(\rho e_t)}{\partial t} + \underline{\nabla} \cdot (\rho \underline{u} e_t) + \frac{\partial p}{\partial t} + \underline{u} \cdot \underline{\nabla} p + (\underline{\nabla} \cdot \underline{u}) p \,.$$

The transformation keeps the viscous term $\underline{\nabla} \cdot (\underline{\underline{\tau}} \cdot \underline{u})$ unchanged but yields, for the pressure term, the time derivative $\partial p/\partial t$. The conservation equation reads:

$$\frac{\partial(\rho h_t)}{\partial t} + \underline{\nabla} \cdot (\rho \underline{u} h_t) = \frac{\partial p}{\partial t} + \underline{\nabla} \cdot (\underline{\underline{\tau}} \cdot \underline{u}) + \underline{\nabla} \cdot (\lambda \underline{\nabla} T) + \rho \underline{f} \cdot \underline{u} + \dot{\mathcal{Q}} \,. \tag{1.15}$$

Total non-chemical enthalpy H. The equation for the total non-chemical enthalpy H, defined as $H = h_t - \sum_m \Delta h^0_{f,m} Y_m$, simply contains the additional source term

$$\dot{\omega}_T = -\sum_m \Delta h^0_{f,m} \dot{\omega}_m \,, \tag{1.16}$$

compared to which the diffusive species term is neglected. This reads

$$\frac{\partial \rho H}{\partial t} + \underline{\nabla} \cdot (\rho \underline{u} H) \;=\; \frac{\partial p}{\partial t} + \underline{\nabla} \cdot \left(\underline{\underline{\tau}} \cdot \underline{u}\right) + \underline{\nabla} \cdot (\lambda \underline{\nabla} T) + \rho \underline{f} \cdot \underline{u} + \dot{\mathcal{Q}} + \dot{\omega}_T \,. \tag{1.17}$$

In a similar way, the total non-chemical energy E may be defined as $E = e_t - \sum \Delta h^0_{f,m} Y_m$ and satisfies

$$\frac{\partial(\rho E)}{\partial t} + \underline{\nabla} \cdot (\rho \underline{u} E) = -\underline{\nabla} \cdot (p\underline{u}) + \underline{\nabla} \cdot (\underline{\underline{\tau}} \cdot \underline{u}) + \underline{\nabla} \cdot (\lambda \underline{\nabla} T) + \rho \underline{f} \cdot \underline{u} + \dot{\mathcal{Q}} + \dot{\omega}_T \,. \quad (1.18)$$

Kinetic energy. An equation for the kinetic energy $\frac{1}{2}|\underline{u}|^2$ is obtained by multiplying the momentum equation by $\underline{u}$. Since in Eq. (1.2) the viscous and pressure terms read $-\underline{\nabla} p + \underline{\nabla} \cdot \underline{\underline{\tau}}$, the conservation equation for the kinetic energy involves $\underline{u} \cdot (-\underline{\nabla} p + \underline{\nabla} \cdot \underline{\underline{\tau}})$:

$$\rho \frac{\partial(\frac{1}{2}|\underline{u}|^2)}{\partial t} + \rho \underline{u} \cdot \underline{\nabla}(\tfrac{1}{2}|\underline{u}|^2) = \underline{u} \cdot (-\underline{\nabla} p + \underline{\nabla} \cdot \underline{\underline{\tau}}) + \rho \underline{f} \cdot \underline{u} \,. \quad (1.19)$$

Sensible enthalpy h_s. The total non-chemical enthalpy may be decomposed into sensible enthalpy and kinetic energy: $H = h_s + \frac{1}{2}|\underline{u}|^2$, where

$$h_s = \sum_m h_{s,m} Y_m = \sum_m Y_m \int_{T_{\text{ref}}}^{T} C_{p,m}(T') \mathrm{d}T' \,. \quad (1.20)$$

Thus the h_s transport equation is the difference between Eq. (1.17) and Eq. (1.19): the pressure term reads $\partial p/\partial t + \underline{u} \cdot \underline{\nabla} p$, while the viscous term is equal to

$$\underline{\nabla} \cdot (\underline{u} \cdot \underline{\underline{\tau}}) - \underline{u} \cdot (\underline{\nabla} \cdot \underline{\underline{\tau}}) = \underline{\underline{\tau}} : \underline{\underline{\nabla u}} \,. \quad (1.21)$$

This term represents the power of the internal viscous forces, which dissipate kinetic energy into heat. It is always a positive term in the enthalpy equation. The conservation equation for h_s reads:

$$\frac{\partial(\rho h_s)}{\partial t} + \underline{\nabla} \cdot (\rho \underline{u} h_s) \;=\; \dot{\omega}_T + \left(\frac{\partial p}{\partial t} + \underline{u} \cdot \underline{\nabla} p \right) + \underline{\nabla} \cdot (\lambda \underline{\nabla} T) + \underline{\underline{\tau}} : \underline{\underline{\nabla u}} + \dot{\mathcal{Q}} \quad (1.22)$$

It may be noted that the power of the external forces $\underline{f}$ cancels out and is not present in the resulting equation.

1.2 Dispersed phase

This section presents the model employed in this work for the dispersed phase. It is formulated to describe the behavior of a dilute dispersed liquid phase in a gas, characterized by a large liquid-to-gas density ratio $\rho_l/\rho \sim \mathcal{O}(10^3)$ and a small volume fraction $\alpha_l \ll 1$. The validity of this modeling framework in our case will be discussed in Section 3.2.1.

1.2.1 Descriptive formalism

Achieving a comprehensive description of a liquid spray is not straightforward. In this work, the considered droplets have diameters of the order of a few tens of millimeters and are carried by the gas on distances of several centimeters, *i.e.* two to three orders

of magnitude larger than the smaller particles. A capture of the full range of scales of the flow fluctuations generated by this displacement is impossible. On the scale of an individual droplet, a boundary layer and a wake are to be expected in the gaseous phase, as well as possible internal circulation in the liquid. The required resolution may be five to six orders of magnitude smaller than the largest simulated dimensions, and is therefore computationally out of reach. Therefore, approximations are required for the resolution of both the dispersed phase and the continuous phase.

As far as the spray is concerned, the particles may be individually identified and treated in a way that does not require a full resolution of their inner structure. A reference work by Williams in 1958 introduced one of the first such statistical description of the spray [Williams 58]. Droplets are assumed independent and undifferentiated (all subject to the same form of equations). In the present work, a droplet is characterized by its position $\underline{x}$, velocity $\underline{u}$, diameter d and temperature T. A single composition is assumed for the liquid so there is no variation in density. The probability density function (pdf) of a particle is defined on the joint $(\underline{x}, \underline{u}, d, T)$-space and as a function of time such that

$$f(t, \underline{x}, \underline{u}, d, T)\mathrm{d}\underline{x}\,\mathrm{d}\underline{u}\,\mathrm{d}d\,\mathrm{d}T \tag{1.23}$$

is the probability of finding the droplet with position in $[\underline{x}; \underline{x} + \mathrm{d}\underline{x}]$, velocity in $[\underline{u}; \underline{u} + \mathrm{d}\underline{u}]$[1], diameter in $[d; d + \mathrm{d}d]$ and temperature in $[T; T + \mathrm{d}T]$ at time t. Formally,

$$f(t, \underline{x}^*, \underline{u}^*, d^*, T^*) = \langle\, \delta(\underline{x}^* - \underline{x}(t))\delta(\underline{u}^* - \underline{u}(t))\delta(d^* - d(t))\delta(T^* - T(t))\,\rangle\,, \tag{1.24}$$

where $\langle . \rangle$ denotes the ensemble average operator.

The expression in Eq. (1.23) may also be seen, using an ergodicity argument, as the proportion of droplets, among all spray realizations, with properties in the aforementioned intervals, at time t. As a pdf, f satisfies

$$\int_{\underline{x}}\int_{\underline{u}}\int_{d=0}^{\infty}\int_{T=0}^{\infty} f(t, \underline{x}, \underline{u}, d, T)\mathrm{d}\underline{x}\,\mathrm{d}\underline{u}\,\mathrm{d}d\,\mathrm{d}T = 1, \quad \forall t\,. \tag{1.25}$$

The spray as a whole may be characterized by a multiple-particle joint pdf f_{spray} which, because of particle independence, is defined as the product of the single-particle pdf f:

$$f_{\text{spray}}(t, \underline{x}^{(1)}, \underline{u}^{(1)}, d^{(1)}, T^{(1)}, \ldots, \underline{x}^{(N)}, \underline{u}^{(N)}, d^{(N)}, T^{(N)}) = \prod_{k=1}^{N} f(t, \underline{x}^{(k)}, \underline{u}^{(k)}, d^{(k)}, T^{(k)}) \tag{1.26}$$

with N the number of droplets of the spray and $^{(k)}$ referring to the properties of the k-th droplet.

Historically, in the context of Fluid Mechanics, a transport equation for the pdf of the velocity field was first derived by Lundgren [Lundgren 67] and for the pdf of scalar reacting fields by Dopazo & O'Brien [Dopazo 74]. A paper summarizing the

[1] Using an *ad hoc* extension of the 1D interval notation $[\ldots]$ to 3D.

approach was published by Pope [Pope 85]. Here, f satisfies the Langevin equation (see [de Chaisemartin 09], Section 1.2.1):

$$\frac{\partial f}{\partial t} + \underline{\nabla} \cdot \left(\frac{\mathrm{d}\underline{x}}{\mathrm{d}t} f \right) + \underline{\nabla}_{\underline{u}} \cdot \left(\frac{\mathrm{d}\underline{u}}{\mathrm{d}t} f \right) + \frac{\partial}{\partial d} \left(\frac{\mathrm{d}d}{\mathrm{d}t} f \right) + \frac{\partial}{\partial T} \left(\frac{\mathrm{d}T}{\mathrm{d}t} f \right) = 0 \,. \tag{1.27}$$

The physical modeling of the particles' behavior appears in this generic formulation in the time derivatives of $\underline{x}$, $\underline{u}$, d and T. It is detailed in the next two sections. The numerical approach for solving Eq. (1.27) is presented in the next chapter, Section 2.2.

A particle-laden flow with a mass loading of the order of unity or larger is expected to behave in a significantly different way than a single-phase flow [Crowe 96, Bini 08]. Here, the effect of the particles on the gaseous phase is approximated with the point-source approach, widely used for exploratory studies [Boivin 98, Okong'o 04, Bini 08] as well as practical applications [Apte 03b, Jones 10c]. The mass, momentum, energy and scalar transfer from particles to the gas is described by means of punctual source terms. This formalism was shown to be valid in cases where the particles are smaller than the Kolmogorov lengthscale or separated from each other by distances large compared to their diameter, because the gas fluctuations induced by the droplets are then dissipated by viscous forces quickly enough for their effect on other particles to be negligible [Boivin 98]. A noteworthy model that takes into account the fluid displacement caused by the particles and is thus fit for dense particulate flows, not used here, was investigated by Apte *et al.* [Apte 08]. Resulting equations are examined in Section 1.2.4, and further discussion on this assumption in the case studied here is presented in Section 3.2.1.

To summarize, the gas is seen as a continuous phase, populated with a number of liquid particles, each with individual properties. The behavior of a droplet depends on its own properties as well as on those of the gas at its position. The action of the dispersed phase on the carrier is described through point-source terms at the particle positions.

1.2.2 Droplet kinematics

A distinction between gas and particle properties is introduced in the notations with the subscript $_p$ for all particle properties, while the gas properties notations are left blank: $\underline{u}_p$ is the particle velocity, and $\underline{u}$ refers to that of the gas.

In this study, droplets are assumed to be spherical. This point is later discussed in Section 3.2.1. A direct consequence is the expression of a particle's mass as a function of its diameter:

$$m_p = \rho_l \frac{\pi}{6} d_p^3 \,. \tag{1.28}$$

Position

The position of a particle is governed by the evident point mechanics relation

$$\frac{\mathrm{d}\underline{x}_p}{\mathrm{d}t} = \underline{u}_p \,, \tag{1.29}$$

which is internal to the droplet properties and conveys no information on the particle's interaction with its environment.

Momentum

The velocity equation reads

$$m_p \frac{\mathrm{d}\underline{u}_p}{\mathrm{d}t} = \underline{F}\,, \tag{1.30}$$

where $\underline{F}$ is the resultant of the external forces, classified into three types [Fukagata 00]:

- body forces, such as gravitational force,
- surface forces from the surrounding fluid, such as drag and lift,
- impulsive forces occurring at collisions with the wall or with other particles.

In the present study, only the contributions of gravity and drag are modeled (see justification in [Dufour 05]): $\underline{F} = \underline{F}_g + \underline{F}_D$, as detailed below.

Gravity. The gravitational force is written

$$\underline{F}_g = (\rho_l - \rho)\frac{\pi}{6} d_p^3 \underline{g} \tag{1.31}$$

and in the present case, since $\rho_l \gg \rho$, the buoyancy effects may be neglected, so that

$$\underline{F}_g = m_p \underline{g}\,. \tag{1.32}$$

Drag. Although the liquid volume fraction α_l was assumed small, the mass loading $\alpha_l \rho_l / \rho$ can be comparable or substantially larger than one, resulting in a non-negligible momentum interaction between the phases. Typical liquid densities are of the order of $\rho_l \simeq 10^3\,\mathrm{kg.m^{-3}}$, while gas densities at 293 K are a thousand times lower.

The non-dimensional parameter characterizing the gas-droplet momentum interaction is the particle Reynolds number, defined as

$$\mathrm{Re}_p = \frac{d_p |\underline{u}_p - \underline{u}|}{\nu}\,, \tag{1.33}$$

which involves the gas-droplet slip velocity $\underline{u}_p - \underline{u}$. The response timescale of the droplet to the slip velocity fluctuations is written

$$\tau_p = \frac{4}{3 C_D \mathrm{Re}_p} \frac{\rho_l}{\rho} \frac{d_p^2}{\nu}\,, \tag{1.34}$$

where C_D is the drag coefficient and depends on the particle Reynolds number as

$$C_D \mathrm{Re}_p = \begin{cases} 24\,(1 + 0.15\,\mathrm{Re}_p^{0.687}) & \text{if } \mathrm{Re}_p < 10^3 \\ 0.44\,\mathrm{Re}_p & \text{else} \end{cases} \tag{1.35}$$

The first case in the above equation corresponds to the Stokes regime, in which the drag coefficient varies inversely with Re_p. For $\mathrm{Re}_p < 1$, $C_D \simeq 24/\mathrm{Re}_p$ and the classical Stokes law (1851) is satisfied, with:

$$\tau_p = \frac{1}{18} \frac{\rho_l}{\rho} \frac{d_p^2}{\nu}\,, \quad \mathrm{Re}_p < 1\,. \tag{1.36}$$

The first expression in Eq. (1.35) is an extension of the Stokes law to intermediary particle Reynolds number, and is a widely used empirical correlation proposed by Schiller & Naumann in 1935 [Schiller 35]. The drag coefficient increases with Re_p until the latter reaches 10^3, that is for large droplets or very high slip velocities, where it stabilizes around 0.44 or 0.45 [Crowe 98].

The expression for the drag force is based on that of the momentum relaxation time Eq. (1.34), and reads

$$\underline{F}_D = m_p \frac{1}{\tau_p}(\underline{u}_p - \underline{u}) \,. \tag{1.37}$$

Neglected contributions. Additional effects are not taken into account. They consist of:

- lift force, a lateral force due to particle rotation (slip-spin lift) or to shear of the surrounding fluid (slip-shear lift) [Fukagata 00],
- added mass effect, a contribution due to droplet acceleration,
- Basset force, a history effect caused by a temporal shift between the droplet action on the gas and the actual gas response to this action.

The above contributions can all be neglected because of the large liquid-to-gas density ratio [Boivin 98, Dufour 05]. Moreover, because of the problem geometry, interactions with the walls, in the vicinity of which the drag coefficient is known to increase, need not be described in the present work.

Due to the low volume loading, inter-particle collisions are neglected.

1.2.3 Droplet thermodynamics

The relations pertaining to the evolution of the droplet's diameter and temperature are obtained from mass and energy conservation applied on the droplet system. The framework of the problem and related hypotheses are presented in a first part, from where mass and temperature equations are then derived in subsequent subsections. The specific case of saturation is addressed in a final paragraph. The analyses presented here summarize approaches followed by Kuo [Kuo 86], Sirignano [Sirignano 10], Sazhin [Sazhin 06] and Boileau [Boileau 07].

Model hypotheses

A schematic of the gas–droplet system is shown in Fig. 1.1. Some notations used in the following are listed here:

$_\infty$	Far-field gas property
$_{\mathrm{surf}}$	At the droplet's surface
$_m$	Related to species m
$_F$	Related to the fuel

The main assumptions on which the derivation of the droplet behavior is based are examined below.

Velocity field. A reference frame instantaneously travelling at the velocity of the center of the droplet is used; the droplet appears stationary and the gas moves past it: in the far-field, $\underline{u} = \underline{u}_\infty$.

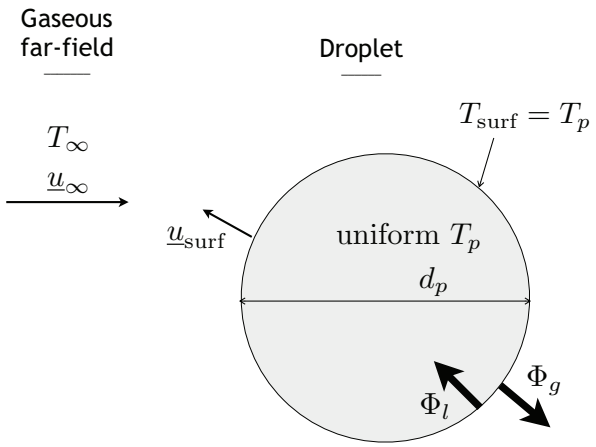

Figure 1.1: Schematic view of the droplet model and notations used in the model.

While the far-field velocity is considered uniform, in the neighborhood of the droplet relative fluid motion may occur, in the form of the so-called Stefan flux: the evaporation of the liquid creates gaseous matter which must move away from the surface since $\rho_l > \rho_g$, therefore $\underline{u}_{\text{surf}} \cdot \underline{e}_r > 0$ (in the case of condensation, the radial velocity is negative). Given the high liquid-to-gas density ratio, the position of the droplet surface may be assumed stationary.

As far as the liquid is concerned, no internal fluid circulation is accounted for.

Thermal response. Fourier heat conduction is assumed, so the temperature equation, which holds separately in the liquid and gaseous phases, involves the flux gradient term

$$\frac{\partial T}{\partial t} \sim \kappa \left(\underline{\nabla} \cdot \underline{\nabla} T \right) . \tag{1.38}$$

where the thermal diffusivity is denoted by $\kappa = \lambda/(C_p \rho)$ taken with liquid- or gas-phase values depending on whether $r < d_p/2$ or $r > d_p/2$. This raises the characteristic heat transfer times

$$\tau_{\text{cond},l} = \frac{d_p^2}{\kappa_l} \qquad \tau_{\text{cond},g} = \frac{d_p^2}{\kappa_g} \tag{1.39}$$

characterizing the thermal response times of respectively the droplet and its surrounding gas film.

The thermal diffusivity of liquids is much lower than that of gases, leading to a smaller thermal response time of the gas phase. Taking values relevant to the present case (ethanol droplet in 293 K O_2-CO_2 mixture[2]), the liquid phase timescale of a 10-µm droplet is about 1.1 ms while that of the surrounding gas layer is rather about 5 µs. Therefore, the thermal response may be assumed quasi-steady in the gas phase, and time derivatives be neglected there, while kept for the liquid phase.

Within the droplet, the density ρ_l and heat capacity $C_{p,l}$ are taken independent of temperature.

Species mass fractions. The droplet phase is considered a single component liquid, referred to as 'fuel'. At the droplet surface, the gas is described as a two-

[2]Using $\kappa_l = 8.4 \times 10^{-8}\,\text{m}^2.\text{s}^{-1}$ for liquid ethanol at 300 K and $\kappa_g = 1.9 \times 10^{-5}\,\text{m}^2.\text{s}^{-1}$ for air

component non-reactive mixture of the newly vaporized fuel and the ambient gas, of respective mass fractions Y_F and $Y_{\neq F} = 1 - Y_F$. The properties of the non-fuel mixture are assumed to be uniform from the droplet surface to the far field. This implies in particular that no flame is located close to the droplet: the gas farther away may be reacting or fully burnt and will influence the droplet's behavior through far-field quantities such as T_∞, but only mixing between the far-field fluid and the freshly evaporated fuel is taken into account in the droplet's vicinity.

The droplet's surface is assumed at phase equilibrium. This yields an expression of the fuel partial pressure p_F through the Clausius-Clapeyron relation:

$$p_F(T) = p_{\text{ref}} \exp\left(\frac{W_F L_V}{\mathcal{R}}\left(\frac{1}{T_{\text{boil}}} - \frac{1}{T}\right)\right) \tag{1.40}$$

where T_{boil} is the boiling point at pressure p_{ref} (arbitrary, usually taken equal to 1 atm), and $L_V = L_V(T_{\text{boil}})$ is the latent heat of vaporization[3]. From there, the fuel molar fraction $X_F = p_F/p$ may be used to express the fuel mass fraction

$$Y_F = \frac{X_F W_F}{X_F W_F + (1 - X_F) W_{\neq F}}\,, \tag{1.41}$$

where the molar weight of the non-fuel mixture is uniform from the surface to the far-field and expressed through

$$W_{\neq F} = \frac{1 - Y_{F,\infty}}{1 - Y_{F,\infty} W_\infty / W_F} W_\infty\,. \tag{1.42}$$

Final system. The gas layer surrounding the droplet ($r > d_p/2$) is described, given the general hypotheses formulated above, by the following equations of an incompressible flow:

$$\text{Mass:} \qquad \underline{\nabla} \cdot (\rho \underline{u}) = 0 \tag{1.43}$$

$$\text{Fuel mass fraction:} \qquad \underline{\nabla} \cdot (\rho \underline{u} Y_F) = \underline{\nabla} \cdot (\rho \mathcal{D} \underline{\nabla} Y_F) \tag{1.44}$$

$$\text{Temperature:} \qquad \underline{\nabla} \cdot (\rho \underline{u} (C_p T)) = \underline{\nabla} \cdot (\lambda \underline{\nabla} T) \tag{1.45}$$

The mass and momentum evolution equations, derived below, are obtained by first considering the reference stagnant case, $\underline{u}_\infty = \underline{0}$, and then extending it to the case of a moving droplet.

Mass evolution

The evolution of the droplet's mass and temperature is best examined, in a first approach, for the case $u_\infty = 0$. Because of the spherical symmetry of the problem in this case, the velocity field is purely radial in the reference coordinate system:

$$\underline{u}(r) = u(r) \underline{e}_r\,. \tag{1.46}$$

[3]The Clausius-Clapeyron relation presented here stems from the integration of the differential expression $\mathrm{d}p = L_V(T)\,\mathrm{d}T/(T\Delta V)$ with the approximations $\Delta V \simeq V$, since the volume of the gaseous phase is very large compared with that of the liquid one, and L_V constant along the integration path $(p_{\text{cc}}, T_{\text{cc}}) \to (p, T)$, valid in practice even on a T variation of up to 100 K.

In the gas, mass conservation (1.43) then leads to

$$4\pi r^2\,\rho u = -\dot{m}_p\,, \tag{1.47}$$

implying that $\rho r^2 u$ is a constant. The quantity $\dot{m}_p \equiv \mathrm{d}m_p/\mathrm{d}t$, is the first unknown of the problem. Consequently, fuel mass fraction conservation (1.44) reads here

$$-\dot{m}_p\frac{\partial Y_F}{\partial r} = \frac{\partial}{\partial r}\left(\rho\mathcal{D}r^2\frac{\partial Y_F}{\partial r}\right)\,. \tag{1.48}$$

Integrating this equation between the surface, $r = d_p/2$, and the far field, $r = \infty$, yields (see [Boileau 07]):

$$u_{\mathrm{surf}}\,\frac{d_p}{2} = \mathcal{D}\log\left(\frac{1-Y_{F,\infty}}{1-Y_{F,\mathrm{surf}}}\right)\,. \tag{1.49}$$

This expression is reformulated by introducing two convenient coefficients, the Spalding mass transfer number B_M

$$B_M = \frac{Y_{F,\mathrm{surf}} - Y_{F,\infty}}{1-Y_{F,\mathrm{surf}}} \tag{1.50}$$

and the Sherwood number $\mathrm{Sh} = 2$. Finally, the mass evolution equation reads:

$$\dot{m}_p = -\pi d_p \mathrm{Sh}\,(\rho\mathcal{D})\log(1+B_M)\,. \tag{1.51}$$

The "1/3-rule". In the previous equation, $\rho\mathcal{D}$ is considered constant, although it depends on properties (temperature and composition) of the gas surrounding the droplet which vary between the surface to the far field. It is common practice to assume that such quantities can be computed as functions of a reference T_{ref} and composition $(Y_m)_{\mathrm{ref}}$, defined as a 2/3–1/3 weighted interpolation of surface values and far-field values [Hubbard 75]:

$$T_{\mathrm{ref}} = 2/3\,T_{\mathrm{surf}} + 1/3\,T_\infty \tag{1.52}$$

$$Y_{m,\mathrm{ref}} = 2/3\,Y_{m,\mathrm{surf}} + 1/3\,Y_{m,\infty}\,. \tag{1.53}$$

In the following, all gas properties for which this assumption is made are denoted by the subscript $_{\mathrm{ref}}$:

$$Q_{\mathrm{ref}} = Q\,(T_{\mathrm{ref}}, (Y_m)_{\mathrm{ref}})\,. \tag{1.54}$$

Diameter evolution. The droplet diameter evolution is deduced from Eq. (1.51) by observing that

$$\mathrm{d}m_p = \frac{\pi}{2}\rho_l d_p^2\,\mathrm{d}d_p \tag{1.55}$$

and therefore

$$\frac{\mathrm{d}d_p}{\mathrm{d}t} = -2\,\frac{\mathrm{Sh}\,\mu_{\mathrm{ref}}}{\rho_l\,\mathrm{Sc}_F}\log(1+B_M)\frac{1}{d_p}\,. \tag{1.56}$$

Introducing the characteristic mass evaporation timescale

$$\tau_m = \frac{\rho_l (d_p^0)^2\,\mathrm{Sc}_F}{4\,\mathrm{Sh}\,\mu_{\mathrm{ref}}\log(1+B_M)} \tag{1.57}$$

leads to the reformulation

$$\frac{\mathrm{d}d_p}{\mathrm{d}t} = -\frac{(d_p^0)^2}{2d_p\tau_m} \,. \tag{1.58}$$

The well-known linear behavior of d_p^2 is recovered: $\mathrm{d}(d_p^2)/\mathrm{d}t = -(d_p^0)^2/\tau_m$.

Convection effects. The case $u_\infty \neq 0$ is addressed by using a modified Sherwood coefficients. A classical empirical expression, proposed by Ranz & Marshall [Ranz 52],

$$\mathrm{Sh} = 2 + 0.55\,\mathrm{Re}_p^{1/2}\,\mathrm{Sc}_F^{1/3} \,, \tag{1.59}$$

accounts for the fact that evaporation is enhanced by relative gas motion. Sirignano [Sirignano 10] points out the limitations of this correlation, that should not be applied if transient heating, regressing interface effects or internal circulation are modeled. However in the present case it is sufficient and will be used hereafter.

Temperature evolution

The analysis starts, here also, from the spherically symmetric stagnant case. The energy balance at the droplet's surface may be written

$$\Phi_l = \dot{m}_p L_V - \Phi_g \tag{1.60}$$

where Φ_g and Φ_l denote the conductive flux contributions, oriented away from the surface in both the liquid and gaseous phases, as illustrated in Fig. 1.1. The quantity Φ_l is the cause for the variation of the droplet temperature T_p:

$$m_p C_{p,l} \frac{\mathrm{d}T_p}{\mathrm{d}t} = \Phi_l \,, \tag{1.61}$$

which enables to write

$$m_p C_{p,l} \frac{\mathrm{d}T_p}{\mathrm{d}t} = \dot{m}_p L_V - \Phi_g \,. \tag{1.62}$$

The same integration as that done for Y_F above is performed on the temperature equation. Eq. (1.45) is cast into

$$-\dot{m}_p C_p \frac{\partial T}{\partial r} = \frac{\partial}{\partial r}\left(\lambda \frac{\partial T}{\partial r}\right) \,, \tag{1.63}$$

which, integrated between the surface and the far field, gives

$$u_{\mathrm{surf}} \frac{d_p}{2} = \frac{\lambda}{\rho C_p} \log\left(1 + \frac{u_{\mathrm{surf}}\,\rho C_p (T_{\mathrm{surf}} - T_\infty)}{[\partial T/\partial r]_{\mathrm{surf}}}\right) \,. \tag{1.64}$$

Like previously, two coefficients are introduced, the heat transfer number B_T

$$B_T = \frac{-\dot{m}_p C_{p,\mathrm{ref}} (T_{\mathrm{surf}} - T_\infty)}{\Phi_g} \tag{1.65}$$

and the Nusselt number $\mathrm{Nu} = 2$. Using the link between Φ_g and the temperature gradient at the particle's surface,

$$\Phi_g = -\pi d_p^2 \lambda \left[\frac{\partial T}{\partial r}\right]_{\mathrm{surf}} \,, \tag{1.66}$$

a new expression for the mass change rate arises:

$$\dot{m}_p = -\pi d_p \mathrm{Nu} \left(\frac{\lambda}{C_{p,\mathrm{ref}}} \right) \log(1 + B_T) \,. \tag{1.67}$$

Combined with the previous expression (1.51), this provides a relation between B_T and B_M:

$$B_T = (1 + B_M)^{\frac{\mathrm{Sh}\,\mathrm{Pr}}{\mathrm{Nu}\mathrm{Sc}_F}} - 1 \,. \tag{1.68}$$

The surface convective flux in the gas may be written as a function of the transfer coefficients:

$$\Phi_g = \frac{1}{d_p} \frac{\mathrm{Nu}\,\mu_{\mathrm{ref}}\, C_{p,\mathrm{ref}}}{\mathrm{Pr}} \frac{\log(1 + B_T)}{B_T} (T_{\mathrm{surf}} - T_\infty) \tag{1.69}$$

$$= \frac{1}{d_p} \frac{\mathrm{Sh}\,\mu_{\mathrm{ref}}\, C_{p,\mathrm{ref}}}{\mathrm{Sc}_F} \frac{\log(1 + B_M)}{B_T} (T_{\mathrm{surf}} - T_\infty) \,. \tag{1.70}$$

Finally, injecting Eq. (1.69) into Eq. (1.62) leads to the droplet temperature evolution equation

$$\frac{\mathrm{d}T_p}{\mathrm{d}t} = \frac{\dot{m}_p}{m_p C_{p,l}} \left(\frac{C_{p,\mathrm{ref}}}{B_T} (T_{\mathrm{surf}} - T_\infty) + L_V \right) . \tag{1.71}$$

Assuming the surface temperature in the gas T_{surf} is equal to the bulk droplet temperature T_p, this becomes

$$\frac{\mathrm{d}T_p}{\mathrm{d}t} = -\frac{1}{\tau_h} \left[T_p - \left(T_\infty - \frac{L_V\, B_T}{C_{p,\mathrm{ref}}} \right) \right] \tag{1.72}$$

with the characteristic heating time

$$\tau_h = \frac{\mathrm{Sc}_F}{6\,\mathrm{Sh}} \frac{B_T}{\log(1 + B_M)} \frac{C_{p,l}}{C_{p,\mathrm{ref}}} \frac{\rho_l d_p^2}{\mu_{\mathrm{ref}}} = \frac{\mathrm{Pr}}{6\,\mathrm{Nu}} \frac{B_T}{\log(1 + B_T)} \frac{C_{p,l}}{C_{p,\mathrm{ref}}} \frac{\rho_l d_p^2}{\mu_{\mathrm{ref}}} \tag{1.73}$$

which compares with the mass evaporation time as:

$$\tau_h = \frac{2}{3} \frac{B_T C_{p,l}}{C_{p,\mathrm{ref}}} \tau_m \,. \tag{1.74}$$

Convection effects. Relative gas motion is taken into account through a correlation on Nu similar to Eq. (1.59):

$$\mathrm{Nu} = 2 + 0.55\,\mathrm{Re}_p^{1/2}\,\mathrm{Pr}^{\,1/3} \,. \tag{1.75}$$

Saturation

The set of relations derived above presents singularities as the droplet temperature T_p nears the boiling temperature T_{boil}: the gaseous layer at the droplet surface then reaches saturation, *i.e.* $Y_{F,\mathrm{surf}}$ tends to 1, and B_M diverges to infinity, see Eq. (1.50). Another system may be written in this situation.

The droplet is boiling, with a constant temperature

$$T_p = T_{\text{boil}} \,, \tag{1.76}$$

so that, in Eq. (1.72), $\mathrm{d}T/\mathrm{d}t = 0$ and a saturated heat transfer coefficient may be introduced

$$B_T^{\text{sat}} = \frac{C_{p,\text{ref}}(T_\infty - T_{\text{boil}})}{L_V} \,. \tag{1.77}$$

The mass evolution equation is modified. In Eq. (1.60), $\Phi_l = 0$ and therefore

$$\dot{m}_p = \frac{\Phi_g}{L_V} \,. \tag{1.78}$$

Eq. (1.69) still holds, with $B_T = B_T^{\text{sat}}$, so that

$$\dot{m}_p = -\pi d_p \frac{\mathrm{Nu}\,\mu_{\text{ref}}}{\mathrm{Pr}} \log(1 + B_T^{\text{sat}}) \,. \tag{1.79}$$

or also, on the same pattern as the non-saturated relation (1.51),

$$\dot{m}_p = -\pi d_p \frac{\mathrm{Sh}\,\mu_{\text{ref}}}{\mathrm{Sc}_F} \log(1 + B_M^{\text{sat}}) \,, \tag{1.80}$$

with B_M^{sat} consistently related with B_T^{sat} according to Eq. (1.68).

1.2.4 Two-way coupling

The transfer of mass, momentum, energy and scalars from the droplets to the gas is described by source terms appended to the equations governing the continuous phase.

$$\frac{\partial \rho}{\partial t} + \underline{\nabla} \cdot (\rho \underline{u}) = S_M \tag{1.81}$$

$$\frac{\partial (\rho \underline{u})}{\partial t} + \underline{\nabla} \cdot (\rho \underline{u} \otimes \underline{u}) = -\underline{\nabla} p + \underline{\nabla} \cdot \underline{\underline{\tau}} + \rho \underline{f} + \underline{S}_D \tag{1.82}$$

$$\begin{aligned} \frac{\partial (\rho e_t)}{\partial t} + \underline{\nabla} \cdot (\rho \underline{u} e_t) &= -\underline{\nabla} \cdot (p \underline{u}) + \underline{\nabla} \cdot (\underline{\underline{\tau}} \cdot \underline{u}) + \underline{\nabla} \cdot (\lambda \underline{\nabla} T) \\ &\quad + \rho \underline{f} \cdot \underline{u} + \dot{\mathcal{Q}} + S_E \end{aligned} \tag{1.83}$$

According to the point-source approximation discussed above, these source terms are localized at the particles' positions, and related to their individual property variations: the mass source term may be expressed as

$$S_M(\underline{x}, t) = \frac{1}{\Delta V} \sum_{k=1}^{N} -\dot{m}_p^{(k)} \delta\big(\underline{x} - \underline{x}_p^{(k)}(t)\big) \,, \tag{1.84}$$

where δ is the Dirac function and ΔV a control volume, theoretically of the order of the particle dimension (point-source hypothesis) but usually chosen to be, in the practice of simulation, of the order of the local spatial resolution. The momentum

source term corresponds to the reaction of the particles to the force exerted on them by the gas, which in the present case comes down to the drag force:

$$\underline{S}_D(\underline{x},t) = \frac{1}{\Delta V}\sum_{k=1}^{N} -\underline{F}_D^{(k)}\delta\big(\underline{x}-\underline{x}_p^{(k)}(t)\big)\ . \tag{1.85}$$

The energy source term involves the energy flux transferred from the droplet to the gas, Φ_g. According to Eq. (1.62),

$$S_E(\underline{x},t) = \frac{1}{\Delta V}\sum_{k=1}^{N}\left(-m_p^{(k)}C_{p,l}\frac{\mathrm{d}T_p^{(k)}}{\mathrm{d}t} + \dot{m}_p^{(k)}L_V\right)\delta\big(\underline{x}-\underline{x}_p^{(k)}(t)\big)\ . \tag{1.86}$$

Additionally, the transported scalars affected by the local creation of fuel vapor also see an evaporation source term appear in their balance equation. This is the case of the species mass fractions: denoting by $Y_{m,\mathrm{fuel}}$ the value of Y_m in pure fuel vapor, Eq. (1.10) becomes:

$$\frac{\partial(\rho Y_m)}{\partial t} + \underline{\nabla}\cdot(\rho\underline{u}Y_m) = \underline{\nabla}\cdot(\rho\mathcal{D}\underline{\nabla}Y_m) + \dot{\omega}_m + Y_{m,\mathrm{fuel}}\,S_M\ . \tag{1.87}$$

1.3 Filtered equations for LES

The numerical simulations carried out in this work are Large-Eddy Simulations. They aim at solving only the large structures of the turbulent flow while its small-scale features are modeled. This approach is justified by the idea that the smaller eddies, in the inertial range, present more universal characteristics (isotropy, short lifetime,...) than the large eddies that are directly impacted by the geometry, boundary conditions and physical properties of the fluid.

The scale separation is obtained by a spatial filtering of the unknown fields, resulting in equations examined in a first paragraph (Section 1.3.1). Unclosed terms arise, for which expressions are found by invoking the model assumptions formulated for the smaller scales. In this section, only the closure of turbulent terms is discussed (Section 1.3.2); models for chemistry are presented in the chapter devoted to combustion (Section 4.2). Assumptions for the coupling of the continuous phase with the spray are finally formulated in Section 1.3.3.

1.3.1 Filtering

The filtering operator is the spatial convolution with a filter function $\mathcal{G}_\Delta$, characterized by its size Δ (see usual filters in [Poinsot 05]); a scalar field $\phi(\underline{x},t)$ becomes, once filtered:

$$\overline{\phi}(\underline{x},t) = \iiint_{-\infty}^{\infty}\phi(\underline{x}',t)\mathcal{G}_\Delta(\underline{x}'-\underline{x})\mathrm{d}\underline{x}'\ . \tag{1.88}$$

The departure from the filtered value, displaying sub-filter spatial fluctuations, is denoted by

$$\phi' = \phi - \overline{\phi}\ . \tag{1.89}$$

The filter function must satisfy the following normalization rule

$$\iiint_{-\infty}^{\infty} \mathcal{G}_\Delta(\underline{x})\mathrm{d}\underline{x} = 1 \tag{1.90}$$

and commute with derivation in time or space:

$$\frac{\partial\overline{\phi}}{\partial t} = \overline{\frac{\partial\phi}{\partial t}} \quad \text{and} \quad \underline{\nabla}\overline{\phi} = \overline{\underline{\nabla}\phi}\,. \tag{1.91}$$

The definition (1.88) implies that the filtering operation is linear. Commutativity with spatial derivation is ensured if $\mathcal{G}_\Delta$ is isotropic and Δ uniform in space, and with time derivation if Δ is constant.

In practice however, numerical simulations often rely on non-uniform filter sizes (irregular meshes) and locally anisotropic filter functions (next to domain boundaries). Hypothesis (1.91) is only partly satisfied, but it is a commonly accepted approximation: For non-uniform filtering, it was shown that the commutative error is negligible provided that Δ has $n-1$ vanishing moments, n being the order of the spatial integration scheme of the LES [Vasilyev 98]. Addressing this question further is beyond the purpose of this work.

The density-weighted filtering, also referred to as Favre filtering, is defined as

$$\widetilde{\phi} = \frac{\overline{\rho\phi}}{\overline{\rho}}\,, \tag{1.92}$$

with the unresolved part denoted by $\phi'' = \phi - \widetilde{\phi}$. It is a notion convenient for the filtering of compressible Navier–Stokes equations (1.1)–(1.3) and (1.10), which yields [Poinsot 05]:

$$\frac{\partial\overline{\rho}}{\partial t} + \underline{\nabla}\cdot(\overline{\rho}\widetilde{\underline{u}}) = \overline{S}_M \tag{1.93}$$

$$\frac{\partial(\overline{\rho}\widetilde{\underline{u}})}{\partial t} + \underline{\nabla}\cdot(\overline{\rho}\widetilde{\underline{u}}\otimes\widetilde{\underline{u}}) = -\underline{\nabla}\,\overline{p} + \underline{\nabla}\cdot\left(\overline{\underline{\tau}} - \overline{\rho}\,\underline{\underline{\mathcal{T}}}\right) + \overline{\rho}\widetilde{\underline{f}} + \overline{S}_D \tag{1.94}$$

$$\begin{aligned}\frac{\partial(\overline{\rho}\widetilde{e}_t)}{\partial t} + \underline{\nabla}\cdot(\overline{\rho}\widetilde{\underline{u}}\widetilde{e}_t) &= -\underline{\nabla}\cdot(\overline{p\underline{u}}) + \underline{\nabla}\cdot(\overline{\underline{\tau}\cdot\underline{u}}) \\ &+ \underline{\nabla}\cdot\left[\overline{\lambda\underline{\nabla}T} - \overline{\rho}\,(\widetilde{\underline{u}\widetilde{e}_t} - \widetilde{\underline{u}}\,\widetilde{e}_t)\right] + \overline{\rho}\widetilde{\underline{f}\cdot\underline{u}} + \overline{\dot{\mathcal{Q}}} + \overline{S}_E\end{aligned} \tag{1.95}$$

$$\frac{\partial(\overline{\rho}\widetilde{Y}_m)}{\partial t} + \underline{\nabla}\cdot(\overline{\rho}\widetilde{\underline{u}}\widetilde{Y}_m) = \underline{\nabla}\cdot\left[\overline{\rho\mathcal{D}_m\underline{\nabla}Y_m} - \overline{\rho}\left(\widetilde{\underline{u}Y}_m - \widetilde{\underline{u}}\,\widetilde{Y}_m\right)\right] + \overline{\dot{\omega}}_m + \overline{S}_{Y_m} \tag{1.96}$$

Several terms in these equations require modeling:

- A closure must be provided for the unresolved Reynolds stress

$$\underline{\underline{\mathcal{T}}} = \widetilde{\underline{u}\otimes\underline{u}} - \widetilde{\underline{u}}\otimes\widetilde{\underline{u}} \tag{1.97}$$

  of components $\mathcal{T}_{ij} = \widetilde{u_iu_j} - \widetilde{u}_i\widetilde{u}_j$. A classical eddy-viscosity approach is used in the simulations of this work: turbulent fluxes are modeled by an expression similar to the laminar definition Eq. (1.4) as

$$\underline{\underline{\mathcal{T}}} = \mu_t\left(\underline{\underline{\nabla}}\,\widetilde{\underline{u}} + {}^{\mathrm{T}}\underline{\underline{\nabla}}\,\widetilde{\underline{u}} - \frac{2}{3}(\underline{\nabla}\cdot\widetilde{\underline{u}})\,\underline{\underline{1}}\right)\,, \tag{1.98}$$

where $\mu_t = \overline{\rho}\nu_t$ is referred to as the turbulent viscosity. An expression must be provided for ν_t from the knowledge of the sole resolved fields. This is the purpose of subgrid turbulence models, examined below in Section 1.3.2.

- On a similar pattern, the unresolved energy flux and species fluxes are respectively modeled with a turbulent Prandtl number Pr_t

$$(\widetilde{\underline{u}e_t} - \widetilde{\underline{u}}\,\widetilde{e}_t) = -\frac{\nu_t}{\mathrm{Pr}_t}\underline{\nabla}\widetilde{e}_t \tag{1.99}$$

and a turbulent Schmidt number Sc_t

$$\left(\widetilde{\underline{u}Y_m} - \widetilde{\underline{u}}\,\widetilde{Y}_m\right) = -\frac{\nu_t}{\mathrm{Sc}_t}\underline{\nabla}\widetilde{Y}_m, \quad m = 1, \ldots, N_s \tag{1.100}$$

Like their laminar counterparts, Pr_t and Sc_t are set as constants in the present simulations.

- For the filtered laminar diffusion fluxes, simple assumptions are made:

$$\overline{\lambda\underline{\nabla}T} = \overline{\lambda}\underline{\nabla}\widetilde{T} \quad \text{and} \quad \overline{\rho\mathcal{D}_m\underline{\nabla}Y_m} = \overline{\rho}\overline{\mathcal{D}}_m\underline{\nabla}\widetilde{Y}_m\,. \tag{1.101}$$

- The pressure velocity term $\underline{\nabla}\cdot(\overline{p\underline{u}})$ is approximated by $\underline{\nabla}\cdot(\overline{p}\widetilde{\underline{u}})$.
- The closure of the filtered chemical source terms $\overline{\dot{\omega}}_m$ represents an important part of the modeling effort in LES of turbulent reacting flows; this topic is the object of Section 4.2.

1.3.2 Sub-filter scale turbulence models for LES

The two sub-filter turbulence models that have been used in the present work are briefly presented below.

The Smagorinsky model

This model is derived by assuming the production and dissipation (ε) terms in the sub-filter kinetic energy transport equation are higher than the others and thus balance each other [Smagorinsky 63]. This leads to $\nu_t = \varepsilon/(2|\underline{\underline{S}}|^2)$ where $\underline{\underline{S}} = \frac{1}{2}(\underline{\underline{\nabla}}\,\underline{u} + {}^{\mathrm{T}}\underline{\underline{\nabla}}\,\underline{u})$ and, with a dimensional analysis, gives the estimation

$$\nu_t = \sqrt{2}(C_s\Delta)^2|\widetilde{\underline{\underline{S}}}|\,, \tag{1.102}$$

the norm of a second-order tensor being defined as $|\underline{\underline{S}}| = (S_{ij}S_{ij})^{1/2}$. C_s is the so-called Smagorinsky constant, usually prescribed to lie in the $[0.1; 0.2]$ range, and Δ is the filter size.

In the present work, C_s is determined by means of a dynamic procedure [Germano 91a, Germano 91b], based on a deduction of the sub-filter scale behavior from the smallest resolved scale, and that requires the filtering, at a scale larger than Δ of the resolved velocity field.

The Wall-Adapting Local Eddy-viscosity (WALE) model

This model was introduced in 1999 by Nicoud & Ducros [Nicoud 99], and aims, by including the effect of strain rotation, at a better prediction in high-vorticity regions – in particular, it reproduces near wall scaling $\nu_t = \mathcal{O}(y^3)$. It involves the traceless symmetric part of the resolved velocity gradient tensor $\underline{\underline{S}}$, denoted by $\underline{\underline{s}}^d$:

$$\underline{\underline{s}}^d = \frac{1}{2}\left[(\underline{\underline{\nabla}}\,\underline{u})^2 + {}^{\mathrm{T}}(\underline{\underline{\nabla}}\,\underline{u})^2\right] - \frac{1}{3}\mathrm{Tr}(\underline{\underline{\nabla}}\,\underline{u})\underline{\underline{1}}\,. \tag{1.103}$$

ν_t is formulated as

$$\nu_t = C_{\mathrm{W}}^2 \Delta^2 \frac{|\widetilde{\underline{\underline{s}}}^d|^3}{|\widetilde{\underline{\underline{S}}}|^5 + |\widetilde{\underline{\underline{s}}}^d|^{5/2}}\,. \tag{1.104}$$

1.3.3 Sub-filter-scale liquid–gas coupling

On top of the approximations already needed for the deterministic description of particle-laden flows (Section 1.2.1), additional modeling is necessary in LES, where only the resolved scales are available. In this section, the formulation of the sub-filter two-way coupling is discussed.

Impact of the dispersed phase on the sub-filter turbulence

The modeling of unresolved terms examined in the previous section pertained to single-phase flows. The first question is whether these sub-filter turbulence models are still valid in the presence of particles. As soon as the mass loading is larger than about one, at least two impacts may be expected at sub-filter scales: first, a modified energy spectrum and cascade process, with a higher dissipation of the gas turbulent energy at length scales of the order of the particle dimensions [Boivin 98]; second, the preferential concentration of the particles at the edge of sub-filter vortices [Fessler 94, Reveillon 07] may locally increase or decrease the effects of the two-way coupling. Boivin *et al.* [Boivin 00] noted however that the sub-filter modeling of turbulence is less critical for two-phase flows because the particles catch a large part of the dissipated energy coming from the large scales. Moreover, an *a posteriori* study of a temporal mixing layer by Leboissetier *et al.* [Leboissetier 05] concluded that sub-filter models presented the same strengths and weaknesses in two-phase flows as in single-phase flows. Apart from an isolated study by Yuu *et al.* [Yuu 01] in which a specific two-phase turbulent model was used, the usual single-phase models are used.

In exploratory studies [Okong'o 04, Leboissetier 05], the Smagorinsky model was found to be less than optimal for two-phase flows. However, most practical studies, including the recent ones [Jones 10b, Wang 10a, Jones 11, Sanjosé 11] have successfully used this model, and a similar choice is made here. Future work should assess the impact of this simplifying assumption.

Impact of the gaseous sub-filter fluctuations on the dispersed phase

The dispersed phase equations, and consequently the droplet source terms for the continuous phase, involve local gas properties ϕ, but in LES only the resolved part $\widetilde{\phi}$ is

known[4]. In the present paragraph, ϕ stands for the quantities involved in Eqs. (1.37), (1.50), (1.52–1.53) and (1.65), namely $\underline{u}$, $Y_{F,\infty}$, $Y_{m,\infty}$ and T_∞.

The reproduction of the sub-filter fluctuations is an important matter : "In an LES of a dilute spray, the magnitude of any error associated with the use of an unmodified single phase sgs model is likely to be much smaller than that due to an inadequate representation of the dispersion effects of the unresolved gas fluctuations on the liquid dispersed phase" [Okong'o 04, Bini 08]. At stake is the prediction of the particle dispersion and preferential concentration.

As described in [Okong'o 04], several alternatives can be considered to express ϕ from accessible quantities: (i) neglecting the sub-filter fluctuations, taking $\phi = \widetilde{\phi}$ (ii) random, where ϕ is a random variable following a Gaussian law with mean $\widetilde{\phi}$ and a modeled standard deviation σ_ϕ^{sgs} (iii) deterministic, using $\phi = \widetilde{\phi} - \overline{\sigma}\,\text{sign}(\underline{\nabla}^2\widetilde{\phi})$, with $\overline{\sigma}$ written as a function of σ_ϕ^{sgs}, $\widetilde{\phi}$ and $\widetilde{\phi\phi}$. The authors conclude that the baseline approach (i) yields better results than the random model (ii) but still not as good as the deterministic model (iii). Other models are available, as summarized by Pozorski & Apte [Pozorski 09]. The latter authors themselves propose a stochastic Langevin model and assess its results in terms of preferential concentration prediction. In a competing work, Bini & Jones advocate the use of a more general method, which accounts for the dependence of the particle drag time with Re_p outside of the Stokes regime – see Eq. (1.35) – and the resulting heavy-tailed probability density function for the particle acceleration [Bini 07]. The utilization of this model in subsequent works [Bini 08, Bini 09, Jones 10b, Jones 10c] yields good predictive capabilities of the long term particle dispersion.

The two-phase flow simulated in the present study does not require such an advanced prediction of the particle interaction with high flow frequencies: as will be discussed in Section 3.2.2, the particles act almost exclusively, over their short lifetime, as momentum sources not sinks, and the overall spray behavior, upstream of its quick evaporation in the flame, is expected to be relatively insensitive to more than the resolved flow. Since, at this stage, the main interest is the study of the flame structure, the sub-filter fluctuations are neglected and approach (i) is followed: $\underline{u}_\infty = \widetilde{\underline{u}}$.

Similar to the small-scale velocity fluctuation modeling, sub-filter modeling for the temperature fluctuations, relevant to the prediction of evaporation, was also proposed [Bini 09]. But again, for simplicity reasons, the baseline model $T_\infty = \widetilde{T}$ is used here.

1.4 Parameterization of mixing

One of the objectives of the present work is to address combustion problems that involve complex mixing configurations. In this section, general results about the parameterization of mixing by passive scalars are discussed; in particular the mixture fraction scalars are introduced.

[4]and in LES of reactive flows, some quantities themselves, such as $\widetilde{T}$, need to be modeled.

1.4.1 Passive scalars and N-fluid problem

In the cases studied in this work, the large number of species and radicals, which can reach several hundreds, makes it impossible to solve a transport equation for each of them. The introduction of the mixture fraction scalars Z_k is meant to alleviate this difficulty. These quantities track, in each point of the flow, the local proportions of fluids originating from the different inlet streams. They are blind to any other phenomenon than mixing, and especially to the chemical reaction.

The mixture fractions behave as passive scalars. In this section, general results on this class of physical quantities are first given, the notion of an N-fluid problem is defined, and the practical definition of the Z_k is then detailed.

Passive scalars

A fluid mechanics problem is considered, where the flow is subsonic and the boundary conditions are of three types: inlet, outlet and no-slip walls. In this paragraph, the following result is proved: *if there are N_{inlet} inlets, the maximum number of passive scalars to carry independent information is N_{inlet}. Any additional passive scalar is necessarily a linear combination of the others.*

Let ϕ be a passive scalar, obeying the conservative, source-term-free transport equation

$$\rho\frac{\partial\phi}{\partial t} + \rho\underline{u}\cdot\underline{\nabla}\phi = \underline{\nabla}\cdot(\rho\mathcal{D}\underline{\nabla}\phi) \ , \tag{1.105}$$

and constrained at the inlet boundary conditions by constant and uniform ingoing values, defined on the inlet boundaries denoted by $\mathcal{B}_i$, $i = 1, \ldots, N_{\text{inlet}}$:

$$\phi(\underline{x}, t) = \phi_i^{\text{bc}}, \quad \forall \underline{x} \in \mathcal{B}_i \ . \tag{1.106}$$

In the conditions defined above, such a problem is mathematically well-posed: using the NSCBC formalism, for instance [Poinsot 92, Lodato 08a], the characteristic wave involving ϕ is outgoing at walls and at the outlets, and ingoing at the inlet. The values ϕ_i^{bc} are necessary and sufficient requirements to pose the problem.

Let ψ be another passive scalar, obeying the same transport equation, and the boundary conditions ψ_i^{bc} defined on the same set subdivision $\{\mathcal{B}_i\}$. The linearity of Eq. (1.105) implies that any linear combination of ϕ and ψ, $a_\phi\phi + a_\psi\psi$ is also a passive scalar, verifying the same equation, and the solution of the problem with boundary conditions $a_\phi\phi_i^{\text{bc}} + a_\psi\psi_i^{\text{bc}}$, $i = 1, \ldots, N_{\text{inlet}}$.

Linearity and the fact that a passive scalar is fully determined by its set of N_{inlet} inlet boundary conditions lead directly to the desired result: the problem is linear, of dimension N_{inlet}. Two passive scalars are independent if and only if vector ϕ_i^{bc} and ψ_i^{bc} are not colinear. Furthermore, any two sets of N_{inlet} passive scalars are linearly related.

In a practical context, since a constant and uniform field equal to one is a solution of the passive scalar equation, it is never necessary to transport more than $N_{\text{inlet}} - 1$ passive scalars to retrieve the information carried by this class of fields.

N-fluid problem

Considering a fluid mechanics problem as defined above, and only from a mixing, non-reacting, point of view (imagining all chemical reactions are disabled), the configuration may be defined as an N-fluid problem if the number of degrees of freedom of the inlet properties is $N-1$. This means that there exist N reference fluid conditions such that any of the inlets $i = 1, \ldots, N_{\text{inlet}}$ is a mixture of these N fluids. Considering a property Q which is linearly conserved by mixing (such as energy/enthalpy or the mass fractions), there exist N constant reference values $Q_1, Q_2, \ldots, Q_N$ such that for any $i = 1, \ldots, N_{\text{inlet}}$, Q_i^{bc} is a linear combination of them.

It must be stressed that this value N is independent of the number of inlets (with only the inequality $N \leq N_{\text{inlet}}$ holding).

In a standard configuration, $N = N_{\text{inlet}}$, so that the reference conditions are superposed with those of the inlets. Most often the combustion problem consists of the mixing (and reaction, but this does not enter the present discussion) of an oxidizer (Ox) and a fuel (F), forming a two-fluid problem. The REOXAL configuration, studied in Chapter 6 of this study, involves a third fluid, whose properties are not linearly related with those of the other two. It forms a three-fluid problem.

1.4.2 Mixture fractions

Mixture fractions are scalars describing the mixture that, given some hypotheses, are passive scalars. Their definition is given here and their properties discussed.

Elemental mass fractions Z'_p

The most rigorous definition of a mixture fraction is based on atomic elements, *i.e.* C, H or O in the hydrocarbon flames that are the subject of this work. Denoting the number of atoms of element p in species m by $a_{m,p}$ (for example $a_{\text{CH}_4,\text{C}} = 1$, $a_{\text{CH}_4,\text{H}} = 4$), the quantity Z'_p is defined as

$$Z'_p = \sum_{m=1}^{N_s} a_{m,p} \left(\frac{W_p}{W_m} \right) Y_m \, . \tag{1.107}$$

This scalar obeys the following transport equation, obtained by a linear combination of several instances of Eq. (1.10) thanks to the hypothesis $\mathcal{D}_m = \mathcal{D}$:

$$\frac{\partial(\rho Z'_p)}{\partial t} + \underline{\nabla} \cdot (\rho \underline{u} Z'_p) = \underline{\nabla} \cdot (\rho \mathcal{D} \underline{\nabla} Z'_p) + \underbrace{\sum_m a_{m,p} \left(\frac{W_p}{W_m} \right) \dot{\omega}_m}_{0} \, . \tag{1.108}$$

The source term of this equation is necessarily zero, because of the conservation of elements: any set of chemical reactions, leading to the source term $\dot{\omega}_m$ for species m, is neutral as far as the elements p are concerned. As a consequence, the Z'_p are passive scalars.

Mixture fractions Z_i

The mixture fractions are defined as normalizations of one of the elemental mass fractions Z'_p. The most common case of a two-fluid problem – where a single mixture fraction Z is sufficient to parameterize the mixing state – is first presented; then, a generalization of the formalism to a larger number of degrees of freedom $N > 2$ is proposed.

Two-fluid configuration. A problem is considered in which the flow can be described as the mixing of two fluids 1 and 2 forming the reference conditions (see the above discussion on the definition of an N-fluid problem). The following quantities are introduced:

$$\begin{aligned} Z_{p,1} &= \frac{Z'_p - Z'_{p,2}}{Z'_{p,1} - Z'_{p,2}} \,, \\ Z_{p,2} &= \frac{Z'_p - Z'_{p,1}}{Z'_{p,2} - Z'_{p,1}} = 1 - Z_{p,1} \,, \end{aligned} \tag{1.109}$$

where $Z'_{p,1}$ and $Z'_{p,2}$ are the values of the elemental mass fraction Z'_p in the reference conditions 1 and 2, by hypothesis constant in time. The scalar field $Z_{p,1}$ is equal to 1 in the pure fluid-1 conditions and to 0 in pure fluid-2 conditions, and, since it is a passive scalar, remains in the interval $[0;1]$ in the rest of the flow[5], and vice versa for $Z_{p,2}$. First of all, $Z_{p,1}$ and $Z_{p,2}$ are passive scalars, since they depend linearly on Z'_p. Second of all, they are indifferent to the choice of p, since they obey the same passive scalar equation and have identical ingoing boundary conditions. Notice only that p should be chosen such that $Z'_{p,1} \neq Z'_{p,2}$, otherwise the definitions in Eq. (1.109) are invalid.

Since $Z_{p,2} = 1 - Z_{p,1}$, the two quantities provide redundant information, and only one is needed. Classically, in a canonical oxidizer–fuel case, the definition of the mixture fraction Z is that which enables $Z = 0$ in pure oxidizer (Ox) conditions and $Z = 1$ in pure fuel (F) conditions. Thus,

$$Z = \frac{Z'_p - Z'_{p,\mathrm{Ox}}}{Z'_{p,\mathrm{F}} - Z'_{p,\mathrm{Ox}}} \,, \tag{1.110}$$

where p is indifferent, often taken as C or O.

N-fluid configuration. The generalization of the definition above to a larger number $N > 2$ of reference conditions is straightforward. For any couple $(j,k) \in [1;N]^2$, $j \neq k$, the mixture fraction $Z_{j,k}$ is introduced, defined as

$$Z_{j,k} = \frac{Z'_p - Z'_{p,k}}{Z'_{p,j} - Z'_{p,k}} \tag{1.111}$$

[5]Due to the absence of a source term, the purely diffusive equation of a passive scalar ϕ leads to a systematic "erosion" of peak values: in the vicinity of a local maximum, considering a control volume $\mathcal{V}$ stagnant in a frame of reference at velocity $\underline{u}$ that follows this local maximum, the average divergence of the flux $\mathcal{D}\underline{\nabla}\phi$ in $\mathcal{V}$ is negative, meaning the average value of ϕ in the control volume decreases. The converse is true for a local minimum.

Therefore, if the limit conditions of ϕ are bounded by $[0;1]$, its value stay enclosed in this interval throughout the flow.

with p chosen for each (j,k) such that the denominators are non-zero. $Z_{j,k}$ is equal to 0 in pure fluid-j conditions and to 1 in pure fluid-k conditions. With this definition, $N(N-1)$ variables have been introduced, which are in excess compared with the $N-1$ degrees of freedom which necessitate only $N-1$ variables. It is sufficient to fix j and to define the $N-1$ mixture fractions of the problem as

$$Z_k = Z_{j,k}, \quad j \text{ fixed}, \quad k = 1, \ldots, N,\ k \neq j \tag{1.112}$$

so that all Z_k are equal to 0 in pure fluid-j conditions.

Chapter 2

Numerical implementation

The numerical simulations performed in this work involve two computational flow solvers and rely on three different formalisms for the Eulerian resolution of the Navier–Stokes equations:

- SiTCom (**Si**mulating **T**urbulent **Com**bustion) is a fully compressible solver designed for Cartesian meshes, used here for the development of the FCCT combustion model and applied to the computation of a single-phase turbulent lifted jet flame (Chapter 5).
- YALES2 (**Y**et **A**nother **LES S**olver) is a low-Mach solver, employed, when it comes to the gaseous phase, in two frameworks: the incompressible formulation of the Navier–Stokes equations (`ics` solver), convenient for addressing the frozen flow properties (Chapter 3), and a variable-density formulation (`vds` solver), for the reactive flows (Chapter 4).

YALES2 also includes a Lagrangian spray solver, with which the simulation of the SAFIR burner is performed in this work. A discussion on this solver is the object of Section 2.2.

SiTCom and YALES2 are designed for running in parallel on a large number of processors; in Section 2.3 the strategies of both solvers regarding this point are presented.

A number of contributions has been brought to YALES2 in the context of this work, as listed here:

- the implementation of the droplet evaporation model in the solver (Section 2.2.3)
- the development of a particle-aware load-balancing approach (Section 2.3.2)
- the development of an approach for conveniently comparing the simulated spray properties with experimental measurements of droplet properties statistics (Section 2.4.1)
- the design of algorithms for realistic particle injection (Section 2.4.2)

These contributions extended the range of two-phase configurations that YALES2 is able to tackle, from relatively simple textbook cases to realistic spray flows, like the SAFIR burner.

Contents

2.1 Continuous phase

In this section, we introduce the theoretical framework of the different formalisms and present the characteristics of the solvers.

2.1.1 Fully compressible: SiTCom

Finite volume formulation. SiTCom solves the filtered Navier–Stokes equations (1.93–1.96) by an explicit finite volume approach and is written for cartesian grids. The balance equations may be symbolically written as

$$\frac{\partial \overline{\rho}\widetilde{\phi}}{\partial t} + \underline{\nabla} \cdot \underline{\mathcal{F}}_{\phi}^{\text{conv}} = \underline{\nabla} \cdot \underline{\mathcal{F}}_{\phi}^{\text{diff}} + \overline{S}_{\phi} \,, \tag{2.1}$$

where ϕ stands for either of the transported quantities, including 1 for the density equation, and $\underline{\mathcal{F}}^{\text{conv}}$ and $\underline{\mathcal{F}}^{\text{diff}}$ respectively denote the convective and diffusive fluxes. The filtered source terms are gathered in S_ϕ. Integrated spatially on a control volume $\mathcal{V}$ of surface $\mathcal{S}$ and in time on an interval $[t^n; t^{n+1}]$ such that $\Delta t = t^{n+1} - t^n$, this equation becomes:

$$\begin{aligned} \int_{t^n}^{t^{n+1}} \int_{\mathcal{V}} \overline{\rho}\widetilde{\phi} \, \mathrm{d}V \mathrm{d}t \;\; + \;\; & \int_{t^n}^{t^{n+1}} \int_{\mathcal{S}} \underline{\mathcal{F}}_{\phi}^{\text{conv}} \cdot \underline{n} \, \mathrm{d}S \mathrm{d}t \\ = \;\; & \int_{t^n}^{t^{n+1}} \int_{\mathcal{S}} \underline{\mathcal{F}}_{\phi}^{\text{diff}} \cdot \underline{n} \, \mathrm{d}S \mathrm{d}t + \int_{t^n}^{t^{n+1}} \int_{\mathcal{V}} \overline{S}_{\phi} \, \mathrm{d}\underline{x} \mathrm{d}t \,. \end{aligned} \tag{2.2}$$

This is reformulated as:

$$(\widehat{\overline{\rho}\widetilde{\phi}})^{n+1} - (\widehat{\overline{\rho}\widetilde{\phi}})^{n} = \int_{t^n}^{t^{n+1}} (-\mathbb{C} + \mathbb{D} + \mathbb{S})\,\mathrm{d}t\,, \tag{2.3}$$

where

$$\widehat{Q}^n = \frac{1}{\mathcal{V}} \int_{\mathcal{V}} Q(\underline{x}, t^n)\,\mathrm{d}\underline{x} \tag{2.4}$$

is the average value of a quantity $Q(\underline{x}, t)$ on the control volume $\mathcal{V}$ at time t^n.

Discretization. The division of the computational domain into control volumes follows the orthogonal hexahedra of the cartesian grid. The values $\widehat{Q}$ are stored at the center of the cells.

Spatial integration. The convective terms $\mathbb{C}$ are solved with a fourth-order skew-symmetric-like scheme [Ducros 00]; the diffusive fluxes $\mathbb{D}$ are handled with a fourth-order centered scheme. Artificial viscosity is added in Eq. (2.3) as a term $\mathbb{A}$, following the High-Resolution Switched Scheme [Tatsumi 95]. Boundary conditions are solved according to the 3D-NSCBC formalism [Lodato 08b]. The reader is referred to Lodato's PhD thesis for extensive details on SiTCom [Lodato 08a].

Temporal integration. An explicit third-order TVD (total variation diminishing) Runge-Kutta is used as the temporal scheme: quantities at time $n+1$ are computed following:

$$(\widehat{\overline{\rho}\widetilde{\phi}})^{+} = (\widehat{\overline{\rho}\widetilde{\phi}})^{n} + \Delta t\,(-\mathbb{C}^n + \mathbb{D}^n + \mathbb{A}^n + \mathbb{S}^n)\,, \tag{2.5}$$

$$(\widehat{\overline{\rho}\widetilde{\phi}})^{*} = \frac{3}{4}(\widehat{\overline{\rho}\widetilde{\phi}})^{n} + \frac{1}{4}(\widehat{\overline{\rho}\widetilde{\phi}})^{+} + \frac{\Delta t}{4}\left(-\mathbb{C}^{+} + \mathbb{D}^{+} + \mathbb{A}^{+} + \mathbb{S}^{+}\right)\,, \tag{2.6}$$

$$(\widehat{\overline{\rho}\widetilde{\phi}})^{n+1} = \frac{1}{3}(\widehat{\overline{\rho}\widetilde{\phi}})^{n} + \frac{2}{3}(\widehat{\overline{\rho}\widetilde{\phi}})^{*} + \frac{2\Delta t}{3}\,(-\mathbb{C}^{*} + \mathbb{D}^{*} + \mathbb{A}^{*} + \mathbb{S}^{*})\,, \tag{2.7}$$

where the marked terms $\mathbb{C}, \mathbb{D}, \mathbb{S}$ are evaluations of their counterparts in Eq. (2.3) at times t^n, t^+ and t^*, likewise for $\mathbb{A}$ the artificial dissipation term. The time step is limited by Courant–Friedrichs–Lewy (CFL) and Fourier conditions, imposing approximately

$$\Delta t \leq \mathcal{C} \times \min\left[\frac{\mathcal{V}}{(|\underline{u}| + c)\mathcal{S}}, \frac{\mathcal{V}^2}{|\underline{u}|\mathcal{S}^2}\right] \tag{2.8}$$

where $\mathcal{C} = 1$ for the present TVD formulation, $c = \sqrt{\gamma p/\rho}$ is the sound velocity, and the minimum is computed on all control volumes of the computational domain (see [Lodato 08a] for more details).

Thermochemistry. Although the code can tackle thermochemistry in several ways, the SiTCom computations presented in this work invariably involve tabulated chemistry. The justifications and approaches for building such chemical tables are the object of dedicated subsequent chapters; here, the implementation of this approach in the flow solver is presented.

The purpose of a turbulent chemical table is to provide the solver with values for filtered thermochemical quantities $\widetilde{Q}_1, \widetilde{Q}_2, \ldots, \widetilde{Q}_{N_{\mathrm{data}}}$ that would otherwise be difficult or computationally costly to close directly (for example via a literal expression)

from the other scalars solved. The tabulation is based on the parameterization of these thermochemical quantities by a small number of variables, $\psi_1, \psi_2, \ldots, \psi_{N_{\text{param}}}$, forming a vector denoted by $\underline{\psi}$. The filtered values of these parameters, $\widetilde{\underline{\psi}}$, are computed in the LES, and the quantities of interest are retrieved from the table as

$$\widetilde{Q}_1(\widetilde{\underline{\psi}}), \widetilde{Q}_2(\widetilde{\underline{\psi}}), \ldots, \widetilde{Q}_{N_{\text{data}}}(\widetilde{\underline{\psi}}) \,. \tag{2.9}$$

In the version of SiTCom used here, a turbulent chemistry table contains:

- the filtered energy source term, $\widetilde{\dot{\omega}}_T$, defined in Eq. (1.16)
- the filtered average molecular mass of the gas mixture, $\widetilde{W}$
- the filtered mass fractions of a set of species, $\widetilde{Y}_{m_1}, \widetilde{Y}_{m_2}, \ldots, \widetilde{Y}_{m_{N_{s,\text{table}}}}$ necessary to retrieve $\widetilde{T}$ from $\widetilde{E}$, in that m_k, $k = 1, N_{s,\text{table}}$ are in $[1; N_s]$ such that the approximation

$$C_v(T) \simeq \sum_{k=1}^{N_{s,\text{table}}} C_{v,m_k}(T) Y_{m_k} \tag{2.10}$$

may be considered valid on a range of temperature $[T_{\min}; T_{\max}]$ expected in the flow [Galpin 08].

Additionally, a separate database containing second-order polynomial interpolations of the C_{v,m_k} integrals is available: it contains three sets $a_{k,i}$, $b_{k,i}$, $c_{k,i}$, $k = 1, N_{s,\text{table}}$, $i = 1, (N_T - 1)$, such that

$$\int_{T_{\text{ref}}}^{T} C_{v,m_k}(T')\,\mathrm{d}T' \simeq a_{k,i}T^2 + b_{k,i}T + c_{k,i} \quad \text{on} \quad T \in [T_i; T_{i+1}] \tag{2.11}$$

where $T_i = T_{\min} + (i-1)/(N_T - 1) \times (T_{\max} - T_{\min})$. N_T must be large enough for this quadratic regression to be accurate.

The energy source term $\widetilde{\dot{\omega}}_T$ is retrieved from the table and used in the total non-chemical energy E transport equation, see Eq. (1.18). At the end of each time step, the equation of state is enforced in each control volume through the following steps (the filtering notations are omitted in the terms below):

1. The integral $\widehat{\mathcal{E}} = \int_{T_{\text{ref}}}^{\widehat{T}} C_v(T')\mathrm{d}T'$ is computed as

$$\widehat{\mathcal{E}} = \widehat{E} - \frac{1}{2}|\underline{\widehat{u}}|^2 - \frac{\mathcal{R}T_{\text{ref}}}{\widehat{W}} \,, \tag{2.12}$$

where $\widehat{W}$ is retrieved from the table and T_{ref} is an arbitrary reference temperature .

2. The temperature $\widehat{T}$ is extracted from $\widehat{\mathcal{E}}$ and the table's mass fractions, thanks to the approximation (2.10) and tabulation (2.11), by an inversion of the second-order polynomial

$$\left(\sum_{k=1}^{N_{s,\text{table}}} a_{k,i}\widehat{Y}_{m_k}\right) T^2 + \left(\sum_{k=1}^{N_{s,\text{table}}} b_{k,i}\widehat{Y}_{m_k}\right) T + \left(\sum_{k=1}^{N_{s,\text{table}}} c_{k,i}\widehat{Y}_{m_k}\right) \tag{2.13}$$

with i taken in each control volume as the index corresponding to the previous temperature.

3. Pressure is then computed as

$$\widehat{p} = \frac{\widehat{\rho}\mathcal{R}\widehat{T}}{\widehat{W}} \,. \tag{2.14}$$

2.1.2 The low-Mach-number variable-density solver in YALES2

Like SiTCom, the `vds` (variable-density) solver in YALES2 is based on the finite volume method, but in a formalism of low Mach number Ma, the ratio of the flow velocity to the sound velocity c. This restricts the simulation to subsonic flows. The treatment of acoustic waves is eliminated as they are assumed to travel instantaneously. The CFL condition on explicit time stepping is relaxed, but an implicit Poisson equation needs to be solved. Precisions are given in the following.

Low Mach number approximation. The Navier–Stokes equations may be rewritten in the limit case $\mathrm{Ma} \ll 1$. To obtain the new system, Eqs. (1.1), (1.2) and (1.5) are first non-dimensionalized:

$$\frac{\partial \rho}{\partial t} + \underline{\nabla} \cdot (\rho \underline{u}) = 0 \tag{2.15}$$

$$\frac{\partial (\rho \underline{u})}{\partial t} + \underline{\nabla} \cdot (\rho \underline{u} \otimes \underline{u}) = -\underline{\nabla} p + \frac{1}{\mathrm{Re}} \underline{\nabla} \cdot \underline{\underline{\tau}} + \rho \underline{f} \tag{2.16}$$

$$p = \frac{\rho T}{\gamma \mathrm{Ma}^2} \,, \tag{2.17}$$

where all above quantities have been normalized by their reference values u_r^*, l_r^*, ρ_r^*, μ_r^* and T_r^* (the dimensional quantities are marked with * and the nondimensional ones are left blank, in this paragraph only) and $\mathrm{Ma} = u_r^* / \sqrt{\gamma \mathcal{R}^* T_r^*}$.

The asymptotic expansion of all variables in powers of the square of the Mach number:

$$\phi = \phi_0 + \mathrm{Ma}^2 \phi_1 + \dots \tag{2.18}$$

where ϕ stands for $\underline{u}$, ρ, μ, e_t, except for the pressure, written as:

$$p = \frac{1}{\mathrm{Ma}^2} p_0 + p_1 + \dots \,, \tag{2.19}$$

are plugged into the mass and momentum conservation equations (2.15–2.16). At the order $1/\mathrm{Ma}^2$:

$$\underline{\nabla} p_0 = \underline{0} \tag{2.20}$$

implying that p_0 is a uniform field, called the "thermodynamic pressure". In this work it will be assumed constant in time. The equation of state becomes

$$p_0 = \frac{\rho_0 T_0}{\gamma} \,, \tag{2.21}$$

and the rest of the system reads

$$\frac{\partial \rho_0}{\partial t} + \underline{\nabla} \cdot (\rho_0 \underline{u}_0) = 0 \,, \tag{2.22}$$

$$\frac{\partial (\rho_0 \underline{u}_0)}{\partial t} + \underline{\nabla} \cdot (\rho_0 \underline{u}_0 \otimes \underline{u}_0) = -\underline{\nabla} p_1 + \frac{1}{\mathrm{Re}} \underline{\nabla} \cdot \underline{\underline{\tau_0}} + \rho_0 \underline{f} \,. \tag{2.23}$$

The fluctuating part of the pressure, p_1, is referred to as the "dynamic pressure". The equations (2.21–2.23) form a system with five unknowns: ρ_0, the three components of $\underline{u}_0$, and p_1.

Integration. The integration of the above equations involves simultaneously an explicit time advancement, an implicit resolution of the Poisson equation satisfied by p_1, and an enforcement of the equation of state. It is illustrated here, back in dimensional form and for the filtered values, in a case where the spray two-way coupling terms are mentioned. The subscripts $_0$ and $_1$ have been omitted for the sake of simplicity, only p_0 is written explicitly. p thus denotes the dynamic pressure.

The velocity is computed at integer time steps t^n, while density and pressure and the scalars are at staggered time values, and denoted accordingly with the superscripts $^{n+1/2}$, $^{n+3/2}$, etc.

For each control volume, an integration step is structured as follows (for the sake of clarity, the filtering notations $\bar{\cdot}$ and $\tilde{\cdot}$ have been omitted under the hat symbol):

1. A density predictor ρ^* is computed in one step from the mass conservation equation, along:
$$\rho^* = \widehat{\rho}^{n+1/2} + \Delta t \, (-\mathbb{C}_\rho^n + \widehat{S}_M^{n+1/2}) \tag{2.24}$$
where it is noteworthy that the convective term in Eq. (2.24) is evaluated at the integer time n:
$$\mathbb{C}_\rho^n = \int_{\mathcal{S}} (\overline{\rho}\widetilde{\underline{u}})^n \cdot \underline{n} \, \mathrm{d}S \,. \tag{2.25}$$

2. Scalars are advanced in their conservative form with the desired temporal scheme, solving in fractional steps:
$$(\widehat{\rho\phi})^* = (\widehat{\rho\phi})^{n+1/2} + \alpha^* \Delta t \, (-\mathbb{C}_\phi^{n+1/2} + \mathbb{D}_\phi^{n+1/2} + \widehat{S}_\phi^{n+1/2}) \tag{2.26}$$
$$\tag{2.27}$$
where the rhs terms are evaluated from primitive values computed with the density predictor, as $\phi^* = (\widehat{\rho\phi})^*/\rho^*$.

3. The density $\widehat{\rho}^{n+3/2}$ is computed as a relaxation between the predictor value ρ^*, and a value coming from the equation of state, ρ_{eos}:
$$\rho_{\mathrm{eos}} = \frac{p_0 \widehat{W}^*}{\mathcal{R} \widehat{T}^*} \,. \tag{2.28}$$
As mentioned above, p_0 is a constant of the problem; the temperature and average mass fraction are an output of the themochemistry model, examined below. For the density, it reads
$$\widehat{\rho}^{n+3/2} = \alpha_{\mathrm{relax}} \rho_{\mathrm{eos}} + (1 - \alpha_{\mathrm{relax}}) \rho^* \,, \tag{2.29}$$

from which the value at t^{n+1} is then assessed as

$$\widehat{\rho}^{n+1} = \frac{1}{2}(\widehat{\rho}^{n+1/2} + \widehat{\rho}^{n+3/2}) \,. \tag{2.30}$$

A value $\alpha_{\text{relax}} = 0.7$ is convenient for an installed configuration; at the development stage, when the equation of state might abruptly vary from one run to the next, $\alpha_{\text{relax}} = 0.5$ offers more flexibility.

4. A velocity predictor is advanced with the desired temporal scheme. Denoting by $^+$ the value obtained at the penultimate step, this reads:

$$(\widehat{\rho\underline{u}})^* = (\widehat{\rho\underline{u}})^n + \Delta t\,(-\underline{\mathbb{C}}_{\underline{u}}^{n,+} - \underline{\nabla}\widehat{p}^{n-1/2} + \underline{\mathbb{D}}_{\underline{u}}^{+} + \underline{\widehat{S}}_D^{n+1/2}) \tag{2.31}$$

where

$$\underline{\mathbb{C}}_{\underline{u}}^{n,+} = \int_{\mathcal{S}} \left[(\overline{\rho}\widetilde{\underline{u}})^n \otimes \widetilde{\underline{u}}^+\right] \cdot \underline{n}\,\mathrm{d}S \,. \tag{2.32}$$

5. This predictor does not satisfy the continuity equation. The pressure is advanced from $t^{n-1/2}$ to $t^{n+1/2}$ as a corrector to enforce this condition, in such a way that:

$$\underline{\nabla}\widehat{p}^{n+1/2} = \underline{\nabla}\widehat{p}^{n-1/2} + \frac{(\widehat{\rho\underline{u}})^{n+1} - (\widehat{\rho\underline{u}})^*}{\Delta t} \tag{2.33}$$

where the momentum at t^{n+1} must satisfy the mass conservation, as:

$$\begin{aligned} \underline{\nabla} \cdot (\widehat{\rho\underline{u}})^{n+1} &= -\left(\frac{\partial\widehat{\rho}}{\partial t}\right)^{n+1} \\ &\simeq \frac{\widehat{\rho}^{n+3/2} - \widehat{\rho}^{n+1/2}}{\Delta t} \,. \end{aligned} \tag{2.34}$$

Therefore, the pressure $\widehat{p}^{n+1/2}$ is computed from the resolution of the Poisson equation obtained by porting Eq. (2.34) into the divergence of Eq. (2.33):

$$\underline{\nabla}^2(\widehat{p}^{n+1/2} - \widehat{p}^{n-1/2}) = \frac{\widehat{\rho}^{n+3/2} - \widehat{\rho}^{n+1/2}}{\Delta t^2} - \frac{\underline{\nabla} \cdot (\widehat{\rho\underline{u}})^*}{\Delta t} \,. \tag{2.35}$$

6. Velocity is corrected to take into account the new pressure gradient.

7. The scalars are corrected to take into account the corrected velocity.

Spatial discretization. The solver can handle unstructured grids made of multiple types of elements, from triangles or quadrilaterals in 2D, to tetrahedra (used in the present work), prisms, pyramids or hexahedra in 3D. The control volumes on which the finite volume equations are based are constructed around each node, as schematically illustrated in Fig. 2.1. Volume-averaged data $\widehat{Q}$ are stored at the nodes. Further detail on this discretization is given in Vantieghem's PhD thesis [Vantieghem 11]. Notations are given below when necessary.

Numerics. Several spatial and temporal schemes may be selected by the user. The explicit time advancement may be done by third-, fourth- or fifth- order Runge-Kutta schemes, or a recently developed, soon to be published, fourth-order scheme

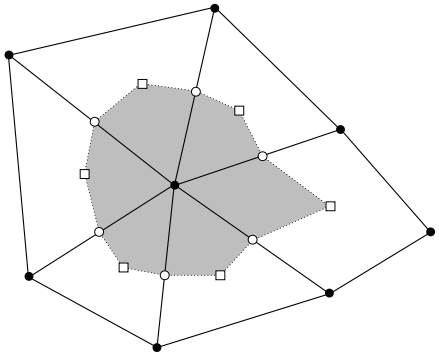

Figure 2.1: Schematic illustration of a node-centered control volume in YALES2, here on a two-dimensional mesh. •: node; ○: middle of an edge; □: face center

combining Runge-Kutta and Lax-Wendroff, called TFV4A [Kraushaar 11]. As far as spatial integration is concerned, both second-order and fourth-order precisions are available. The addition of artificial viscosity follows the fourth-order Cook & Cabot scheme [Cook 04]. The linear Poisson solvers include PCG [Van der Vorst] and Deflated PCG [Nicolaides 87], the BIGSTAB, BIGSTAB2 and BIGSTAB(2) schemes, as well as their deflated counterpart [Van der Vorst].

In the present work, the schemes that were used were fourth order in space, TFV4A and DPCG.

Thermochemistry. In the integration approach presented above, no energy equation is directly involved in the resolution loop, all thermochemical information is carried by the equation of state (2.28): in YALES2, the thermochemical model must simply provide ρ_{eos}, and optionally a temperature $\widetilde{T}$ and a mean molecular mass $\widetilde{W}$ that are consistent with it through the equation of state.

An extra remark may be made at this stage: in the low-Mach-number framework, the sensible enthalpy $h_s = \int_{T_{\text{ref}}}^{T} C_p$, introduced in Section 1.1.3 may be considered to behave like a transported reactive scalar if the work of the viscous forces $\underline{\underline{\tau}} : \underline{\underline{\nabla u}}$ is neglected. Indeed, the pressure term in Eq. (1.22) is zero at the lowest order in Ma, and, noting that by definition $\mathrm{d}h_s = C_p \mathrm{d}T$, one has

$$\frac{\partial \rho h_s}{\partial t} + \underline{\nabla} \cdot (\rho \underline{u} h_s) \simeq \dot{\omega}_T + \underline{\nabla} \cdot \left(\frac{\mu}{\mathrm{Pr}} \underline{\nabla} h_s \right) + \dot{\mathcal{Q}} \,. \tag{2.36}$$

Diffusion for the enthalpy is controlled by the Prandtl number, the same way as the Schmidt number for the scalars.

2.1.3 Incompressible: the constant-density solver in YALES2

The Navier–Stokes equations may be formulated in the framework of incompressible flows, in which the density is assumed constant. This goes farther than simply neglecting the propagation of acoustic waves coupling pressure and density fluctuations: here, density is not even impacted by changes in temperature, which in practice restricts this solver to cases where the heat release is negligible. The incompressible solver is fit for non-reacting cases.

Formulation. The incompressible formulation of the equations solved by YALES2 reads

$$\underline{\nabla} \cdot \underline{u} = 0 \tag{2.37}$$

$$\frac{\partial \underline{u}}{\partial t} + \underline{\nabla} \cdot (\underline{u} \otimes \underline{u}) = -\frac{1}{\rho}\underline{\nabla} p + \frac{1}{\rho}\underline{\nabla} \cdot \underline{\underline{\tau}} + \underline{f} \tag{2.38}$$

Numerics and integration. The numerical schemes available in the `ics` solver are the same as in the `vds` solver. The time advancement is based on the same steps, with an explicit approach for the scalars and velocity and an implicit computation of pressure, but are simpler since no density variation needs to be predicted.

2.2 Dispersed phase

Several approaches have emerged in the last decade to solve the evolution of sprays, described formally in the pdf equation (1.27). Both Lagrangian and Eulerian methods are possible alternatives, each with their strengths and weaknesses, as discussed in a first subsection (Section 2.2.1). In YALES2, a Lagrangian solver is used; the numerical treatment of two-way coupling is addressed in a subsequent paragraph (Section 2.2.2), then the particle time advancement algorithm is described (Section 2.2.3).

2.2.1 Spray solving approaches

Like all pdf transport problems, the formalism introduced by William's spray equation (1.27) may be tackled by both Eulerian and Lagrangian methods.

Let it first be noted that an exact solution of Eq. (1.27) contains much more information than the observed spray evolution (positions and other properties of the particles over time). Rather, f embeds the probabilities of all possible spray states, which at a given time include the one observed to happen, but also all the unobserved others. The goal of a spray simulation is not to obtain this type of information, which in most cases is unneeded.

The idea of the Eulerian approach, introduced by Février *et al.* [Février 05] is to compute spatial fields of the pdf f's statistical moments, such as the particle number density (zeroth order):

$$n(\underline{x}, t) = \int_{\underline{u}} \int_{d=0}^{\infty} \int_{T=0}^{\infty} f(t, \underline{x}, \underline{u}, d, T)\, \mathrm{d}\underline{u}\, \mathrm{d}d\, \mathrm{d}T\,, \tag{2.39}$$

the averages (first order), here for velocity:

$$\langle \underline{u} \rangle (\underline{x}, t) = \int_{\underline{u}} \int_{d=0}^{\infty} \int_{T=0}^{\infty} f(t, \underline{x}, \underline{u}, d, T)\, \underline{u}\, \mathrm{d}\underline{u}\, \mathrm{d}d\, \mathrm{d}T\,, \tag{2.40}$$

or the variances (second order), here for velocity in direction i:

$$\left\langle (u_i - \langle u_i \rangle)^2 \right\rangle (\underline{x}, t) = \int_{\underline{u}} \int_{d=0}^{\infty} \int_{T=0}^{\infty} f(t, \underline{x}, \underline{u}, d, T)\, u_i^2\, \mathrm{d}\underline{u}\, \mathrm{d}d\, \mathrm{d}T - \langle u_i \rangle^2\,, \tag{2.41}$$

solved from transport equations that are derived from Eq. (1.27). An advantage of this method is its easy insertion into classical finite volume gaseous flow solvers, benefitting in particular from all optimizations for parallel computing. However, the restriction of the spray pdf to its moments makes the treatment of such phenomena as polydispersion (inhomogeneous particle sizes) or out-of-equilibrium velocity distributions (for example two particle streams crossing each other) a delicate matter, as addressed in Chaisemartin's PhD thesis [de Chaisemartin 09]. Response strategies include the introduction of discretized conditional moments, or the recourse to presumed conditional pdf. In practice, the Eulerian resolution of the dispersed phase coupled with an Eulerian solver for the continuous phase, forms the so-called Euler–Euler, or "two-fluid", framework [Boileau 08a].

The Lagrangian approach provides a more intuitive description of the spray, since it is based on the tracking of computational particles whose individual behavior, described in Section 1.2.1, is similar to the actual droplets. Compared to the Eulerian method, it offers low numerical dispersion and a straightforward handling of all diameter or velocity distributions. Moreover, its computational cost is made flexible by the numerical weighting of each particle (denoted by $w^{(k)}$ for particle k). A realistic description of the spray may be achieved by setting all weights to one, $w^{(k)} = 1$; in this case, referred to as Direct Particle Simulation, the computed particles match exactly the actual spray droplets. To keep the number density unchanged, the average particle weight must be inversely proportional to the number of computational particles. An increase in the number of particles can be used for an accurate resolution of the pdf f in Williams's equation, through a Monte-Carlo simulation. The pdf moments may be computed on localized sets of particles as

$$\langle \phi \rangle \simeq \frac{\sum_k w^{(k)} \phi^{(k)}}{\sum_k w^{(k)}} \,. \tag{2.42}$$

Conversely, a decrease of the computational cost is easily obtained by an increase of the numerical weights, which enables the transport of a reduced number of particles. Computational droplets are then also referred to as "stochastic parcels". Too strong a reduction of the parcel number may lead to an unacceptable loss of accuracy, with strong intermittency effects [Okong'o 04].

The discussion on the pros and cons and modeling strategies for Lagrangian and Eulerian methods is similar when it comes to the sgs modeling of turbulent combustion, see Section 4.2.

The dispersed phase solver in YALES2 is Lagrange-based. Numerical weighting varies, depending on the cases, between one (full spray simulation) and 4–20, reducing the number of particles by a factor 6. It is naturally well suited, when it comes to the phase coupling, to the point-source approximation presented in Section 1.2.4, as is explained in the next section.

2.2.2 Two-way coupling

The implementation of two-way coupling in the Euler–Lagrange framework is worth a look since the two phases are described by fundamentally different data structures.

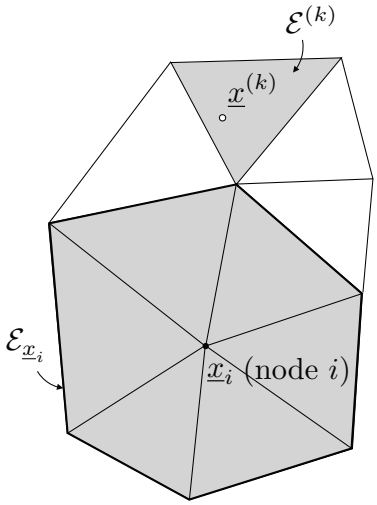

Figure 2.2: Illustration of notations relative to two-way coupling and Euler–Lagrange communications.

Notations

The notations relative to two-way coupling and used in the following are listed below and illustrated in Fig. 2.2.

$\underline{x}_i, \phi_i$	Position of/property at grid node i
$\underline{x}^{(k)}, \phi^{(k)}$	Position/property of particle k
$\mathcal{E}_j$	Grid element j
$\mathcal{N}(\mathcal{E}_j)$	Set of nodes of grid element j: $i \in \mathcal{N}(\mathcal{E}_j)$
$\mathcal{E}_{\underline{x}}$	Elements "connected" to $\underline{x}$. That is, if $\underline{x}$ is inside a grid element, this element; if $\underline{x} = \underline{x}_i$ is a node, the set of adjacent elements (of which i is a node – the set of $\mathcal{E}_j$ such that $i \in \mathcal{N}(\mathcal{E}_j)$)
$\mathcal{E}^{(k)}$	Element in which particle k is located, that is $= \mathcal{E}_{\underline{x}^{(k)}}$ by extension of the above definition.

Particle-to-grid interpolation

The "particle-to-grid" interpolation operator $\{\cdot\}_i$ is introduced and defined as follows. Given a set of particles and their property ϕ, a grid node i and its set of adjacent elements $\mathcal{E}_{\underline{x}_i}$, the interpolation of the Lagrangian quantity ϕ at $\underline{x}_i$ may be written

$$\{\phi\}_i = \sum_{k|\underline{x}^{(k)} \in \mathcal{E}_{\underline{x}_i}} g_{i,k}\, \phi^{(k)} \tag{2.43}$$

where $g_{i,k}$ is an inverse-distance weight:

$$g_{i,k} = \frac{1/|\underline{x}^{(k)} - \underline{x}_i|}{\sum_{i' \in \mathcal{N}(\mathcal{E}^{(k)})} 1/|\underline{x}^{(k)} - \underline{x}_{i'}|}\,. \tag{2.44}$$

The computational weight of the droplets may be taken into account by interpolating the weighted fields $\{w\phi\}_i$.

The first application of this operator is expressing the spray source terms S_M, S_D, S_E, defined in Section 1.2.4, involved in the transport equations of the continuous phase. The point source hypothesis is implemented, in the discrete framework, in a filtered fashion:

$$(\widehat{S}_M)_i = \{wS_M\}_i \,, \tag{2.45}$$

meaning the source contribution of each particle is split between the nodes of the element it is localized in. Thus, conservation is ensured thanks to the definition of $g_{k,i}$ that satisfies, for each particle k, $\sum_i g_{i,k} = 1$. Moreover, distributing the term between several nodes rather that fully assigning it to the control volume where the particle is located amounts to a filtering of the point source at the grid size level.

Finally, this particle-to-grid interpolation can target the grid elements rather than the nodes. It is then denoted by and defined as:

$$\{\phi\}_{\mathcal{E}_j} = \sum_{k|\underline{x}^{(k)}\in\mathcal{E}_j} \phi^{(k)} \,. \tag{2.46}$$

This expression is also conservative.

Grid-to-particle interpolation

Conversely, the "grid-to-particle" interpolation operator allows the evaluation of fields defined on the grid at a particle's position. It is based on the same inverse-distance weighting as above, according to:

$$\{\phi\}^{(k)} = \sum_{i\in\mathcal{E}^{(k)}} g_{i,k}\,\phi_i \,. \tag{2.47}$$

It is employed in the particle advancement routine to compute the far-field properties involved in the kinematic and evaporation models and denoted by the subscript $_\infty$, see Sections 1.2.2 and 1.2.3.

2.2.3 Particle advancement

The particle temporal advancement is based on a third-order Runge-Kutta approach, applied to each particle on substeps Δt_p of the main Eulerian time step Δt. For each particle, the amplitude of a substep is computed as the smallest of the mass evaporation timescale τ_m, heat evaporation timescale τ_h and kinematic response time τ_p. It was tested that this choice for Δt_p is sufficiently accurate, see Section 4.4.4.

Over a time substep Δt_p, advancing from $t^{n'}$ to $t^{n'+1}$, the new position, diameter and temperature of the particles are computed, along with the drag, mass and optionally heat source terms, that are accumulated and ultimately passed to the Eulerian solver at the end of the total time step. The algorithm is presented as a chart flow in Fig. 2.3, with some details given in the lines below.

(A) The far-field quantities $\underline{u}_\infty$, T_∞, $Y_{F,\infty}$ are updated at every substep Δt_p, and assumed constant over the Runge-Kutta iterations. Similarly, the reference viscosity μ_{ref} and reference heat capacity $C_{p,\text{ref}}$ are updated only between two

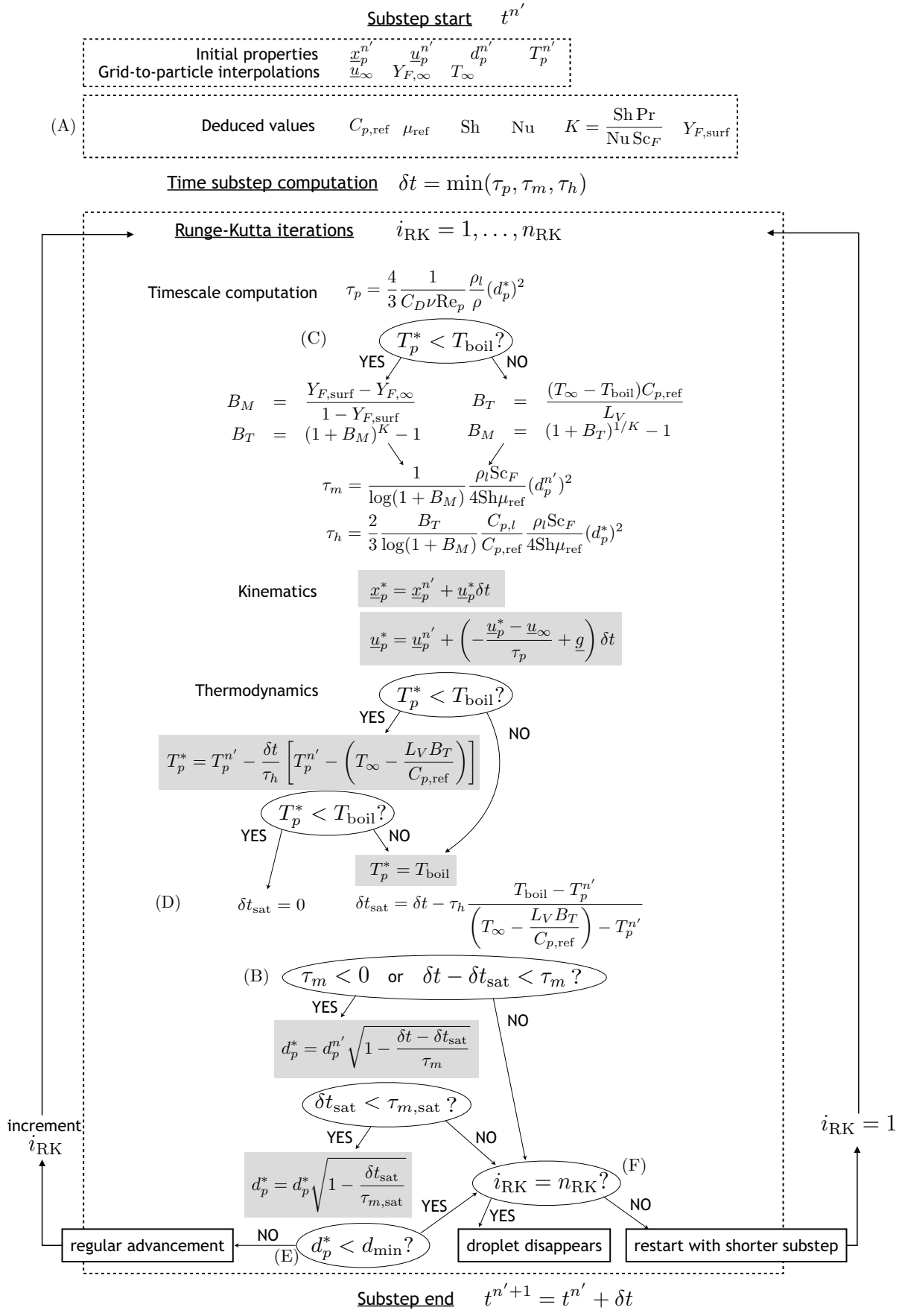

Figure 2.3: Chart flow of the particle temporal advancement algorithm. One loop represents a Runge-Kutta iteration.

time substeps. Finally, the Clausius-Clapeyron formula (1.40) providing the fuel mass fraction at the droplet surface $Y_{F,\text{surf}}$ is computed only each substep, due to its computational cost.

(B) The diameter evolution on a time interval δt is kept nonlinear, from the exact solution to Eq. (1.58) with a constant mass timescale τ_m:

$$d_p(t+\delta t) = d_p(t)\sqrt{1-\frac{\delta t}{\tau_m}}\,. \tag{2.48}$$

This equation indicates that the diameter reaches zero if $\delta t = \tau_m$. Notice also that the mass timescale may sometimes become negative, when $Y_{F,\text{surf}} < Y_{F,\infty}$, meaning condensation is occurring; the diameter evolution equation still holds.

(C) As was presented in Section 1.2.3, the equations for the droplet evaporation are different whether in saturated regime ($T_p = T_{\text{boil}}$) or not, and the evolution is thus treated separately depending on this condition.

(D) Over a Runge-Kutta iteration, simulating a forward time advancement $\delta t = \alpha_{\text{RK}}\Delta t_p$, the sub-interval of time spent at saturation is denoted as δt_{sat}.

(E) The drop disappearance is handled as follows: a minimum diameter value is set, under which a particle is considered fully evaporated and its diameter automatically set to zero; in the present case $d_{\min} = 1\,\mu\text{m}$.

(F) Additionally, if the diameter reaches this minimum value before the last Runge-Kutta iteration, one considers that the time substep Δt_p was unduly set too large and the substep is restarted with a smaller value, either τ_m or $\delta t - \delta t_{\text{sat}}$.

2.3 Parallel computing

The utilization of several processors to compute flow dynamics is a natural response to the increasing number of cells required by ever larger domain dimensions and smaller resolutions. Both SiTCom and YALES2 are developed for parallel computing. The distribution of tasks between processors is briefly presented in this section. In a first part, the strategies for grid splitting in both codes are discussed – they concern the Eulerian solvers. The handling of Lagrangian particles in YALES2 is addressed in a second subsection.

2.3.1 Grid splitting and inter-processor data communications

A mesh comprised of N_{cell} cells is considered, that is to be split into as many subdomains as there are computing cores, N_{core}.

Equal distribution of the number of cells among processors

A domain decomposition must offer an optimal repartition of the workload between the processes, to avoid some processes waiting for others to complete their time step advancement. In a purely Eulerian context, the primary requisite is to split the domain into subdomains containing equivalent numbers of elements.

In SiTCom, the domain is invariably a regular hexahedron, of $N_{\text{cell}} = N_x \times N_y \times N_z$ cells. The mesh can easily be split up in each direction, forming a set of $N_{\text{core}} = N'_x \times N'_y \times N'_z$ smaller hexahedra, provided each N_i is an integer multiple of N'_i, $i = x, y, z$.

The splitting of an unstructured mesh is less straightforward. In YALES2, this procedure is based on a graph-partitioning algorithm implemented in a library called METIS [Karypis 95]. One considers the undirected graph formed by vertices matching the N_{cell} cells of the mesh, and edges describing the face connections between cells (pairs of vertices/cells $(j_1, j'_1), \ldots, (j_M, j'_M)$ where M is the number of edges and the j_m, j'_m are in $[1; N_{\text{cell}}]$). The algorithm determines how the N_{cell} vertices may be arranged into N_{core} disjoint subgraphs that minimize the number of cut edges and have as closely as possible an equal number of vertices. In terms of the mesh, the result is a set of cell subdomains with approximately $N_{\text{cell}}/N_{\text{core}}$ cells each and with a minimum number of face connections with each other.

Minimizing data exchange

In the context of multiple-core parallel computation, a given process does not have access to the memory containing data at positions beyond the extent of its assigned subdomain. As a consequence, spatial derivatives cannot be directly computed near the inter-processor boundaries, and a data communication procedure between processes is required. The number of nodes or cells involved in these exchanges increases with the size of the stencil involved in the spatial integration scheme.

To minimize the computational cost of these inter-processor communications, the connectivity surface must be as small as possible. The regular mesh splitting in SiTCom, yielding exchange buffers localized on the faces of the subdomains, is optimal on this criterion too. And this explains why the mesh splitting algorithm, used for YALES2 as described above, involves a minimization of the edge cuts.

Double domain decomposition

In YALES2, the exchanged data, localized along the connectivity surfaces entailed by the mesh decomposition, are organized in specific data structures called communicators.

A specific feature of the solver was developed to further optimize the performance of computations carried out on very large numbers of processors: double domain decomposition [Moureau 11a]. Each subdomain, obtained from the primary mesh splitting, is itself decomposed into so-called "cell groups", forming the basic data structures. Their size is set so that the information they contain occupies a memory within the cache capacity. This enables all group operations to be carried out at once, without repeated access to the cache. This approach additionally offers much flexibility for potential dynamic load-balancing or local grid refinement, which can be performed at the level of the cell groups instead of down to the cell level, with only partial connectivity reconstruction necessary. Moreover, the coarse mesh formed by the cell groups is exploited by the linear solver of the Poisson equation (2.35).

As a consequence, the solver involves two types of communicators, as described in Fig. 2.4: the external communicators, corresponding to the primary decomposi-

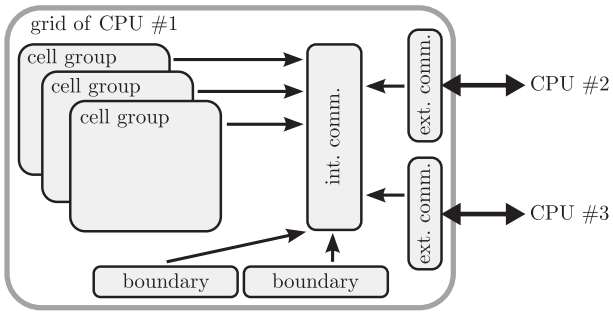

Figure 2.4: Schematized view of the internal and external communicators in YALES2. Taken from [Moureau 11a].

tion, through which exchanges between processors are performed; and the internal communicators, enabling the exchanges between cell groups within a core.

Automatic mesh refinement

The YALES2 solver has been developed to enable parallel computations on meshes of several billion cells. To that purpose, an automatic mesh refinement feature is available, that tessellates each tetrahedron into eight smaller elements of similar skewness. Details are given in [Moureau 11a]. This circumvents the limitation of mesh-generating softwares which cannot handle grids larger than about 50 million cells. Starting from a mesh half this limit size, one level of refinement, performed directly at the start of the computation, yields a mesh of 200 million cells, and a second level of refinement reaches a level of 1.6 billion cells. This tool is a significant contribution for the progress towards highly-resolved large-scale computations; it has enabled to reach resolutions at which the thermal flame thickness is resolved [Moureau 11b], and was exploited here, with further details provided in Section 3.3.2, for the computation of the ethanol spray flame.

2.3.2 Lagrangian transport

Memory spatialization

In YALES2, the localization of Lagrangian particles on the Eulerian grid takes advantage from the double domain decomposition technique. Particles are organized as so-called "particle groups", which contain particles localized in the grid elements of a given cell group. This spatial clustering makes operations affecting large numbers of particles faster and less memory-transfer consuming. For example, the computational loops involved in a grid-to-particle interpolation are performed particle group per particle group; for each of them, there is only one corresponding cell group, easily retrieved, and the search for the cells $\mathcal{E}^{(k)}$ involved in the summation in Eq. (2.47) is restricted to the cell group. This saves a costly search through the entire set of cells in the process' grid.

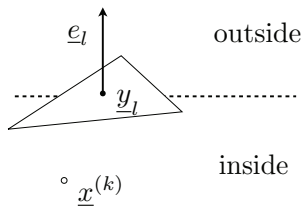

Figure 2.5: Schematic of a face and notations for the particle localization algorithm.

Particle tracking

The algorithm checking if a particle (position $\underline{x}^{(k)}$) lies within an element is based on a comparison of vector directions: given the l-th face of an element, characterized by its center $\underline{y}_l$ and outward normal vector $\underline{e}_l$, the particles is contained in the space delimited by these faces if

$$\forall l = 1, \ldots, N_{\text{face}}, \quad (\underline{y}_l - \underline{x}^{(k)}) \cdot \underline{e}_l \geq 0 \,, \tag{2.49}$$

as seen in Fig. 2.5.

Particles must be tracked during their displacement, and their location on the grid (cell number, cell group and process) be updated each time step. To that end, a search algorithm called "known-vicinity algorithm" is used. The particle's initial position and grid location are known, as well as the new position. The new containing cell must be determined. It is searched for by advancing through the cells, neighbor to neighbor, starting from the initial one, and checking each time whether the particle lies within their limits. It takes advantage of the dot products computed in Eq. (2.49) to determine which neighbor to pick: the one connected by face l such that the dot product involving $\underline{y}_l$ and $\underline{e}_l$ is the largest of all N_{face} values. This algorithm was shown to be more efficient than brute force methods, and also than another approach involving a directional search, in which the direction of motion is taken into account [Apte 03b].

Along the search, it may happen that the particle has crossed a boundary between two cell groups or even CPU grids: in the former case, it must then be localized in the particle group corresponding to the new cell group; in the latter case, it must be sent to another process. Specific memory buffers structured along the internal and external communicators mentioned above are employed to that purpose.

Load balancing in two-phase configurations

The strategies described above to balance the computational workload between computational cores for the resolution applied to purely Eulerian problems. The Lagrangian transport involved in the spray simulation, because of its different nature, calls for adaptations in the load balancing.

As described in papers by Boileau *et al.* [Boileau 08a, Boileau 08b], two strategies can be envisioned to cope with the transport of particles on multiple cores: either reserving a portion of the processes exclusively for the Lagrangian transport, with the rest devoted to the Eulerian computations; or having all processes tackle both the continuous and dispersed phases of their assigned subdomains. Since the particle

equations and gas equations are coupled, a huge amount of data must be sent back and forth, in the first approach, between all Eulerian processes and all Lagrangian processes; the second approach, since it is localized in physical space, is less costly on this point, and is the one implemented in YALES2.

However, the particles are not expected to be homogeneously scattered throughout the computational domain, which leads to workload imbalance between the cores. This negatively affects the overall efficiency of the solver. A natural response to this issue is to make the domain decomposition sensitive to the particles, not only to the number of cells [Ham 03].

Such an approach was developed in YALES2 in the context of the present work. The number of computational particles (parcels) in an element j is first computed, with the particle-to-grid interpolation formalism introduced in Section 2.2.2, as:

$$\mathrm{n}_j = \{1\}_{\mathcal{E}_j} = \sum_{k|\underline{x}\in\mathcal{E}_j} 1\,. \tag{2.50}$$

The graph-partitioning algorithm in METIS can take into account weighted nodes (grid cells) and edges (grid faces), denoted respectively by w_j, $j = 1, \ldots, N_{\text{cell}}$ and w'_m, $m = 1, \ldots, M$. The resulting set of subgraphs $\mathcal{V}_k$ have approximately equal total weights $\sum_{j\in\mathcal{V}_k} w_j$ and minimizes the weight of the cut edges. The particle-independent grid partitioning described above corresponded to node and edge weights set to one. Here, the node weights are defined as

$$w_j = 1 + \alpha_w \langle \mathrm{n}_j \rangle\,, \tag{2.51}$$

where α_w is an adjustable constant and $\langle\cdot\rangle$ denotes time averaging performed over a sufficient duration.

This domain decomposition can be carried out only once at a time, at the start of a computation, and is therefore not optimal for cases where the parcel density strongly varies on large characteristic times. However, in the case studied in this work, the departure $|\mathrm{n}_j - \langle \mathrm{n}_j \rangle|$ is low in amplitude and occurs at high frequencies, and this approach enables an up to 62 % reduction of the computational cost, as will be presented in Section 3.3.2.

2.4 Towards complex spray configurations

The two-phase problem addressed in the present work, extensively described in the next chapters, involves non-trivial particle diameter and velocity distributions, and complex boundary conditions (spray injection). Therefore, simulating tools have been developed in YALES2 that enable: i) a straightforward evaluation of the spray property statistics, and ii) particle injection with highly configurable features, both in terms of geometry and property distributions. Each development is presented in a devoted subsection, and the tools are illustrated in a reference example, forming the final part of this section.

2.4.1 Grid-interpolated particle statistics

The computation of statistics of the spray in space is a useful feature that was developed in the context of the present work. In the Lagrangian framework used here, the spray modeling involves a large number of parcels whose purpose is to carry information representative of the population properties, in a fine-grained fashion; but, echoing the principle behind the Eulerian description of the spray, it is interesting to compute moments of the statistical distributions. In the experimental practice – as will be detailed for the case of the SAFIR burner, see Section 3.1 –, diagnostic tools retrieve spray properties at a fixed location and statistics are obtained over a significant period of time. Comparison of simulation results with such data therefore requires to interpolate the moving particles' statistics onto the grid. Time averaging may subsequently be performed in a straightforward way, like for gas properties.

Grid-interpolated spray statistics may be computed from the time averages of the interpolated fields defined in Section 2.2.2. As a first step, particle-to-grid interpolation conditional on a variable ψ may be performed by selecting, for the average computation in Eq. (2.43), only the particles whose $\psi^{(k)}$ is equal to the target value ψ^* with an accuracy $\Delta\psi$: it may be written

$$\{\phi|\psi^*,\Delta\psi\}_i = \sum_{k|\underline{x}^{(k)}\in\mathcal{E}_{\underline{x}_i}} g_{i,k}\delta_{\Delta\psi}(\psi^{(k)}-\psi^*)\,\phi^{(k)}\,, \tag{2.52}$$

with $\delta_{\Delta\psi}(\psi)=1$ if $|\psi|\leq\Delta\psi$ and 0 else. Any droplet property can be used as the reference variable ψ, but the formalism below is based on the diameter since most experimental spray statistics are conditioned on this variable.

At a given node position $\underline{x}_i$, the time-averaged diameter number distribution histogram on intervals Δd_p may be obtained from

$$f(d_p;\underline{x}_i) \simeq \frac{1}{\Delta d_p}\frac{\langle\{w|d_p\}_i\rangle}{\langle\{w\}_i\rangle}\,, \tag{2.53}$$

where the mention of Δd_p in the conditional interpolation operator has been omitted for the sake of legibility. Also, diameter-conditioned time averages of quantities, and in particular of velocity, may be evaluated as

$$\langle\underline{u}(\underline{x}_i)|d_p\rangle \simeq \frac{\langle\{w\underline{u}|d_p\}_i\rangle}{\langle\{w|d_p\}_i\rangle}\,. \tag{2.54}$$

Another interesting quantity is the velocity fluctuation, defined formally, from conditional ensemble averages $\langle\cdot\rangle$ on the particle population, as – here in direction j –

$$u_{j,\mathrm{rms}}(\underline{x}|d_p) = \left\langle u_j^2(\underline{x})|d_p\right\rangle - \langle u_j(\underline{x})|d_p\rangle^2\,. \tag{2.55}$$

They are estimated as

$$u_{j,\mathrm{rms}}(\underline{x}_i|d_p) \simeq \frac{\left\langle\{wu_j^2|d_p\}_i\right\rangle}{\langle\{w|d_p\}_i\rangle} - \left(\frac{\langle\{wu_j|d_p\}_i\rangle}{\langle\{w|d_p\}_i\rangle}\right)^2\,. \tag{2.56}$$

To summarize, the comparison of the experimentally-obtained diameter pdf and diameter-conditioned velocity moments with the YALES2 simulation results requires the computation of the field $\{w\}$ and, for as many d_p values as deemed necessary, of the fields $\{w|d_p\}$, $\{w\underline{u}|d_p\}$ and $\{wu_j^2|d_p\}$.

2.4.2 Particle injection

Computationally, particle injection involves the data structure called "injector", defined by the following properties:

- an **injection rate** through which the number of particles injected at each time step is controlled. At each time step, particles are injected one by one and their properties set, or drawn randomly, as prescribed. This is performed as long as the injection rate condition is not reached. The most common and realistic case is the mass flow rate constraint, which is enforced through

$$\sum_{k \text{ injected}} w^{(k)} m_p^{(k)} \leq \dot{m}_{\text{injector}} \mathrm{d}t \; . \tag{2.57}$$

  Two alternatives are either to enforce a number flow rate:

$$\sum_{k \text{ injected}} w^{(k)} \leq \dot{n}_{\text{injector}} \mathrm{d}t \; , \tag{2.58}$$

  or a momentum flow rate:

$$\sum_{k \text{ injected}} w^{(k)} m_p^{(k)} |\underline{u}^{(k)}| \leq \dot{g}_{\text{injector}} \mathrm{d}t \; . \tag{2.59}$$

- a **geometry**, such as: 0D – point, 1D – line, circle, or 2D – disk, annulus, cone surface. Since particles must be localized on the grid at their generation, the injection boundaries that are not points must be divided into sub-surfaces small enough for the localization algorithm not to lose track of a newly injected parcel. Once their position has been linked to a grid element, the algorithm (described in Section 2.3.2) is efficient in tracking them along their trajectory, but it requires a starting point where the particles first enter the system. In practice, an injector with a flow rate constraint $\dot{m}$ is split up into N sub-injectors with flow rate constraints $\dot{m}/N$ partitioned accordingly. This also takes into account the possibility that an injector surface spans the domains of several processors.

- the definition of the particle properties' **distributions**, that can be fixed or random. The support for a wide range of classical random laws has been inserted in YALES2: uniform, normal, log-normal. Common diameter distributions have also been implemented: Rosin–Rammler, Nukiyama–Tanasawa. Definitions, properties and generation methods are listed in Appendix A.

  Since particles are injected one by one, the solver bases the generation of their random properties, say ϕ, on the knowledge of a *number* distribution f_0. It is defined so that $f_0(\phi^*)\mathrm{d}\phi$ is the ratio of the number of particles with $|\phi - \phi^*| \leq \mathrm{d}\phi$ to the total number of particles. This is an important remark because distributions such as Rosin–Rammler are defined from their volume distributions f_3 which may be misleading. All details of the determination of f_0 are given in Appendix A.

Additionally, manually configurable discrete and histogram distributions have also been enabled. A noteworthy feature is the possibility to condition the parcel weight with the diameter (see Section A.5.2). A practical application is for example to assign a large weight on small-diameter parcels, which may, if they form a significant volume ratio of the liquid phase, represent very large numbers of physical droplets (hence high computational costs). The larger droplets may retain a unity weight, because they may turn up less numerous, but especially because they affect their environment more strongly, making the simulation benefit from an individual tracking of their evolution.

2.4.3 Illustrating example: a particle channel

A simple simulation is performed to illustrate the features described in the previous sections. A laminar, steady channel flow of velocity $\underline{u}$, in a box of length L in the flow direction, is considered, as shown in Fig. 2.6. Particles are injected uniformly along a line, with an initial velocity $\frac{1}{2}\underline{u}$. Two-way coupling is disabled, the particles are subjected to drag but do not transfer momentum to the carrier phase.

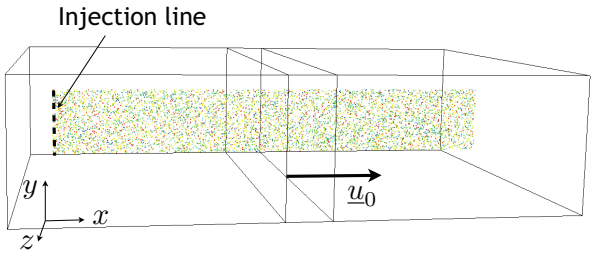

Figure 2.6: Schematic illustration of the particle channel.

Particle velocity relaxes towards $\underline{u}_0$ with a characteristic time τ_p – see Eq. (1.34) –proportional to the square of their diameter. This dependency can be seen by computing the particle velocity conditional to d_p, $\langle u|d_p\rangle$, as presented in Section 2.4.1. It is plotted along the channel in Fig. 2.7 a, with statistics collected over two flow-through times L/u_0. The larger particles display higher relaxation times than the smaller.

In the case presented in Fig 2.7, particles are injected with a discrete diameter distribution f_0, defined as follows:

d_p (µm)	20	40	60	80	100
f_0	0.05	0.2	0.25	0.4	0.1

The diameter number distribution as defined in Eq. (2.53) is plotted for this discrete set of values along the channel direction in Fig. 2.7 b. As expected, these ratios are recovered downstream, whereas close to the injection, smaller particles are in default because of their faster acceleration compared with the larger, slower ones, in excess (initial velocity $u_0/2$).

In the configuration of Fig. 2.7, the particles are injected as computational parcels of constant unity weight : $w = 1$. Other constant weight settings are tested: $w = 2$,

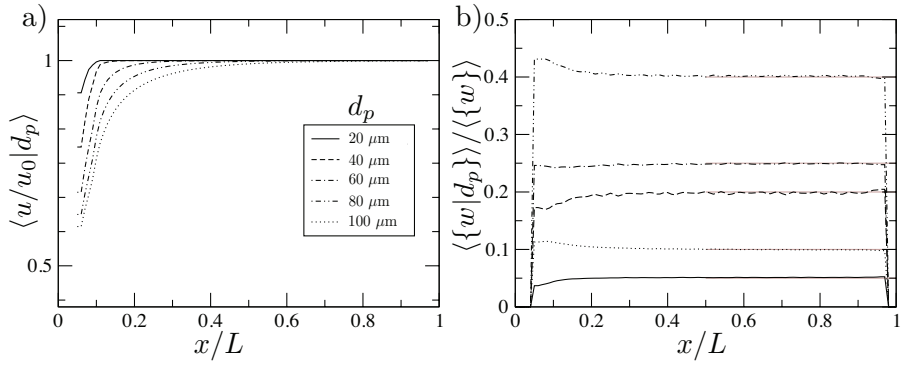

Figure 2.7: a) Time-averaged particle velocity conditional to the diameter. b) Time-averaged diameter number distribution along the channel for different values of d_p. Grey lines: theoretical values.

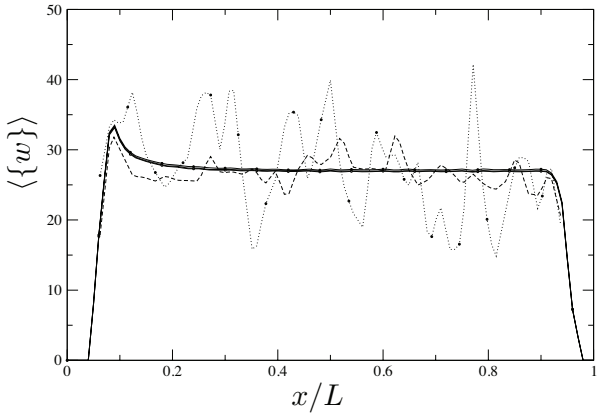

Figure 2.8: Collapsing solid lines: time-averaged particle density $\langle\{w\}\rangle$ for the same size distribution but different weight correlations: constant $w = 1$, $w = 2$, $w = 10$ and diameter-dependent w. Dotted lines: instantaneous particle density, no symbol: $w = 1$, black circle: $w = 10$.

$w = 10$, as well as a diameter-dependent weight, defined for the present dummy case as $1, 2, 3, 4, 5$ for the five diameter values. The number ratios of the computational parcels are automatically adjusted to maintain the simulated diameter number distribution. This may be seen in Fig. 2.8, where the overall particle density, computed as $\langle\{w\}\rangle$, is plotted along the flow. While the time-averaged density are all equivalent, the instantaneous values display much higher fluctuations around the time average if the weighting is large. This intuitive result echoes the observation made by Okong'o & Bellan in their DNS study [Okong'o 04].

Finally, to show a continuous distribution, a normal diameter law was simulated, of mean 65 µm and standard deviation 15 µm. The computed number distribution obtained downstream ($x/L > 4$) is compared for several values of d_p in Fig. 2.9 with the theoretical distribution imposed at injection. Both collapse on each other, as expected.

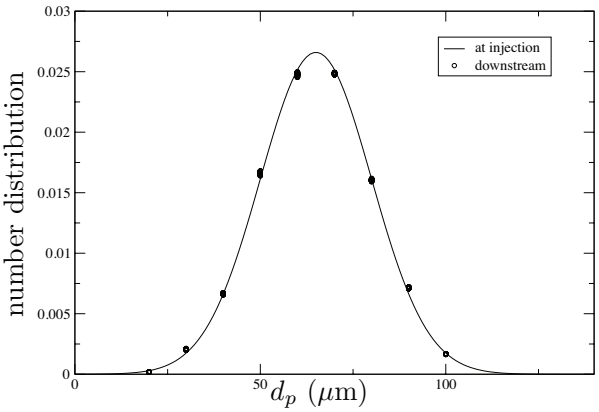

Figure 2.9: Comparison between the normal distribution imposed at the injection and that retrieved downstream as defined in Eq. (2.53), with $\Delta d_p = 2\,\mu\text{m}$.

Part II

SAFIR spray flame simulation

Chapter 3

Modeling and simulation of spray injection

Part II of this report is concerned with the Large-Eddy Simulation of the SAFIR spray flame. As discussed in the introduction, liquid ethanol fuel is atomized into a co-flow of oxygen mixed with carbon dioxide. The experimental apparatus allows for imposing different dilutions of the oxidizer, and the co-flow velocity can also be varied. Both two-phase modeling and combustion modeling are by themselves self-standing disciplines. Given the complexity of the problem, only one configuration has been simulated here, where the flame is lifted and not impacted by the recirculating burnt gases.

Principles and numerical tools behind two-phase simulation have already been introduced in earlier chapters. In the present chapter, they are put into practice to simulate the spray atomization and dispersion, in a non-reactive context.

The chapter is structured as follows: first, the spray properties are discussed, and the large set of experimental data that have been collected is presented. A part of them was initially meant to serve as limit conditions, but the YALES2 solver became available in the course of this work that offered the possibility of a full spray simulation. The objective became, as discussed in a second section, to design a numerical spray injection that yielded the experimental statistics obtained downstream. The different steps of this attempt, its initial insufficiencies and subsequent improvements, are detailed in a third and last section.

Contents

3.1 Spray properties

In this section, the properties of the simulated spray are presented. Its general features are first discussed; available experimental data are then examined.

3.1.1 Apparatus and liquid flow structure

In the following, the origin of the coordinate system is set at the center of the spray nozzle. The longitudinal direction is denoted by coordinate x, while all radial properties are studied along the radius coordinate r.

The spray nozzle is designed to produce a cylindrically-symmetric, 23.3-kW ethanol flame, ensured by a 3.96 liter-per-hour flow rate. The nozzle diameter is 0.23 mm; outer dimensions are shown in Fig. 3.2. It is a so-called simplex injector [Lefebvre 89b]: atomization is caused by the high liquid velocity (bulk inlet velocity 83 $\mathrm{m.s^{-1}}$, hence

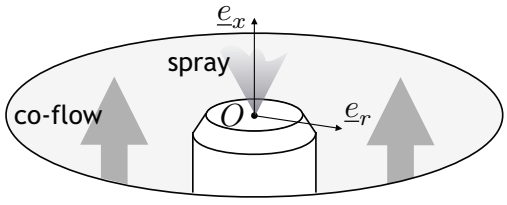

Figure 3.1: Schematic view of the spray injection configuration and coordinate notations.

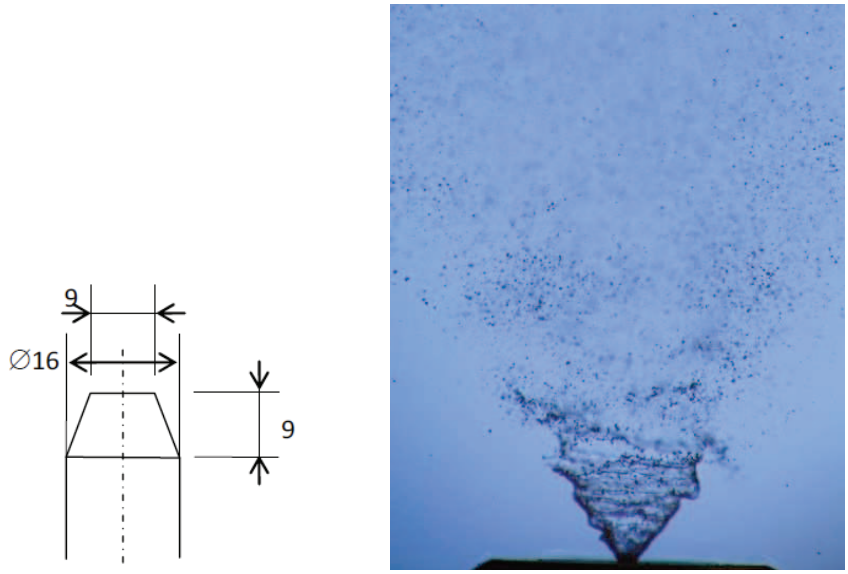

Figure 3.2: Dimensions of the spray injector in mm and photograph of the liquid spray, taken from [Cessou 10].

a large supply pressure of 2.2 MPa) compared with the relatively low gas velocity outside (co-flow velocity about 0.5 $m.s^{-1}$).

The device design produces a conical liquid sheet and subsequent break-up droplets that move upwards and radiate away from the symmetry axis with no azimuthal velocity component. Observations show that the liquid sheet may be considered fully atomized at a distance of 6 mm from the nozzle plane [Cessou 10]. This is visible in the photograph of Fig. 3.2. Most of the injected liquid mass concentrates around an angle of 30 degrees, however the lower angles are also populated, if less densely.

It is noteworthy that here, atomization is not induced by the gaseous phase, as is the case for air-assisted injectors [Lasheras 00]. In the following, this turns out to be an important point because kinetic energy comes mainly from the liquid and is transferred to the gas phase in the process of atomization. The turbulence thus generated is expected to have particular properties that classical sub-filter turbulence models may have difficulty to predict in the context of large-eddy simulation.

3.1.2 Available experimental data

A large set of measurements has been gathered to accurately document the behavior of the spray and flame, and to provide the simulation work with input and comparison data.

Gas phase. Non-intrusive velocity measurements of the gas phase were conducted with and without the spray, from as close as 0.5 mm to the chamber bottom. In the regions without ethanol droplets, velocity tracking was obtained by Doppler-Laser Anemometry (DLA) after seeding the co-flow with small DEHS droplets ($< 5\,\mu m$). In the spray areas, the smallest ethanol droplets ($< 5\,\mu m$) were used as gas-velocity trackers, with velocities estimated by Particle-Doppler Anemometry (PDA). This is based on the assumption that they fully follow the gas movements, which is yet to

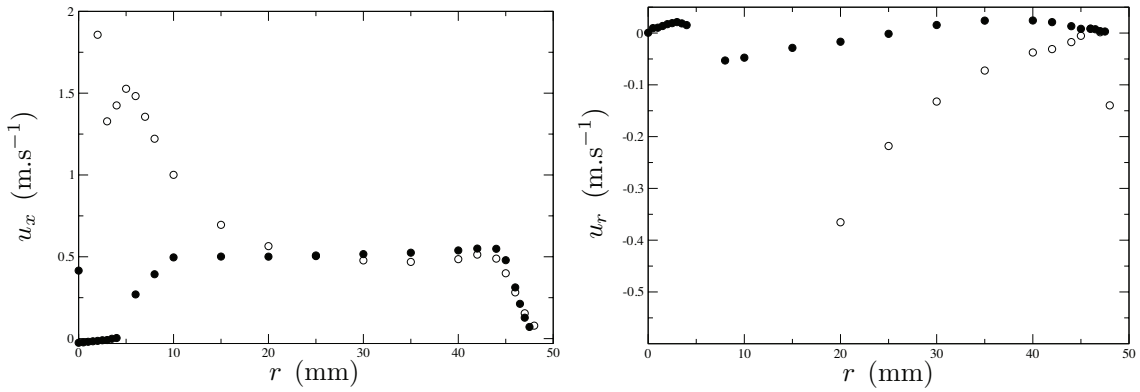

Figure 3.3: Axial and radial components of the mean gas velocity along a line 2 mm downstream of the nozzle, experimentally measured without (•) and with (○) the spray. Measurement points at velocity below $-0.6\,\mathrm{m.s^{-1}}$ are available but left here out of the plot range, for the sake of clarity.

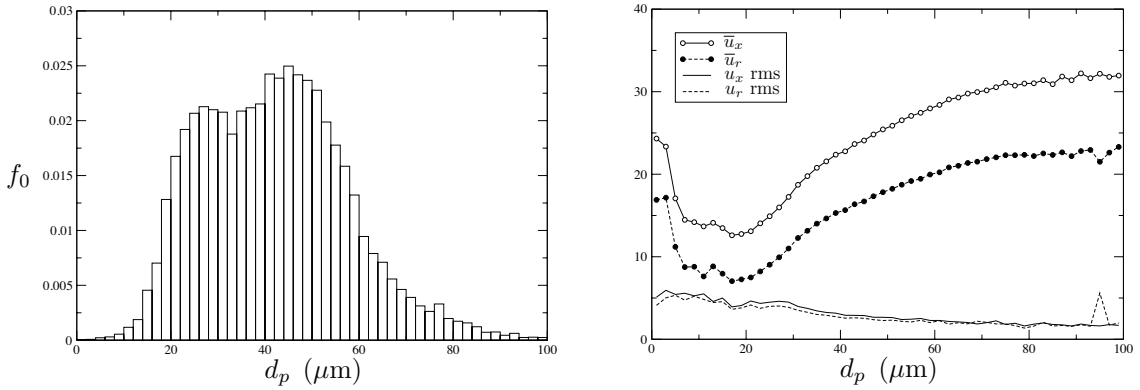

Figure 3.4: Example of PDA measurements at position $x = 6\,\mathrm{mm}$, $r = 4\,\mathrm{mm}$. *Left*: droplet diameter number distribution; *right*: conditional mean and rms velocities.

be confirmed by a Stokes-number analysis [Cessou 10].

As an illustration, the role of the spray on gas velocity is shown in Fig. 3.3. The strong, localized impact of the spray close to the centerline is visible on the axial component. The radial component shows the entrainment effect of spray on the gas co-flow: without spray, the u_r profile is characteristic of a bluff-body wake: positive behind the nozzle, due to the recirculation zone in the atomizer's wake, negative next to it, due to a weak entrainment of the co-flow. In presence of the spray, entrainment becomes much stronger, and the radial component decreases strongly as one nears the nozzle's edge.

A comparison of such DLA measurements with the simulation results will enable a validation of the momentum two-way coupling, as discussed in Section 3.3.

Liquid phase. Extensive measurements of the droplet diameter statistics and conditional velocities have been performed. They provide diameter distributions on the range 0–100 µm with 2 µm-buckets, and mean and rms velocities conditional to these diameter buckets. An example of such a data set in one point is given in Fig. 3.4, at the tip of the liquid sheet.

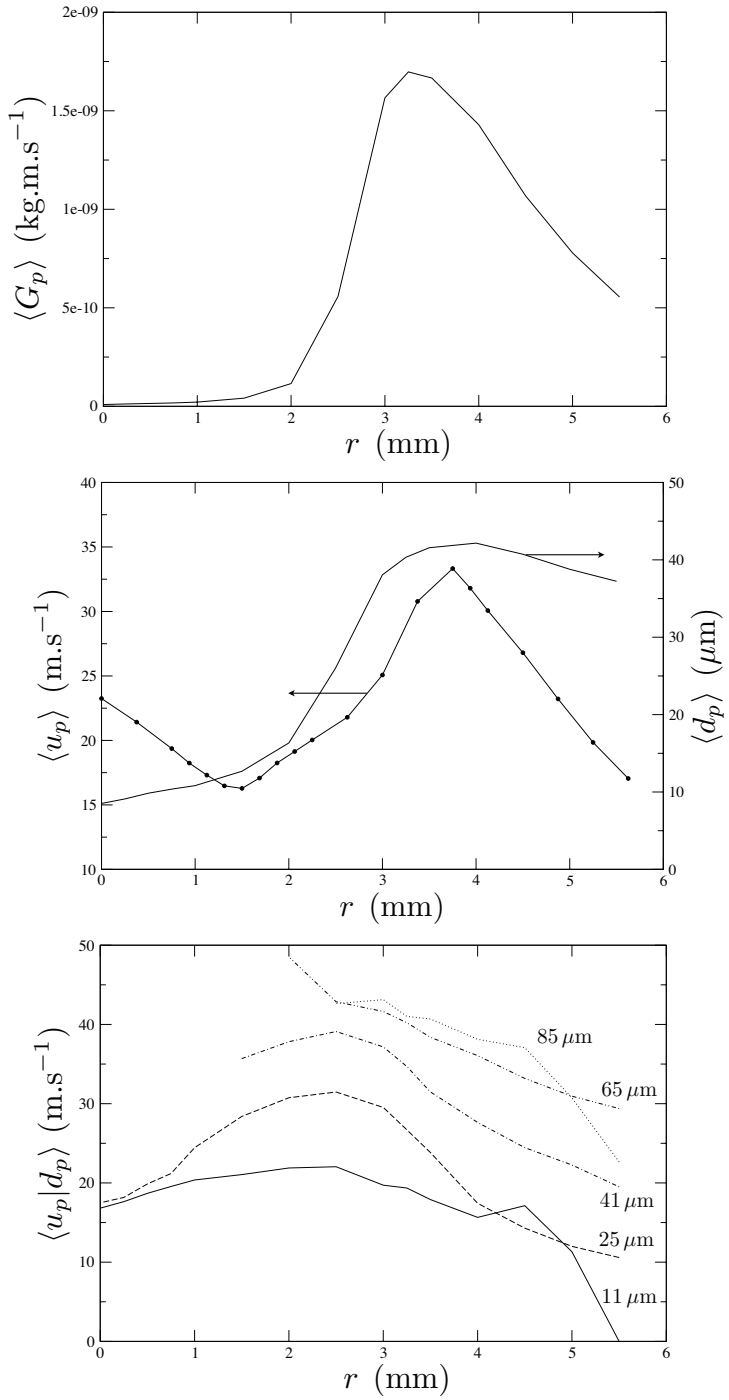

Figure 3.5: *Top:* average droplet momentum $\langle G_p \rangle = \langle (\pi/6)\rho_l d_p^3 |\underline{u}_p| \rangle$ at a distance $x =$ 6 mm from the inlet; *center:* average droplet diameter and velocity magnitude; *bottom:* droplet velocity magnitude conditional to the diameter. All data as obtained by PDA measurements.

Even though these measurements were performed in the presence of the flame for safety reasons, the flame is positioned downstream and does not impact the gas and liquid flows up to 15 mm from the nozzle.

As an illustration of the overall spray characteristics, the mean droplet momen-

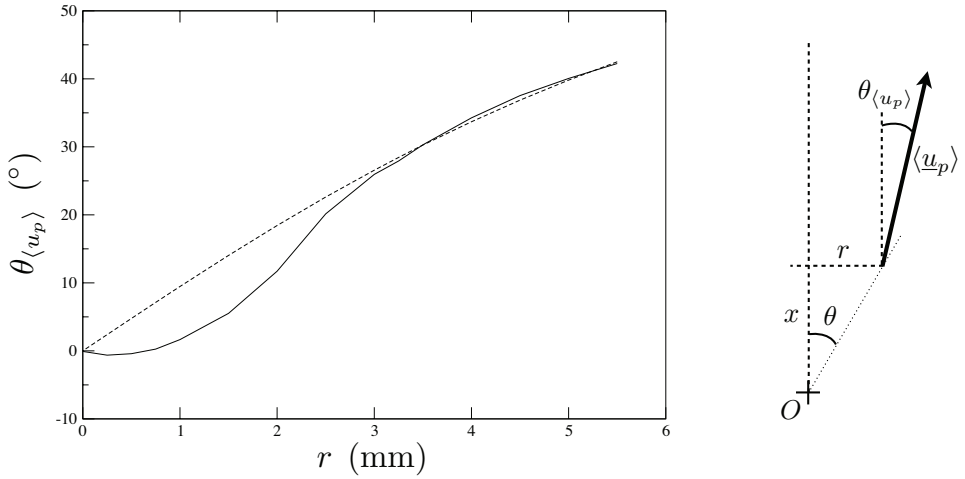

Figure 3.6: Angle of the average velocity to the centerline (dashed line: azimuthal angle $\theta = \text{atan}(r/x)$, as illustrated on the right) at a distance $x = 6\,\text{mm}$ from the inlet, as obtained by PDA measurements.

tum is plotted in Fig. 3.5 at the outset of the secondary atomization region, just after the tip of the liquid sheet. It is visible that the highest-momentum droplets are concentrated within a 1.5-mm-wide crown around the position $r = 3.25\,\text{mm}$, corresponding to the 23°–36° cone-angle interval. The mean droplet diameter and mean droplet velocity magnitude are plotted below: $\langle d_p \rangle$ is roughly only increasing from the centerline towards the interior of the spray. Diameter-conditional velocities increase with d_p and display a maximum at radii positions that increase with d_p, see Fig. 3.5 bottom. Finally, droplet emission directions are compared to a radial emission from the nozzle in Fig. 3.6. It may be seen that close to the centerline, droplet movement tends to be aligned with the symmetry, while at larger azimuth positions droplets move in a direction that radiates from the nozzle center.

Note that non-spherical droplets are excluded from the PDA statistics; this will prove of importance when assessing the ability of simulation to reproduce the spray behavior (see Section 3.3.4). They will have to be artificially taken into account.

Finally, these statistics are also available further downstream in the reaction zone; this part will be discussed in the next chapter.

Other configurations. The spray measurements presented and discussed in this study are limited to one dilution/inset diameter configuration, as discussed in the introduction, but the cases of other inset diameters and co-flow dilutions were also explored. Similar set of measurements are available [Cessou 10]; they will be the object of future simulations and will prove a valuable data set to improve the prediction capabilities of spray LES.

3.2 Modeling the spray as a limit condition

This section is devoted to the modeling of the spray injection.

A brief review of the common approaches for describing or predicting atomization is first given. The applicability, in the present configuration, of the two-phase model-

ing framework introduced in Part I (Section 1.2) is discussed in a second part: close to the nozzle, the liquid phase takes up a large portion of the fluid volume, and it is thus not straightforward to invoke the dispersed droplet framework. As then detailed in Section 3.2.3, the purpose here is not to predict atomization itself, but rather to impose relevant limit conditions based on the experimental measurements, in both the gaseous and liquid phases, through the *ad hoc* injection of numerical particles.

3.2.1 Atomization modeling

Atomization is a complex process, a field of study in itself and the object of extensive ongoing research [Lefebvre 89a, Ashgriz 11]. Full understanding of the mechanism is still out of reach. Empirically, spray properties have been found to depend strongly on as various parameters as the injector geometry, liquid mechanical properties (viscosity μ_l, density ρ_l, surface tension σ), inlet velocity, turbulence level in the liquid and the gaseous flows [Reitz 82]. In the context of combustion, key properties of the spray are, in addition, droplet size distribution and conditional velocities, since they directly impact the fuel vapor field on which the flame will develop.

There have been various attempts at developing descriptive and predictive tools, from empirical laws to detailed atomization models. Empirical laws expressing global spray properties, such as mean droplet diameter and opening angle of the cone, as functions of the injector and fluid characteristics, have been formulated since the 1980s [Lefebvre 89b]. Since optical access to some areas of the atomizing jet is difficult, in particular close to the nozzle, detailed numerical simulations have also been used to improve the understanding of the process of both primary and secondary atomization [Ménard 07, Desjardins 08].

Yet, when it comes to large-eddy simulations where the spray is but an inlet condition, it is neither affordable to fully simulate its development nor sufficient to know only global quantities such as mean diameters and velocities. The polydisperse character of spray must be accounted for, and full diameter distributions and velocity correlations must be provided. Several empirical size distributions are used that may be characterized by a limited number of parameters. Their list and description are given in a review by Babinsky *et al.* [Babinsky 02]; as mentioned in Chapter 2, they were implemented in YALES2 and are listed at the end of this document in Appendix A. An example of their use may be found in a recent work by Bini & Jones [Bini 08]: Nukiyama–Tanasawa functions that interpolate experimental findings are prescribed at the inlet as the spray droplet diameter distributions.

Comprehensive predictive models have also been developed, mainly for Euler–Lagrange LES, where droplet break-up is described from the determination of a characteristic instability frequency, a function of sub-filter gas-phase turbulence and properties of the numerical parcels (velocity, viscosity). These models are generally formulated to reproduce secondary atomization but may be used for predicting primary atomization too, by modeling the liquid sheet as droplets of diameter equal to that of the nozzle [Apte 03a, Apte 09a, Jones 10a].

3.2.2 Validity of the spray modeling framework for the present application

The liquid phase modeling presented in Chapter 1 has theoretical limitations and its validity must therefore be assessed in the light of the present simulation. In this paragraph the assumptions earlier formulated when deriving the droplet behavior equations are listed and examined in the conditions of the SAFIR experiment.

Sparseness. One of the main assumptions behind the Lagrangian transport model is a low volume loading, say $\alpha_l \leq 10^{-2}$ for a conservative criterion, that enables to assume the droplets are isolated. This condition is not totally met in the spray atomization region. The average volume fraction occupied by the liquid within the full cone opening is relatively small: computed over the cone section just downstream of the nozzle, of longitudinal dimension 1 mm and angular opening of 40°, and assuming an average output velocity of $40\,\mathrm{m.s^{-1}}$, $\overline{\alpha}_l \simeq 3.7 \times 10^{-2}$; 5 mm farther downstream the volume fraction has decreased more than a hundredfold. Yet obviously, these averaged estimations must be adjusted because the liquid density is heterogeneous. In the 30°-azimuthal direction, where most of the ethanol mass is ejected, the fuel forms a liquid sheet which cannot be expected to behave like a set of discrete droplets. Preferential repartition can reasonably be assumed to yield local volume fractions α_l a hundred times larger than the full-cone-averaged value $\overline{\alpha}_l$; with this estimation, the isolated droplet framework is valid only downstream of a distance of 4 mm from the nozzle.

Sphericity. For liquid drops, sphericity is the result of predominant surface tension compared with the deformation effects of external stress (coming from the inner liquid or the outer gas). The ratio of their intensity is characterized by the Weber number,

$$\mathrm{We} = \frac{d_p \rho |\underline{u} - \underline{u}_p|^2}{\sigma}, \tag{3.1}$$

with ρ the gas density and σ the surface-tension coefficient[1]. Liquid droplets at low Weber numbers ($\mathrm{We} < 1$) may safely be considered spherical, while a departure from the spherical shape is to be expected at larger We, including possible break-up ($\mathrm{We} > 10$) [Sirignano 10].

Values of the Weber number for ethanol droplets in the configuration of the SAFIR experiment are plotted in Fig. 3.7 (CO_2–O_2 gaseous atmosphere at 293 K). Typical dimensions of droplets encountered here are below 100 µm; it may be seen that for relative velocities below $10\,\mathrm{m.s^{-1}}$, the Weber remains well below one.

The relative velocities in the present SAFIR configuration are now examined. Their largest values are expected to be found at the tip of the liquid sheet: droplets have just been ejected from the sheet whose velocity dissipation by momentum transfer to the gas has been limited. Droplet velocities at this position, $x = 6$ mm, $r = 4$ mm, are shown in Fig. 3.4. The gas velocity may be estimated as equal to that of the smallest droplets, due to their very small drag response time: in [Cessou 10], the 5-µm class is used as the velocity tracer within the spray. Even though droplets

[1] value at 293 K for ethanol: 22.3 mN/m, for water: 72.8 mN/m.

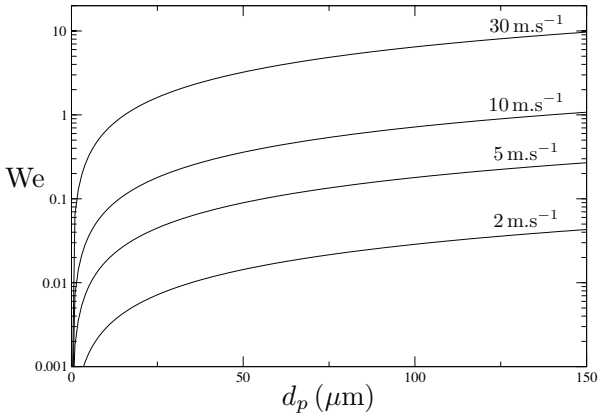

Figure 3.7: Weber number of an ethanol droplet of characteristic diameter d_p in the 293 K-atmosphere of the SAFIR experiment, at various values of the relative velocity $|\underline{u} - \underline{u}_p|$, indicated on the plot.

smaller than 5 µm do not display uniform velocities, using the most conservative estimation, it appears that gas–liquid relative velocities are larger than 10 m.s^{-1} only for very large droplets, of diameter above 80 µm.

This validates the sphericity assumption for the most part of the droplet population. Again, the largest droplets are few but take up a significant portion of the mass and momentum fluxes, so this result must be used with caution. The practical handling of large droplets will be addressed in a subsequent part, see Section 3.3.4.

Interaction with turbulence. The present configuration features the notable property that the momentum is mostly carried by the liquid spray: the injected liquid momentum flux equals 7.2×10^{-2} N while that of the gaseous co-flow, evaluated at 8.9×10^{-4} N – considering a uniform velocity at the chamber inlet of 0.5 m.s^{-1}– , is a hundred times smaller.

The spray dispersion occurs simultaneously with liquid-to-gas momentum transfer, and no easy evaluation of the turbulence properties can be carried out. A simplistic attempt at giving an order of magnitude for the turbulent length scales[2], based on homogeneous isotropic turbulence, yields a dissipative length scale of 0.1 mm comparable with the droplet dimensions.

At any rate, the spray dispersion models invoked in this work have not been designed for the present case, and may be expected to be limited in their predictive capabilities.

3.2.3 Present approach

In this paragraph we present the approach followed to impose limit conditions that will lead to correct gas and spray properties downstream. Upstream of 6 mm to the nozzle, the primary atomization is not complete and no liquid phase measurement is

[2]In isotropic turbulence, $l_\eta \simeq L_f \mathrm{Re}_{L_f}^{-3/4}$ with Re_{L_f} the large-eddy Reynolds number, based on L_f the integral lengthscale and u' the quadratic velocity fluctuation [Bailly 03]. The present numerical application is for $L_f \simeq 10$ mm and $u' \simeq 2$ m.s^{-1}, and yields $l_\eta \simeq 76$ µm.

available. Downstream of this position, spray measurements cover the azimuthal interval 0°–45° (grayed area in Fig. 3.8). Beyond 45° the droplet population is expected to be negligible.

The objective here is not to directly model atomization, but rather to determine the spray limit conditions so that experimental measurements made downstream, both for the gas and the liquid phase, are reproduced. Throughout the flow, the spray is modeled as the sparse phase of isolated spherical droplets presented in Part I and discussed above, even in the very dense areas where non-sphericity is obvious. Despite the evident shortcomings of this approach, we designed settings that result in relevant spray and gas statistics – and that will more likely lead to a realistic flame structure (as seen in the next chapter).

In the very droplet-dense area, from the inlet to about where measurements become possible at 6 mm, spray and gas behaviors are strongly inter-linked. Momentum transfer tends to occur from the larger droplets to the gas, and from the gas to the smaller droplets, in a continuum that makes it difficult to accurately control the spray statistics downstream, from only the injection definition. Moreover, as is discussed below, no information is available on the azimuthal distribution of the liquid mass flow rate.

The construction of inlet conditions that, despite these difficulties, are considered satisfactory, is presented here in four sections; their objective is to show the steps followed and the problems that arose with the successive attempts.

First of all, simulated gas flow statistics are compared with the spray-free experimental measurements, the like of those plotted with black circles in Fig. 3.3. This is presented in Section 3.3.1.

The spray injection modeling has followed several steps, as illustrated in Fig. 3.8. In a first, natural, attempt (A) we have tried to inject all droplets directly from the nozzle. But the smaller droplets gather early along the centerline and statistics retrieved at 6 mm are far from satisfactory. Consequently, a second try (B) has consisted in injecting droplets partly from the liquid sheet position, in order to approximately reproduce primary atomization. This enabled to obtain correct 6-mm statistics, although they are found to deteriorate farther downstream. Due to subsequent observations, the last option chosen for the flame simulation (C) was to inject droplets directly from the 6-mm plane, and to fully remove small droplets. The latter option is addressed in the next chapter, dedicated to the reactive-flow simulations.

In addition to Sections 3.3.2, 3.3.4 and 4.4.1 discussing respectively steps (A), (B) and (C), Section 3.3.3 is devoted to numerical measures taken to reduce the simulations' computational cost.

3.3 Steps towards a relevant injection simulation

3.3.1 Gas-only case definition

Mesh and geometry

The problem geometry, cylindrically symmetric, is shown in Fig. 3.9. For the computations described in this section, a 27-million-tetrahedron mesh was used, hereafter

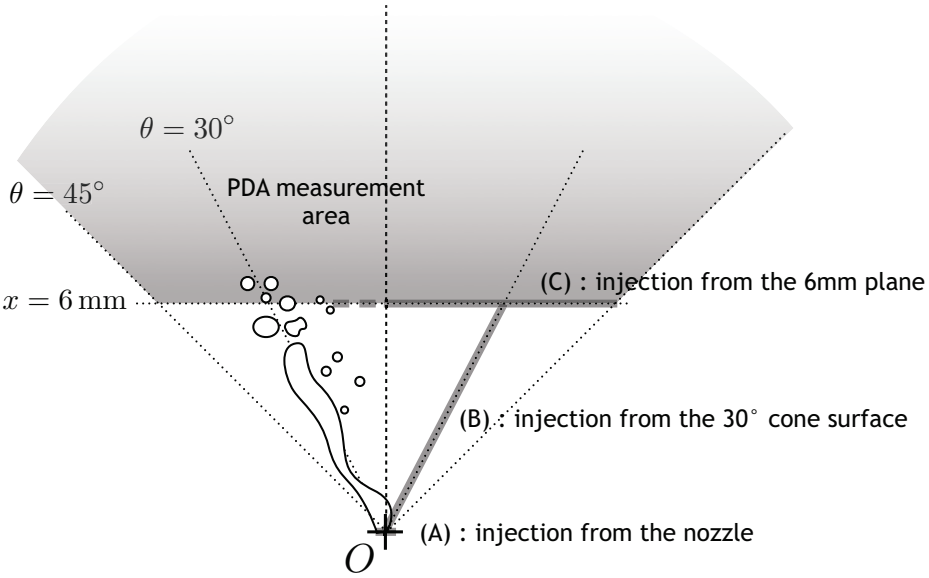

Figure 3.8: Schematic illustration of the atomization process (left) and the different numerical injection approaches (right).

referred to as the "reference" mesh. The mesh properties are summarized in Table 3.1. Cell dimensions at the nozzle are such that the injector's head diameter is discretized in 18 segments.

#	Designation	Number of cells	Number of nodes	Smallest cell (near nozzle)	Largest cell (near outlet)
1	Reference	26.8M	4.88M	500 µm	10 mm
2	Refined at nozzle	26.7M	4.85M	100 µm	10 mm
3	Uniformly refined	215M	39.9M	250 µm	5 mm

Table 3.1: Summary of the different mesh characteristics

Inlet conditions

In the experimental setup, the co-flow turbulence is generated at the inlet of a converging section by a 200-mm-wide and 40-mm-long tranquilizing chamber, followed by 50 mm of 3-mm beads held together by two 1-mm grids. A turbulence grid is also placed in the middle of this converging section, that is not directly accounted for in the simulation. It is a 1-mm square grid made of 400-µm wire.

As far as simulation is concerned, the gas turbulence properties are imposed as a boundary condition with a numerical algorithm where homogeneous isotropic turbulence with a Passot–Pouquet spectrum is injected; velocity fluctuations of amplitude $1.2\,\mathrm{cm.s^{-1}}$ and characteristic wavelength 8 mm are imposed at the entrance of the converging section.

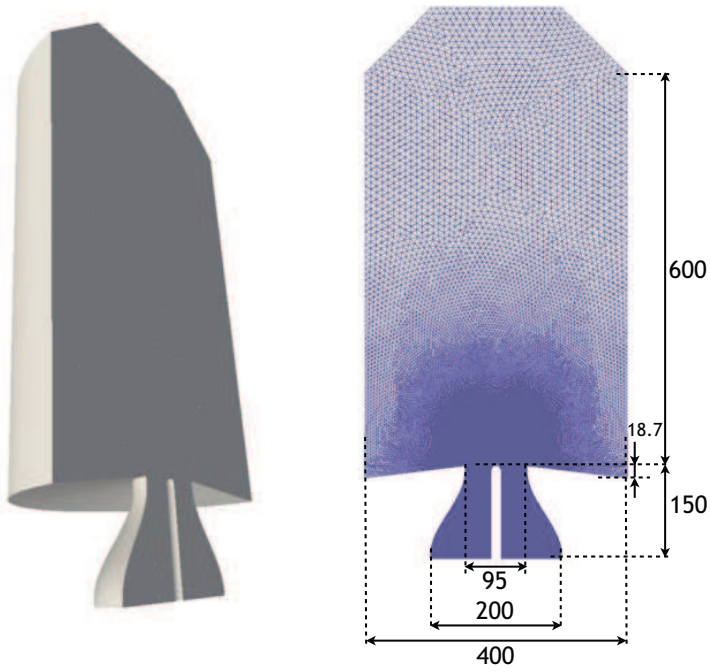

Figure 3.9: Problem geometry and general view of the reference mesh.

Spray-free velocity profiles

As presented in Section 3.1.2, DLA velocity measurements are available very close to the chamber bottom, at $x = 2\,\text{mm}$, in the absence of spray injection. The initial purpose of this measurement was to supply a structured-mesh simulation with inlet boundary conditions. With the development of YALES2, it was decided to simulate the co-flow establishment and this collected data has finally a validation role.

Overall, the simulation results are in conformity with experimental mean observations, as shown in Fig. 3.10. Statistics have been accumulated over a duration of 2.5 s. The largest mean velocity component u_x is accurately predicted, from the centerline to the brim of the inset. The radial component is correctly reproduced close to the centerline, but the entrainment of chamber gas by the co-flow is too strong in the simulation: for $r > 25\,\text{mm}$, u_r remains negative in the LES, in contradiction with the experimental measurements. Close to the centerline, where the flow is protected from the chamber gas movements by the co-flow, the rms curves show correct trends and amplitudes. But within the co-flow and near the inset's edge, the rms levels are virtually zero in the simulation, although measurements show it should reach up to 10 % of the mean velocity magnitude. All these prediction errors suggest that the chamber/co-flow stream interaction is incorrectly captured: it may be due to low-frequency fluctuations that insufficient computational time has prevented us from observing. Or simply we have not given the chamber flow enough time for flow establishment.

At any rate, these shortcomings are of limited importance, for the flow behavior is mainly driven by the spray, of much higher momentum than the gaseous co-flow. The present results, very satisfactory close to the nozzle, enable us to safely go forward with the spray injection.

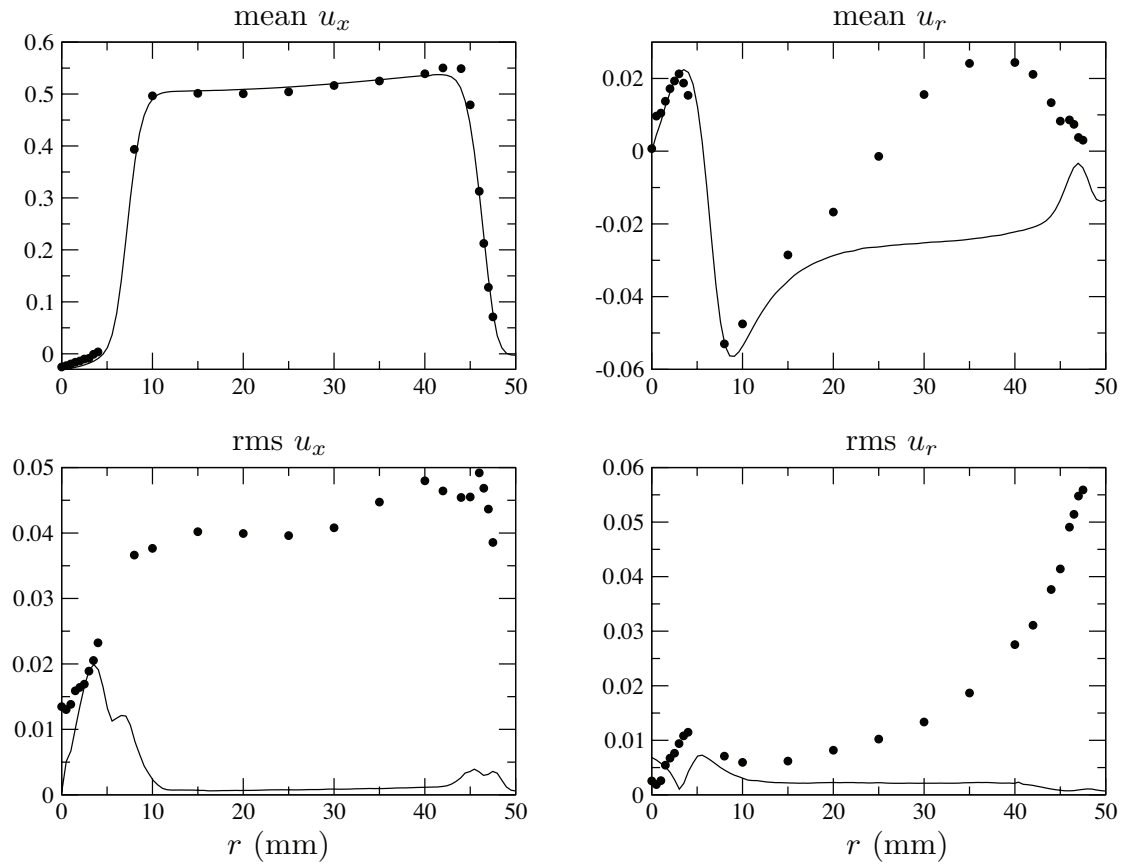

Figure 3.10: Comparison of the simulated (—) velocity statistics with the experimental measurements (•), in the absence of spray.

3.3.2 (A) Injection from the nozzle only

In this section the first attempt at defining spray inlet properties is described. Numerical spray parcels are all injected directly at the nozzle center O. The way in which their statistics are imposed is discussed below.

Statistics angular discretization

At $x = 6\,\text{mm}$, the closest distance at which spray statistics have been gathered, data is available in 15 locations between $r = 0\,\text{mm}$ and $r = 5.5\,\text{mm}$. These target points are used to impose the spray properties at the nozzle inlet, based on an angular discretization in $N_c = 15$ "sub-cones" $\mathcal{C}_1, \mathcal{C}_2, \ldots, \mathcal{C}_{N_c}$, each of them encompassing one of the measurement points, as illustrated in Fig. 3.11. The delimiting angles of the sub-cones form a continuous sequence $\theta_1, \theta_1, \ldots, \theta_{N_c+1}$, with $\theta_1 = 0$, so that $\mathcal{C}_i$ is the cone fraction $\{\theta \in [\theta_i; \theta_{i+1})\}$.

Within each sub-cone, droplets are injected in direction

$$\underline{e}_{\text{inj}} = \cos\theta\ \underline{e}_x + \sin\theta\ (\cos\phi\ \underline{e}_y + \sin\phi\ \underline{e}_z), \tag{3.2}$$

where θ and ϕ are uniform random variables respectively on $[\theta_i; \theta_{i+1})$ and $[0 : 2\pi)$. A similar discretization approach may be found in [Bini 09].

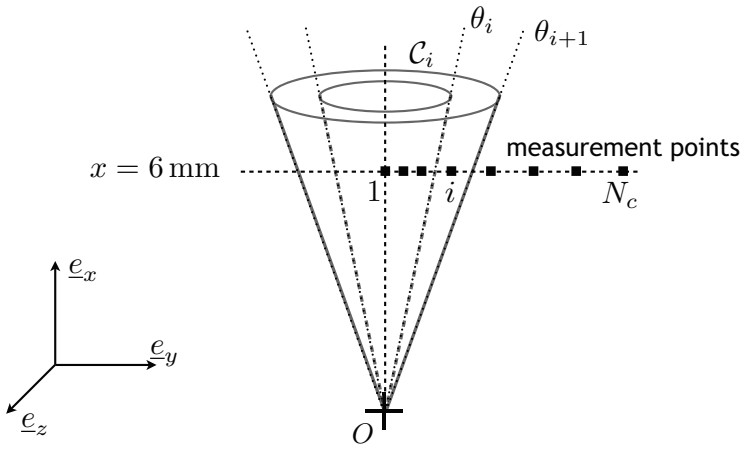

Figure 3.11: Schematic illustration of the angular discretization into $N_c = 15$ sub-cones, from the measurement points at $x = 6\,\text{mm}$.

To each sub-cone $\mathcal{C}_i$ is assigned a droplet diameter number distribution $f^{(i)}(d_p)$, a histogram pdf defined on $N_d = 50$ diameter buckets, each one of width $2\,\mu\text{m}$, between 0 and $100\,\mu\text{m}$, similar to the statistics collected by PDA (see Fig. 3.4). Also consistent with the available statistics, droplet velocity magnitude at injection follows a random law conditioned on the diameter class: for sub-cone $\mathcal{C}_i$ and diameter bucket j, u is set as a Gaussian variable, of mean $u^{(i)}|_j$ and standard deviation $u^{(i)}_{\text{rms}}|_j$.

In this approach (A), the diameter properties measured at 6 mm are directly applied to the droplets at injection. As for the velocity means and rms, the statistics collected at 6 mm are multiplied by a function of the diameter equal to or larger than one and applied to the inlet conditions. Several shapes for this function have been tried: uniform (with values from 1 to 2), tanh from 1 for large diameters to 2 or more for small diameters (heavy droplets are not expected to lose much velocity over this distance, while light ones are).

The knowledge of these properties is not sufficient for a full setup of the spray numerical injection. Most important an information is the repartition of the total mass flow rate ($q_{\text{total}} = 3.96\,\text{L.h}^{-1}$, that is $8.689 \times 10^{-4}\,\text{kg.s}^{-1}$) between the sub-cones $\mathcal{C}_i$, which is determined with the approach described below.

Mass flow rate profile

In each of these points, the PDA measurement device has collected information on a maximum of 20,000 droplets over a duration not exceeding 90 s. Thus, in addition to velocity and diameter properties, it returned – for each measurement point i – the number $n^{(i)}$ of droplets included in the sample population and the mean time $\Delta t^{(i)}_{\text{inter}}$ between two such successive droplets. This last data is not a fully reliable measure of the droplet passing frequency at the targeted location, as the device automatically excludes from its sample droplets that appear non-spherical. However, $n^{(i)}$ and $\Delta t^{(i)}_{\text{inter}}$ represent the only access to an estimation of the mass flow rate angular profile of the spray.

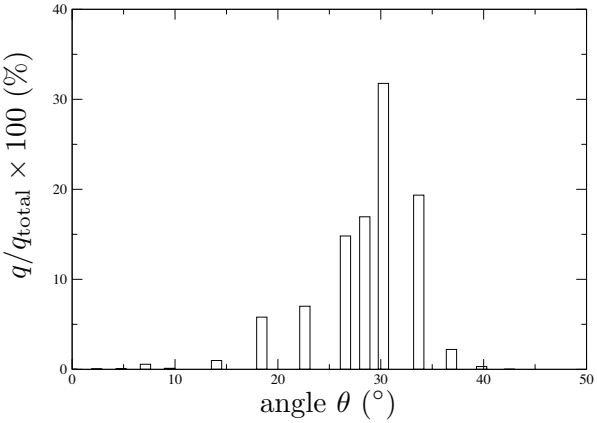

Figure 3.12: Total mass flow rate repartition among sub-cones $\mathcal{C}_i$ as estimated from Eqs. (3.3) and (3.4).

The mass flow rate per unit surface at the measurement point i is estimated as:

$$q_s^{(i)} = K \frac{n^{(i)}}{\Delta t_{\text{inter}}^{(i)}} \frac{\pi}{6} \rho_l \left(d_{32}^{(i)} \right)^3 , \tag{3.3}$$

where d_{32} is the measured SMD and K a dimensioning constant, assumed independent of the sub-cone i: the measurement volume is considered identical for all the N_c PDA target points.

The total mass flow rate emitted into sub-cone $\mathcal{C}_i$ is then computed from its counterpart per unit surface $q_s^{(i)}$ through the following normalization:

$$q^{(i)} = \frac{q_{\text{total}}}{\sum_i q_s^{(i)}} \underbrace{\pi \left(r_{i+1}^2 - r_i^2 \right)}_{S_i} , \tag{3.4}$$

where $r_i = \tan\theta_i \times 6\,\text{mm}$, such that S_i is the intersecting surface of sub-cone $\mathcal{C}_i$ with the plane $x = 6\,\text{mm}$. With Eq. (3.4), giving a value to K is thus unnecessary. The obtained mass flow rate profile is shown in Fig. 3.12.

Results

Whatever the adjustments made to the inlet definition, the results of the injection approach (A) are not satisfactory. As plotted in Fig. 3.13, a systematic peak in the longitudinal mass flow rate is observed near the centerline, in disagreement with the estimated profile shown in Fig. 3.12 – used as the nozzle profile. The mass flow rate profile does not remain self-similar along the spray expansion.

While velocity means and rms are found responsive to variations in the inlet conditions, and statistics of large droplets ($> 50\,\mu\text{m}$) are correctly captured, a deficit of small droplets (11 µm) in the outer region pdf is invariably observed, along with an excess of 25- to 40-µm droplets. Figure 3.14 shows, in six points along a line 6 mm downstream of the nozzle, the local diameter number distribution. 11-µm droplets are in excess compared with measurements at $r = 1\,\text{mm}$, but in deficit farther from the centerline. As for 25-µm parcels, their occurrence is over-predicted across the range $r = 2$–$4\,\text{mm}$.

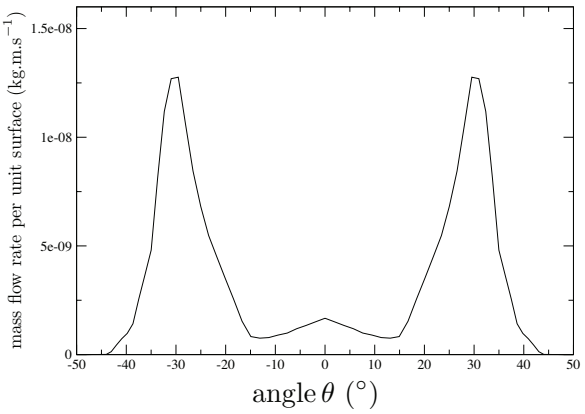

Figure 3.13: Cylindrical mean of the mass flow rate per unit surface at $x = 6\,\text{mm}$, representative of simulations of type (A), with spray injection from the nozzle.

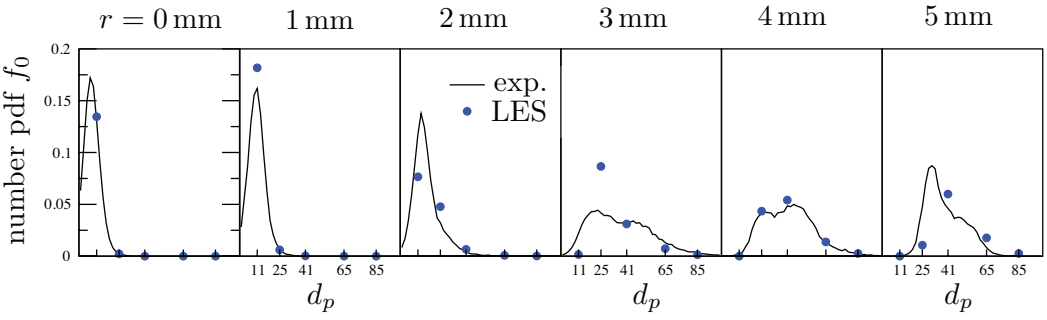

Figure 3.14: Comparison between droplet diameter number pdf at $x = 6\,\text{mm}$ measured experimentally (full line) and obtained from LES at sub-sampled diameters (blue circles), for an injection approach (A).

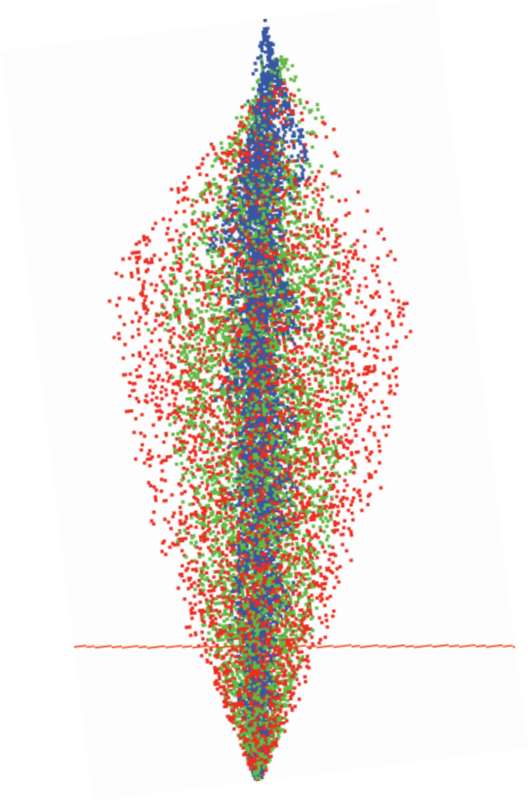

Figure 3.15: Illustration of the preferential concentration of small immaterial droplets along the centerline when issued from the nozzle: seeding of the injector in case (A) by one-way-coupled 11-µm (blue), 25-µm (green) and 41-µm (red) droplets.

The formulation imposing the 6-mm spray statistics directly as the nozzle inlet conditions shows clear limitations when it comes to the small-droplet behavior. While it is justified for the largest droplets, which do not change direction and see their velocity remain virtually constant on this distance, droplets smaller than about 40 µm are of much smaller drag relaxation time τ_p – scaling as d_p^2, Eq. (1.34) – and their trajectories are deviated by the surrounding gas velocity field.

To illustrate this effect, a test is carried out: superposed to the present spray injection, droplets of three different sizes are injected as immaterial tracers: for them only, the liquid-to-gas momentum transfer is deactivated. The injection direction is uniform within a 30° cone. Results are presented in Fig. 3.15: whatever their initial direction, the droplets are deviated towards the centerline, strongly for the 11-µm class, imperceptibly for the 41-µm class.

This proves that with the transport model, mesh, and large-droplet dynamics used here, no injection of the small droplets exclusively from the nozzle can lead to the expected statistics at 6 mm.

Mesh refinement

As far as the mesh is concerned, one factor could explain these unsatisfactory results: an insufficient refinement near the spray opening. As can be seen in Fig. 3.16 (left) and in Table 3.1, the reference mesh resolution near the spray injection is 500 µm.

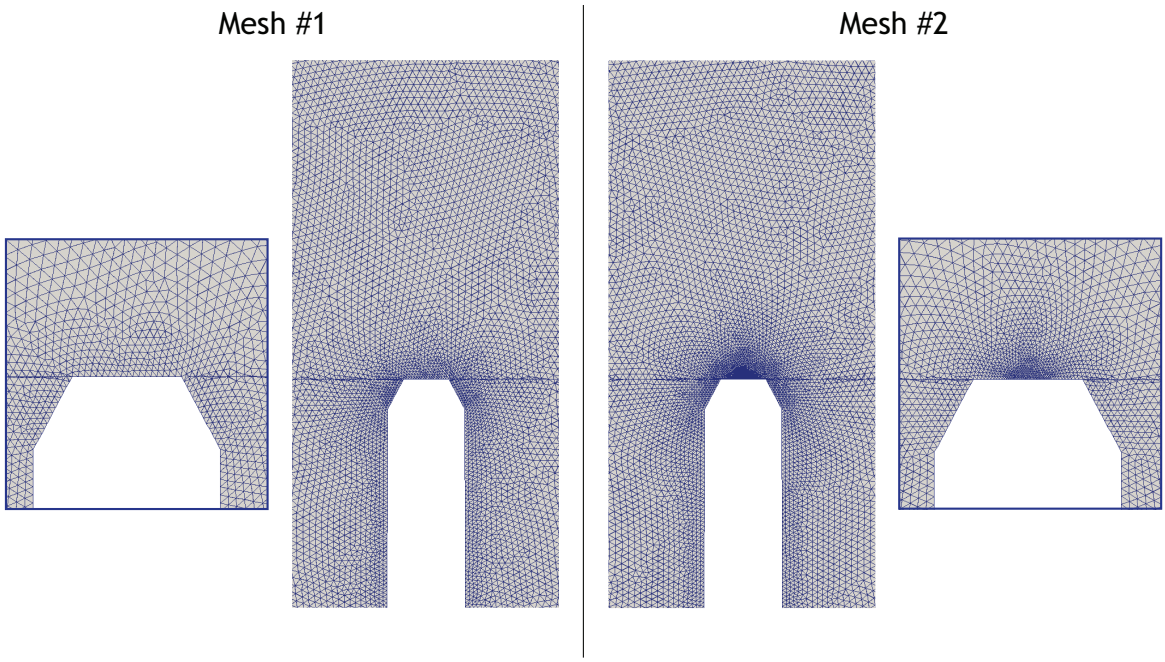

Figure 3.16: Enlarged views of the nozzle region for the reference mesh, left, and after a refinement near the nozzle exit, right.

The nozzle diameter itself is 230 µm: while it was unrealistic, for this first mesh, to aim at a full resolution of the injection, the first cell (highlighted in the figure) that welcomes the bulk of the liquid mass flow is large. Owing to the cylindrical symmetry, moreover, the velocity resultant in this first cell is aligned with the axis, while it really is radiating from the origin O.

This hypothesis is examined by attempting the same tracer-droplet simulation with mesh #2, which is more refined near the injection point, see Fig. 3.16 (right). But the same gathering of small particles along the centerline was observed, ruling out the role of the mesh resolution. Since the nozzle-refined mesh imposes, due to the CFL constraint on the first cell (higher volume-averaged velocity and smaller dimensions), a much smaller time step to the whole computation, the reference mesh is recovered in the following.

3.3.3 Numerical improvements

As the first simulation attempts, discussed above, were performed, several numerical improvements were implemented to keep the computational cost under control. These include:

- truncation, in the injected diameter pdf, of the small-droplet population
- load balance improvement from particle-aware mesh partitioning
- automatized numerical weighting of the parcels

as discussed in the paragraphs below.

Small droplet truncation

The transport of small droplets requires higher computational time than that of large ones, due to a necessary sub-stepping procedure. Indeed, the drag relaxation timescale scales as d_p^2 and imposes the sub-step time interval. Moreover, small droplets can represent a significant proportion of the total population, owing to the d_p^3 dependency of their volume. Consequently, it is sensible to impose a minimum droplet size to the inlet conditions. In practice, the mass flow rate carried by droplets of diameter bins $j < j_{\min}$ (*i.e.* $d_p < (j_{\min} - 1) \times 2\,\mu\text{m}$) is transferred onto bin $j_{\min}$. In YALES2 this is formulated in terms of number distribution: given the initial histogram pdf f_j, the truncated pdf f'_j is defined as

$$\begin{cases} f'_j = 0\,, & j < j_{\min} \\ f'_{j_{\min}} = \sum_{k=1}^{j_{\min}} f_k\,, & \\ f'_j = f_j\,, & j > j_{\min} \end{cases} \tag{3.5}$$

This transformation does not strictly conserve momentum; to achieve conservation, the inlet velocity conditional to diameter bucket $j_{\min}$ could be adjusted. Yet the overall impact is negligible if the truncation diameter is low, and it was preferred to keep the conditional droplet velocities unchanged.

In the present case, the truncation diameter is set to 6 µm. Compared to cutting at 4 µm, it yields a limited 1.5 % gain in particle population but enables a 22 % reduction of the overall computation time, while not impacting the spray statistics. No direct comparison with the original diameter pdf (no truncation) was carried out.

It is worthwhile noting that this truncation only intervenes at the inlet condition definition, and does not concern the diameter decrease due to evaporation. The numerical procedure described in Section 2.2.3 involves a threshold diameter $d_{\min} = 1\,\mu\text{m}$ for droplet vanishing. All droplets are reaching this small size before evaporating, but this happens within the flame where the evaporation rates are very high, leading to no significant increase of the transport cost.

Numerical weighting

To go further in the droplet population reduction, a diameter-dependent numerical weighting is implemented. It enables to give a larger weight to parcels corresponding to smaller, more numerous droplets, while retaining a low weight on the fewer, larger droplets that impact the gas velocity field more strongly.

A tanh-shaped weight is applied to the droplets; all parcels in the same diameter bucket are given the same weight, so that the latter can be indexed by j:

$$w_j = w_{\text{small}} + (w_{\text{large}} - w_{\text{small}}) \tanh\left(-\frac{d_p|_j - d_0}{\Delta d}\right)\,, \tag{3.6}$$

this expression involving four parameters w_{small}, w_{large}, d_0 and Δd.

The population reduction can be estimated literally from the diameter distribution: for a given mass flow rate q and number pdf f_j, the reduction in the number

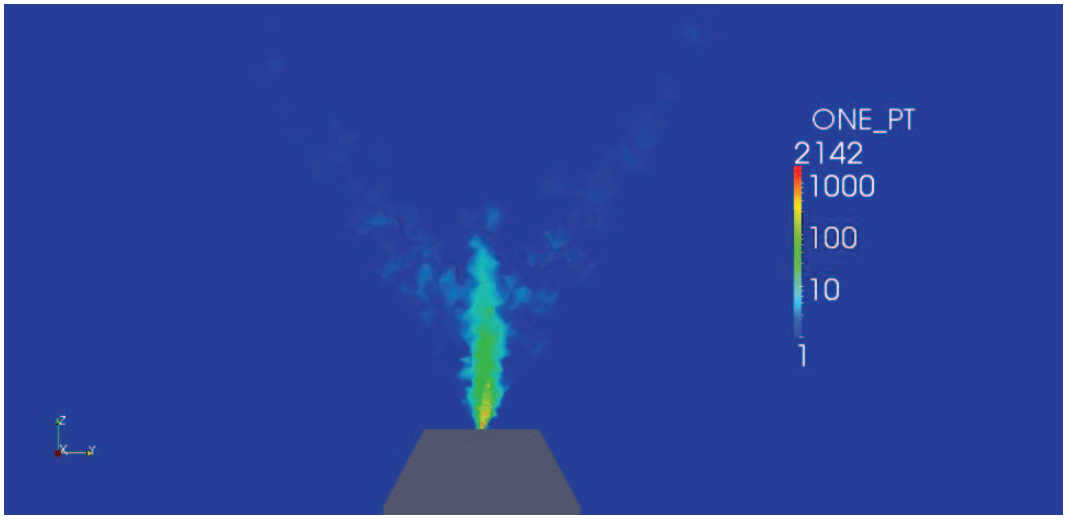

Figure 3.17: Particle density field as computed in each element to serve as a criterion in the mesh partitioning process.

of particles thanks to weighting can be estimated as

$$\frac{N_w}{N_1} \simeq \frac{\sum f_j d_p|_j^3}{\sum w_j f_j d_p|_j^3} \,. \tag{3.7}$$

In the present computations, typical values for the weight interval ranged from 1–5 to 4–20; one refined computation was done with full unity weighting; the center and width of the tanh function were respectively around 40 µm and 10 µm. The reduction in particle population reached 6.4 between the highest weighting case and the unrefined spray computation.

Particle-aware mesh partitioning

The mesh partitioning sensitive to the droplet repartition, introduced in Section 2.3.2, was developed at this stage. It is based on the number of particles in each grid element k, denoted by n_k, shown for the present case in Fig. 3.17. The resulting partition is comprised of subsets with less cells where particles are concentrated and more numerous ones in particle-scarce zones. A variable weight coefficient α_w is used to adjust the sensitivity to n_k: results for different values of α_w are shown in Fig. 3.18. So high is the particle concentration in some cells that values of α_w higher than 80 were impossible to reach because it led to empty subsets.

For $\alpha_w = 75$, the computational time reduction reached 62 %, as shown in Fig. 3.19, but an intermediary value $\alpha_w = 25$ was retained for the following, still offering a 40 % acceleration while avoiding too small mesh partition subsets.

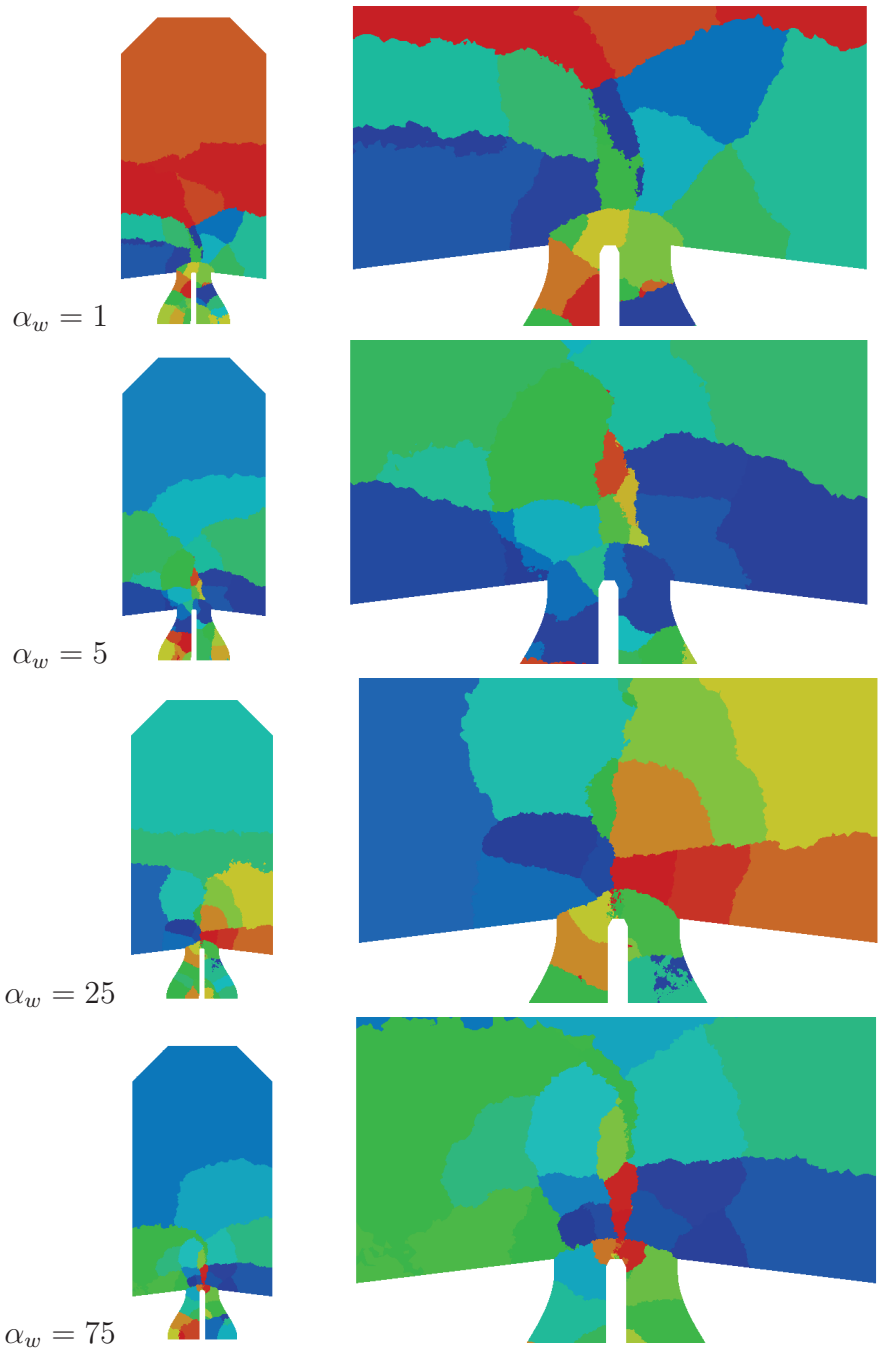

Figure 3.18: Partitionings of the mesh resulting from different choices of the α_w coefficient.

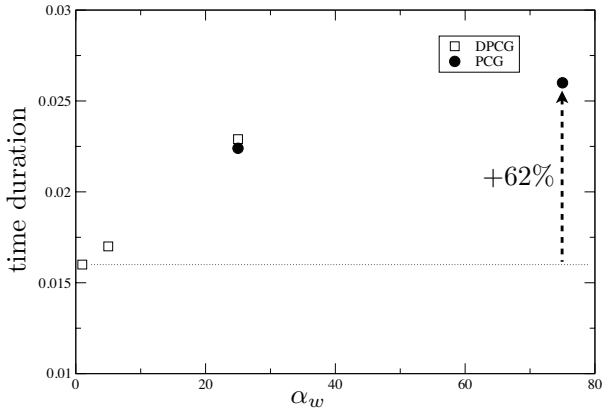

Figure 3.19: Comparison of the physical time computed in one hour of run on 512 processors, for the same configuration on grid partitionings with different α_w, see Eq. (2.51).

3.3.4 (B) Attempt at simulating primary atomization: injection from the 30°-cone surface

Initial approach

Having observed, with approach (A), the incorrect behavior of small droplets when injected from the nozzle, it was necessary to extend the injection area downstream. The 30°-cone surface imposed itself as a natural candidate since this is where the liquid sheet is located in the actual process, along which atomization occurs (see illustration in Fig. 3.8).

The injection conditions are set as follows:

- The purpose is to inject the smallest droplets from the 30°-cone surface rather than from the nozzle. Starting from the diameter distributions $f^{(i)}$ injected in each sub-cone $\mathcal{C}_i$ at the nozzle in approach (A), the smallest droplets are removed from the nozzle distributions, modified and renamed $f^{(i)}_{\text{nozzle}}$, "collected" and merged into a distribution f_{30° that is to be injected from the cone surface – see an illustration in Fig. 3.20. In practice, the mass flow rates are split according to:

$$q^{(i)}_{\text{nozzle}} = q^{(i)} \frac{\sum_{j>j_{\text{cut}}} f^{(i)}_j V_j}{\sum_{j=1}^{N_d} f^{(i)}_j V_j} \,, \tag{3.8}$$

$$q_{30^\circ} = \sum_{i=1}^{N_c} \left(q^{(i)} - q^{(i)}_{\text{nozzle}} \right) \tag{3.9}$$

  where j_{cut} is the cutting diameter index, and $V_j = \int_{d_p|_{j-1}}^{d_p|_j} x^3 \,\mathrm{d}x$ is a factor to which the volume portion of bucket j is proportional. The diameter number distributions remaining at the nozzle then read

$$f^{(i)}_{\text{nozzle}}|_j = \frac{1}{\sum_j f^{(i)}_{\text{nozzle}}|_j} \begin{cases} f^{(i)}|_j \,, & \text{if } j > j_{\text{cut}} \\ 0 \,, & \text{else} \end{cases} \,, \tag{3.10}$$

while the merged pdf for the cone surface injection is obtained by weighting the contributions of each sub-cone with its related mass injection rate:

$$f^{(i)}_{30^\circ}|_j = \frac{1}{\sum_j f^{(i)}_{30^\circ}|_j} \sum_{i=1}^{N_c} (q^{(i)} - q^{(i)}_{\text{nozzle}}) \frac{f^{(i)}_j - f^{(i)}_{\text{nozzle}}|_j}{\sum_j \left(f^{(i)}_j - f^{(i)}_{\text{nozzle}}|_j \right) V_j} \,. \tag{3.11}$$

A cutting diameter $d_{\text{cut}} = 35\,\mu\text{m}$ was found optimal, which is reasonable since it was seen that 41-µm droplets are about the smallest droplets not significantly deviated between the nozzle and the 6-mm plane. Other attempts were made where the division between nozzle and cone-surface injections is smoothed. The mass diverted from the nozzle to the cone surface amounted to between 5 and 10 % of the total mass flow rate, depending on the configurations.

- The liquid mass injection rate repartition over the cone injection surface must be defined in an appropriate way too. Three configurations were tested: (B1) droplets are injected uniformly along the x-axis; (B2) droplet injection is homogeneously spread on the surface, meaning that the mass flow rate is proportional to x; both approaches produce insufficiently satisfactory results, therefore (B3) a customized mass flow rate tanh-profile is adopted: the cone surface is divided into 10 sub-surfaces of equal x-extent, and their liquid mass injection rate satisfies a discretized version of the following law:

$$1 + \tanh\left(\frac{x - x^*}{\Delta x} \right) \,, \tag{3.12}$$

  where convenient parameters were found to be $x^* = 2\,\text{mm}$ and $\Delta x = 0.6\,\text{mm}$.
- Finally, a profile must be given to the initial droplet velocity. For the sake of simplicity, velocity properties are in a first approach applied to droplets independently from their size: velocity amplitude is set constant, $u_{30^\circ} = 30\,\text{m.s}^{-1}$; the injection angle made with the centerline direction is randomly drawn for each droplet, uniformly on a $[\theta_{\min}; \theta_{\max}]$ interval. Various intervals were tested: $[20^\circ; 40^\circ]$, to orient droplets symmetrically around the 30°-cone, to reproduce a possibly spontaneous ejection from the liquid sheet, due to surface instabilities; $[5^\circ; 30^\circ]$, or even $[-20^\circ; 20^\circ]$, to make droplet injection convergent towards the cone interior, illustrating the potential role of the gas flow entrained through holes in the liquid sheet and reaping droplets off its surface.

Additional droplet size differentiation

The statistics at 6 mm were found mostly sensitive to two degrees of freedom in this procedure: the cutting diameter (sharp or smooth) and the injection velocity angle. However, it was found that whatever the choice of parameters, the droplet behavior differs significantly between the 0–15 µm and the 15–35 µm categories. With d_{cut} at 35 µm, droplets above 15 µm prove responsive to the injection conditions: in this case, the statistics downstream are optimal when the injection angle is centered around 30 °; but the diameter distribution at the center is too uniform, leading to too high a $\langle d_p \rangle$. Conversely, decreasing the cutting diameter enables more control

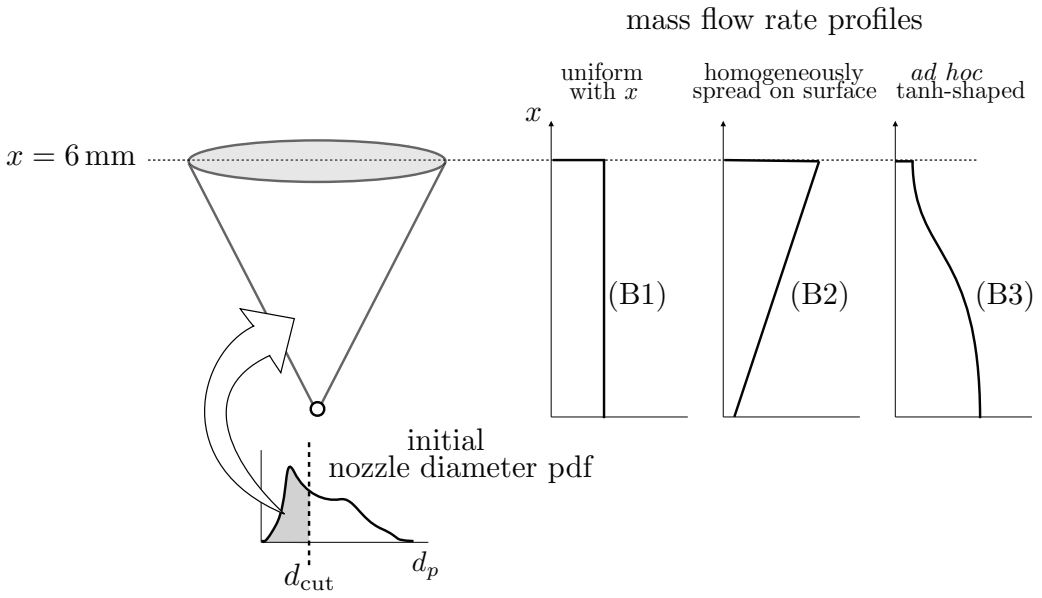

Figure 3.20: Schematic illustration of the liquid mass injection rate repartition procedure.

on the smallest droplets, but leads the larger ones (still below 35 µm) to gather too strongly at the center, as in approach (A).

A natural response to this is to separate the injection velocity properties between smallest (0–15 µm) and larger (15–35 µm) particles. Two groups are formed, with a smooth separation function (tanh-shaped), so that the 15-µm droplets are evenly split between the two, and 99 % of droplets smaller than 13 µm or larger than 17 µm are exclusively gathered in one or the other. The velocity magnitude is kept at $30\,\mathrm{m.s^{-1}}$ for both of the particle groups. For the smaller particles, the injection angle is inwards-oriented: $[-20°; 20°]$; for the larger ones, it is centered around 30°: $[15°; 45°]$.

This approach yields satisfactory results in terms of diameter distributions and velocities. In Figs. 3.21, 3.22 and 3.23, the statistics downstream of $x = 6\,\mathrm{mm}$ are shown, with the simulation results in blue and the experimental measurements in black. While the diameter pdf and conditional velocities are very well captured at 6 mm, the statistics' quality tends to degrade farther downstream, in a more pronounced way at larger radii. This degradation, visible in Fig. 3.21, starts at a distance $x = 10\,\mathrm{mm}$: the simulated mean diameter and droplet momentum are too low compared with the experiment; this is in accordance with the diameter distributions in Fig. 3.22, where it may be seen, in the plots of the upper right corner, that the 25- to 41-µm droplets are in excess.

Adding large droplets

It was found difficult to limit this d_p distribution distortion by only acting on the droplet dispersion through modifications in the injection settings: directing more intermediary-size particles inwards, which would be expected to increase the mean diameter in the outer region, impacts in turn the central region where the predicted mean diameter is correct.

Instead, another reason for the underpredicted mean diameter may be found in the experimental setup: as mentioned in Section 3.1.2, non-spherical droplets, *i.e.* large ones, are shunned from the statistical treatment by the PDA diagnostic device. These droplets may undergo secondary atomization over their trajectory and produce smaller, spherical particles, that farther downstream can be accepted by the granulometry device. It can then be thought that downstream statistics are more relevant than those upstream, which may be a consistent explanation of why statistics look correct at 6 mm, but deteriorate farther downstream. With the approach presented above, the overall diameter distribution is conserved, the total number of droplets in each size bucket is constant and equal to that extracted from the 6-mm statistics, as discussed in Section 3.3.2.

In response to this observation, statistics are now modified and large droplets are added to the injection: total mass injection rate is kept unchanged, and diameter distributions are tilted towards the larger values. In practice, a bell-shaped pdf-function f_+, centered in 65 µm and of width 15 µm, is added to the injection distributions of sub-cones with angles larger than about 25°, with a weight α_i equal to zero if $\theta_i < 25°$ and to maximum 0.2 if $\theta_i > 29°$:

$$f_+(d_p \text{ in µm}) = \exp\left[-\left(\frac{d_p - 65}{15}\right)^2\right] \tag{3.13}$$

$$\alpha_i = \alpha\left(\frac{\theta_i + \theta_{i+1}}{2}\right) \quad \text{with } \alpha(\theta \text{ in }°) = 0.2 \times \frac{1}{2}\left[1 + \tanh\left(\frac{\theta - 27}{2}\right)\right] \tag{3.14}$$

so that the modified diameter distribution, for sub-cone i, reads:

$$f'^{(i)}(d_p) = (1 - \alpha_i)\, f^{(i)}(d_p) + \alpha_i f_+(d_p)\,. \tag{3.15}$$

Expectedly, the addition of large droplets changes the upstream statistics, making them depart from the measurements, but improves those downstream. The mean droplet momentum and diameter are plotted in Fig. 3.24. It appears that the mean droplet momentum is significantly more impacted by the change than is the mean diameter: the addition of large droplets increases $\langle d_p \rangle$ and simultaneously makes droplets less prone to losing velocity; hence the augmented effect on $\langle G_p \rangle$.

Gaseous phase

The impact of the spray on the gas flow is also examined. Mean velocity streamlines are shown in Fig. 3.25. Although flow statistics have not been accumulated long enough downstream, the entrainment of the co-flow by the spray is clearly visible: streamlines converge into the spray cone and become abruptly aligned in the x-direction as they pass the spray sheet.

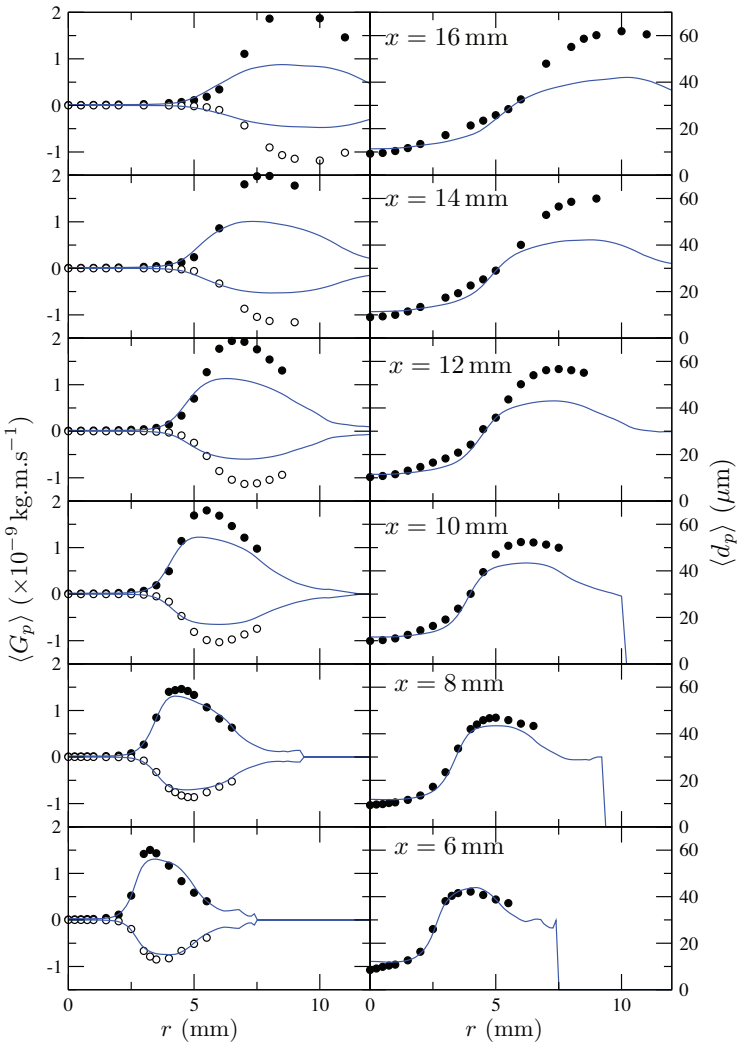

Figure 3.21: Mean droplet momentum (left) and diameter (right) along radial profiles at different distances x from the nozzle, in a simulation of injection following approach (B3). Full blue line: simulation; circles: experimental measurements, with the axial and radial components of the momentum respectively in full and empty symbols.

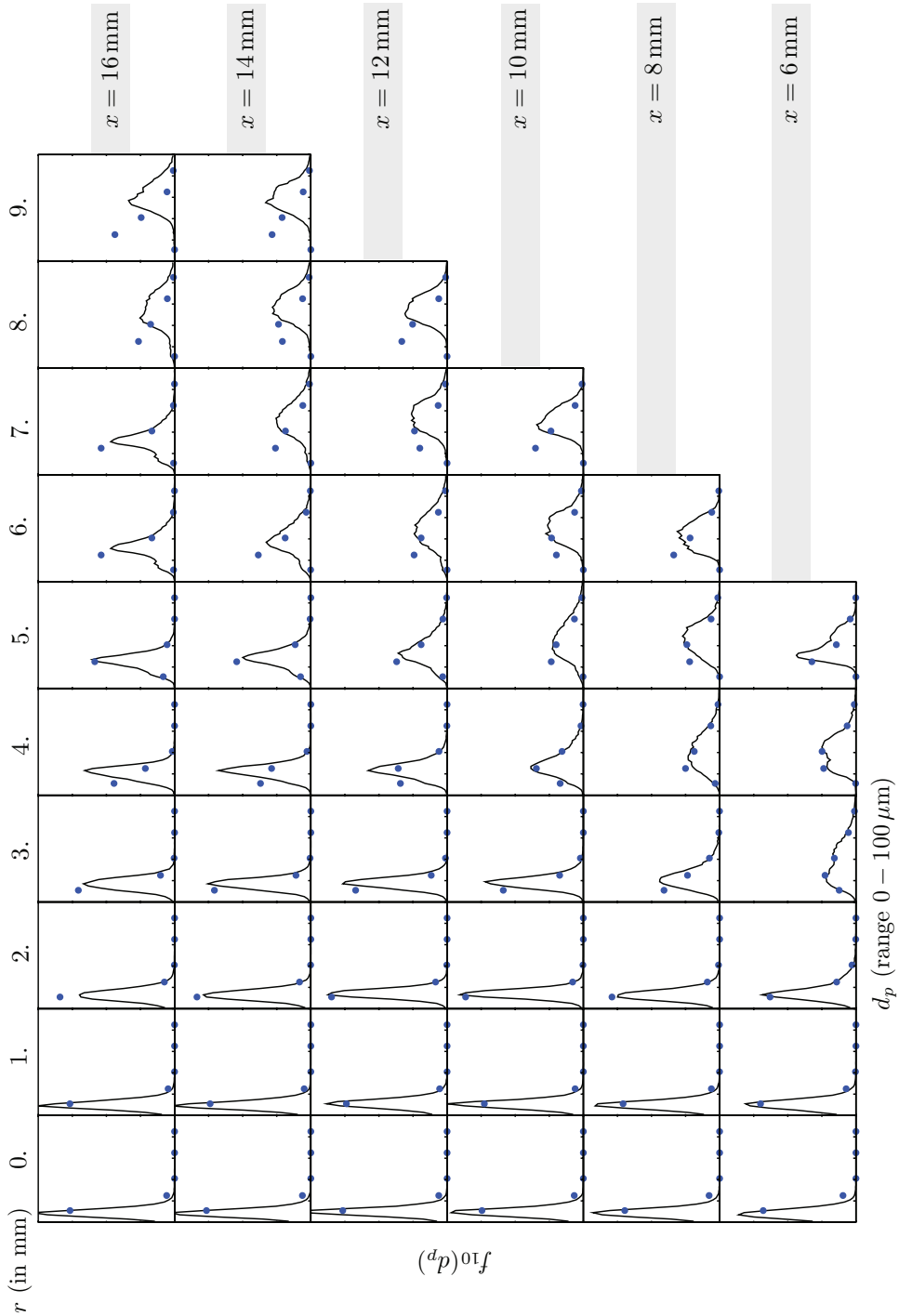

Figure 3.22: Diameter number distributions at different axial and radial positions in the measurement area, in a simulation of injection following approach (B3). Blue symbols: simulation; full black lines: experimental measurements.

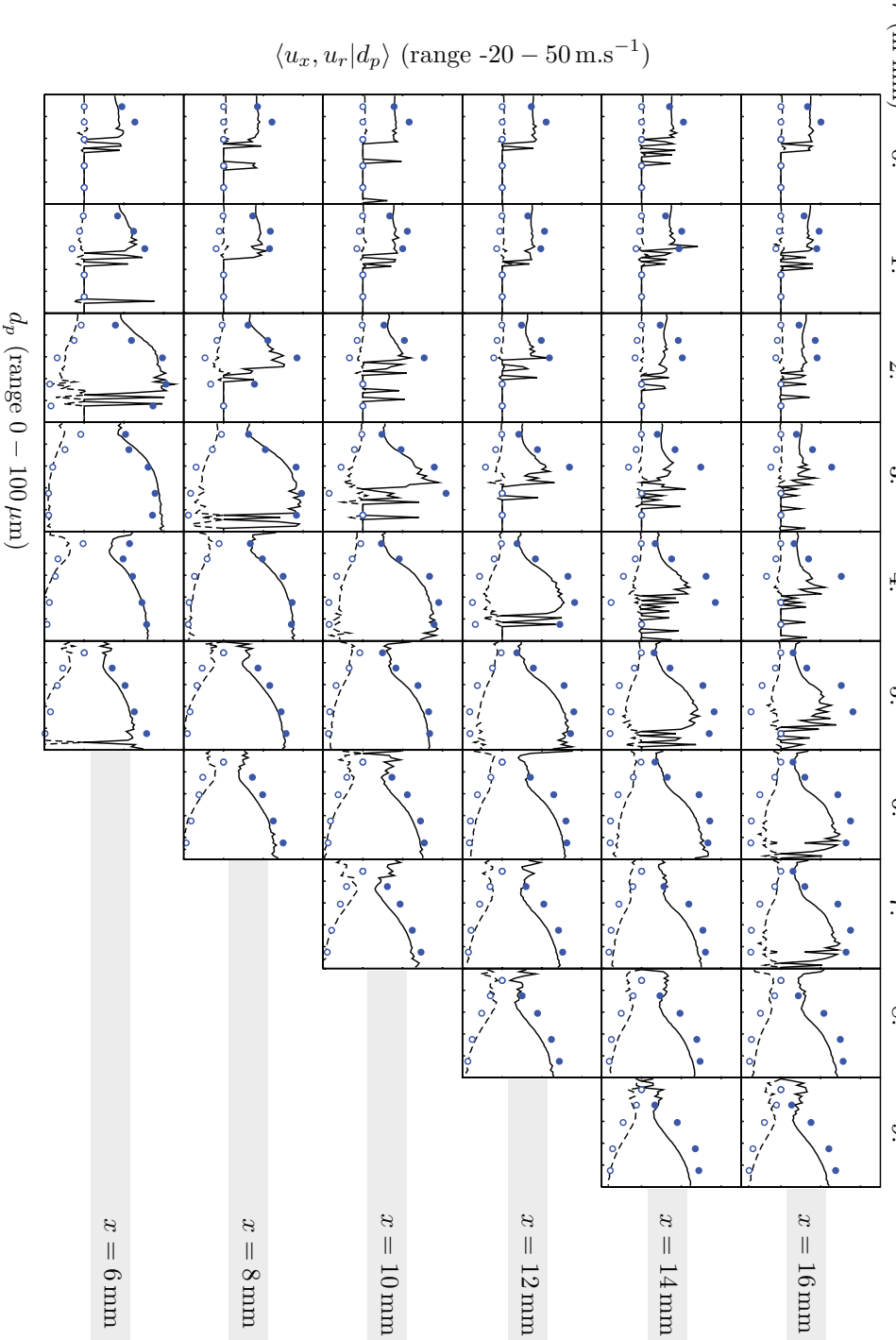

Figure 3.23: Mean velocities conditional to d_p at different axial and radial positions in the measurement area, in a simulation of injection following approach (B3). Blue symbols: simulation; full black lines: experimental measurements.

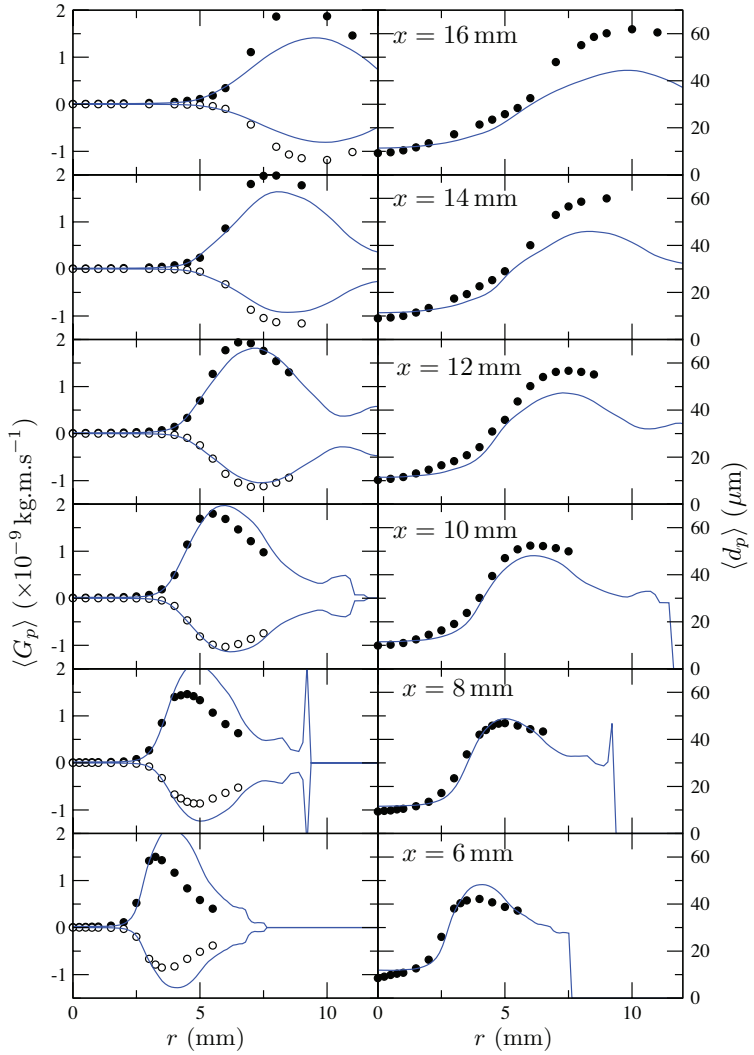

Figure 3.24: Mean droplet momentum (left) and diameter (right) along radial profiles at different distances x from the nozzle, in a simulation of injection following approach (B) **with addition of large droplets** (compare with Fig. 3.21). Full blue line: simulation; circles: experimental measurements, with the axial and radial components of the momentum respectively in full and empty symbols.

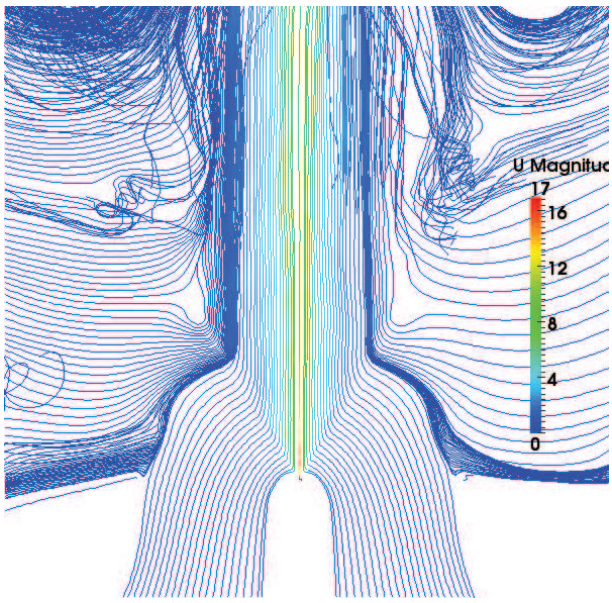

Figure 3.25: Mean velocity streamlines, colored with instantaneous velocity, for approach (B3) with addition of large droplets (the velocity mean is not fully converged downstream).

The mean and rms velocity radial profiles at several axial positions are plotted in Fig. 3.26, in the case where injection is modeled with approach (B3), without addition of large droplets. It is worthwhile mentioning here that the addition of large droplets does not significantly change the velocity profiles: this can be explained by the fact that the liquid mass injection rate is not changed, and that the large droplets never impact the diameter distribution with a factor larger than 0.2.

Looking at the comparison between LES and experimental results, notice first of all that simulations have been performed without combustion model, while the measurements were done in presence of the flame. The latter being stabilized at about 20 mm from the nozzle, there is a probable impact of the flame on the gaseous flow downstream of 15 mm that cannot be taken into account here. Overall, the trends are quite well captured up to $x = 10$ mm, with the velocity magnitude somewhat underpredicted: the liquid phase does not transfer enough momentum to the gas phase. This must probably be attributed to the large difference between the modeling framework and the actual liquid phase properties. Also, already observed above in Section 3.3.1, the predicted rms levels are too low far from the centerline. However, nearer to the spray center, in the droplet-populated area, the velocity fluctuations are correctly captured.

Downstream of $x = 14$ mm, the axial velocity component displays a decrease as $r \to 0$, that is not captured by the simulation. It will appear in the next chapter that the presence of the flame enables to recover this effect.

3.3.5 Concluding comments

The work presented in this chapter on numerically representing spray atomization through the injection of droplet parcels from the nozzle and along a 30°-cone, is fully

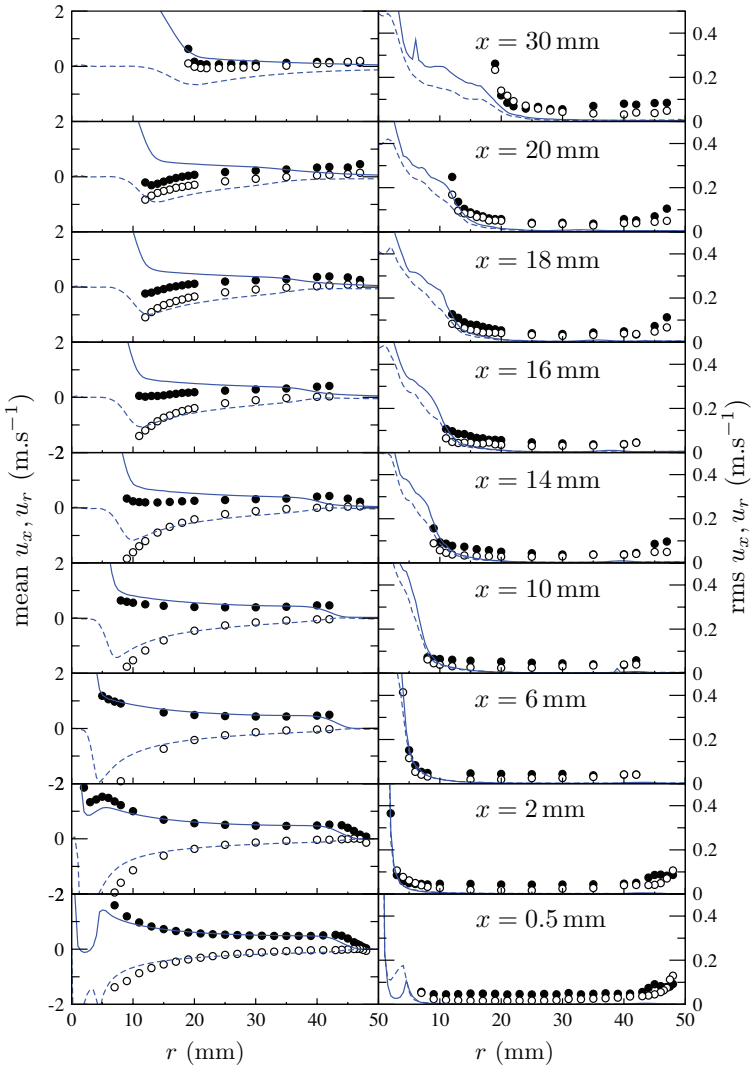

Figure 3.26: Mean and rms velocity profiles along radial profiles at different distances x from the nozzle, in a simulation of injection following approach (B3) without addition of large droplets. No combustion model is activated. Blue line: simulation (full: u_x, dashed: u_r); circles: experimental measurements.

successful in capturing statistics at the desired distance of 6 mm, initially meant to serve as input conditions. The mass flow angular distribution is a crucial information for imposing spray limit conditions, and its absence here is a cause for uncertainty.

Farther away from the nozzle, statistics deteriorate and it was not possible to make the simulation output match all available experimental measurements – themselves having to be considered with caution. We think it would be possible, with extreme care and a very substantial amount of additional work, to achieve an accurate capture of both the upstream and downstream behaviors.

However, such a result would not lead to the design of a systematic, general method for reproducing, from the present isolated droplet model, a full spray atomization, with liquid-dense areas, a liquid sheet and secondary atomization.

At any rate, the present two-phase flow has properties that make it intrinsically difficult to be reproduced by the spray model used here. First of all, the gaseous flow features peculiar turbulence characteristics since the overwhelming majority of the momentum is imposed by the radial liquid injection. Thus, even in areas where droplets are expected to be scarcer and more spherical than close to the nozzle, the dispersion model, that neglects sub-filter scale contributions, is probably unable to predict correct dispersion patterns. Second of all, the liquid forms a sheet for which the gas–spray momentum transfers cannot be described by an isolated droplet model. In these conditions, a prolonged attempt at fully reproducing measured statistics by simulation would be a waste of time. On the other hand, we cannot conceive of a different approach than one particular-based to describe the spray, because the liquid sheet does not behave like a wall: gas passes through it, intermittent holes being observed in the experiment.

We can thus outline the model improvements necessary for a more realistic treatment of the present liquid jet configuration: a) a droplet interaction model accounting for high liquid density [Sirignano 10]; b) a sub-filter-scale two-way momentum coupling (see Section 1.3.3), first developed for homogeneous turbulence, that would enable, at least in a degraded way, the input of specific turbulence properties as those encountered here (see Section 3.2.2).

Since the core objective of the present work is the study of combustion, we will favor, for the rest of the SAFIR experiment simulation, an empirical approach (C) where droplets are injected in an *ad hoc* manner from the 6-mm plane. It will lead to a successful reproduction of the flame general structure, making it possible to study two-phase combustion models.

Chapter 4

Spray flame simulation

The present work's objective is to simulate a two-phase reactive flow. In the previous chapter a simulation of the dense-spray atomization and subsequent dispersion in the SAFIR experiment has been performed in non-reactive conditions. Here, turbulent combustion modeling is added to the simulation system.

This chapter is structured in four sections. In a first, introducing part, a presentation of the SAFIR flame addressed by our simulation is given. The second section is devoted to a theoretical description of turbulent combustion models, reviewing the classical, so-called statistical approaches. Then the practical chemistry table construction, for our ethanol combustion problem, is examined. A discussion is conducted on the PCM–FPI modeling framework that is invoked here, and its application to the present two-phase-flow context. In a fourth and last section, the simulation results are examined and discussed.

Contents

4.1 The SAFIR flame structure

In this section we reproduce the results on flame structures summarized in the final SAFIR report [Cessou 10], with an emphasis on the particular case of concern in the present simulations.

4.1.1 Stability diagram

Three main flame structures are observed when the inset diameter and the CO_2 dilution in the co-flow are varied. They are summarized on a two-dimensional plot in Fig. 4.1.

- The first flame type, referred to as *type A*, corresponds to a flame stabilized at the nozzle. There are actually two flames, one inside the liquid sheet, the other anchored at the tip of the sheet. Two subtypes may be distinguished: type A', where the outer flame is more luminous than the inner one, and the converse, type A".
- In *type B* flames are stabilized at the tip of the liquid sheet: compared to type A, no inner flame is observed.
- *Type C* flames are stabilized downstream of the liquid sheet.

At low co-flow velocities ($< 2\,\mathrm{m.s^{-1}}$), the three types A, B and C are successively observed as the dilution ratio increases from 0 % (pure O_2) to about 70 %. The flame blows off at higher CO_2 contents. In practice, the mass flow rate of oxygen gas is kept constant so that increasing dilution comes with increased velocities. Type A transitions to type B around $\alpha = 40\,\%$ for the 200- and 95-mm insets, and around $\alpha = 35\,\%$ for the 45-mm inset, and type B to type C around $\alpha = 55\,\%$, 50 % and 40 % respectively for the 200-, 95- and 45-mm insets. Type A flames are, in these cases, A' flames.

At larger co-flow velocities ($7\,\mathrm{m.s^{-1}}$), obtained for the smallest inset (diameter 23 mm), only type A" flames are observed; the outer flame cannot sustain on its own the surrounding velocities, and an increase in the dilution leads to a blow-off beyond $\alpha \simeq 41$–$42\,\%$.

In the present work, only one lifted flames, *i.e.* of type C, has been simulated. Carbon dioxide dilution amounts to 60 % and the inset diameter equals 95 mm.

4.1.2 Lifted flame

The flame simulated in the present work, like all those of type C, features a dual structure, with an outer and an inner flame. The bottom of this structure is stabilized on the spray cone, at a distance from the nozzle that increases with the dilution ratio.

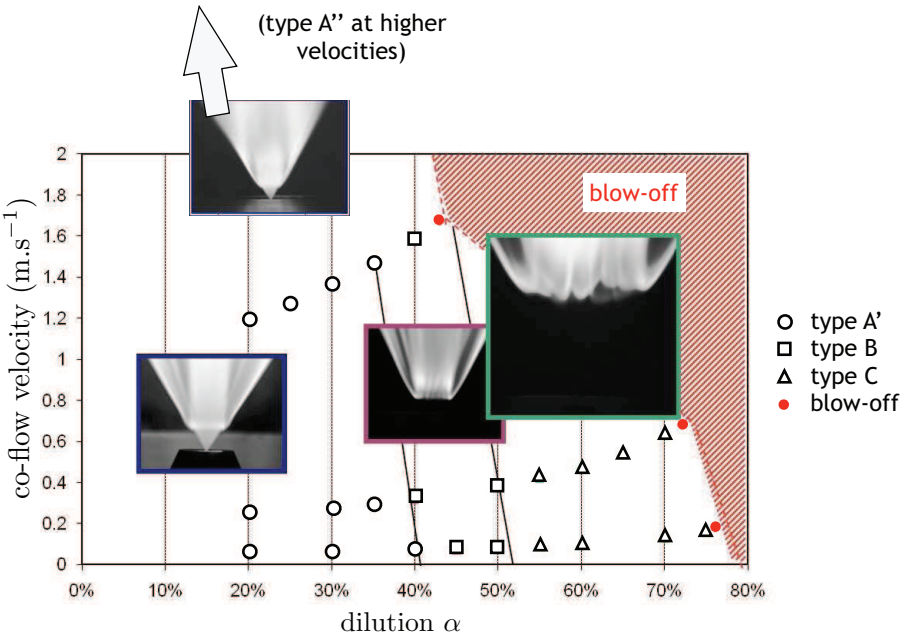

Figure 4.1: Flame structure diagram in the co-flow velocity *vs.* dilution space, taken from [Cessou 10].

The outer flame is located along a surface bending downstream; the inner flame is thicker than the latter. A time-averaged OH^*-chemiluminescence image has been produced and Abel-inversed, and is presented along with a standard picture of the flame in Fig. 4.2. Notice that the existence of stable lobes in the flame structure, probably due to asymmetries in the atomization, causes parasitic traces on these pictures.

4.2 Statistical modeling of turbulent combustion

In this section the modeling of turbulent combustion based on statistical approaches is presented. All turbulent chemistry modeling in the present work is based on such approaches: PCM–FPI in YALES2 for the present two-phase reactive flow, and the FCCT approach, the object of Part III. They form one of the main groups of available modeling strategies, next to geometrical or analytical points of view, themselves described in numerous books and reviews [Poinsot 05, Veynante 02] or PhD dissertations [Naudin 08, Lecocq 10, Yoshikawa 10].

Combustion chemistry is characterized by highly non-linear behaviors of energy production and composition changes *vs.* such thermodynamical quantities as temperature or pressure. The related phenomena occur over very short timescales and very small length scales, making their simulation in LES and RANS formalisms challenging. Moreover, hydrocarbon combustion, as is the interest here, involves dozens of species and hundreds of elementary reactions.

All modeling strategies must take this complexity into account while limiting the computational cost of simulation. The statistical approaches may be described by several modeling steps, formulated mathematically in a generic fashion in Sec-

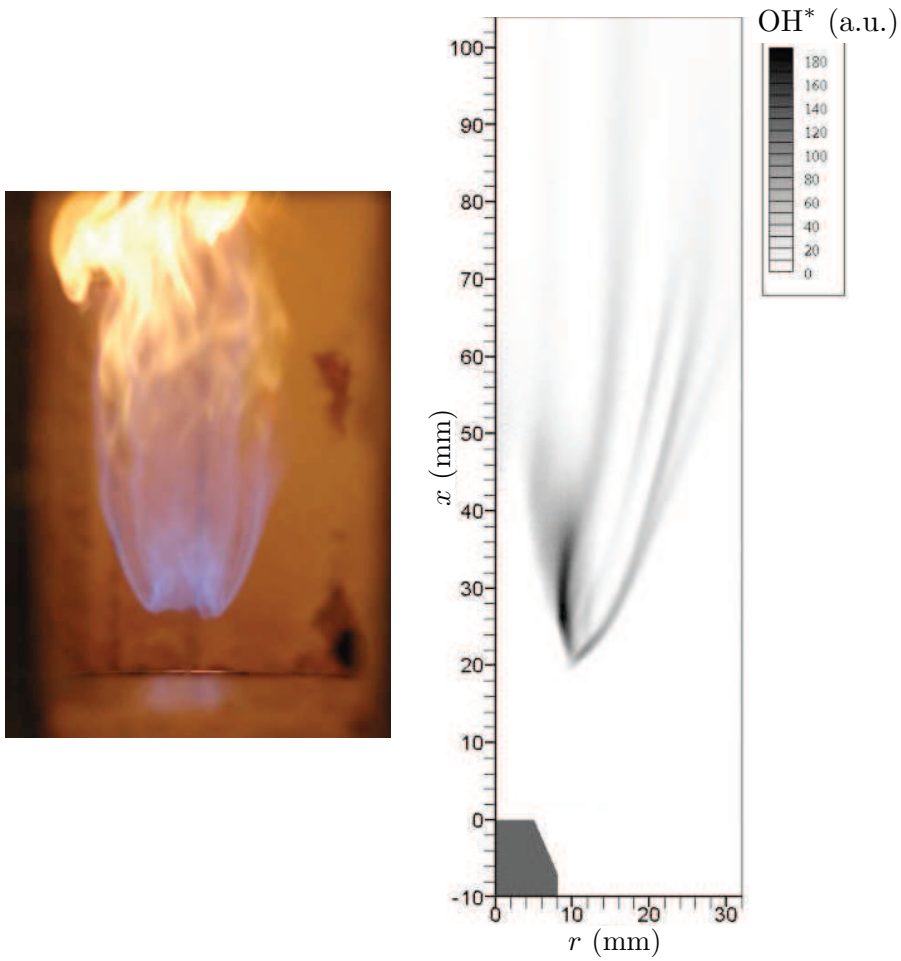

Figure 4.2: Flame picture and Abel-inversed OH*-chemiluminescence image, taken from [Cessou 10].

tion 4.2.1, then detailed in the subsequent paragraphs.

- The starting point is to describe the problem's chemical framework. The possibly large number of variables driving chemistry may be reduced by appropriate parameterization. In Section 4.2.2, kinetic mechanisms and common chemical parameters are presented.
- Parameterization should be adapted to the combustion configuration addressed, and enable the construction of a chemical database that describes chemistry at the molecular level. This is commonly done by solving archetypal problems, as examined in Section 4.2.3.
- Then, a formalism must be developed to capture, at the resolved level (spatially filtered in LES or temporally averaged in RANS), the turbulent behavior that results from the multi-scale interaction of turbulence and diffusion–reaction. The sub-filter fluctuations (resp. temporal variations) of chemical quantities require modeling, in the same way as sub-filter velocity fluctuations do in non-reacting turbulent flows (see Section 1.3.2). Different strategies exist, that form the core of turbulent chemistry modeling, as discussed in Section 4.2.4.

4.2.1 Generic formalism for statistical modeling approaches

The core "reactive turbulence" problem is described by the N_s species mass fractions balance equations (1.10), in addition to that of an energy-related quantity (temperature T, or one of the quantities listed in Section 1.1.3). In the present discussion, the aerodynamic quantities – velocity, pressure – are assumed conveniently coupled with chemistry. Therefore, the physical quantities that the turbulent combustion modeling is concerned with are Y_m, T or an equivalent, and the chemical and energy source terms. Within the RANS or LES context, the quantities that must be an output of the simulation are the filtered or time-averaged counterparts of these variables. Here, only the LES formalism will be invoked but in most cases equations are compatible with RANS.

Following notations already laid out in Eq. (2.9), the fundamental role of the model is to provide a way to determine the unknown variables, denoted by the vector $\underline{\widetilde{Q}}$, from the resolved ones $\underline{\widetilde{\psi}}$. The set of variables $\underline{\widetilde{Q}}$ requiring modeling depends on the implementation of thermochemistry in the flow solver, described in Section 2.1. As already discussed then, $\underline{Q}$ stands for

- in SiTCom: T, $\dot{\omega}_T$ and a calibrated number of Y_m and their source term $\dot{\omega}_m$
- in YALES2: ρ_{eos} and optionally T, W, as well as any number of additional quantities like mass fractions or source terms.

In a statistical modeling approach, the filtered-scale expression $\underline{\widetilde{Q}}(\underline{\widetilde{\psi}})$ is formulated, from an *a priori* knowledge of the small-scale (molecular level) properties

$$\underline{Q}(\underline{\psi}) \tag{4.1}$$

by means of a joint-$\underline{\psi}$ distribution[1] that depends on the solved variables $\widetilde{\underline{\psi}}$, following

$$\widetilde{\underline{Q}} = \int_{\underline{\psi}} Q(\underline{\psi}) p(\underline{\psi}) \, \mathrm{d}\underline{\psi} \, . \tag{4.3}$$

This distribution function p is formally similar to that of Williams' Eq. (1.23), except it is here defined continuously on space; the time and space dependencies were tacitly omitted in the above equation, the pdf's actual signature reads:

$$p(t, \underline{x}; \underline{\psi}) \, . \tag{4.4}$$

Note that this function should, strictly speaking, be referred to as a "filtered mass density function", but the term "pdf" is retained by usage.

Corresponding to the two equations above, two main steps must be completed: first, determine the small-scale expression of Eq. (4.1); second, give an expression for the pdf in Eq. (4.3).

As far as point one is concerned, it is the role of kinetic mechanisms to provide a complete description of thermochemistry, namely

$$\dot{\omega}_m(T, \{Y_{m'}, m' = 1, \ldots, N_s\}). \tag{4.5}$$

From this data, it is possible to then reduce the complexity of such expressions by designing privileged parameters which will finally form the set of solved variables $\underline{\psi}$. A chemical database is built that finally yields the contents of Eq. (4.1). Sections 4.2.2 and 4.2.3 discuss the physical aspects and implications of these steps, referred to as parameterization and tabulation.

As for the second point, formulating expressions for the joint-$\underline{\psi}$ distributions yielding realistic $\widetilde{\underline{Q}}$ is the core of turbulent combustion modeling. Classical approaches are examined in Section 4.2.4.

4.2.2 Description of chemistry

Kinetic mechanisms

The combustion modeling community relies on research in chemical kinetics which designs chemical reaction schemes, or mechanisms, consisting of a list of species and elementary reactions with their Arrhenius parameters; their purpose is to describe as realistically as possible the chemical behaviors of given sets of fuels and oxidizers in various reactive configurations, from laminar flamelet propagation to self-ignition to *e.g.* pyrolysis.

[1] The set of variables $\underline{\psi}$ is not necessarily identical to the set of resolved variables, meaning $\widetilde{\underline{\psi}}$ may be different from $\widetilde{\underline{\psi}}^{\mathrm{sol}}$. In the case where the two are equal, the pdf first moments must satisfy

$$\widetilde{\underline{\psi}} = \int_{\underline{\psi}} \underline{\psi} \, p(\underline{\psi}) \, \mathrm{d}\underline{\psi} \, . \tag{4.2}$$

However, to illustrate their common role as parameters, the letter ψ is used to denote both of them.

Some kinetic schemes are very detailed, containing several dozens of species and hundreds of reactions: they aim at offering an accurate prediction of minor species, but are memory-expensive: each mass fraction Y_m, $m = 1, \ldots, N_s$ must be transported and the source terms be computed from the numerous elementary reactions. Additionally, the evolution timescales are extremely short and impose for the resolution (and for any simulation that would directly utilize these schemes) to advance at a very slow pace. Conversely, some others are very reduced schemes, with as few as four or five species and three reactions; storing the chemical behavior of mixtures thus described is cheap, but at the cost of accuracy: only general properties of reaction are captured, and significant prediction errors must be expected. Typical examples of mechanisms for methane oxidation are, on the detailed side, the GRI-MECH 3.0 [Smith], with 53 species and 325 reactions; on the reduced side, Jones & Lindstedt [Jones 88], with 5 species and 4 reactions. Further discussion on chemical mechanism reduction may be found in [Vicquelin 09]. It is often easier for end users to integrate detailed mechanisms than very reduced ones in homogeneous reactor or stationary flamelet computations, because the latter tend to induce stiffer equation systems. At any rate, it is important to keep in mind that kinetic schemes are usually developed for certain applications and validated on limited numbers of comparisons with experiments (adiabatic flame temperatures, laminar flamelet velocity, self-ignition time) and that inaccuracies remain even for detailed schemes.

In some modeling frameworks, it is unaffordable and unnecessary to keep track of all species involved in the reaction; nevertheless, for most complex combustion problems, reduced schemes are too inaccurate to be convenient. The usual response to both these limitations is to decrease the number of degrees of freedom used in the description of chemistry. Chemical evolution is assumed to be restricted, in the mass fraction space, to a low-dimensional manifold. This is the object of the so-called "chemistry parameterization", further examined here.

Mixture fraction

The mixture fraction, described in Section 1.4.2 as a variable for characterizing mixing, is a useful parameter for combustion: it takes an oxidizer and a fuel that mix with each other for reaction to occur. Two such fluids are considered in the following, conform to notations of Eq. (1.110): notation 'Ox' refers to the oxidizer, where $Z = 0$, and 'F' to the fuel, where $Z = 1$. Stoichiometric proportions are met when $Z = Z_{\text{st}}$, higher values mean rich conditions, lower values lean conditions. An alternative variable is the equivalence ratio ϕ, the quotient of the F-to-Ox mass ratio with its value at stoichiometry, and is thus related to Z and Z_{st} through:

$$\phi = \frac{Z}{1 - Z} \times \frac{1 - Z_{\text{st}}}{Z_{\text{st}}} \,. \tag{4.6}$$

ϕ tends to infinity when Z tends to one.

Progress variable

To describe the progress of combustion, the most common parameter is a variable describing the advance of reaction from an unburnt state to a state of chemical

equilibrium. Depending on the chemical framework, it can take several forms.

A standard, intuitive way to describe the progress of reaction is to follow temperature: T itself is sometimes a good candidate, in particular for premixed combustion: since no mixing takes place, a temperature increase is fully related with reaction progress. It is common practice to normalize this variable between its value in cold mixture T_0 and its equilibrium value T_{eq}, to form

$$c = \frac{T - T_0}{T_{\text{eq}} - T_0} \,, \tag{4.7}$$

that varies from 0 to 1 as reaction goes. c is often referred to as a "progress variable".

In the context of detailed chemistry, the choice is often made to define reaction progress through a linear combination of species mass fractions, such that

$$Y_c = \sum_{m=1}^{N_s} \alpha_m Y_m \,. \tag{4.8}$$

This variable should be monotonic from the unburnt to the burnt gases, along a direction suitably chosen for the given problem (as explained below, it is mostly used in the context of premixed flames) and for the targeted configuration range. Like above, a progress variable c is defined as the normalized reaction progress:

$$c = \frac{Y_c - Y_{c,0}}{Y_{c,\text{eq}} - Y_{c,0}} \,. \tag{4.9}$$

4.2.3 Archetypal combustion problems

The usual approach for tabulating chemistry, in other words for building a reference chemical database[2], is to formulate archetypal combustion configurations, compute the chemistry behavior with the detailed kinetic mechanism and store the obtained chemical quantities with a limited number of parameters, such as those defined in the previous section. The obtained manifold is to serve as a database for all subsequent chemistry modeling in the LES, so the choice of configuration depends on the target problem. Classical approaches are discussed below.

Propagation in premixed combustion: laminar flamelet

For premixed combustion, the steady unstrained laminar flamelet is a natural candidate. A given equivalence ratio ϕ is considered, equivalent to fixing a mixture fraction Z. A set of $N_s + 1$ one-dimensional balance equations is then solved, comprising N_s equations for the species mass fractions – Eq. (1.10) – and one enthalpy

[2]Notice that the word "tabulation" is also used for some *turbulent* chemistry models, because data is stored in a lookup table, as discussed in the next section. The step described here deals with describing chemistry at the molecular diffusion scale, in other words with feeding data to the parameterization, and is the basis for subsequent development of the turbulent combustion models described here.

balance equation, for example Eq. (1.22), formulated in a frame of reference that follows the flame front at the laminar burning velocity $S_L(Z)$. For the mass fractions, this reads

$$\rho_0(Z)S_L(Z)\frac{\partial Y_m}{\partial x} = \frac{\partial}{\partial x}\left(\rho\mathcal{D}_m\frac{\partial Y_m}{\partial x}\right) + \dot{\omega}_m \,, \tag{4.10}$$

$$Y_m(x \to -\infty) = (1-Z)Y_{m,\mathrm{Ox}} + ZY_{m,\mathrm{F}}, \tag{4.11}$$

$$\frac{\partial Y_m}{\partial x}(x \to -\infty) = 0, \tag{4.12}$$

$$\frac{\partial Y_m}{\partial x}(x \to \infty) = 0, \tag{4.13}$$

$$\tag{4.14}$$

where the premixed unburnt mixture forms the upstream limit condition, Eq. (4.11), of density $\rho_0(Z)$. The downstream limit condition necessarily sees a composition at chemical equilibrium, since the zero-gradient condition on Y_m imposes $\dot{\omega}_m = 0$.

In the above set of equations, the source terms $\dot{\omega}_m$ are computed with the desired detailed reaction scheme. The resolution of this problem, which is not numerically straightforward (see for example discussion in [Poinsot 05], Sections 2.2 and 2.3), may be obtained by devoted numerical softwares like PREMIX [Kee 85].

Furthermore, this computation is only possible within the physical boundaries of the flammability domain: below and above certain equivalence ratio values, the flame is totally quenched and no propagation is experimentally observed.

ILDM–FPI/FGM. Two reference models based on a mixture fraction–progress variable parameterization of laminar premixed flamelets are FPI ("Flame Prolongation of ILDM") [Gicquel 00] and FGM ("Flamelet-Generated Manifold") [van Oijen 00], which were developed simultaneously by different research teams just before 2000. The chemical quantities Y_m, T, $\dot{\omega}_m$ and $\dot{\omega}_T$ are expressed as functions of (Z, Y_c) where Y_c is a linear combination of the species mass fractions satisfying, as a progress variable, monotony through all flame fronts of the mixture fractions of interest.

From a mathematical standpoint, this parameterization comes down to selecting the larger timescales of the problem and leaving the smallest ones aside: in the N_s-dimensional composition space, the (Z, Y_c)-described chemical evolution is an attractor of all possible initial states, with trajectories converging towards this manifold at a quick rate compared with that of Z and Y_c's evolutions. This was formalized in the ILDM ("Instrinsic Low-Dimensional Manifold") method [Maas 92], from which FPI derives its name.

The apparition of these approaches, that offer both a reduction of the memory requirement (less parameters) and slow-timescale description of chemistry, jumpstarted the prospects of large and complex combustion problems simulations, and indeed the scope and magnitude of LES applications expanded rapidly thereafter.

Additional parameters. The steady flamelet described above may be tabulated by projection on a mixture fraction–progress variable space. Yet it may happen that additional degrees of freedom must be accounted for in the problem addressed. The formulation can be extended to strained flamelets, by adding a sink term in the rhs of density, mass fraction and energy equations [Delhaye 08, Subramanian 10a]. As

a natural extension, it is possible to compute temporal evolution of these flamelets in the case of unsteady strain [Barths 98, Delhaye 08]. In the latter case, additional timescales, characteristic of the unsteadiness, are added to the problem, and adequate parameterization must be formulated if this chemistry is to be tabulated [Pitsch 00, Coelho 01].

Spray flamelets. Although it is not used in the present work, a formalism by Gutheil, called "spray flamelets", is worth being mentioned [Gutheil 98, Hollmann 98]. Laminar spray diffusion flames, consisting of an oxidizer stream directed against a gas that carries a mono-disperse spray. The system thus defined then depends on the scalar dissipation rate, like its gaseous counterpart, but also on the initial droplet size, velocity and overall equivalence ratio, as the authors point out. Choices must be made when building the database to limit the number of parameters.

Mixing–reaction interaction in non-premixed combustion: laminar diffusion flame

In a way similar to the premixed case, it is reasonable to tabulate non-premixed chemistry by solving a set of laminar diffusion flames.

The diffusion flame problem is more complex than the premixed flame, as thoroughly discussed in [Poinsot 05]. We recall simply here that from a parameterization point of view, no intrinsic timescale or flame thickness exists for diffusion flames, and that they are fundamentally described by two parameters: the mixture fraction Z and scalar dissipation $\chi_Z = 2\mathcal{D}|\underline{\nabla} Z|^2$, illustrating the dependence of the flame behavior on both reaction *and* mixing. The archetypal mass fraction equations may be written in Z space, for the steady case:

$$Z(x \to -\infty) = 0\,, \tag{4.15}$$

$$Z(x \to \infty) = 1\,, \tag{4.16}$$

$$\frac{1}{2}\rho\chi_Z \frac{\partial^2 Y_m}{\partial Z^2} + \dot{\omega}_m = 0\,. \tag{4.17}$$

No space dependency explicitly appears in Eq. (4.17) but it is embedded in χ_Z, which depends on space. The above equations define a locally one-dimensional flamelet structure. Often the scalar dissipation rate profile is parameterized with a single constant a in s^{-1}, for example the value of χ_Z at the stoichiometric point $Z = Z_{\mathrm{st}}$, enabling a simpler two-variable tabulation: the output chemical quantities Y_m, T and their source terms may be formulated as functions of (Z, a). The chemical progress variable c, if any is defined, will also be an output $c(Z, a)$. It is important to note that it is not monotonic across the flame, as shown in Fig. 4.3. As a consequence, chemistry tabulation through diffusion flames is complex in practice [Michel 08].

The domain on which the diffusion flamelets can be computed is restricted by quenching point and ignition point: these are limit values a_q and a_i of the scalar dissipation rate between which a hysteresis, the so-called "S-shape" behavior, is observed: starting from a frozen flow flamelet, at high strain, decreasing a progressively will lead to ignition when $a = a_i$; starting from a burning flamelet, at low strain, increasing a up to a_q leads to quenching. In between ($a_i \leq a \leq a_q$), there exists a weak branch of burning unstable equilibrium [Poinsot 05, Veynante 02, Ihme 08].

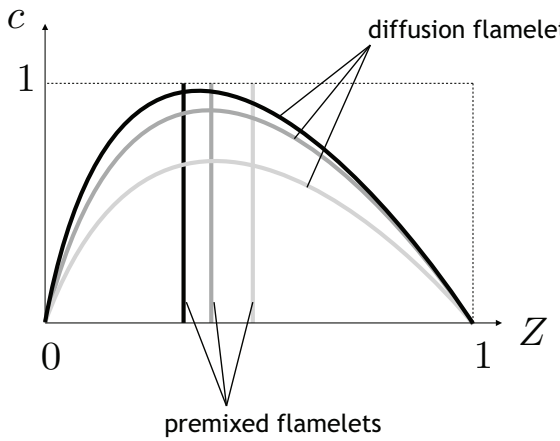

Figure 4.3: Schematic illustration of premixed and diffusion flame structures in the mixture fraction Z and progress variable c space. The main parameter for the former is Z, and for the latter χ_Z. It may be seen that c is not monotonic across the diffusion flame front.

Self-ignition: perfectly-stirred reactor (PSR)

The textbook problem for mixture ignition is the perfectly-stirred reactor, or PSR: whether in self-ignition or in forced ignition, the spatial gradients can sometimes be neglected compared to the chemical source terms. The handling of equations is then much simpler than for flamelets; in the baseline configuration where no mixing is considered, the mass fraction equation reads:

$$\rho \frac{\partial Y_m}{\partial t} = \dot{\omega}_m \, . \tag{4.18}$$

In the formulation above, the mixture is a closed system, with fixed equivalence ratio and only the progress variable varying as self-ignition occurs. With the evolution $c(t)$, the system may be tabulated such that $Y_m^{\mathrm{tab}}(c(t)) = Y_m(t)$. Forced ignition may also be simulated this way, but an enthalpy increase must be modeled at some point, that should in theory lead to the insertion of an additional parameter [Lacaze 09]. Often, though, the forced ignition behavior is mapped onto the self-ignition manifold by modeling the enthalpy increase by a progress variable increase [Boileau 08b, Triantafyllidis 09, Subramanian 10b].

Additional parameters. Mixing events and variations in Z can be taken into account by considering a plug flow reactor: the PSR is connected to a flow input with given mass flow rate and composition. For mass conservation, an output with mass flow rate instantaneously equal to that of the inlet is also implemented. The inlet mass fractions are denoted by Y_m^{in} and the ratio of inlet mass flow rate to the mass contained in the reactor is inverse to a characteristic injection, or engulfment, timescale, τ_{inj}, that will be discussed in Part III of this study (see Section 5.3.3). The resulting equation reads

$$\frac{\partial Y_m}{\partial t} = \dot{\omega}_m + \frac{Y_m^{\mathrm{in}} - Y_m}{\tau_{\mathrm{inj}}} \, . \tag{4.19}$$

If the inlet mixture composition belongs to the (Z, c) manifold, such that $Y_m^{\text{in}} = Y_m(Z^{\text{in}}, c^{\text{in}})$, the system may then be tabulated with the three parameters Z, c and τ_{inj}.

Like above, the controlling variables of the problem may be made unsteady, enabling mass flow rate (through τ_{inj}) and composition (through $Z^{\text{in}}, c^{\text{in}}$) to vary in time.

Partially premixed combustion

Most combustion problems that are not fully premixed display a partially premixed behavior: rather than strict diffusion flame structures where homogeneous pure fuel on one side reacts with homogeneous pure oxidizer on the other side, there exist mixture fraction gradients on both sides. A typical structure of this phenomenon is the well-known triple flame, described experimentally in 1965 [Philips 65] and later captured numerically [Vervisch 98] and studied by asymptotical analysis, see among others [Boulanger 02].

For these cases, the premixed flamelet formulation lacks diffusion in the Z direction: a two-dimensional problem should be solved. In this context, a notable flamelet resolution approach may be mentioned: Nguyen *et al.* [Nguyen 10] formulate the premixed flamelet equation in the reduced parameter space (Z, Y_c) rather than in space. It allows a straightforward introduction of diffusion across the equivalence ratio space ($\partial^2 \cdot / \partial Z^2$ terms). It also happens to enable a quicker computation of the first flamelet solution, most often a delicate matter.

4.2.4 Turbulent combustion modeling

The modeling work concerned with combustion's turbulent behavior has to describe the sub-filter scale statistics of the chemical parameters $\underline{\psi}$ chosen in the parameterization step discussed above. Mathematically, the aim is to provide an expression for the joint-variable pdf $p(\underline{\psi})$ of Eq. (4.3). The modeling work also has to ensure that p's formulation makes the computation of the unknown fields $\underline{\widetilde{Q}}$ through Eq. (4.3) accurate enough at a reasonable computational cost.

Classical approaches are presented in the following paragraphs. A schematic summary of the approaches is given in Fig. 4.4.

Transported pdf

A natural strategy is to attempt a direct resolution of the joint-parameter distribution. Formally, p's balance equation is similar to the spray equation, Eq. (1.27), except that the fields are continuous not discrete; but variable density and the unclosed sub-filter-scale terms add complexity to it [Jaberi 99] :

$$\begin{aligned}\frac{\partial(\overline{\rho}p)}{\partial t} + \underline{\nabla}\cdot(\overline{\rho}\,\underline{\widetilde{u}}\,p) &= -\underline{\nabla}\cdot\left(\overline{\rho}\left[\overline{\langle\underline{u}|\underline{\psi}\rangle} - \underline{\widetilde{u}}\right]p\right) \\ &\quad + \frac{\partial}{\partial\underline{\psi}}\cdot\left(\overline{\rho}\overline{\left\langle\frac{1}{\rho(\underline{\psi})}\underline{\nabla}\cdot\underline{\underline{J}}_{\underline{\psi}}\,\middle|\,\underline{\psi}\right\rangle}\,p\right) + \frac{\partial}{\partial\underline{\psi}}\cdot\left(\overline{\rho}\,\underline{\dot{\omega}}(\underline{\psi})\,p\right). \quad (4.20)\end{aligned}$$

In the rhs' second term, $\underline{\underline{J}}_{\underline{\psi}}$ is the tensor of $\underline{\psi}$'s diffusion fluxes in space (*e.g.* for a mass fraction, $\underline{J}_{Y_m} = -\mathcal{D}\underline{\nabla} Y_m$). Most importantly, the last term is closed since $\underline{\dot{\omega}}$, the source terms for $\underline{\psi}$'s component variables, is known from the chemical database previously discussed. Multiplying Eq. (4.20) with $\underline{\psi}$ to form transport equations of $\underline{\psi}\, p$ and taking their first density-weighted moment yields the Favre-filtered Navier-Stokes equations for $\underline{\psi}$ (mass fractions, temperatures, etc.), recovering Eqs. (1.95)–(1.96) formulated in Part I.

To solve this equation in a practical way, a numerical method must be implemented that addresses the two challenges of 1) restricting p's infinite-dimension functional space to a finite number of unknowns, and 2) closing the first two rhs terms that carry the subfilter-scale convection and diffusion processes [Haworth 09]. Lagrangian Monte-Carlo procedure [Pope 85] is behind one class of such methods; it echoes the spray transport formalism discussed in Part I. Lagrangian numerical particles, carrying individual position, velocity, and $\underline{\psi}$ properties (likewise indexed by $^{(k)}, k = 1, \ldots, N_p$) , are transported in physical space by the filtered velocity field as well as molecular and sub-filter diffusion, for which the same discussions as those concerning the turbulent transport of spray parcels in Section 1.3.3 apply. The latter are carried by the first term in Eq. (4.20). In addition, the particles' $\underline{\psi}$ undergo the mixing–reaction processes carried by the remaining two terms. While chemistry is closed, mixing must be modeled and this makes up the most delicate part of the whole method. Discrete particle interaction models have been developed that aim at reproducing the effect of molecular and sub-filter turbulent diffusion on the scalar fields. They are the object of numerous studies [Correa 95, Subramaniam 99, Ren 04, Meyer 09] and continuing developments [Duplat 10, Shetty 10]; one of them in particular, the EMST model [Subramaniam 98], is involved in this work's Part III.

The stochastic particle set defines a space-localized fine-grained distribution

$$\frac{1}{N_p} \sum_{k=1}^{N_p} \delta(\underline{\psi} - \underline{\psi}^{(k)}(t)) \delta(\underline{x} - \underline{x}^{(k)}(t)) \,, \tag{4.21}$$

that may then be used to approximate the joint-$\underline{\psi}$ pdf through a discretized space-filtering operation

$$p(\underline{\psi}; \underline{x}, t) \simeq \frac{\sum_k \delta(\underline{\psi} - \underline{\psi}^{(k)}(t))\, \mathcal{G}_\Delta(\underline{x}^{(k)}(t) - \underline{x})}{\sum_k \mathcal{G}_\Delta(\underline{x}^{(k)}(t) - \underline{x})} \tag{4.22}$$

or any convenient weighted-average operation [Jaberi 99]. In practice, this expression is combined with Eq. (4.3) to compute directly the filtered quantities $\widetilde{Q}$ of interest (among which $\underline{\widetilde{\psi}}$ themselves):

$$\widetilde{Q}(\underline{x}, t) = \frac{\sum_k Q(\underline{\psi}^{(k)})\, \mathcal{G}_\Delta(\underline{x}^{(k)}(t) - \underline{x})}{\sum_k \mathcal{G}_\Delta(\underline{x}^{(k)}(t) - \underline{x})} \,. \tag{4.23}$$

An alternative resolution method, similarly to the spray resolution approaches, is to approximate the joint-$\underline{\psi}$ pdf by the computation of several Eulerian stochastic fields [Valino 98, Sabel'nikov 05, Jones 10d].

Balancing their mixing-model-related limitations, one of the most attractive features of pdf transport methods is to make estimations of the filtered chemical source terms unnecessary. In theory, a fully detailed chemical scheme may be used without reduction. However, these methods are computationally costly, because like all Monte-Carlo techniques, the prediction error decreases as the inverse square root of the number of samples, making a large number of stochastic particles or fields required for accuracy. Thus, it is favorable to use them combined with reduced kinetic schemes or tabulated chemistry. For example, in the case of a flamelet-based chemistry, a physical interpretation of the pdf transport method is that the turbulent flame is assumed to be formed by multiple flamelet portions: the molecular-diffusion-scale structure is embedded in the chemical table; their individual properties Z and Y_c evolve, at the sub-filter scale, by reaction (closed $\dot{\omega}_{Y_c}(Z, Y_c)$) and turbulent and diffusion interactions predicted by the mixing model.

The approach is compatible with the RANS formalism, in which case pdf integration is used to compute the time-averaged fields.

Presumed pdf: Conditional Moment Closure (CMC)

Pdf transport, described above, aims at preserving all degrees of freedom to the chemical variable $\underline{\psi}$ distribution. In the Conditional Moment Closure (CMC) formalism [Klimenko 99, Bushe 99, Cha 01, Kronenburg 04], the number of degrees of freedom is reduced to a finite set of parameters, which will be used to condition the parameter vector $\underline{\psi}$. This set of parameters is referred to as the conditioning parameters, and denoted by $\underline{\eta}$. Typical such parameters are the mixture fraction Z or the scalar dissipation χ_Z. $\underline{\eta}$ may be a subset of $\underline{\psi}$ or not.

The idea is to *presume* the joint-$\underline{\eta}$ distribution $\mathcal{P}(\underline{\eta})$ and to solve the filtered unknown $\underline{\psi}$ conditional on $\underline{\eta}$:

$$\widetilde{\langle \underline{\psi} | \underline{\eta} \rangle} \,, \tag{4.24}$$

from where the chemical source term will be closed by the first order hypothesis

$$\widetilde{\langle \underline{\dot{\omega}}(\underline{\psi}) | \underline{\eta} \rangle} \simeq \underline{\dot{\omega}} \left(\widetilde{\langle \underline{\psi} | \underline{\eta} \rangle} \right) \,. \tag{4.25}$$

Presumed pdf shapes. Since distribution functions are to some extent impractical to compute directly, as discussed in the previous section on pdf transport, it is a widespread alternative to presume them. Their shape is commonly assumed to be a function parameterized by its first and second moments, which are resolved: for a unique variable η,

$$\mathcal{P}(\eta) = \mathcal{P}_{\widetilde{\eta}, \widetilde{\eta''^2}}(\eta) \,. \tag{4.26}$$

This requires solving only $\widetilde{\eta}$ and $\widetilde{\eta''^2}$, rather than the large number of samples required to make the Monte-Carlo error acceptable in the pdf transport approach. The first moment is usually solved on an Eulerian grid; likewise, the variance can be transported (see [Vervisch 04, Domingo 05a] for its balance equation), or it can be computed from its mother variable resolved field $\widetilde{\eta}$ (see discussion in Section 4.3.2).

The most widely used presumed distribution is the beta-shaped function. For a variable whose variation interval is 0–1:

$$\beta(\eta) = \frac{\eta^{a-1}(1-\eta)^{b-1}}{\int_0^1 \eta^{*a-1}(1-\eta^*)^{b-1}\,\mathrm{d}\eta^*}\,, \tag{4.27}$$

where the parameters a and b are coefficients determined from the first and second moments. They satisfy:

$$a = \widetilde{\eta}\left(\frac{1}{S_\eta} - 1\right)\,, \quad b = a\left(\frac{1}{\widetilde{\eta}} - 1\right)\,, \tag{4.28}$$

where S_η is a normalized variance, or unmixedness factor. It is designed so as to vary between 0 and 1, with a relation to the second order moment η_v reading

$$S_\eta = \frac{\eta_v}{\widetilde{\eta}(1-\widetilde{\eta})}\,. \tag{4.29}$$

Studies from DNS simulations have shown these functions to be satisfactory approximations of the sub-filter distributions of mixture fractions and progress variables [Vervisch 92, Wall 00, Vervisch 04, Moureau 11b].

CMC theory. To implement CMC in a LES computation, the following steps must be taken:

- A relevant set of conditioning variables $\underline{\eta}$ is selected; for computational cost reasons, the smaller the better.
- The $\underline{\eta}$-space is discretized into a number $N_{\underline{\eta}}$ of values $\underline{\eta}^{(i)}$, $i = 1, \ldots, N_{\underline{\eta}}$.
- The $N_{\underline{\eta}}$ sets of conditional filtered parameters $\underline{\Psi}^{(i)} \equiv \widetilde{\langle \underline{\psi} | \underline{\eta}^{(i)} \rangle}$ are solved, they satisfy equations where the chemical source term is closed, thanks to Eq. (4.25), and the other terms must be modeled [Klimenko 99, Bushe 99, Triantafyllidis 09]. These equations must usually be solved on a coarser grid than the rest of the computation, since $N_{\underline{\eta}}$ may count in the dozens.
- On the regular grid, $\underline{\eta}$'s moments are transported so that in each point $\mathcal{P}(\underline{\eta})$ may be presumed. The desired chemical quantities $\widetilde{\underline{Q}}$ can then be evaluated. The filtered mass density function p within the expression

$$\widetilde{\underline{Q}} = \int_{\underline{\psi}} \underline{Q}(\underline{\psi}) p(\underline{\psi})\,\mathrm{d}\underline{\psi} \tag{4.30}$$

  is decomposed using $\underline{\eta}$'s distribution:

$$p(\underline{\psi}) = \int_{\underline{\eta}} \mathcal{P}(\underline{\eta}) p(\underline{\psi}|\underline{\eta})\,\mathrm{d}\underline{\eta}\,, \tag{4.31}$$

  which yields

$$\begin{aligned} \widetilde{\underline{Q}} &= \int_{\underline{\eta}} \mathcal{P}(\underline{\eta}) \left(\int_{\underline{\psi}} \underline{Q}(\underline{\psi}) p(\underline{\psi}|\underline{\eta})\,\mathrm{d}\underline{\psi} \right) \mathrm{d}\underline{\eta} \\ &= \int_{\underline{\eta}} \mathcal{P}(\underline{\eta})\, \underline{Q} \left(\widetilde{\langle \underline{\psi} | \underline{\eta} \rangle} \right) \mathrm{d}\underline{\eta}\,. \end{aligned} \tag{4.32}$$

The values for $\underline{Q}$ under the integral sign are available from the chemical database, and the summation is finally discretized as

$$\widetilde{\underline{Q}} \simeq \sum_{i=1}^{N_{\underline{\eta}}} \mathcal{P}(\underline{\eta}^{(i)}) \underline{Q} \left(\widetilde{\langle \underline{\psi} | \underline{\eta}^{(i)} \rangle} \right) . \tag{4.33}$$

Formulations allowing for second-order closure of the chemical terms [Mastorakos 98] or compatible with spray combustion [Mortensen 09] have been developed.

This technique was first adapted for Reynolds-averaged approaches, and is now used by several teams in LES [Navarro-Martinez 05, Navarro-Martinez 09, Garmory 11]

Presumed Conditional Moments (PCM).

The PCM approach was initially developed for and applied to RANS computations [Vervisch 04, Fiorina 05], then applied to LES [Galpin 08, Domingo 08].

It may be seen as an extension of the CMC model, where the set of conditioning variables is superposed with the entire set of chemical parameters: $\underline{\eta} = \underline{\psi}$. Thus, no conditional average $\underline{\Psi}^{(i)}$ is solved; instead, the full joint-$\underline{\psi}$ distribution must be presumed. In the CMC formalism, Eq. (4.31) simply means that p and $\mathcal{P}$ are now identical objects.

The practical configurations to which PCM has been applied are two-dimensional: chemistry is parameterized by mixture fraction and progress variable. In these cases, it may be argued, based on DNS data [Vervisch 04], that the conditional pdf $p(c|Z)$ is weakly dependent of Z, which leads to the independence assumption:

$$p(Z, Y_c) = p_Z(Z)\, p_c(Y_c) . \tag{4.34}$$

The mixture fraction distribution, like in CMC, is assumed to be beta-shaped: $p_Z = \beta_{\widetilde{Z},\widetilde{Z''^2}}$; balance equations for the first two moments $\widetilde{Z}$ and $\widetilde{Z''^2}$ are solved. The same is applied to the progress variable distribution $p_c = \beta_{\widetilde{c},\widetilde{c''^2}}$; estimates for c's mean and variance are required. Taking advantage of the independence hypothesis, $\widetilde{c}$ may be obtained from the resolution of $\widetilde{Y}_c$:

$$\widetilde{c} = \frac{\widetilde{Y}_c}{\widetilde{Y}_{c,\mathrm{eq}}} \tag{4.35}$$

where the mean equilibrium progress of reaction is computed from the chemical table and the Z distribution:

$$\widetilde{Y}_{c,\mathrm{eq}} = \int_0^1 Y_{c,\mathrm{eq}}(Z) \beta_{\widetilde{Z},\widetilde{Z''^2}}(Z)\, \mathrm{d}Z . \tag{4.36}$$

As a result, the filtered quantities of interest are functions of four parameters

$$\widetilde{\underline{Q}}(\widetilde{Z}, \widetilde{c}, \widetilde{Z''^2}, \widetilde{c''^2}) = \int_0^1 \int_0^1 \underline{Q}(Z, c)\, \beta_{\widetilde{Z},S_Z}(Z)\, \beta_{\widetilde{c},S_c}(c)\, \mathrm{d}Z\mathrm{d}c \tag{4.37}$$

and can be stored into a four-dimensional table with input variables $\widetilde{Z}$, $\widetilde{c}$, S_Z and S_c all in the $[0; 1]$ interval.

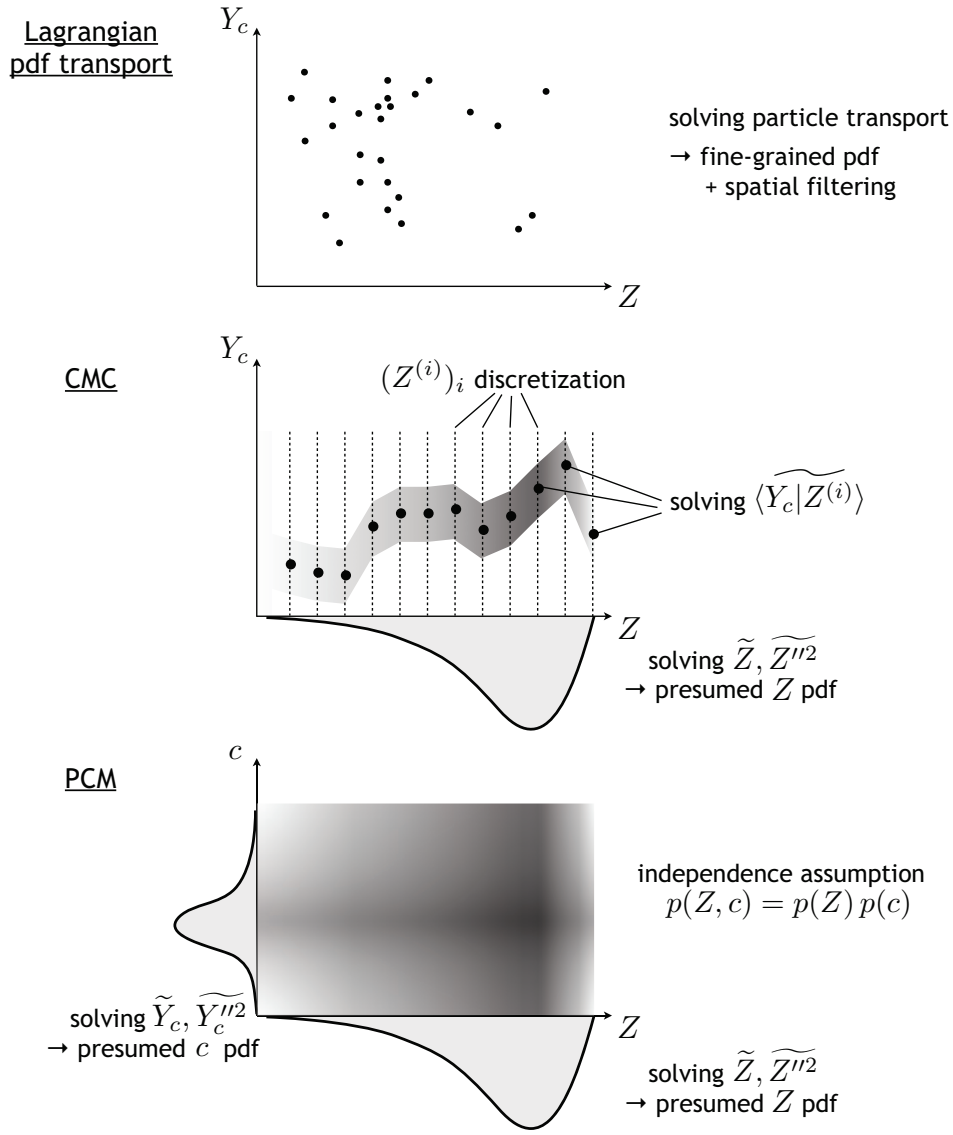

Figure 4.4: Schematic representation of three turbulent combustion models: Lagrangian pdf transport, CMC and PCM, representing the composition space in the two-dimensional case $\underline{\psi} = (Z, Y_c)$. For CMC, the common case where the mixture fraction is used as reference parameter, $\underline{\eta} = Z$, is taken.

Compared with transported pdf, the PCM approach makes a less expensive turbulent combustion model. Tabulation is easily coupled with an Eulerian solver, numerics are more straightforward than those of a Lagrangian particle solver. However, the pdf presumption, and especially the independence assumption, make it difficult to extend PCM to problems that cannot be parameterized by two or less variables. In the case of variable-enthalpy or multiple-inlet configurations, where enthalpy or more than one mixture fraction must be used, no obvious way of presuming the joint pdf is available. By contrast, the transported pdf approach can be applied to these cases with no formal difficulty. In that view, Flow-Controlled Chemistry Tabulation [Enjalbert 11], the turbulent combustion model developed in Part III of this work, is an attempt at reconciling advantages of both methods: using a chemical table based on pdf's that, instead of being presumed, are computed by means of stochastic particle modeling.

MMC

As Cleary *et al.* put it [Cleary 09b], "Multiple Mapping Conditioning (MMC) is a methodology which effectively unifies the joint pdf and CMC approaches". Introduced in the early 2000's [Klimenko 03], it has evolved from a mathematical formulation requiring complex stochastic modeling to a technique well suited for LES, and reasonable as far as computational cost is concerned [Kronenburg 08, Cleary 09a].

The idea is still to solve the transported pdf equation, Eq. (4.20), but to improve the mixing model by conditioning it to a set of reference variables $\underline{\eta}$ (like in CMC, commonly the mixture fraction). The filtered reference variables $\widetilde{\underline{\eta}}$ are solved on the Eulerian LES grid, and the filtered mass-weighted distribution $\widetilde{p}(\underline{\psi}; \underline{x}, t)$ stochastically, by means of Lagrangian particles. Source terms are still fully closed and depend only on the stochastic particles' properties. The reference variables $\widetilde{\underline{\eta}}$ only impact the mixing term [Klimenko 09], which is localized in the composition space thanks to the conditioning. But unlike localized mixing models used in the pdf transport method, such as EMST, which are dependent on the particle distribution and thereby violate scalar independence, here, localization is based on the field, independent, of the reference variables.

Thus, the conditioning makes the mixing modeling much more physical and much more accurate, so that a reduced number of Lagrangian particles is sufficient to yield accurate results. The result in term of computation is a so-called "sparse Lagrangian" resolution of the pdf [Cleary 09a, Cleary 09b, Klimenko 09].

4.3 Chemical table construction for the SAFIR simulation

The objective of this section is to provide practical details on the implementation of PCM–FPI in the present work. This model is used for the simulation of the SAFIR turbulent spray flame. It also plays a role of reference for assessing capabilities of the turbulent chemistry model presented in Part III.

Chemistry parameterization and tabulation are first described. The construction

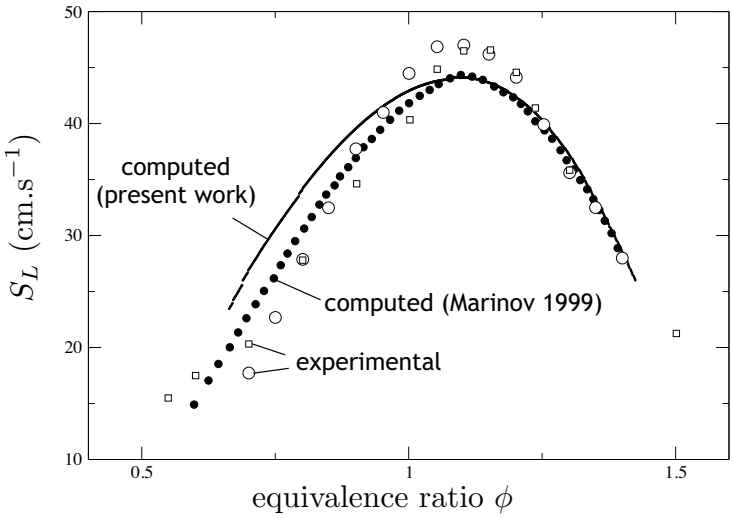

Figure 4.5: Ethanol–air mixtures at 300 K and 1.0 bar: laminar flame speed measured experimentally and predicted by Marinov's mechanism, and results with the present work flamelet software. Data reproduced from [Marinov 99].

of the turbulent combustion lookup table and the formalism elected here for SAFIR are then discussed in a second paragraph. It follows closely the approach followed in the LES of Cabra *et al.*'s turbulent lifted jet flame in a vitiated co-flow [Cabra 05] by the team among which the present work was carried out [Domingo 08, Godel 09]. Finally, a discussion on the validity of PCM–FPI for the present two-phase flow configuration is given.

4.3.1 Chemistry tabulation

Kinetic scheme

A 56-species, 351-reaction kinetic scheme for ethanol oxidation is used, published by Marinov in 1999 [Marinov 99]. The authors validated it against several experimental data: laminar flame speed (ethanol–air mixtures at 300 K under 1.0 and 2.0 bar and at 453 K under 1.0 bar), ignition delay (ethanol–oxygen–argon mixtures at lean to rich equivalence ratios and under pressure between 1.0 and 3.3 bar) and combustion products in jet-stirred reactors (ethanol–air mixtures at temperatures > 1000 K under 1 atm).

Freely propagating laminar flame speed results and model predictions according to Marinov's paper are reproduced in Fig. 4.5. Close to stoichiometry, measured velocities reach 47 cm.s^{-1}, which predictions tend to underestimate by no more than 5 %. Conversely, the model predicts larger values than the experiment in the lean domain.

A number of other models have been developed and published since then, and said to bring improvements compared with Marinov's. Yet this one was chosen for availability reasons. One of them, by Li *et al.*, offers comparisons against a larger set of experimental data, but performs equivalently on the 1-atm 300-K laminar flame speed [Li 07]; an other mechanism, even more recent, looked promising but

	Oxidizer		Fuel		
Z	0		1		
T	293 K		293 K		
$\overline{W}$	39.2 g.mol^{-1}		46.07 g.mol^{-1}		
Composition		$X_{m,\mathrm{Ox}}$	$Y_{m,\mathrm{Ox}}$		$X_{m,\mathrm{F}}$	$Y_{m,\mathrm{F}}$
	O_2	0.4	0.3265	C_2H_5OH	1.0	1.0
	CO_2	0.6	0.6735			

Table 4.1: Summary of SAFIR chemistry's limit conditions.

was released after the present work was initiated [Leplat 11].

Thermochemical properties

As prescribed by the FPI formalism, chemical evolution in the composition space is restricted to the two-dimensional manifold parameterized by mixture fraction Z and progress of reaction Y_c. Z is to vary between 0 and 1, and Y_c between two values that depend on Z: the cold mixture value $Y_{c,0}$ and the equilibrium value $Y_{c,\mathrm{eq}}(Z)$. Following Eq. (4.9), the normalized "progress variable" c is then formed, so that (Z, c) varies on the pair of intervals $[0; 1] \times [0; 1]$.

In the SAFIR experiment targeted by the present study, the fuel limit condition $Z = 1$ is pure gaseous ethanol (atomic formula C_2H_5OH); its boiling temperature under 1 atm is $T_{\mathrm{boil}} = 351.5\,\mathrm{K}$, and latent heat of vaporization $L_V = 837\,\mathrm{kJ.kg^{-1}}$. The oxidizer side of the domain, $Z = 0$, corresponds to the diluted oxygen coflow composition: in volume, 40 % O_2 and 60 % CO_2. Both fluids are at 293 K. Stoichiometry is in $Z_{\mathrm{st}} = 0.135$, as may be estimated by considering the global balance equation

$$C_2H_5OH + 3\,(O_2 + 1.5\,CO_2) \longrightarrow (2 + 3 \times 1.5)\,CO_2 + 3\,H_2O \tag{4.38}$$

yielding stoichiometric mole and mass ratios respectively equal to $s_m = 3\times(1+1.5) = 7.5$ and $s = s_m\,W_{\mathrm{Ox}}/W_{\mathrm{F}} \simeq 6.39$. The estimated stoichiometric mass fraction is obtained from $Z_{\mathrm{st}} = 1/(1 + s) \simeq 0.135$. Table 4.1 summarizes the limit conditions properties.

Equilibrium temperature and major species at equilibrium are plotted as a function of Z in Fig. 4.6. Maximum temperature is obtained in $Z = 0.15$, at 2,429 K. Ethanol is predicted by the chemical model to fully dissociate into methane and carbon oxides at equilibrium.

Flamelet computations

The PREMIX software is used to compute a set of laminar premixed flamelets [Kee 85], consisting of the spatial profiles of temperatures $T(x)$, mass fractions $Y_m(x)$ and their source terms $\dot{\omega}_m(x)$ for a number of mixture fractions. Starting from a computation in stoichiometric conditions, where flammability is granted, the mixture fraction is gradually decreased, and a stationary solution, close to its predecessor, is each time

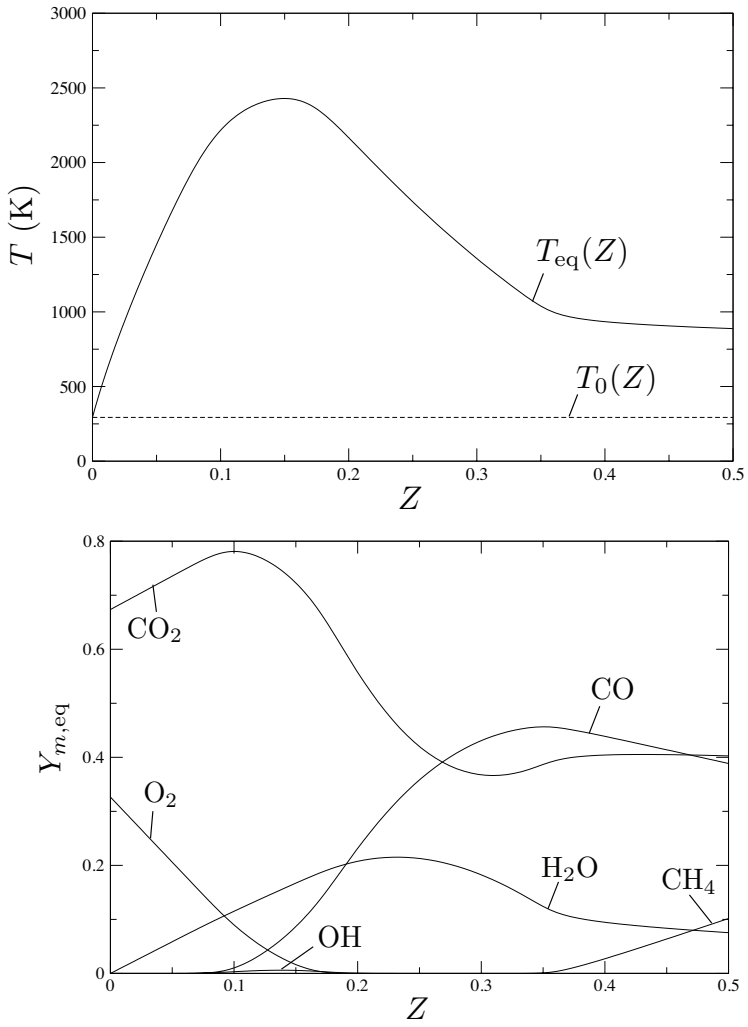

Figure 4.6: Equilibrium temperature and mass composition of ethanol–oxygen–carbon dioxide mixtures in the SAFIR experimental conditions.

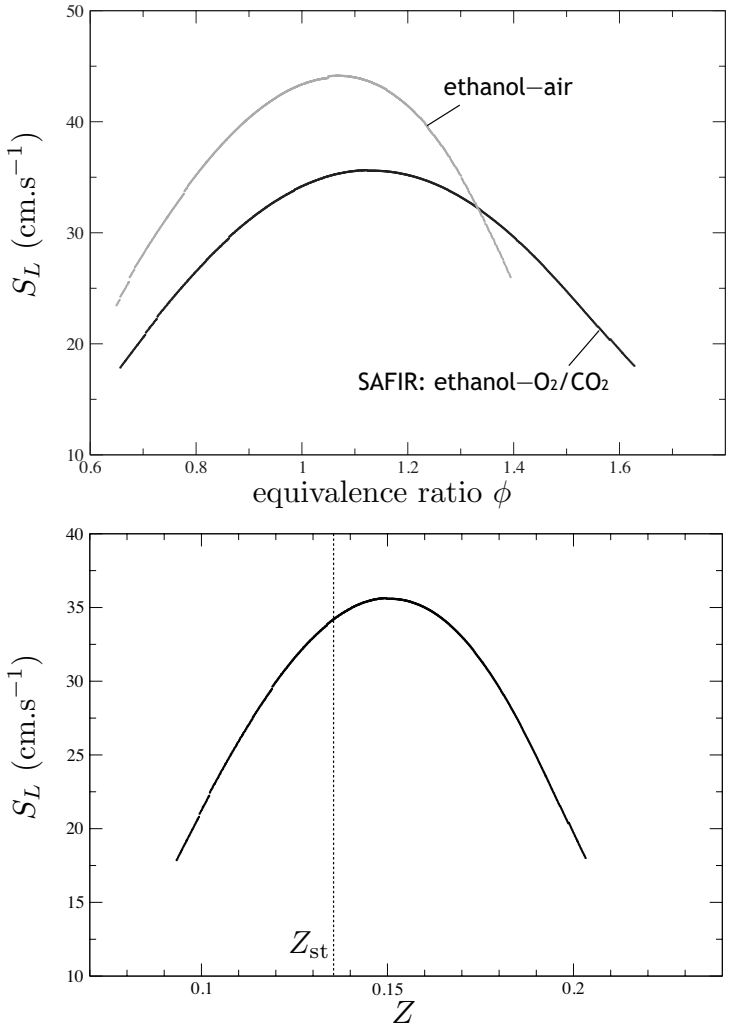

Figure 4.7: Laminar burning flame velocity for the SAFIR ethanol–O_2/60 % CO_2 conditions, plotted *vs.* equivalence ratio (and compared with ethanol–air flame results of Fig. 4.5) and mixture fraction.

computed. This is done until convergence cannot be achieved anymore. The same procedure is then carried out on the fuel-rich side. This method can be expected to give the approximative extent of the flammability domain, insofar as the numerical software can be trusted to succeed in capturing physical flame behaviors. As a matter of fact, this is not completely certain: in Fig. 4.5, the laminar burning velocity obtained from PREMIX is compared with that reported by Marinov's own computations, for well-documented ethanol–air mixtures; a discrepancy between the outputs is observed on the lean side; in addition, our software does not succeed in reaching as low a minimal Z value as Marinov's.

As far as the SAFIR conditions are concerned, the maximum flame speed predicted is 35 cm.s^{-1}, at an equivalence ratio larger than one and even larger than that in the ethanol–air case. Plots *vs.* both ϕ and Z are shown in Fig. 4.7.

Y_c expression		(1)	(2)	(3)	(4)
reverse behavior (×0.01 %)		1.16	0.20	0.17	0.005
max σ_m:	C_2H_5OH	2.17 (2.17)	1.69 (1.69)	1.44 (1.44)	1.44 (1.44)
	CO_2	1054 (8.3)	1549 (11.3)	231 (15.9)	16.3 (16.3)
	CO	616 (5.6)	8.4 (8.4)	11.2 (11.2)	11.2 (11.2)
	O_2	1628 (6.2)	2266 (2.2)	376 (2.9)	2.6 (2.6)
	H_2O	1154 (7.9)	816 (2.1)	121 (2.8)	2.6 (2.6)
	H_2	∞ (105)	∞ (76)	∞ (82)	∞ (89)
	OH	53 (42)	39 (36)	56 (45)	58 (47)

Table 4.2: Evaluation criteria for four progress variable expressions: reverse behavior quantifies bijectivity and the normalized gradients σ_m the mass fraction resolution in the Y_c space. Values between parentheses are computed on a less stringent basis, see explanations in the text body.

Choice of progress variable

From these flamelet data, a convenient expression for Y_c can be determined. Several candidates, all defined as linear combinations of chosen mass fractions, are examined:

(1) $Y_c = Y_{CO_2} + Y_{CO}$

(2) $Y_c = Y_{CO_2} + Y_{CO} + Y_{H_2O}$

(3) $Y_c = Y_{CO_2} + Y_{CO} + Y_{H_2O} - Y_{\text{ethanol}}$

(4) $Y_c = Y_{CO_2} + Y_{CO} + Y_{H_2O} - Y_{\text{ethanol}} + Y_{H_2}$

They are evaluated along two criteria. First, Y_c's bijectivity against the spatial component: $Y_c(x)$ must be as monotonic as possible. Second, the species mass fractions profiles in the Y_c space: they must be as smooth as possible, in practice for each flamelet the normalized gradient

$$\sigma_m(x) = \left|\frac{\mathrm{d}Y_m}{\mathrm{d}Y_c}(x)\right| \Big/ \left(\frac{\max_x Y_m(x) - \min_x Y_m(x)}{\max_x Y_c(x) - \min_x Y_c(x)}\right) \tag{4.39}$$

must be as small as possible across the flamelet front.

Table 4.2 summarizes results obtained for the four alternatives. It gathers the following criteria:

- the amount of "reverse behavior" through the flamelet, that is when Y_c's spatial gradient sign is opposite to that of $Y_c(x_{\max}) - Y_c(x_{\min})$. In Table 4.2, the value given is averaged over all computed flamelets, and indicated as a proportion of the spatial flamelet extent.

- for species of interest (main reactants, products, and significant minor species, like OH), the maximum of σ_m over all computed flamelets is given. Due to the discretization of the Y_c space, this value can reach extremely high values, often at Y_c domain's ends. Therefore an alternative maximum, computed only on points with contiguous Y_c variation larger than one thousandth of the global variation, is also displayed as a less stringent evaluation criterion.

As far as bijectivity is concerned, a significant improvement is obtained when adding H_2O, from expression (1) to expressions (2) and (3): while Y_c is on the whole

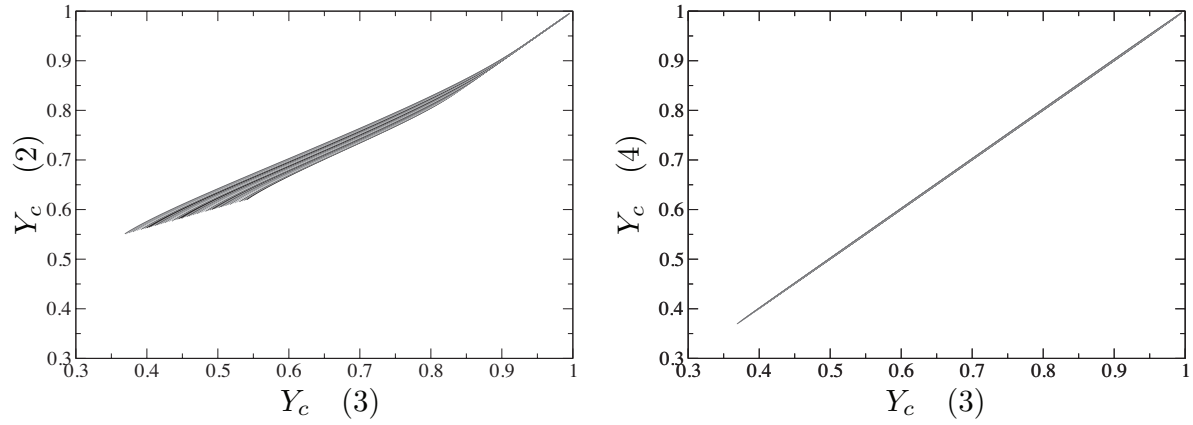

Figure 4.8: Progress variable profiles of expressions (2) and (4) *vs.* expression (3).

increasing through the flamelet, a small drop is observed ahead of the flame front in the first case, which disappears with (2) and (3). The improvement from (3) to (4), is less significant: H_2 is a low concentration species, and has its effect at the two ends of the flame, where Y_c and species evolve very flatly, respectively from their cold flow value and towards their equilibrium value. This is visible in Fig. 4.8 where the Y_c profiles, as given by expressions (2) and (4), are plotted *vs.* expression (3).

The steepness measurement shows that for major species, all expressions lead to overall acceptable gradients. The curves are generally similar for all expressions; distinctions can be made in the detail. Relevant species profiles are plotted *vs.* Y_c (3) in Fig. 4.9. Minor species are harder to capture, in particular H_2 that displays a very strong gradient in the composition space, on the fresh gases side, see Fig. 4.9. Gradients are generally smallest for expression (2) that involves H_2O but not ethanol, as may be seen on Table 4.2's σ_m values between parentheses; yet some points, invisible in the general trend, display much higher gradients for (2) than for (3), as indicated by the raw σ_m indicators.

For the present study expression (3) was chosen: $Y_c = Y_{CO_2} + Y_{CO} + Y_{H_2O} - Y_{\text{ethanol}}$. Flamelet profiles of a selected set of species are plotted in Fig. 4.9. Cold flow and equilibrium values as a function of the mixture fraction are plotted in Fig. 4.10. Note how $Y_{c,0}$ varies with Z and even becomes negative for $Z > 0.4$.

The systematic study presented above had not been carried out when the choice was made, but it proved a satisfactory decision. In further studies, expression (4) may be favored, in particular for very refined LES or DNS studies where the chemical flame structure is not smoothed by high subgrid-scale Y_c variance and when Y_c has therefore a stronger impact on the prediction.

Chemical database completion

The chemical database must then be completed outside of the laminar flamelet range. Following a tried-and-tested approach [Vervisch 04, Domingo 08, Godel 09], chemistry is stored as inert mixing between the cold-flow condition and the equilibrium. Source terms are set to zero.

A full chemical table, constructed on 159 Z points between 0 and 1 (59 flamelets +

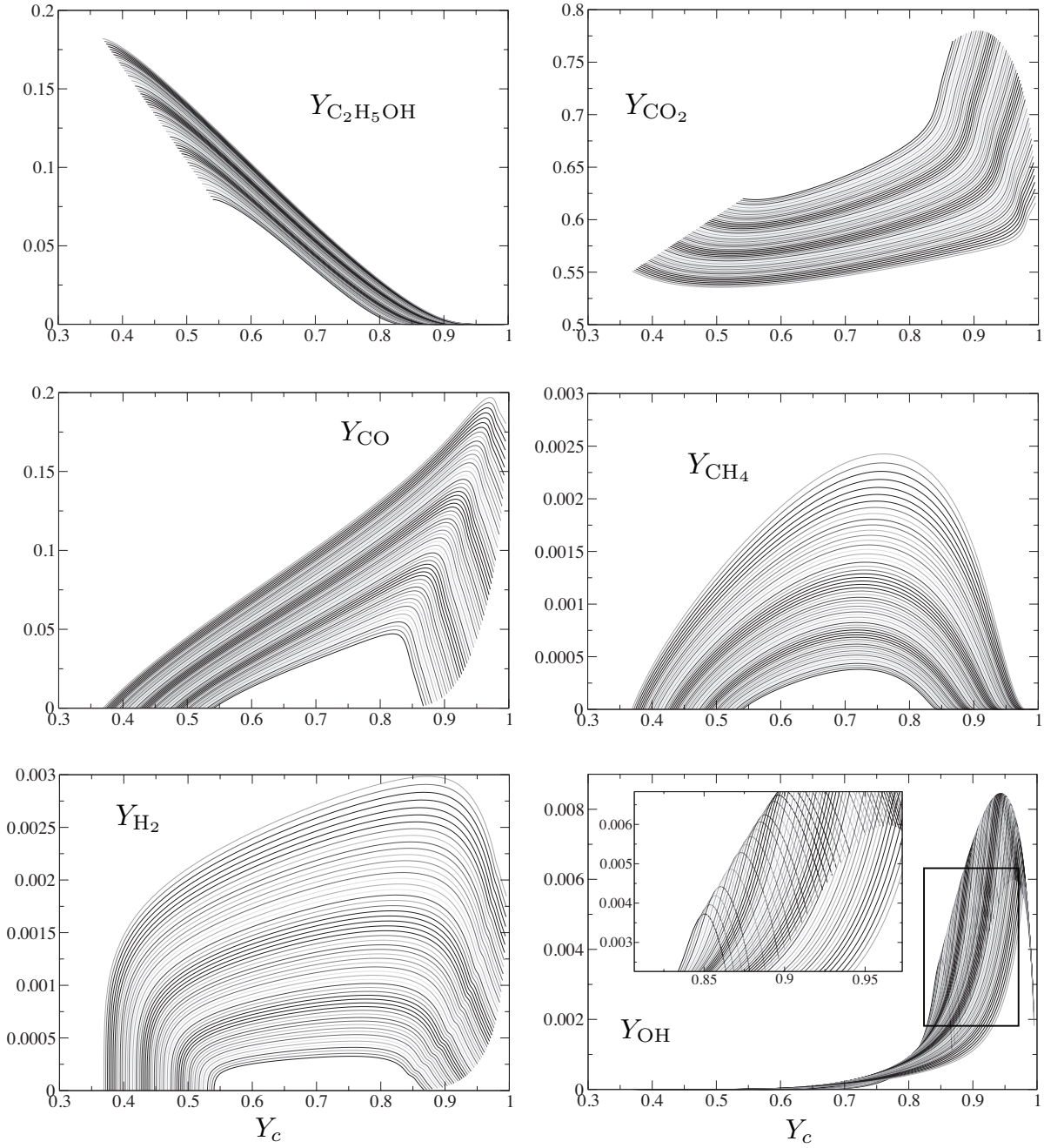

Figure 4.9: Selected set of species plotted *vs.* the progress variable Y_c, for all the computed laminar premixed flamelets.

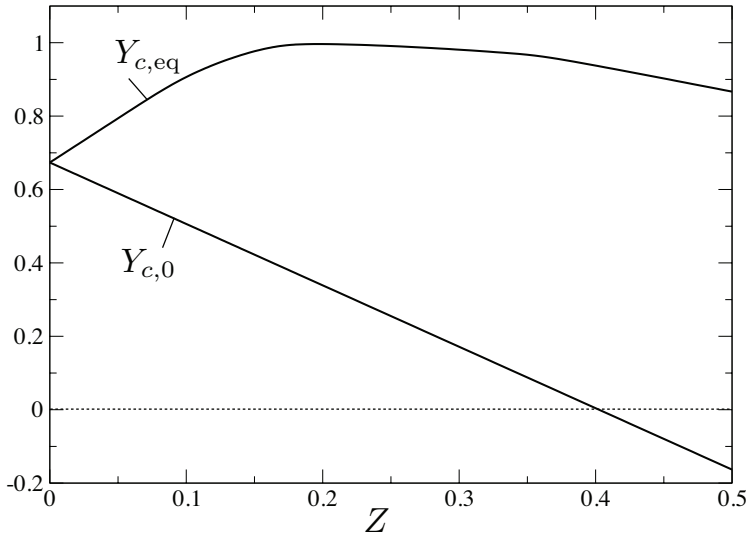

Figure 4.10: Limit condition values for the progress variable as a function of the mixture fraction Z: cold flow $Y_{c,0}(Z)$ and equilibrium $Y_{c,\mathrm{eq}}(Z)$.

100 mixing profiles) and 360 Y_c points, is finally available, that contains the following fields:

$$Y_m(Z,c), m = 1,\ldots,N_s, \quad T(Z,c), \quad \dot{\omega}_{Y_c}(Z,c), \quad \dot{\omega}_T(Z,c)\,. \tag{4.40}$$

4.3.2 PCM–FPI lookup table

The SAFIR large-eddy simulations of this work, carried out with the YALES2 solver, employ the PCM–FPI model as presented in Section 4.2.4. The chemical table $Q(Z,c)$ discussed in the previous section is filtered according to Eq. (4.37) and forms a lookup table $\widetilde{Q}(\widetilde{Z},\widetilde{c},S_Z,S_c)$, accessed from the simulation. In practice this table is an array of values corresponding to a discrete set of points in each direction. Values in any point are retrieved by multilinear interpolation. A mathematical description of the process is given is Appendix C. The $\widetilde{Z}$ and $\widetilde{c}$ directions are discretized into 50 points each, while 10 points are used on the segregation directions. The resulting table occupies about 23 megabytes.

As was introduced in Section 4.2.4 on the presumed pdf approach, PCM–FPI requires the modeling of segregations from the resolved fields. Here the choice was made to express the variances $\widetilde{Z''^2}$ and $\widetilde{c''^2}$ directly from the native variables' gradients, rather than solving balance equations.

Two models are tested:

- A 'gradient' model, which relates linearly variance and the resolved gradient norm:

$$\widetilde{\eta''^2} = K_{\mathrm{grad}}\Delta|\underline{\nabla}\widetilde{\eta}|\,. \tag{4.41}$$

  This expression may be derived from assuming a bi-modal pdf for η [Vervisch 10]. A suggested value for K_{grad} is 0.18.

- A 'mixing' model, introduced in [Veynante 06], suggesting a quadratic dependency:

$$\widetilde{\eta''^2} = K_{\text{mix}} \Delta^2 |\underline{\nabla} \widetilde{\eta}|^2 \,, \tag{4.42}$$

  with the optimal K_{mix} value determined to be 0.08 [Moureau 11b].

The validity of both expressions has been discussed recently by Moureau *et al.* using high-resolution YALES2 computations of a turbulent premixed combustion problem, where the progress variable was resolved across the flame front [Moureau 11b]. It was shown, for the normalized progress variable c, that the behavior tends towards linearity, hence the gradient model becomes more relevant, as the filter width increases.

The segregation is obtained from the variance by normalization, following Eq. (4.29).

4.3.3 PCM–FPI in YALES2 two-phase flow simulation

Here we examine the extent of PCM's relevance in a two-phase context, and suggest possible adaptations of the formulation to the present case.

Enthalpy

The chemical tabulation here is based on gaseous ethanol at 293 K. However this is an approximation, because it is in its liquid form that ethanol has this temperature. Enthalpy must be supplied by the gaseous phase to enable vaporization, and as the mixture fraction Z (ethanol mass fraction) increases, the enthalpy linearly decreases with it with a slope L_V.

This variation may be considered negligible, as the latent heat of vaporization is $L_V \simeq 38.5\,\text{kJ.mol}^{-1}$, while ethanol's heat release (lower heating value) reaches $1.3\,\text{MJ.mol}^{-1}$; the error thus made amounts to a little less than 3 %. In stoichiometric proportions, the error is, in a first approximation, the order of $Z_{\text{st}} \times 3\,\%$; considering a temperature increase of 2,000 K, this error corresponds to about 7 K. In configurations where the flame is less robust, vaporization may locally contribute to flame extinction. In zones where local equivalence ratio reaches higher values, this prediction is not negligible. However, the error is for the moment deemed small enough to be neglected. Therefore, enthalpy has been assumed blind to vaporization in the reactive-flow computation results shown in the next section.

However, it is possible to build a chemical lookup table with an additional sensible enthalpy parameter, h_s. It would require, if chemical reaction is activated, a five-dimensional tabulation. Here, an illustration of the approach is given for a non-reacting case, where only evaporation is accounted for.

A two-dimensional lookup table, containing density and temperature as functions of mixture fraction and enthalpy,

$$\rho(Z, h_s), \quad T(Z, h_s) \tag{4.43}$$

is built from inert mixture computations between the two limit compositions $Z = 0$ and $Z = 1$ given in Table 4.1.

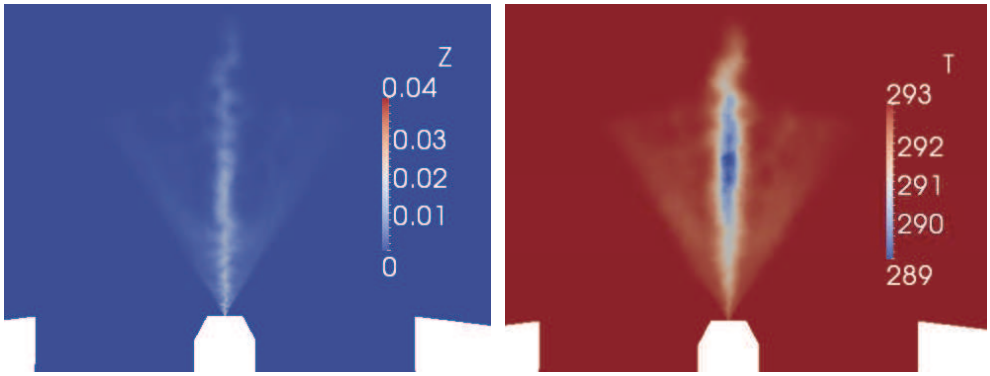

Figure 4.11: Instantaneous mixture fraction and temperature fields obtained for a non-reacting SAFIR spray simulation, injection type (B), where enthalpy drop due to vaporization are taken into account.

In the flow solver, $\widetilde{Z}$ and $\widetilde{h}_s$ are solved from their balance equations. In particular the evaporation source terms $\overline{S}_M$ and $\overline{S}_E$ are computed from particle-to-grid interpolations discussed in Section 2.2.2. Given the close to linear behavior of mixing, subgrid-scale fluctuations may be neglected, so that filtered density and temperature fields are computed from the aforementioned chemical table

$$\overline{\rho} \simeq \rho(\widetilde{Z}, \widetilde{h}_s) \,, \quad \widetilde{T} \simeq T(\widetilde{Z}, \widetilde{h}_s) \,. \tag{4.44}$$

Obtained a short instant after starting the injection (3.3 ms), the filtered mixture fraction (solved) and filtered temperature (looked up in the table) fields are shown. While, without chemical heat release, evaporation remains limited, with a maximum $\widetilde{Z}$ value about .04, the temperature drop is consistent with the mixture fraction field. It reaches about 4 K in the presented case.

Saturation mixture fraction

The mixture fraction field in a spray flame as the one addressed here is expected to differ from that in a purely gaseous flow, where it is purely driven by gaseous mixing. In the present context where all fuel is initially in condensed form, the gaseous fuel reactant (non-zero Z) is entirely the result of evaporation. Therefore, properties of the mixture fraction field should be coupled as closely as possible with the spray. This has an impact on the modeled sgs variance of Z, as was tackled by Pera *et al.* who proposed a balance equation for Z_v in an LES of an evaporating spray [Pera 06]. Here, variances are only estimated from the resolved field.

At another level, the specificity of the evaporation-related Z field potentially undermines the PCM–FPI formulation validity. At droplet temperatures lower than the boiling point, the fuel partial pressure in the droplet vicinity may never surpass the saturation value observed at the surface, defined in Eq. (1.40) and recalled here:

$$p_F(T) = p_{\text{ref}} \exp\left(\frac{W_F L_V}{\mathcal{R}}\left(\frac{1}{T_{\text{boil}}} - \frac{1}{T}\right)\right) \,. \tag{4.45}$$

This puts a limit on the maximum fuel mass fraction that can be found in the gas phase, and that depends on the surrounding species composition. Expressed in terms

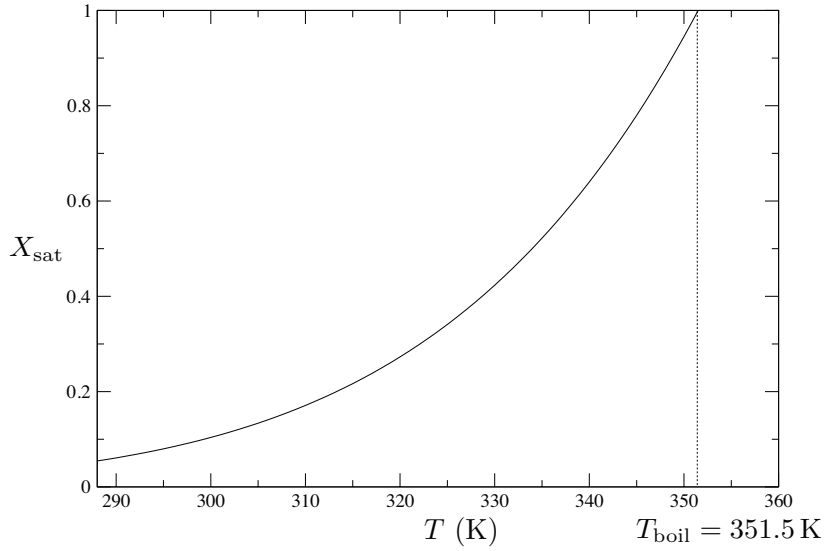

Figure 4.12: Saturation ethanol mole fraction $X_{\rm sat}$ *vs.* temperature.

of parameter Z, it is referred to as the saturation mixture fraction and denoted by $Z_{\rm sat}$. As an illustration, the maximum mole fraction $X_F = p_F/p$ is plotted in Fig. 4.12 as a function of temperature.

The way it is defined in Eq. (4.37), the expression for the filtered fields $\widetilde{\underline{Q}}$ is therefore not physical, for the integration is carried out on the entire $[0;1]$ interval and the integrand may thus include points from beyond the maximum $Z_{\rm sat} < 1$.

This approach may however be deemed an acceptable approximation for two reasons: first, because a low Z variance is expected, making the proportion of the distribution above $Z_{\rm sat}$ not likely significant; second, because the boiling temperature is quite low compared with that of the burnt gases, expected to reach more than 2,000 K (see Fig. 4.6). Thus the region in which Eq. (4.37) may not be valid is confined to the cold edge of the burning zone, and only to where the mixture fraction gradients have started to rise from zero because of the evaporation. Yet on the other hand, this zone is where the chemical reaction is triggered, and the flame structure may be sensitive to the way combustion occurs there. In the present work, this question was not further explored.

Only an improvement suggestion for future work can be given here. It was introduced in [Reveillon 00] and used in some subsequent works, like [Apte 09b]. The idea is to integrate not on $[0;1]$ but on $[0;\widetilde{Z}_{\rm sat}]$, where the upper value is interpolated locally from the surrounding droplets' individual $Z_{\rm sat}^{(k)}$:

$$\widetilde{Z}_{\rm sat} = \langle Z_{\rm sat} \rangle \,. \tag{4.46}$$

In a tabulated formalism, $\widetilde{Z}_{\rm sat}$ becomes an additional parameter, adding a dimension to the lookup table. The filtered quantities read (compare with Eq. (4.37)):

$$\widetilde{Q}(\widetilde{Z},\widetilde{c},S_Z,S_c,\widetilde{Z}_{\rm sat}) = \int_{Z=0}^{\widetilde{Z}_{\rm sat}} \int_{c=0}^{1} \underline{Q}(Z,c)\,\beta'_{\widetilde{Z},S_Z,\widetilde{Z}_{\rm sat}}(Z)\,\beta_{\widetilde{c},S_c}(c)\,{\rm d}Z{\rm d}c\,, \tag{4.47}$$

where β' the beta-function attached to the Z dimension is properly normalized from the $[0;1]$-defined β, Eq. (4.27).

4.4 Simulation results

4.4.1 (C) Direct injection at 6 mm

Initial attempt

It was seen in the previous chapter that injection approach (B) led to relevant spray statistics upstream of 20 mm, where the flame is observed to be stabilized; droplets are injected from both the spray nozzle position and the 30° cone, and with the addition of large droplets unaccounted for in the measurements (details in Section 3.3.4). It is thus natural to try to use it as the baseline configuration for reacting simulations.

Starting from a non-reacting case, a pocket of gases is artificially ignited by setting the progress variable $\widetilde{Y}_c$ to its equilibrium value $Y_{c,\mathrm{eq}}(\widetilde{Z})$. It is a cylindrical volume, centered on the axis, of diameter 2 mm, and extending over the x interval $[7.0;\ 9.0]$ mm[3]. A spark duration of 5 ms was found close to the minimum requirement for ignition to proceed and for a sustained flame to develop. This is an approach commonly used for reproducing forced ignition in tabulated chemistry simulations [Triantafyllidis 09, Subramanian 10b], and it matches the actual ignition procedure, where an igniter device must be introduced within the spray and fired for several seconds.

All runs in this section are performed with Z and c segregations estimated from the 'gradient' variance model, with purposely large constant values $K_{S_Z} = 0.36$ and $K_{S_c} = 0.36$, to prevent risks of unresolvedness.

A flame was able to develop from this procedure, and to stabilize itself downstream of the observed liquid sheet's tip in $x = 6$ mm. The instantaneous chemical source term field $\dot{\omega}_{Y_c}$ is shown in Fig. 4.13. Yet, its structure does not match to experimental observations. A source term pocket is visible, centered on the symmetry axis at a distance of 30 mm from the nozzle. In actuality, chemical reaction is expected to be located along the circle where the flame tip is observed. Instantaneous mixture fraction and its source term are also shown. Consistently, the intense evaporation occurring on the centerline is visible, as is the fuel-rich zone in its wake.

This result seems to proceed from the same effect as that observed in Chapter 3: small droplet dispersion is not correctly predicted, leading to their excessive concentration on the centerline. When combustion is activated, this central flame appears. The mean droplet diameter $\langle d_p \rangle$, shown in Fig. 4.14, is less than 25 µm on the centerline.

Approach (C1): direct injection from the $x = 6$ mm plane

To confirm this result, an additional test is carried out: droplets are injected directly from the $x = 6$ mm plane, with the measured spray statistics. This was the initial objective of spray measurements: to serve as limit conditions. And it enables us to rule out the prediction errors due to the modeled nozzle and spray-cone injection.

The disk $x = 6$ mm, $r \leq 6$ mm is divided into N_c annuli, matching the intersections of sub-cones $\mathcal{C}_i$ with the plane $x = 6$ mm. The procedure is similar to approach (A)

[3] Another geometry was tested, where the spark was toroidal around the $x = 8$ mm, $r = x \times \tan 30\,°$ circle; it led to the same eventual flame structure.

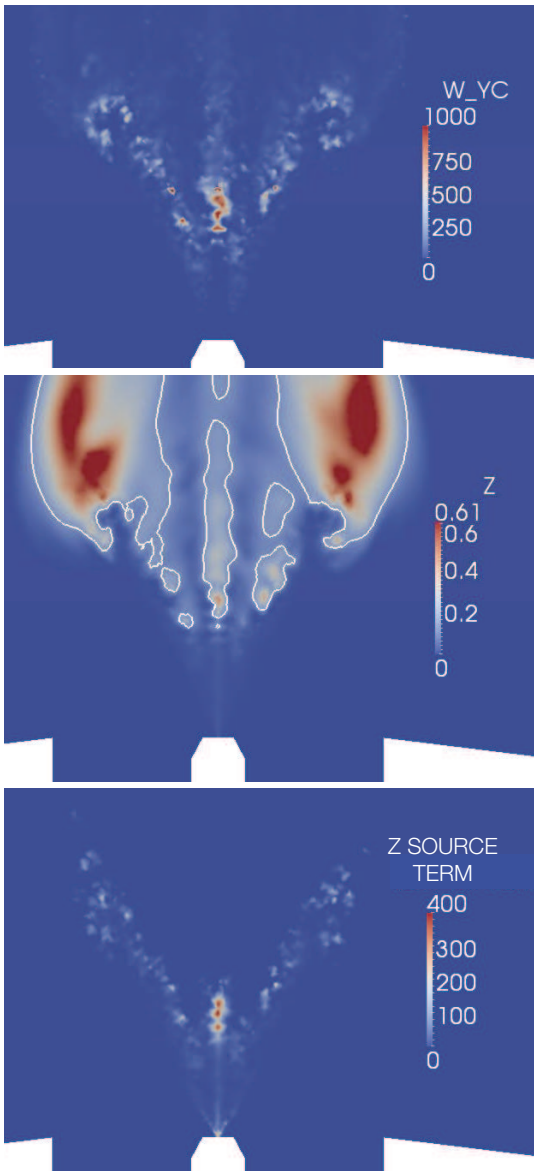

Figure 4.13: Instantaneous fields of chemical source term, mixture fraction and its source term, showing the flame structure when the spray injection follows approach (B). Mixture fraction isoline $\widetilde{Z} = Z_{\mathrm{st}}$.

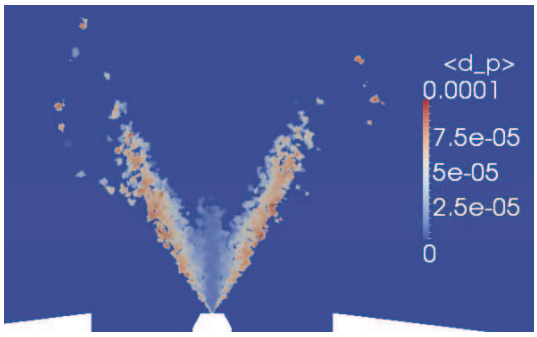

Figure 4.14: Mean instantaneous droplet diameter, showing the flame structure when the spray injection follows approach (B).

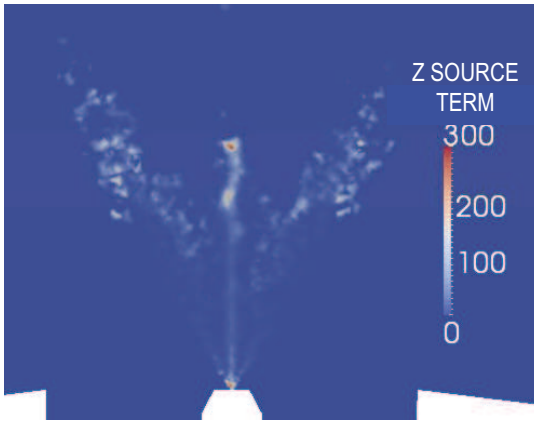

Figure 4.15: Instantaneous mixture fraction source term, showing the flame structure when spray injection is carried out from the 6-mm plane.

where all droplets were injected from the nozzle (Section 3.3.2), except injection now starts from these annuli. Injection is carried out homogeneously on each annulus[4]. Experimentally-observed diameter distributions and velocity mean and averages are imposed without pre-treatment on the droplets.

With this approach only, the zone upstream of 6 mm would be void of droplets. To maintain the same flow pattern there as before, a spray injection following approach (B) is still performed, but with droplets that are flagged into a dummy particle set, and numerically deleted as soon as they cross the 6-mm plane.

The result is not different from previously: small droplets gather along the centerline and are in sufficient concentration for a dominant reaction zone to develop there, unlike what is observed in the experiment. The mixture fraction source term, shown for the present case in Fig. 4.15, features the same structure as with approach (B).

Approach (C2): *ad hoc* injection from the $x = 6$ mm plane

The unsatisfactory flame structures obtained above demonstrate that spray modeling on which the simulations of this work are based is yet insufficient to predict dispersion. As discussed in Section 3.2.1, turbulence in the present problem possesses peculiar properties that are far from the model's expected validity range. Further work on the subgrid-scale gas–spray coupling will be beneficial to prediction accuracy.

However, it is still possible to study the main traits of the combustion model in the context of two-phase combustion. In particular, the constants in the segregation models, the droplet weighting properties and the mesh refinement are three aspects that can be explored, even if spray statistics consistent with the experiment and realistic flame structure have appeared difficult to be obtained simultaneously.

To that end, droplets smaller than 20 µm are removed from the injection distribution. This *ad hoc* injection, referred to as (C2), is designed to yield a realistic flame structure that matches, on the whole, to the experimental observations of a lifted flame stabilized along a circle, at a distance 20 mm from the nozzle.

[4] *i.e.* the injection point's radius and azimuth and the cone angle of the injection direction are determined according to uniform random laws.

The results are shown in Fig. 4.16. The fuel-rich zone close to the centerline has disappeared; the experimental flame anchoring is recovered, if still a little downstream of the expected 20 mm. In the next sections, the effect of model parameters on this structure are examined; even better predictions are obtained.

It may be possible to use a smaller cutting diameter, the role of this parameter has not been examined thoroughly. The purpose here was to obtain a relevant flame structure. It may be that 10 or 15 µm are large enough to prevent the appearance of a central flame. At any rate the prior study shows that dispersion prediction will require improvement, and we now turn our attention to the flame's structure and response to combustion model parameters.

4.4.2 Variance models

Using the injection approach (C2) discussed above, flame computations are run long enough for the simulated fields to stabilize. For both mixture fraction and progress variable unmixedness, the two variance models – 'gradient' and 'mixing' – presented in Section 4.3.2 are tested.

The flame structure, *i.e.* its position and shape, are significantly impacted by the variance model. In a few words, the mixing model predicts a flame shape that seems to match well to the experimental observations, but with the gradient model the flame has the correct lift-off height. Details are given in the analysis and figures below.

Chemical reaction and evaporation. The chemical source term, evaporation and OH species mass fraction are shown in Fig. 4.17, with markers for the x =10, 20 and 30 mm distances. With the gradient model, the flame anchors at a distance $x = 20$ mm, conform to the experiment; with the mixing model, it stabilizes farther downstream, about 30 mm from the nozzle. The angular opening of the flame tips is also larger with the mixing model than with the gradient model.

The latter predicts a more intense chemical reaction, with an outer flame front dominant over the inner flame, which is thicker but short. With the mixing model, the flame front is thin and much longer on the inside than on the outside. Evaporation intensity is comparable between the two models, but its structure follows that of the flame: it can be seen that evaporation starts along the reaction line, as droplets enter the high temperature area, and fades downstream as droplets disappear. The mixing model leads to much higher OH concentrations (.07) than those with the gradient model (.03). The maximum OH mass fractions are observed on the flame fronts least intensely reacting: the inner side with the gradient model, the outer side with the mixing model.

Resulting fields: $\widetilde{Z}$, $\widetilde{T}$, $\widetilde{Y}_{C_2H_5OH}$. Resolved mixture fraction, temperature and ethanol mass fraction fields are shown in Fig. 4.18. Consistently with the observations on the evaporation and reaction intensity, the mixture fraction reaches similar maximum values (about 0.6–0.7) for both variance models (slightly higher for the gradient model), but the ethanol mass fraction is lower with the gradient model, which predicts stronger chemical source terms. The main difference in terms of flame shape is visible on the ethanol mass fraction: while a single line of fuel is visible for

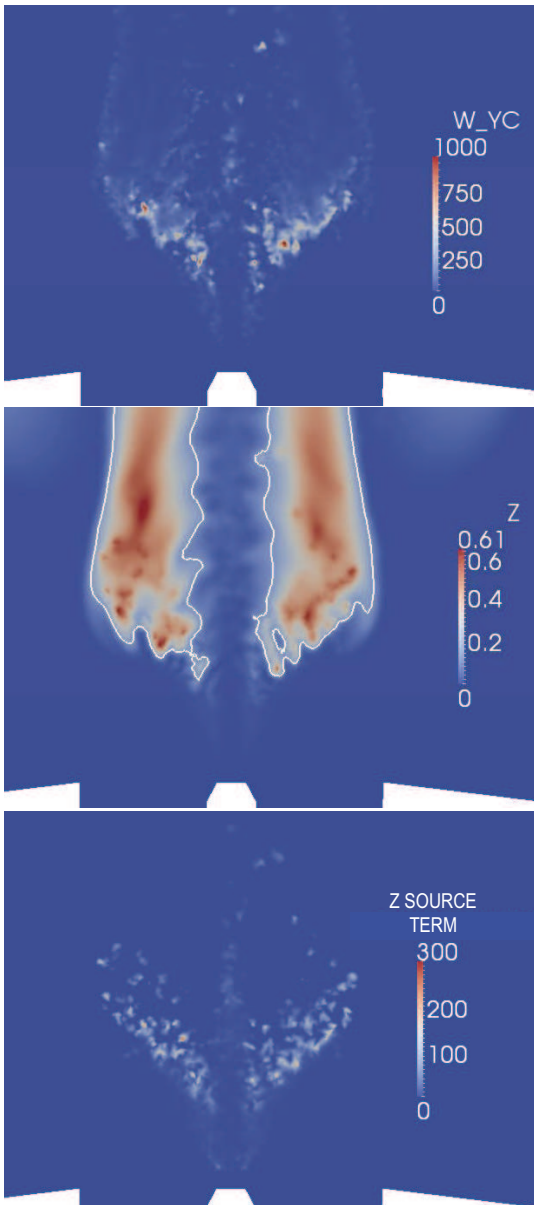

Figure 4.16: Injection approach (C2): removing smaller droplets from the injection distributions suppresses the central fuel-rich zone.

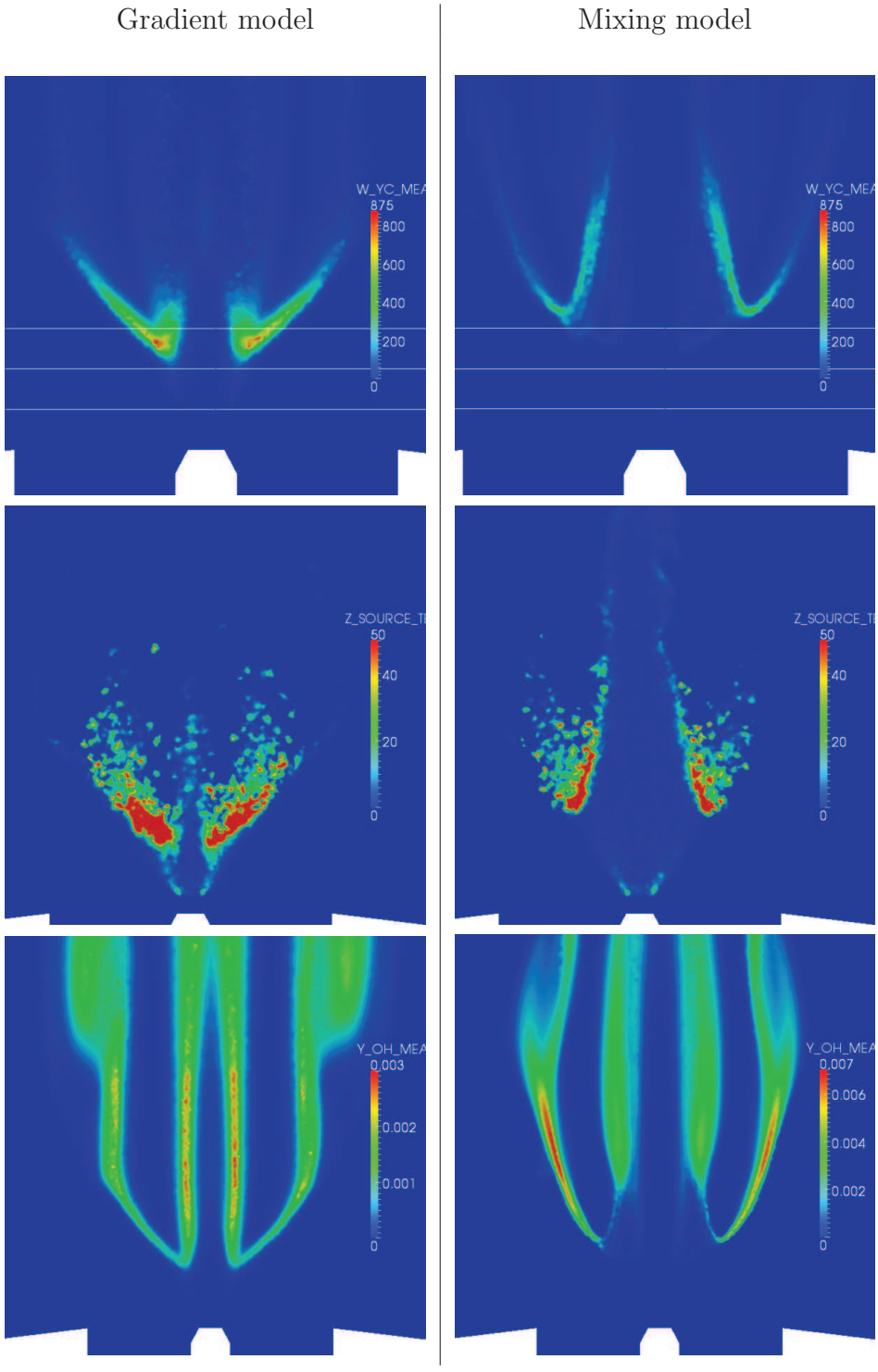

Figure 4.17: From top to bottom, time-averaged chemical source term $\widetilde{\dot{\omega}}_{Y_c}$, instantaneous mixture fraction source term $\overline{S}_M$, and time-averaged OH mass fraction $\widetilde{Y}_{\mathrm{OH}}$, indicator of the flame position. White lines in the top image indicate distances to nozzle $x = 10$, 20 and 30 mm.

the gradient model, the mixing model leads to two branches: a high-concentration thick one, on the outer side, corresponding to the slow-evaporation ($\widetilde{Z}$ source term) and low-reactivity outer branch; and a weaker one, on the inside, where $\widetilde{Y}_{C_2H_5OH}$ does not surpass .03, corresponding to the inner evaporation branch, that can be seen be distorted by the turbulent structures of the flow.

One may advance that with the mixing model, the outer flame front is a diffusion flame, and the inner front is in all likelihood a premixed front, while with the gradient model only two diffusion fronts are predicted. The latter structure seems to be due to the total evaporation of fuel simultaneously with reaction at the base of the flame. Premixed combustion with the mixing model comes from continued evaporation along the low-intensity inner reaction zone. Scalar unmixedness fields are helpful markers of these two behaviors: the mixture fraction segregation S_Z is virtually zero along the inner branch with the mixing model, while with the gradient model it is non-zero everywhere around the $Z > 0$ area. Also, the reaction progress segregation S_c features a distinct non-zero along the inner flame branch predicted by the mixing model.

To further this flame structure analysis, it should prove interesting, in future work, to compute the flame index as defined in [Yamashita 96] and to conduct a similar study as that by Domingo *et al.* [Domingo 05b].

Droplet statistics are now examined. The time-averaged local density $\langle\{w\}\rangle$, mean diameter $\langle d_p \rangle$ and mean temperature $\langle T_p \rangle$, as defined in Section 2.4.1, are shown in Fig. 4.20, superposed with the mixture fraction and ethanol mass fraction isolines. The drop in droplet density due to evaporation and corresponding to a mixture fraction increase, is illustrated by the fact that $\langle\{w\}\rangle$ is virtually zero within the zone bounded by the stoichiometric line. The flame structure impacts the spray properties. The gradient-model flame features relatively high temperatures along the centerline, and sees most droplets disappear beyond 50 mm from the nozzle. The remaining ones see their temperature increase slowly up to T_{boil}. The mixing-model flame allows a large number of droplets to carry on their way along the centerline, with only a slow diameter decrease, because temperature remains low on a wide central corridor. Behind the flame front, in the fuel-rich burnt-gas zone, where gaseous ethanol is in excess (as delimited by the white lines), gas temperature remains relatively mild, and the few droplets that have survived the flame front crossing see their diameter decrease more slowly than within the flame; their temperature is lower than the boiling point. Further study of these patterns will be needed, keeping in mind their dependency to all modeling steps, that are critical at many levels given the strong interrelations between spray properties, evaporation and reaction.

Instantaneous OH **fields.** Finally, a general comparison between the simulated flame structure and the experimental observations is conducted in Fig. 4.21. Instantaneous OH mass fraction is shown for both variance model cases, and compared with a LIF OH-concentration picture taken in a case slightly different from the target configuration: dilution is 40 % instead of 60 %, but the inset diameter, 95 mm, is the same. There is a strong resemblance with the OH field predicted with the mixing model: the inner flame branch is thick and responsive to turbulent vortices; the outer flame is thin and rather straight. By contrast, the inner flame remains a consistent

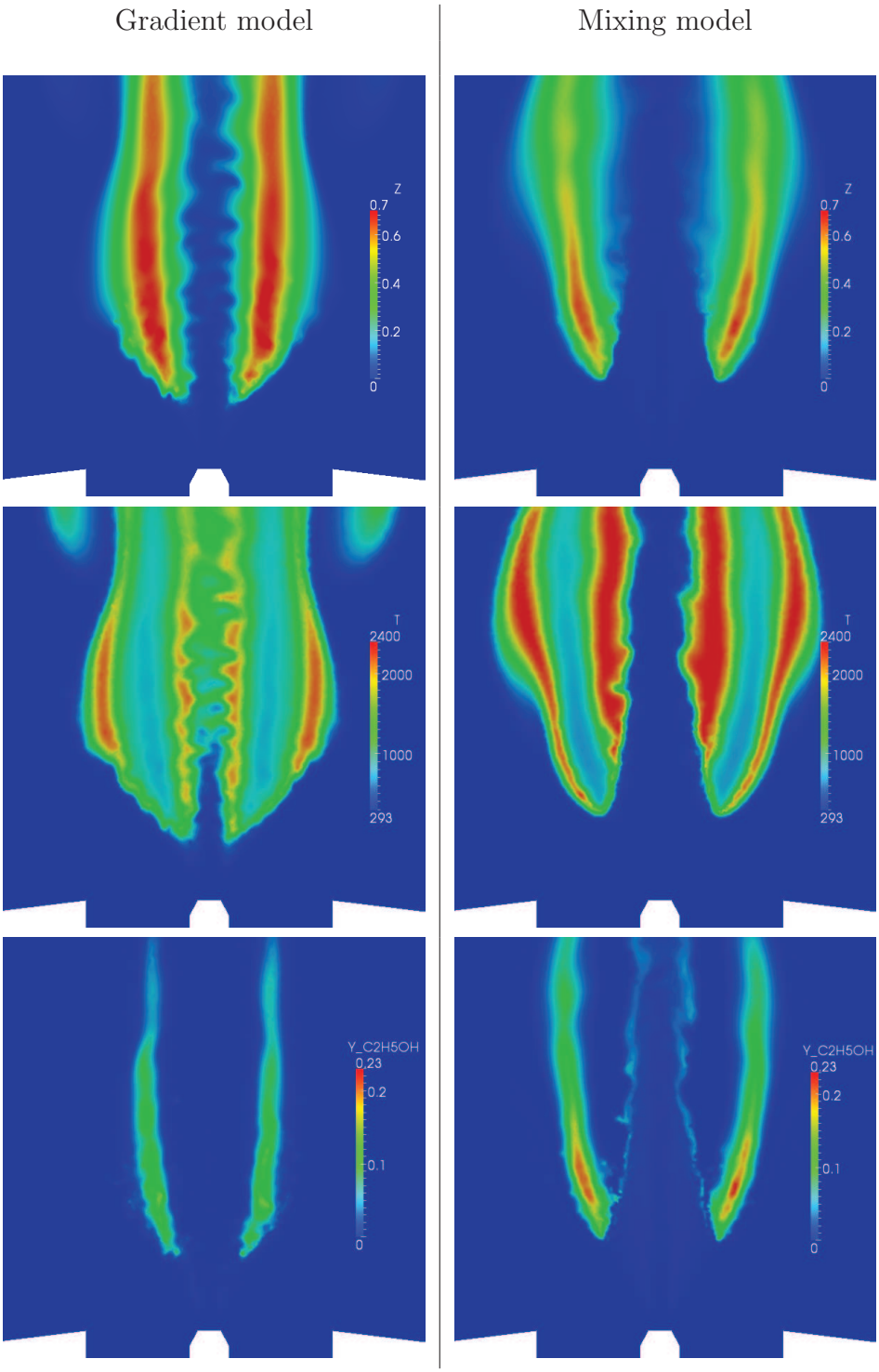

Figure 4.18: From top to bottom, instantaneous fields of mixture fraction $\widetilde{Z}$, temperature $\widetilde{T}$ and ethanol mass fraction $\widetilde{Y}_{C_2H_5OH}$.

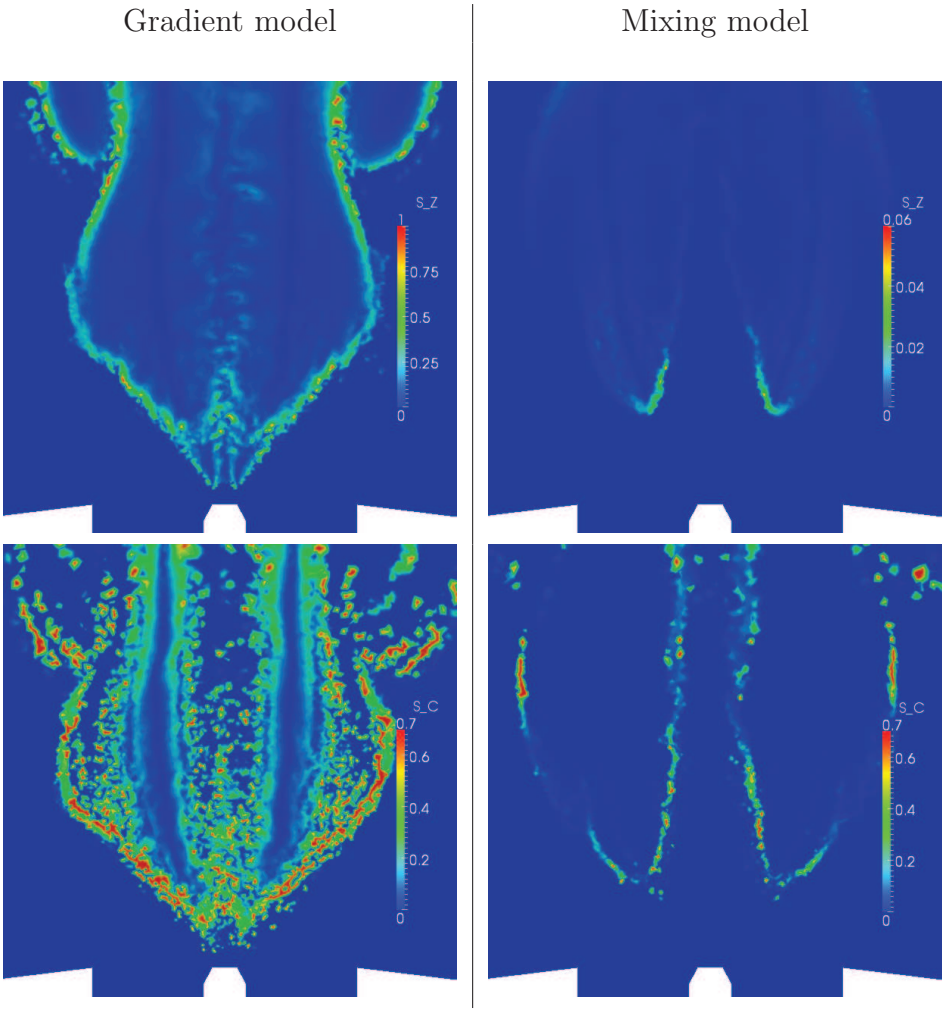

Figure 4.19: *Top:* mixture fraction segregation S_Z; *bottom:* normalized reaction progress segregation S_c.

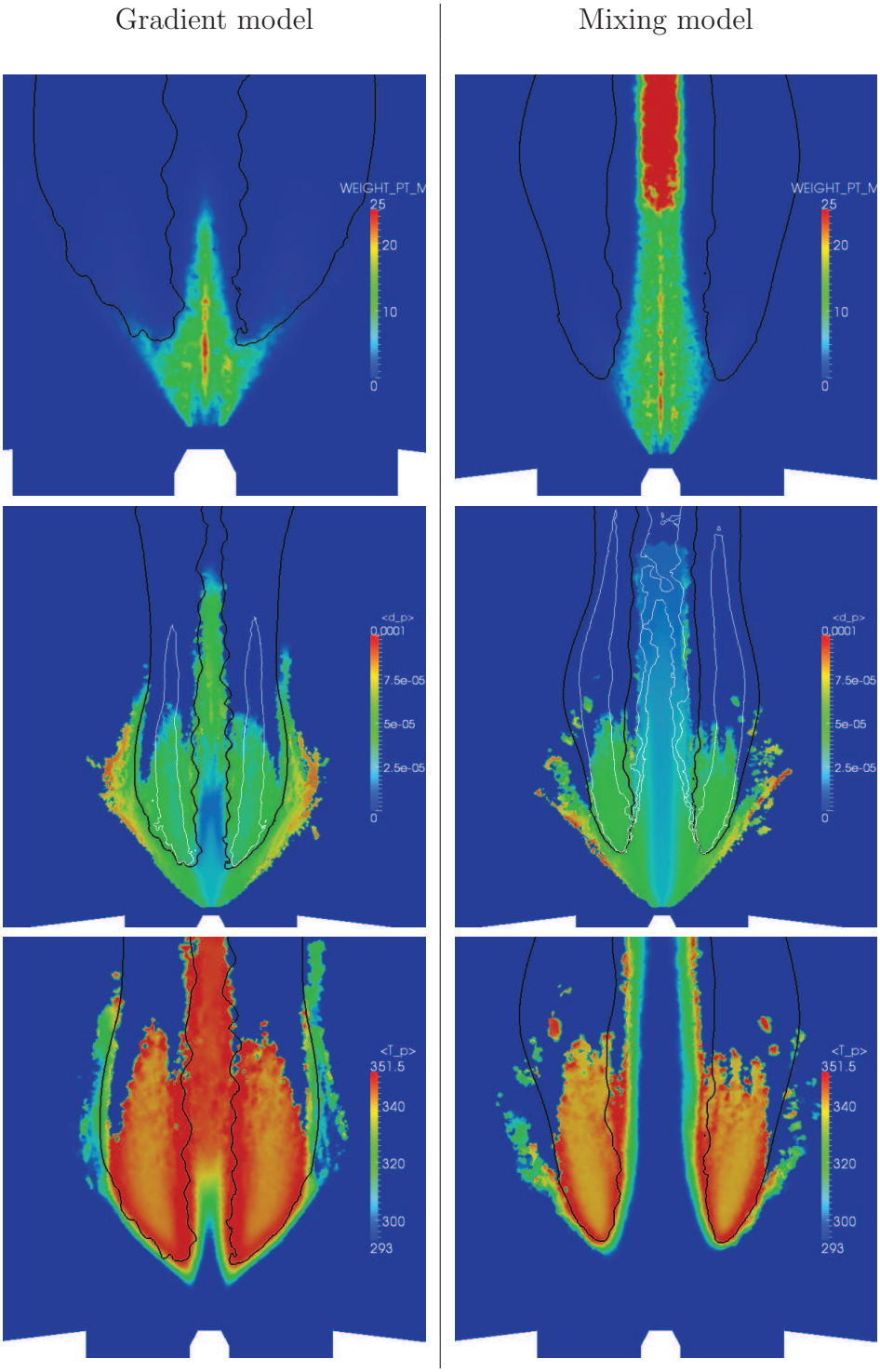

Figure 4.20: Time-averaged particle density $\langle\{w\}\rangle$, local mean diameter $\langle d_p \rangle$ and local mean temperature $\langle T_p$. Black isolines: stoichiometric mass fraction $\widetilde{Z} = Z_{\mathrm{st}}$. White isolines delimit the zone where gaseous ethanol is present: $\widetilde{Y}_{\mathrm{C_2H_5OH}} = 0.02$.

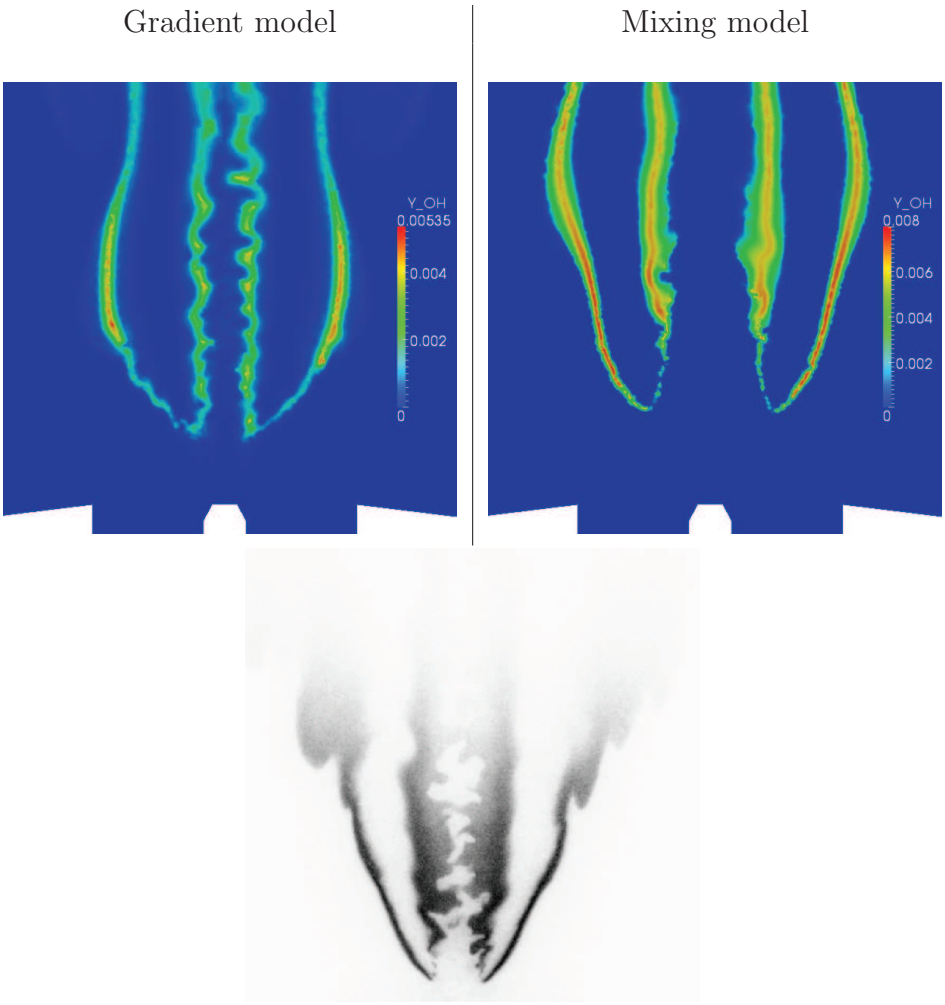

Figure 4.21: *Top:* Instantaneous OH mass fraction fields; *bottom:* experimental LIF capture of OH, on the 40 % CO_2 dilution, 95-mm inset diameter case (simulated case is at 60 % dilution).

front, if wrinkled, with the gradient model.

Gas velocity. As expected, the flame has an impact on the velocity field. Mean and rms gas velocity components are plotted and compared with experimental measurements in Figs. 4.22 and 4.23. First of all, it may be seen that in the region close to nozzle, the velocity means are better captured than with the injection approach (B) examined in the previous chapter. The peak axial velocity is higher here than earlier: this is probably due to the deletion of smaller droplets in favor of larger ones, that leads to a higher liquid-to-gas momentum transfer.

Second, the flow distortion due to the flame is conform to experimental predictions: this is most visible for the gradient model case, for which the flame lift-off height is correctly recovered. The axial component's decrease as $r \to 0$ is actually captured, which was not the case in the cold flow simulations, see Fig. 3.26. In the light of the flame position, this is due to thermal expansion when the flow crosses the flame, whose angle leads to curving the streamlines towards the centerline. In

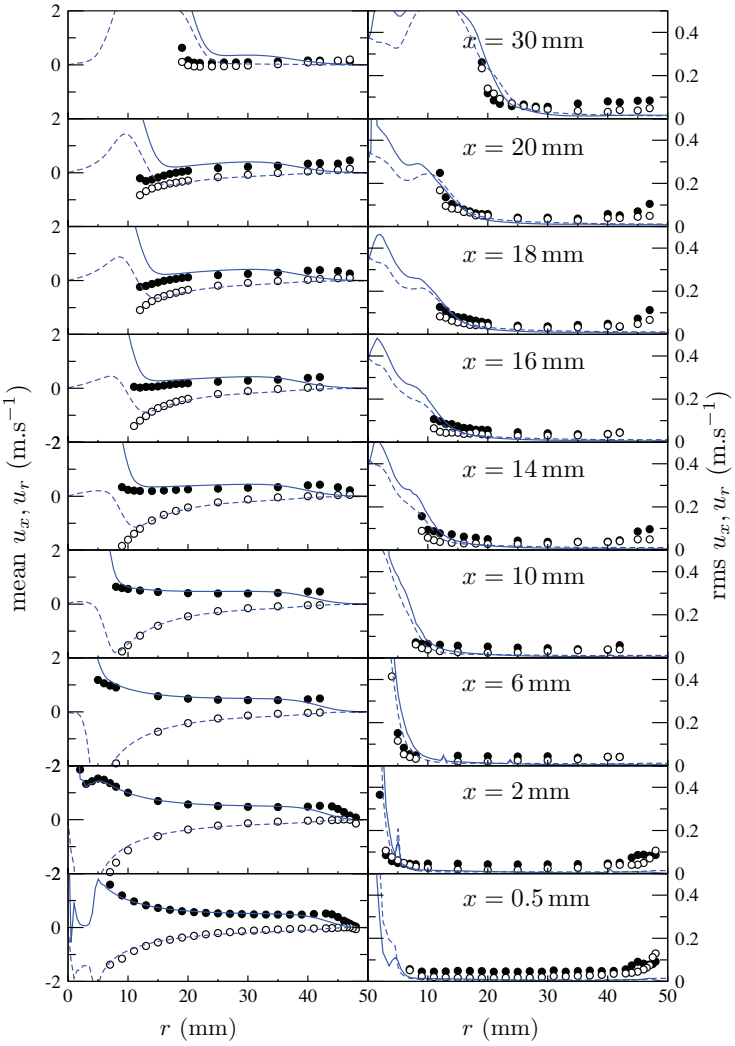

Figure 4.22: Mean and rms velocity profiles along radial profiles at different distances x from the nozzle, for a flame simulated with the **gradient model** for segregations. Blue line: simulation (full: u_x, dashed: u_r); circles: experimental measurements.

addition, correct velocity rms levels are also captured. As for the mixing model, no such trend is visible but this is due to the flame being positioned too far downstream.

4.4.3 Highly resolved simulations

As a tentative step towards more detailed study, preliminary simulations of the SAFIR flame were run at one level of mesh refinement, leading to mesh #3, with cell dimensions reduced by a factor 2. This leads to a 215-million-tetrahedron mesh. The spray computation has been refined as well: numerical droplet weighting is set to one for all parcels. The steady-state number of droplets reaches 107,000. Computations were carried out using, for variances, the gradient model.

Instantaneous mixture fraction, temperature fields are shown in Fig. 4.24, along with a view of the resolved progress variable at the flame tips, and the mesh wireframe

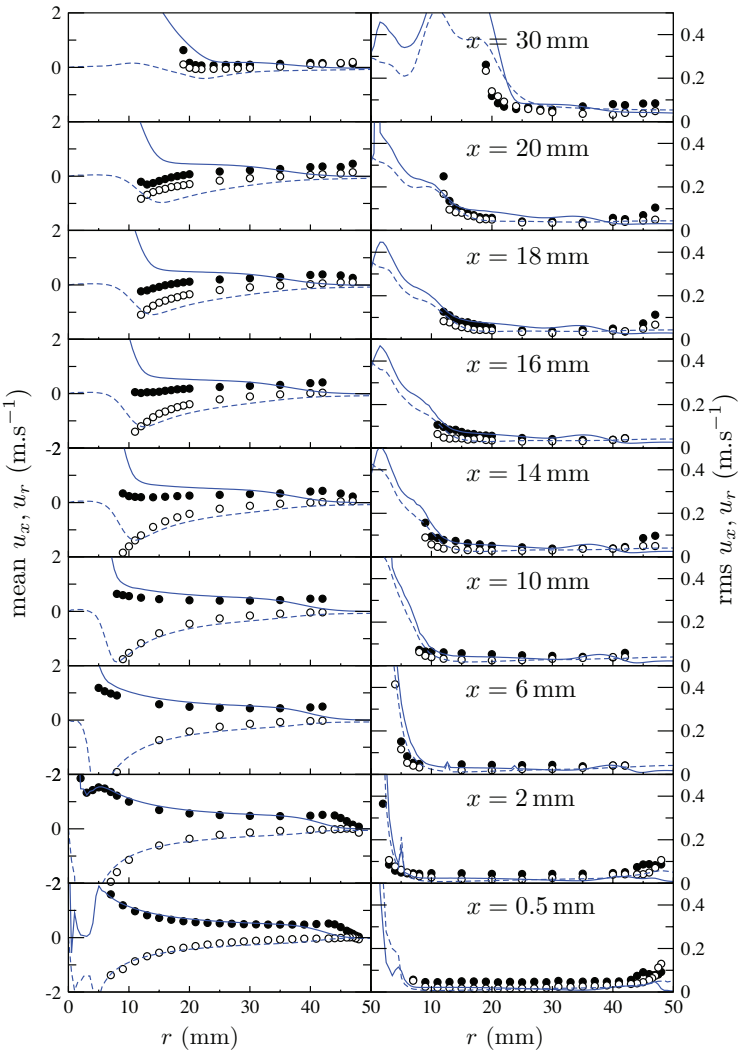

Figure 4.23: Mean and rms velocity profiles along radial profiles at different distances x from the nozzle, for a flame simulated with the **mixing model** for segregations. Blue line: simulation (full: u_x, dashed: u_r); circles: experimental measurements.

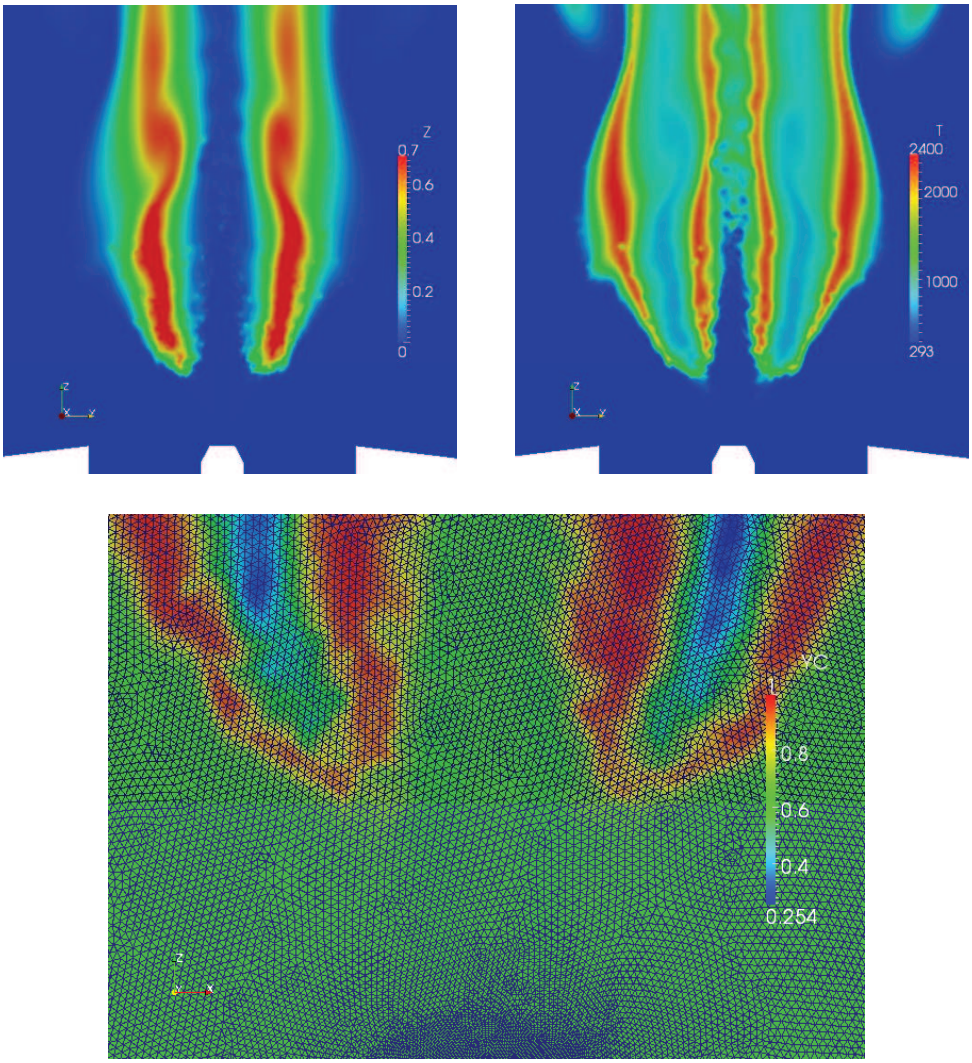

Figure 4.24: Instantaneous mixture fraction $\widetilde{Z}$, temperature $\widetilde{T}$ and progress variable $\widetilde{Y}_c$ flame fields obtained on the highly-resolved, 215m-cell mesh #3, with the gradient model. The mesh's level of resolution is shown in the bottom view.

apparent. It can be seen that the filtered flame front is resolved with 6–7 points through its thickness. The flame structure seems to be slightly impacted by the mesh refinement, in particular the inner flame region where less turbulent structures appear to impact the mixture fraction and temperature fields.

A brief summary of computation efficiency is given in Table 4.3, comparing two runs with the reference mesh, with two levels of numerical droplet weighting, and the refined run.

4.4.4 Validation of the time advancement algorithm

The time advancement algorithm, presented in Section 2.2.3, is based on a particle time sub-step computed as the minimum of characteristic timescales linked to momentum, heat and mass transfer. A validation test is carried out here to ensure that this sub-step is sufficiently small. Two runs in identical conditions (large segregation

	1	2	3
Number of cells	27M	27M	215M
Droplet weighting (large–small)	4–20	1–5	1–1
Number of processors	1024	1024	8192
Number of numerical droplets	16,300	47,600	107,000
Time step (µs)	50.	48.	10.
Reduced efficiency: time/nodes/steps×procs (ms)	7.1	8.8	7.7
% time spent on Lagrangian solver	72 %	76 %	59 %

Table 4.3: Comparison between runs conducted at different Eulerian and Lagrangian resolutions. For all computations, CFL=1.5, Fourier number Fo=0.2.

model constants, $K_g = 0.36$) are compared, one using the standard sub-step, and another where it is divided by two.

Gas-phase and spray-phase properties are shown in Figs. 4.25 and 4.26. Slight differences are visible, but are small enough not to significantly impact the flame and spray structures. This validates the time advancement algorithm.

4.5 Conclusions

A turbulent ethanol spray flame has been simulated with detailed flamelet chemistry on an unstructured mesh reaching a close-to-250-µm resolution in the flame tip. The PCM–FPI approach proves to yield satisfactory results, used with two scale-similarity variance models: a 'gradient' model giving the correct lift-off height and a 'mixing' model that leads to a flame structure matching very well with the experimental observations.

A number of points can be improved in this simulation, in addition to a better accounting of spray atomization and turbulent dispersion, already discussed in Chapter 3, which will be paramount to enhancing the predictions' quality. It should be possible to include the enthalpy drop caused by evaporation, although with a limited impact on the results. A treatment of the sgs fluctuations of mixture fraction that accounts for the saturation value is very feasible, at the cost of one additional dimension in the lookup table. Further than examining spray statistics and the flame structure, bulk fumes properties could also be compared with the available experiment data. Flamelet chemistry has proven effective on this point in earlier works and should accordingly behave well in the present simulation.

Given the large number of configurations studied in the SAFIR experiment and the generally successful output of the present simulations, this study appears as an initiating work that lays the basis for a potent exploration of the impact of oxidizer dilution and co-flow velocity on flame properties, such as lift-off height, structure, maybe pollutant emissions too.

A second step will be to tackle the cases where the inner recirculation of burnt gases within the combustion chamber impacts the flame structure. Accounting for enthalpy losses through radiative transfer will then be a necessity if relevant results are to be expected. This will require the insertion of enthalpy as an additional

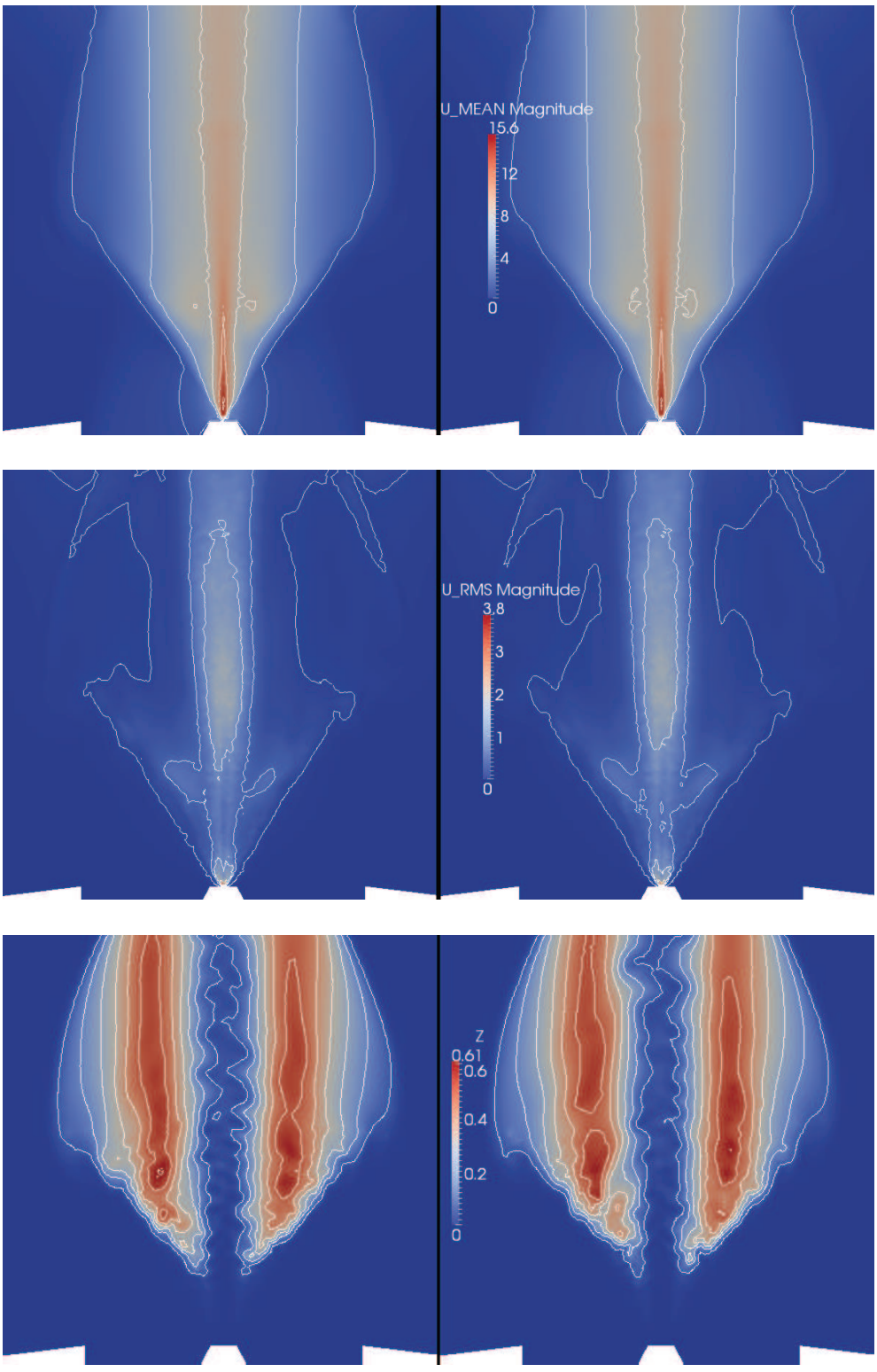

Figure 4.25: Comparison of gas-phase properties of two runs in identical conditions except $\alpha_{\Delta t} = 1$ (left) and $\alpha_{\Delta t} = 0.5$ (right). From top to bottom: mean velocity magnitude, isolines 1.0, 4.5, 8.0, 11.5, 15. $\mathrm{m.s^{-1}}$; rms velocity magnitude, isolines 0.1, 0.5, 1.0, 2.0 $\mathrm{m.s^{-1}}$; instantaneous mixture fraction, regular isolines from 0.05 to 0.6.

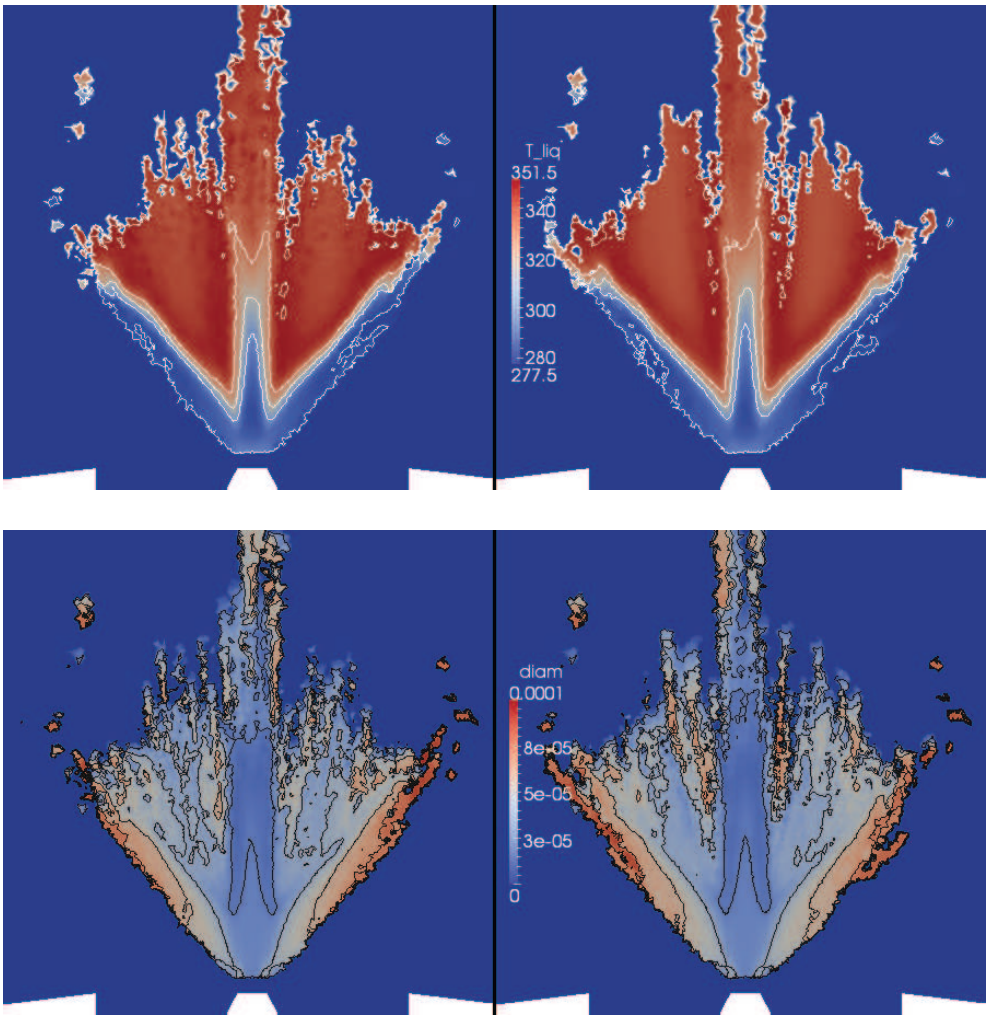

Figure 4.26: Comparison of liquid phase properties of two runs in identical conditions except $\alpha_{\Delta t} = 1$ (left) and $\alpha_{\Delta t} = 0.5$ (right). From top to bottom: mean droplet temperature, isolines of regularly-spaced values from 280 to 350 K; mean droplet diameter, isolines regular from 20 to 90 µm.

parameter in the chemical description. The PCM–FPI formalism is not designed to be naturally extended to a third parameter. Subgrid-scale enthalpy fluctuations could be assumed to be negligible. As an alternative, the FCCT approach, described in Part III, can offer the framework to account for non-trivial sgs distribution of such an additional parameter.

Part III

Flow-Controlled Chemistry Tabulation

Chapter 5

Mixing-time history effects in LES of non-premixed turbulent combustion

The time history of mixing is known to play a crucial and non-trivial role in non-premixed turbulent combustion. The idea behind the Flow-Controlled Chemistry Tabulation (FCCT) approach is to account for the mixing history in a way that will formally enable multiple-parameterization.

After an introduction, Eulerian balance equations are derived in Section 2 for both a flow residence time and a characteristic time of the mixing which the particles gathered in a fluid element have been subjected to in their flow histories. These equations are analyzed and solved in a Large-Eddy Simulation (LES) context for a fuel jet mixing with an oxidizer coflow. Typical responses of filtered mixture fraction *vs.* flow residence time are highlighted. In Section 3, the FCCT tabulation is devised: the effects of unresolved fluctuations of thermochemical variables in LES are simulated, combining partially-stirred reactors with tabulated chemistry. The reactor evolutions are organized to mimick flow engulfment and micro-mixing, so as to reproduce the observed filtered mixture fraction *vs.* residence time response. This allows for dynamically building sub-grid scale joint probability density functions, and thereby the sub-filter response of the non-premixed flames, according to four control parameters: the filtered mixture fraction, the progress of reaction, the flow residence time and a mixing time. Finally, LES of the Cabra *et al.* [Cabra 05] fuel-jet lifted-flame developing in a vitiated oxidizer environment is performed and results are compared against measurements.

This chapter is mainly a reproduction of a journal publication [Enjalbert 11]. It is self-consistent and accepts an independent reading. However, some points may already have been addressed in earlier sections of this manuscript and they are then quoted between parentheses. Additional paragraphs have been inserted that are not included in the publication, but that provide additional information, either on the theory of the FCCT formalism, or on the study of the simulation results.

Contents

5.1 Introduction

The time history of mixing is usually considered as central to turbulent flames, where large-scale unsteady flow motion leads to an imperfect mixing of the reactants, while micro-scale molecular diffusion brings chemical species in contact within thin reaction zones [Bray 66]. In this context, Large-Eddy Simulation (LES) has flourished to simulate the large-scale mixing, while smallest scales are modeled [Moin 02]. However, LES must address the turbulent structures at a resolution fine enough to allow for a reliable prediction of the subgrid-scale (SGS) mixing dynamics [Pope 04], specifically when scalar fields are concerned [Vervisch 10].

Accounting for time history effects in the evaluation of the SGS statistics, while dealing with the double challenge of accuracy and computational cost, is not straightforward. A large set of methods tackle this issue in different ways. The transported probability density function (pdf) and transported mass-weighted pdf methods [Jaberi 99] are formulated precisely to follow the individual history of fluid elements. In their Lagrangian formulation, the evolution of stochastic particles are subjected to chemical sources and turbulent transport, the interaction between mixing and chemistry is reproduced throughout the evolution of particles [Sheikhi 05,

Yaldizli 10]. It was shown that equivalent averaged results may be obtained with an Eulerian formulation, by the computation of several stochastic fields [Valino 98, Raman 06, Jones 10d]. Obviously, the numerical accuracy of these methods is directly sensitive to the number of stochastic particles, or fields, used in the computations.

Fully prescribing the SGS statistics with presumed pdfs oversimplifies the history of fluid parcels. The Presumed Conditional Moments (PCM) formulation [Vervisch 04, Domingo 08, Subramanian 10b, Michel 08] is such an approach; it relies on estimating low order statistical properties of the distributions, like averages and variances. The pdfs are then assumed to take a specific shape, parameterized by these quantities. In the presumed pdf approach, the history of the flow is only taken into account through its effect on these statistical properties and it is the local result of history that is described, not its dynamics. Complex correlations between chemical and mixture parameters cannot be accounted for, and strong hypotheses must often be framed, such as statistical independence between mixture fraction and progress of reaction. Moreover, the transport of statistical higher moments, like scalar variances, is subject to inaccuracies as soon as the filter size – in most cases the mesh – is not sufficiently refined [Vervisch 10]. On the other hand, the filtered flame response may be tabulated with a reduced number of controlling parameters. A lookup table, computed prior to the LES, is then accessed from the simulation, making the additional cost due to chemistry marginal. Methods based on direct computations of conditional means, as Conditional Moment Closure (CMC), have also being explored in the literature [Klimenko 99, Cha 01, Kronenburg 04, Kronenburg 08].

The work presented in this paper proposes an alternative parameterization of the flow for non-premixed jet flames, which enables a tabulation of turbulent chemistry, but avoids presuming joint pdfs. The idea is to describe not the results of flow mixing history, but properties of this history itself. There have been previous attempts to enable the description of history through conditioning scalars: age-related markers were introduced in premixed flames [Bilger 04, Grout 07] and a flamelet lifetime was used for an interactive computation of unsteady diffusion flamelets [Pitsch 98]. In a tabulated chemistry approach for RANS [Kolaitis 06], a residence time was also formerly introduced as a conditioning variable to replace the reaction progress variable.

The present approach, labeled "Flow-Controlled Chemistry Tabulation" (FCCT), consists of both a novel formalism for parameterizing chemistry and a tabulation technique based on Monte-Carlo simulations of a Partially-Stirred Reactor (PaSR). A flow chart in Fig. 5.1 schematizes the method.

- A multi-scale approach is followed: in the LES, in addition to usual continuity, momentum and energy budgets, four quantities are resolved: $\widetilde{Z}$, the filtered mixture fraction; $\widetilde{Y}_c$, the progress of reaction used to tabulated detailed chemistry; the filtered "residence time" $\widetilde{\tau}_{\text{res}}$, defined here as the time duration over which mixing has been acting on a fluid particle and the "mixing time" τ_{mix}, an evaluation of the characteristic turbulent mixing time along the fluid particle trajectory. Two of these resolved fields ($\widetilde{\tau}_{\text{res}}$, $\widetilde{Z}$) are used to find a distribution of mixture fraction *vs.* residence time which is representative of the unsteady mixing dynamics.

- Aside from the flow solution, time sequences of a stochastic PaSR are considered under the mixing constraint given by the $\widetilde{Z}$ *vs.* $\widetilde{\tau}_{\text{res}}$ distribution, which is fulfilled by monitoring reactor injection. In this PaSR, at the microscale level, the balance between molecular diffusion and chemistry is described by a flamelet hypothesis [Gicquel 99, van Oijen 00]; chemistry is thus retrieved from the mixture fraction Z and the progress of reaction Y_c. At an intermediate scale, which is still at the subgrid level in the LES, these flamelets interact with turbulence according to a mixing closure in the stochastic reactor and with the mixing time scale τ_{mix}.
- In the end, a four-dimensional lookup table ($\widetilde{Z}$, $\widetilde{Y}_c$, $\widetilde{\tau}_{\text{res}}$, τ_{mix}) is built, resulting from a treatment of Monte-Carlo simulations of the PaSR, and supplies the unclosed Eulerian terms in the LES. The coupling between this table and LES is similar to presumed pdf approaches with tabulated chemistry, however here the sub-filter joint pdf is not imposed a specific shape but built according to the flow mixing dynamics.

In a first section, the mentioned flow timescales are introduced and their role in describing the turbulent mixing properties is analyzed. The FCCT method is then presented in detail, specifications of the PaSR model are given, and the table generation technique is described. A last part illustrates the method's implementation in the LES flow solver; a simulation of a lifted methane-air jet flame in a vitiated co-flow is carried out and results are compared with experiments [Cabra 05], after studying the output table properties.

5.2 Eulerian description of mixing-time history

5.2.1 Residence time

Let a scalar ϕ be defined by the Lagrangian equation

$$\frac{\mathrm{d}\phi}{\mathrm{d}t} = S\,. \tag{5.1}$$

It may be seen as the property of a single, identifiable particle, and measures the accumulation of the source field S on its trajectory $\mathcal{T} : t \mapsto \underline{x}(t)$; for an initial value ϕ_0, $\phi = \phi_0 + \int_{\mathcal{T}} S(\underline{x}(t), t)\mathrm{d}t$. Considering now $\phi(\underline{x}, t)$ as an Eulerian field, defined on any test volume of the flow as its ensemble average value on the enclosed particles, it satisfies the following conservation equation:

$$\frac{\partial \rho\phi}{\partial t} + \underline{\nabla} \cdot (\rho \underline{u} \phi) = \underline{\nabla} \cdot (\rho \mathcal{D} \underline{\nabla} \phi) + \rho S\,. \tag{5.2}$$

Interactions with particles from surrounding volumes imply the existence of the diffusive term in Eq. (5.2) [Nauman 81], where $\mathcal{D}$ is the molecular diffusivity, assumed to be the same for all species.

With this result, some information on flow history can be retrieved. A first, widely used application [Bilger 04, Nauman 81] is the evaluation of the local residence

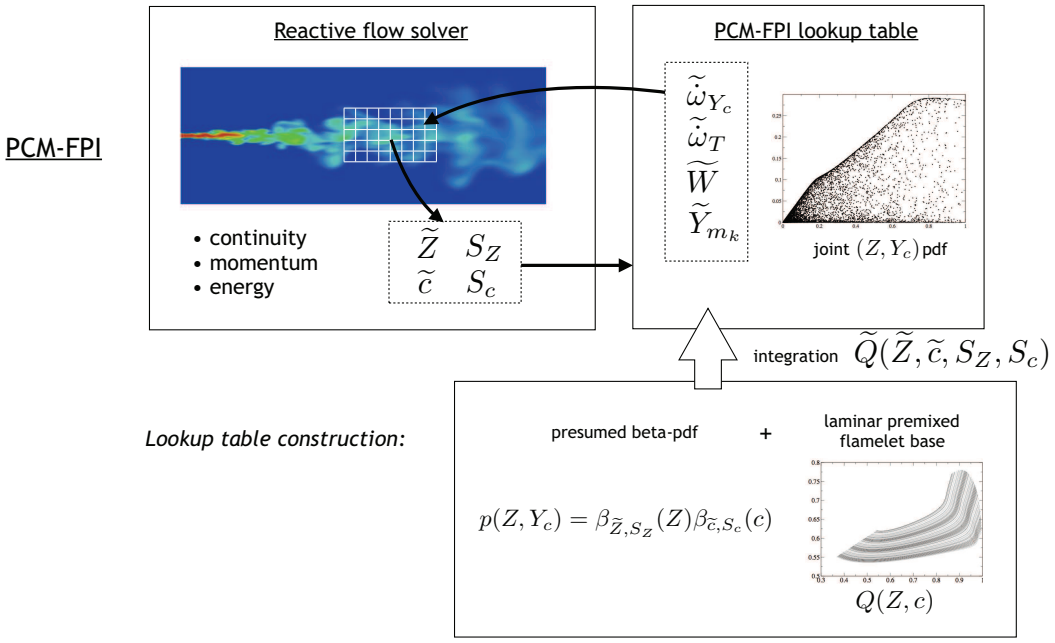

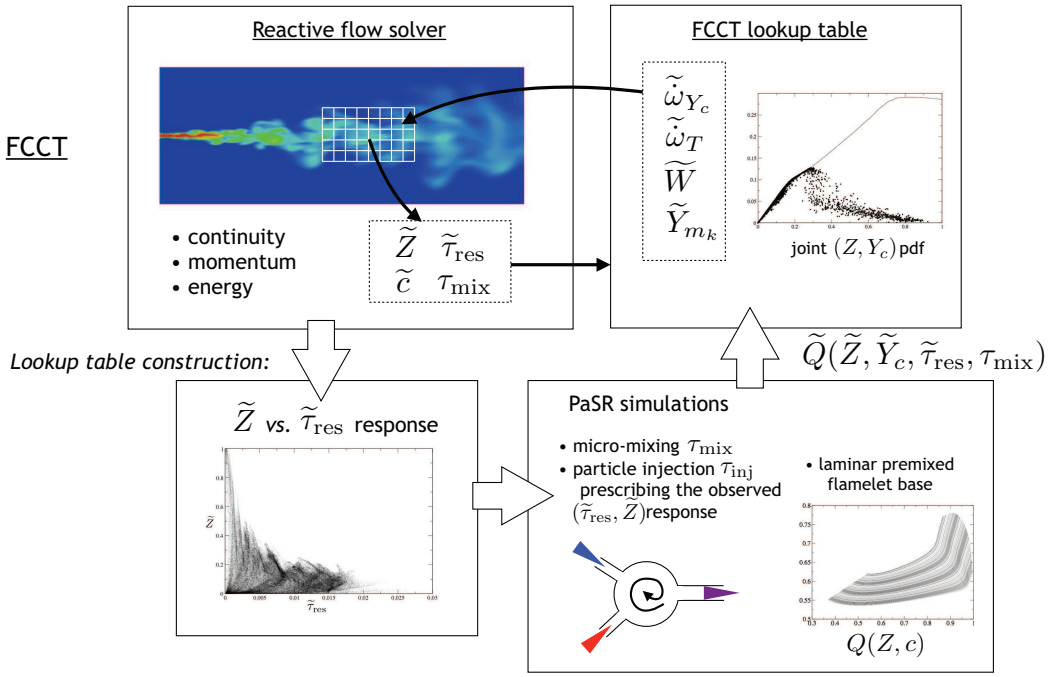

Figure 5.1: Flow charts comparing the PCM and FCCT approaches.

time $\tau_{\rm res}$ [Ghirelli 04], which is the time a particle has spent in the computational domain since its entry. $\tau_{\rm res}$ is a scalar of the kind defined in Eq. (5.1), with S constant and uniform equal to unity: $\tau_{\rm res} = \int_{\mathcal{T}} {\rm d}t$. Therefore, the residence time field obeys

$$\frac{\partial \rho \tau_{\rm res}}{\partial t} + \underline{\nabla} \cdot (\rho \underline{u} \tau_{\rm res}) = \underline{\nabla} \cdot (\rho \mathcal{D} \underline{\nabla} \tau_{\rm res}) + \rho \, . \tag{5.3}$$

Notice that this residence time is an Eulerian quantity, hence the average over fluid particles within a flow volume.

5.2.2 Trajectory-averaged mixing time

The trajectory average of any quantity Q is defined for each particle as

$$\langle Q \rangle_{\mathcal{T}} = \frac{\int_{\mathcal{T}} Q(\underline{x}(t), t) {\rm d}t}{\int_{\mathcal{T}} {\rm d}t} = \frac{Q^{\rm I}}{\tau_{\rm res}} \, , \tag{5.4}$$

where the integral $Q^{\rm I} = \int_{\mathcal{T}} Q(\underline{x}(t), t) {\rm d}t$ satisfies Eq. (5.1), with $S = Q$.

The objective of this work is to address well resolved LES (*i.e.* simulations where more than 80 % of the turbulent kinetic energy is resolved); then, the Eulerian distribution of the residence time $\tau_{\rm res}$ features fluctuations around the space-filtered value that are relatively small. This is justified by the fact that residence time is mostly large-scale-controlled, thereby unresolved contributions to the residence time elapsed along a particular trajectory remain small compared to the space-filtered value. Consequently, the Eulerian field of $\langle Q \rangle_{\mathcal{T}}$ may be computed by making, for the filtering operation denoted by $\bar{\cdot}$, the approximation $\overline{Q^{\rm I}/\tau_{\rm res}} \simeq \overline{Q^{\rm I}}/\overline{\tau}_{\rm res}$, and solving $\overline{Q^{\rm I}}$ and $\overline{\tau}_{\rm res}$ from the filtered Eqs. (5.2) and (5.3). This approach can be applied as an instrument to characterize the turbulence history of a fluid element in the flow.

To account for the SGS mixing effect, a local mixing timescale $\tau^*_{\rm mix}$ is introduced. It characterizes the intensity of turbulence in the unresolved inertial and viscous ranges and its subgrid-variance reduction effect [Dopazo 79, Pera 06, Klimenko 07]:

$$\tau^*_{\rm mix} = \frac{\Delta^2}{2(\mathcal{D} + \mathcal{D}_T)} \, , \tag{5.5}$$

where Δ is the LES filter size and $\mathcal{D}_T \sim \Delta^2 (\widetilde{S}_{ij} \widetilde{S}_{ij})^{1/2}$ the modeled SGS turbulent diffusivity, with $\underline{\underline{S}} = 0.5(\underline{\nabla}\,\underline{u} + \underline{\nabla}^t \underline{u})$. Because of the expected level of spatial resolution, locations exist where $\mathcal{D}_T$ is not large and the molecular diffusivity $\mathcal{D}$ is added to compute $\tau^*_{\rm mix}$ in Eq. (5.5). Along a flow trajectory, the variance v of a passive scalar varies, due to molecular mixing, according to [Dopazo 79]:

$$\frac{{\rm d}v(t)}{{\rm d}t} = -\frac{v(t)}{\tau^*_{\rm mix}} \, , \tag{5.6}$$

and the linear role of $1/\tau^*_{\rm mix}$ may therefore be integrated. The average mixing level that the particles forming a fluid element have been subjected to in their flow histories may thus be measured by

$$\tau_{\rm mix} = \frac{1}{\langle 1/\tau^*_{\rm mix} \rangle_{\mathcal{T}}} = \frac{\tau_{\rm res}}{\int_{\mathcal{T}} (1/\tau^*_{\rm mix}) dt} = \frac{\tau_{\rm res}}{\Theta} \, , \tag{5.7}$$

where $\Theta = (1/\tau^*_{\rm mix})^{\rm I}$ satisfies

$$\frac{\partial \rho\Theta}{\partial t} + \underline{\nabla}\cdot(\rho\underline{u}\Theta) = \underline{\nabla}\cdot(\rho\mathcal{D}\underline{\nabla}\Theta) + \frac{\rho}{\tau^*_{\rm mix}}\,. \tag{5.8}$$

The FCCT closure discussed in this paper is grounded on the two governing relations (5.3) and (5.8). As discussed in the literature [Darabiha 92, Im 99], non-premixed flames may be more sensitive to the time history of strain and mixing rates than to their local and instantaneous values. For instance, a diffusion and reactive layer subjected to a strain-rate level above the steady quenching value, may not be quenched if this high mixing rate is imposed for a short duration of time. The time history of micro-mixing calibrated through the variable Θ can thus be an interesting ingredient for turbulent diffusion flame modeling.

5.2.3 Higher-order history distribution moments

This section is not included in the publication and is not needed for an understanding of the FCCT approach.

The concept presented above of trajectory-averaged scalars can be generalized to achieve a higher-order description of the scalar history along the trajectory.

High-order statistical moments.

The simple computation of the integral $(Q^k)^{\rm I}$, satisfying Eq. (5.1) with $S = Q^k$, gives access to higher-order statistical properties of the scalar history. For example, the trajectory variance may be evaluated as

$$v_{Q\mathcal{T}} = \frac{(Q^2)^{\rm I} - (Q^{\rm I})^2}{\tau_{\rm res}}\,. \tag{5.9}$$

In practice, the accuracy of the computation is limited by the numerical error of the solver, and remains subjected to the approximation $\overline{(Q^k)^{\rm I}/\tau_{\rm res}} \simeq \overline{(Q^k)^{\rm I}}/\overline{\tau}_{\rm res}$.

Interval tracing

Another approach consists of quantifying directly how frequently, along the trajectory, certain values have been taken by Q. Let the scalar's expected variation range be divided into a number N_I of intervals, I_1,I_2,...,I_{N_I}. One may assume, for the present discussion, that they cover the entire variation range:

$$\forall t,\ \forall \underline{x},\quad Q(\underline{x},t) \in \bigcup_{j=1}^{N_I} I_j\,. \tag{5.10}$$

The idea is to assess the amount of time, along the trajectory, spent by Q within each of the intervals. The durations τ_j, $j = 1,\ldots,N_I$, are introduced, each of them satisfying

$$\frac{\partial \rho\tau_j}{\partial t} + \underline{\nabla}\cdot(\rho\underline{u}\tau_j) = \underline{\nabla}\cdot(\rho\mathcal{D}\underline{\nabla}\tau_j) + \rho\chi_j(Q)\,, \tag{5.11}$$

where the source term $\chi_j(Q)$ is a mask function:

$$\chi_j(Q) = \begin{cases} 1 & \text{if } Q \in I_j \,, \\ 0 & \text{else} \,. \end{cases} \tag{5.12}$$

With the hypothesis (5.10), the τ_j's sum up to the total residence time:

$$\sum_{j=1}^{N_I} \tau_j = \tau_{\text{res}} \,. \tag{5.13}$$

A histogram distribution $p_j, j = 1, \ldots, N_I$ of the temporal history of Q along the fluid particle trajectory is then available in each point of the solved flow:

$$p_j = \frac{\tau_j}{\tau_{\text{res}}}, \quad \sum_{j=1}^{N_I} p_j = 1 \,, \tag{5.14}$$

as illustrated in the schematic of Fig. 5.2.

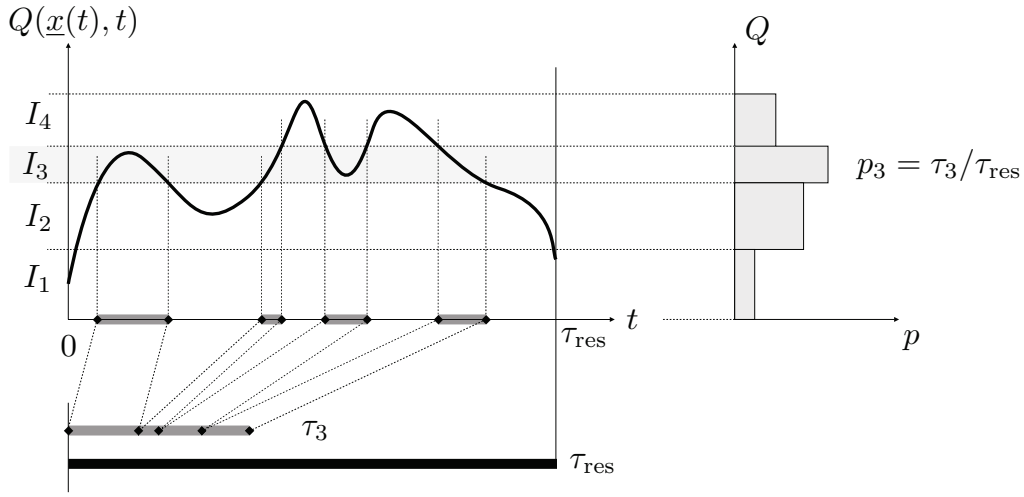

Figure 5.2: Schematic illustration of the construction of a histogram temporal history distribution.

5.2.4 Flow configuration and numerics

All simulations in this study are performed with the structured-mesh SiTCom solver, presented in Part I. Artificial turbulence of the inflow is generated according to the Klein *et al.* approach [Klein 03]. Boundary conditions are determined following the 3D-NSCBC formalism [Lodato 08b], including in the BCs a specific heat ratio γ computed from the local gas composition. The SGS turbulent fluxes are modeled using the Wall-Adapting Local Eddy-viscosity (WALE) closure (Section 1.3.2). The laminar viscosity is computed from Sutherland's law; the laminar and turbulent Prandtl numbers are set to 0.72 and 0.90. The geometry and inlet flows

match those of the Cabra *et al.* [Cabra 05] methane–air experiment, which has been the subject of numerous modeling works [Domingo 08, Michel 08, Gordon 07, Gkagkas 07, Navarro-Martinez 09, Ihme 10]. The jet inlet diameter is $D = 4.57\,\mathrm{mm}$, with a bulk velocity $u_{\mathrm{jet}} = 100\,\mathrm{m.s^{-1}}$, and a uniform co-flow velocity of magnitude $u_\infty = 5.4\,\mathrm{m.s^{-1}}$. The co-flow carries the oxidizer, a mixture of mainly air and H_2O at $T_0 = 1,350\,\mathrm{K}$; the fuel, issuing through the central inlet, is a rich mixture of air and methane at $T_1 = 320\,\mathrm{K}$. In this work, various meshes are considered from 1,950,000 up to 5,700,000 nodes; more details concerning LES of this flame under similar conditions may be found in [Domingo 08, Godel 09].

5.2.5 $(\tau_{\mathbf{mix}}, \tau_{\mathbf{res}})$ properties

In non-premixed flames, the regions of interest are the zones where the mixing between the inlet streams takes place, which can be characterized by $\widetilde{Z}(1-\widetilde{Z}) \neq 0$, where Z is the mixture fraction (a passive scalar equal to unity in pure fuel and vanishing in the oxidizer stream), and $\widetilde{Z} = \overline{\rho Z}/\overline{\rho}$ is its mass-weighted (or Favre) filtered value. Only the history of the flow in these areas is considered, and the residence and mixing timescale integrations are carried out only there, weighting their source term by $S^+_{\widetilde{Z}}$, equal to unity where $\widetilde{Z} \in [\epsilon; 1-\epsilon]$, and zero elsewhere ($\epsilon = 10^{-4}$ is used in the computations). The following two equations are solved:

$$\frac{\partial \overline{\rho}\widetilde{\tau}_{\mathrm{res}}}{\partial t} + \underline{\nabla}\cdot(\overline{\rho}\widetilde{\underline{u}}\widetilde{\tau}_{\mathrm{res}}) = \underline{\nabla}\cdot\left(\overline{\rho\mathcal{D}\underline{\nabla}\tau_{\mathrm{res}}} - T_{\tau_{\mathrm{res}}}\right) + \overline{\rho}S^+_{\widetilde{Z}}\,, \tag{5.15}$$

$$\frac{\partial \overline{\rho}\widetilde{\Theta}}{\partial t} + \underline{\nabla}\cdot(\overline{\rho}\widetilde{\underline{u}}\widetilde{\Theta}) = \underline{\nabla}\cdot\left(\overline{\rho\mathcal{D}\underline{\nabla}\Theta} - T_{\Theta}\right) + \frac{\overline{\rho}}{\tau^*_{\mathrm{mix}}}S^+_{\widetilde{Z}}\,, \tag{5.16}$$

from which the trajectory-weighted mixing time is estimated as (Eq. (5.7)):

$$\tau_{\mathrm{mix}} = \frac{\widetilde{\tau}_{\mathrm{res}}}{\widetilde{\Theta}}\,. \tag{5.17}$$

The SGS turbulent fluxes are $T_{\tau_{\mathrm{res}}} = \overline{\rho\underline{u}\tau_{\mathrm{res}}} - \overline{\rho}\widetilde{\underline{u}}\widetilde{\tau}_{\mathrm{res}}$ and $T_\Theta = \overline{\rho\underline{u}\Theta} - \overline{\rho}\widetilde{\underline{u}}\widetilde{\Theta}$, which are modeled using the WALE closure [Nicoud 99] and the approximation $\overline{\rho\mathcal{D}\underline{\nabla}\tau_{\mathrm{res}}} \simeq \overline{\rho}\mathcal{D}\underline{\nabla}\widetilde{\tau}_{\mathrm{res}}$ is used for the diffusive terms.

To start tackling τ_{res} and τ_{mix} behaviors in the fuel jet configuration, the chemically frozen mixing of fuel and co-flowing streams is simulated. Instantaneous fields of $\widetilde{\tau}_{\mathrm{res}}$ and τ_{mix} are presented in Fig. 5.3, for a run performed on the 1,950,000-node mesh with longitudinal (resp. transverse) characteristic spacing between 1.57 mm and 4.75 mm (resp. 0.28 mm and 4.4 mm); the mesh fineness has an impact on the τ_{mix} value, through the cell size Δ and the SGS turbulent eddy viscosity $\mathcal{D}_T$, see Eq. (5.5).

The $\widetilde{Z}$-dependence of the residence time source term is apparent, in that $\widetilde{\tau}_{\mathrm{res}} = 0$ where $\widetilde{Z}$ equals zero or unity (Fig. 5.3). Co-flow fluid is entrained into the jet and, as the flow develops, the residence time increases. The centerline profile of the time-averaged residence time, $\langle\tau_{\mathrm{res}}\rangle(x)$, is plotted in Fig. 5.4. It correctly matches the fit (Eq. (D.5)):

$$\langle\tau_{\mathrm{res}}\rangle(x) \sim \sqrt{\frac{\rho_\infty}{\rho_0}}x^2\,, \tag{5.18}$$

which may be derived from a one-dimensional steady jet model (see Appendix D). The cross-stream variation of the mixing timescale τ_{mix} reflects the fact that the subgrid turbulent intensity peaks at the edge of the jet.

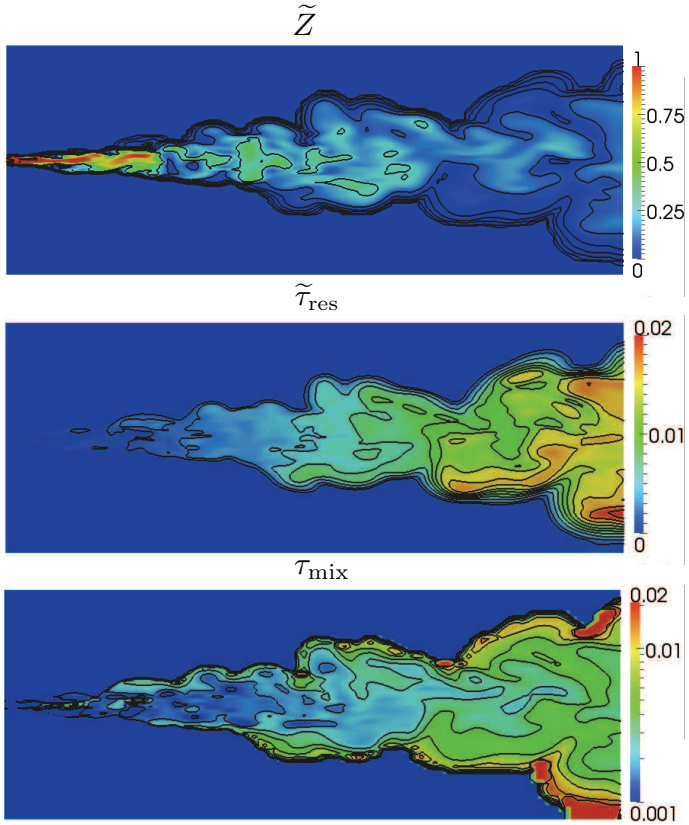

Figure 5.3: Instantaneous fields of $\widetilde{Z}$, $\widetilde{\tau}_{\text{res}}$ (Eq. (5.15)) and τ_{mix} (Eq. (5.17)) in logarithmic scale.

The structure of the average $\widetilde{\tau}_{\text{res}}$ and τ_{mix} fields is illustrated in Fig. 5.5. It may be seen that the residence time isolines and the mixing time isolines are close to perpendicular at the edge of the jet, indicating that they carry complementary information, and supporting their use as conditioning variables. A more detailed description of the properties of the $\widetilde{\tau}_{\text{res}}$ and τ_{mix} fields in a jet flow is now given.

5.2.6 Mixture fraction *vs.* residence time

Simulation of the filtered residence time (Eq. (5.15)) provides information that is useful for studying the temporal development of the mixing process, which is first analyzed in (τ_{res}, Z)-space for the two-stream problem. Subsequently, laminar mixing in a vortical flow configuration is also examined, showing similar mixing patterns in (τ_{res}, Z)-space.

Global properties of mixing in a turbulent jet configuration

An instantaneous distribution of the resolved mixture fraction $\widetilde{Z}$ is plotted against the residence time $\widetilde{\tau}_{\text{res}}$ in Fig. 5.6. The overall shape of this distribution does not

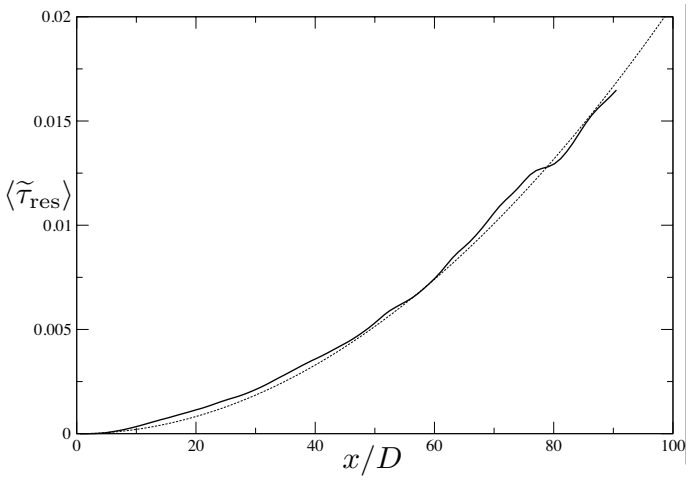

Figure 5.4: Time-average profile of $\widetilde{\tau}_{\rm res}$ on the jet centerline (solid line) and its theoretical fit (dotted line Eq. (D.5)).

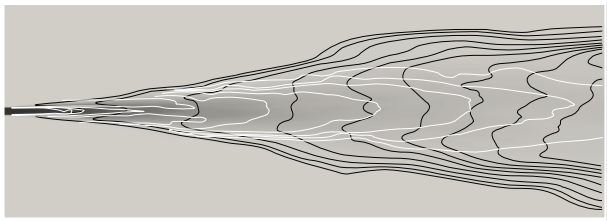

Figure 5.5: Isolines of time-averaged characteristic times. Black lines: residence time. White lines: mixing time.

vary significantly over time. At age zero, only pure fluid is encountered (*i.e.* $\widetilde{Z} = 0$, or 1). The fluid mixes across the entire range $[0; 1]$ rapidly. As turbulent mixing proceeds, and residence time increases, the upper bound of the filtered mixture fraction distribution decreases from its initial value of unity.

This is a clear illustration of turbulence homogenizing the mixture along trajectories in the flow; this also shows that there exists a restricted range of accessible $\widetilde{Z}$ values for a given $\widetilde{\tau}_{\text{res}}$ (Fig. 5.6). In other words, for a given realization, only a subset of the $(\widetilde{\tau}_{\text{res}}, \widetilde{Z})$ plane can be reached.

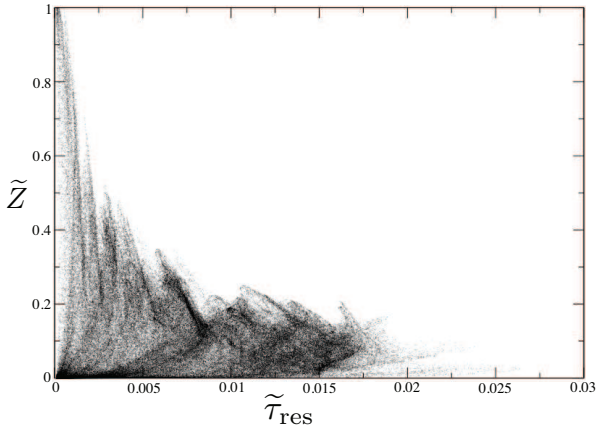

Figure 5.6: $\widetilde{Z}$ *vs.* $\widetilde{\tau}_{\text{res}}$ scatter plot at a representative instant in time.

The evolution of fluid projected on the $(\widetilde{\tau}_{\text{res}}, \widetilde{Z})$-space is expected to depend on the local mixing time τ^*_{mix} (Eq. (5.5)): with the fastest mixing (small τ^*_{mix}) occurring close to the inlet ($\widetilde{\tau}_{\text{res}}$ close to zero), and slower mixing (large τ^*_{mix}) downstream (large $\widetilde{\tau}_{\text{res}}$). This evolution of the mixing rate is observed in Fig. 5.7 which presents instantaneous contours of the mixing time, τ^*_{mix} (Fig. 5.7a), and the trajectory-averaged mixing time, τ_{mix} (Figs. 5.7b,c), overlaid on the $\widetilde{Z}$ *vs.* $\widetilde{\tau}_{\text{res}}$ distribution. The lines in these figures show the boundary of the regions occupied by all occurrences of selected values of τ^*_{mix} or τ_{mix}.

Because τ_{mix} is averaged over the fluid history, its distribution in $(\widetilde{\tau}_{\text{res}}, \widetilde{Z})$-space exhibits less scatter than the distribution of τ^*_{mix}. Contours of τ_{mix} are aligned with lines of constant $\widetilde{Z}/\widetilde{\tau}_{\text{res}}$, whose slopes decrease as τ_{mix} increases.

The same run was carried out on a finer mesh, of 5.7 million cells, featuring a radial resolution ranging between 0.25 mm and 2.9 mm. It appears, as plotted in Fig. 5.7c, that the distinct $(\widetilde{\tau}_{\text{res}}, \widetilde{Z})$ structure is unchanged, despite lower values of the local mixing timescales, as expected after increasing resolution. Also, it has been checked that in the burning case simulated below, the properties of the $(\widetilde{\tau}_{\text{res}}, \widetilde{Z})$ response are not fundamentally modified by heat release.

Mixing timescales in a laminar vortex

Next we examine the residence and mixing timescales in a laminar vortex. As in Meunier and Villermaux [Meunier 03], the flow involves the mixing of a blob of passive scalar initialized within a vortex with velocity field $v_\theta = \Gamma/(2\pi r)$, with r the radial coordinate and Γ the vortex circulation.

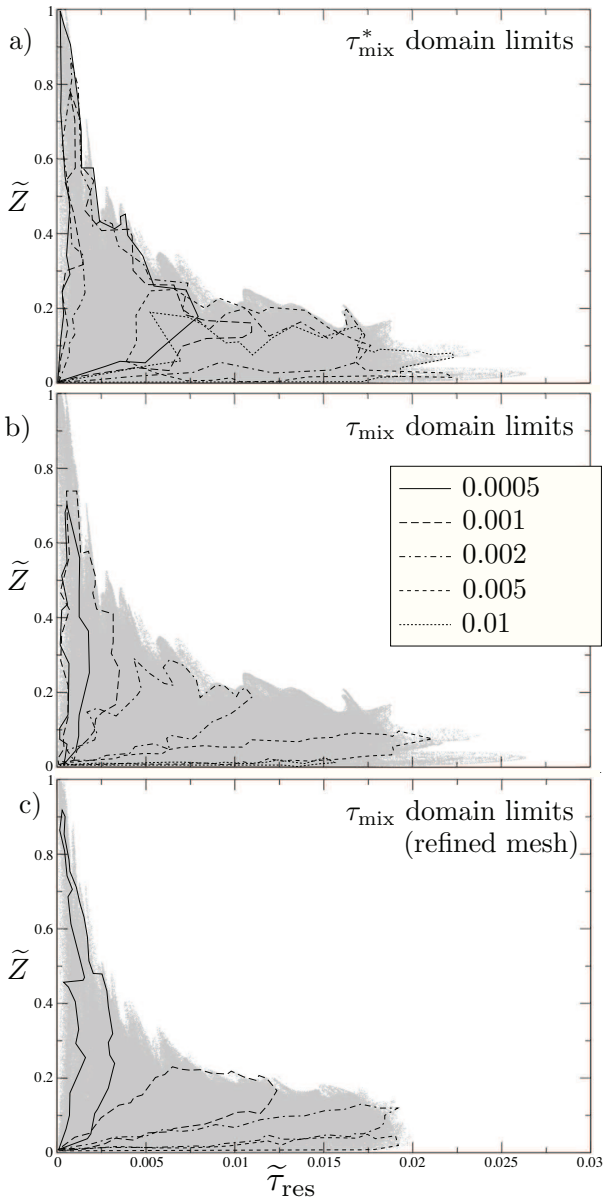

Figure 5.7: Instantaneous contours of a) the mixing timescale τ^*_{mix} (Eq. (5.5)), b) and c) trajectory-averaged mixing timescale τ_{mix} (Eq. (5.17)). Time scale values in legend box of Fig. b). Gray points: instantaneous scatter plot of $\widetilde{Z}$ *vs.* $\widetilde{\tau}_{\mathrm{res}}$.

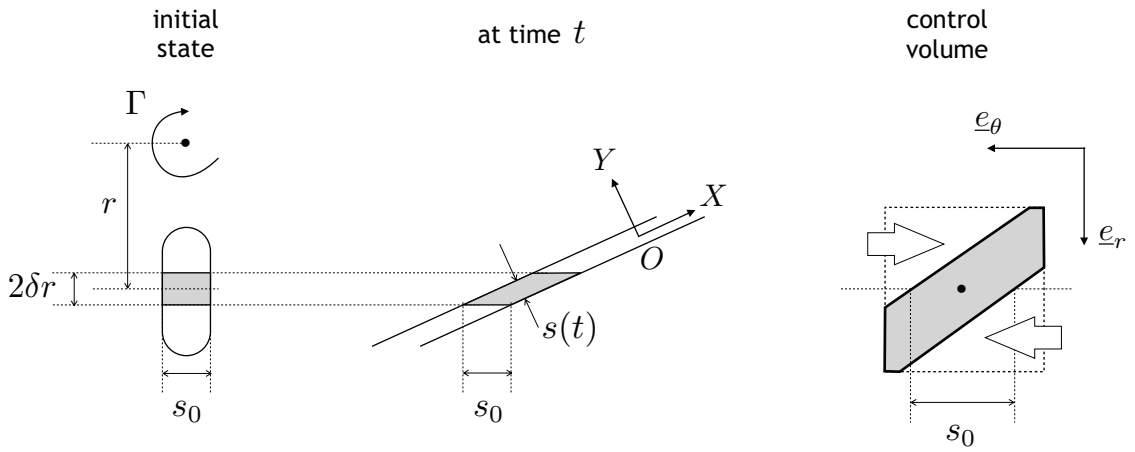

Figure 5.8: Schematic of the micro-mixing problem formulated by Meunier & Villermaux [Meunier 03].

The initial blob, of width s_0, is distorted into a spiral, whose shape can be parameterized by $\theta(r,t) = \Gamma t/(2\pi r^2)$, with a characteristic width in the transverse direction (see [Meunier 03] for further detail), decreasing in time as the streak is elongated (see diagram in Fig. 5.8):

$$s(r,t) = \frac{s_0}{\sqrt{1+\Gamma^2 t^2/(\pi^2 r^4)}} \,. \tag{5.19}$$

The equation satisfied by the tracer concentration Z is written in a frame of reference (O,X,Y) where X is locally aligned with the spiral and Y oriented towards the center of the vortex. After a change of variables $\xi = Y/s(r,t)$ and

$$\tau(r,t) = \int_0^t \frac{\mathcal{D}}{s(r,t')^2}\mathrm{d}t' = \frac{\mathcal{D}\,t}{s_0^2}\left(1+\frac{\Gamma^2 t^2}{3\pi^2 r^4}\right), \tag{5.20}$$

where $\mathcal{D}$ is the molecular diffusion coefficient, it reads like a simple diffusion equation:

$$\frac{\partial Z}{\partial \tau} = \frac{\partial^2 Z}{\partial \xi^2} \,, \tag{5.21}$$

meaning that the evolution of Z in the (ξ,τ) reference system is fully determined by its initial condition. In this coordinate system, the residence time (or age), denoted by $a(\xi,\tau)$, obeys

$$\frac{\partial a}{\partial \tau} = \frac{\partial^2 a}{\partial \xi^2} + \frac{s(t)^2}{\mathcal{D}} S_Z^+ \,. \tag{5.22}$$

The solution of this equation can be computed numerically; the evolution of the spatial profiles is shown in Fig. 5.9.

Plotting the concentration as a function of the age (Fig. 5.10) reveals a behavior similar to that observed in the LES (compare Fig. 5.10a with Fig. 5.6); the upper hull, given by the set of points $(a(0,\tau), Z(0,\tau))$ is a decreasing function of the age. As expected from the form of Eq. (5.22), the relevant non-dimensional age is a/A; $A = s_0^2/\mathcal{D}$ is a characteristic diffusion time, which is the mixing timescale of this laminar problem. As shown in Fig. 5.10b, the upper hull function $Z_{\max}(a/A)$ depends

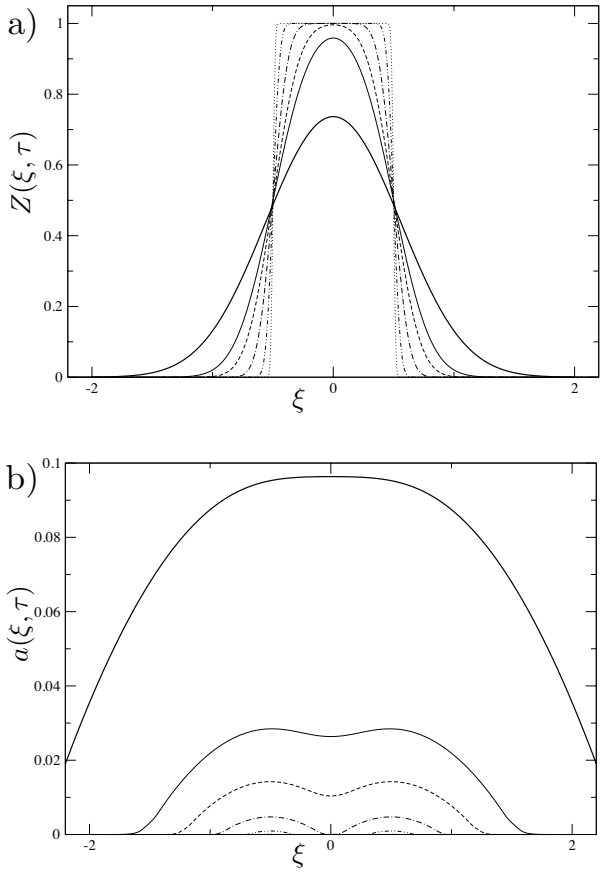

Figure 5.9: Temporal evolution of a) mixture fraction $Z(\xi,\tau)$ and b) $a(\xi,\tau)$ residence time spatial profiles in a canonical micromixing configuration, for $s_0^2/\mathcal{D} = 1.0\,\mathrm{s}$ and $\Gamma/r^2 = 5.0\,\mathrm{s}^{-1}$. Time grows from dotted to solid lines.

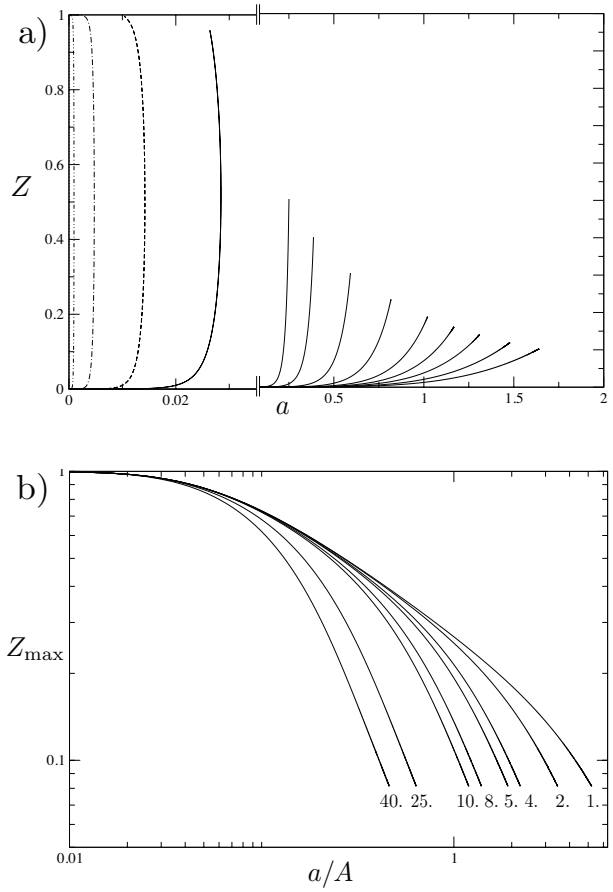

Figure 5.10: a) Temporal evolution of the concentration *vs.* residence time profiles in the conditions of Fig. 5.9, the straight lines on the horizontal axis denote a scale-split. b) Upper hull function $Z_{\max}(a/A)$ for different values of the mixing to injection times ratio $(s_0^2/\mathcal{D})/(r^2/\Gamma)$.

only on the ratio A/B, where $B = \pi r^2/\Gamma$ is the other characteristic timescale of the problem and may be seen as an "engulfment", "entrainment" [Han 01], or "injection" time. Indeed, if one considers a control volume enclosing a portion of the tracer streak (see Fig. 5.8), of side $2\delta r$ and centered in r, the amount of flow replaced every time unit by $Z = 0$ fluid, which enters through its sides is of the order of:

$$\begin{aligned}[v_\theta(r-\delta r) - v_\theta(r)]\delta r &- [v_\theta(r+\delta r) - v_\theta(r)]\delta r \\ &= -2\frac{\mathrm{d}v_\theta(r)}{\mathrm{d}r}\delta r^2 \sim \left(\frac{\Gamma}{\pi r^2}\right)\delta r^2 = \left(\frac{1}{B}\right)\delta r^2 \,. \end{aligned} \quad (5.23)$$

The bounding function decrease becomes steeper as the A/B ratio increases.

No further conclusion should be formulated from the results of this micro-mixing problem, or be generalized to multiple-scale problems. In this configuration, the mixing time is varying with time and depends on the injection time; it cannot be seen as fully equivalent to a large-scale problem such as the turbulent jet considered in this study. However, two timescales have arisen, which reflect the effects of the two phenomena involved in turbulent mixing, as evidenced by Villermaux *et al.* [Villermaux 99]: a dissipation process through which the homogeneity of the fluid increases (here, the molecular diffusion; in an LES, subgrid scale turbulent mixing as characterized by τ_{mix}), and a creation process, through which the interface between two mixing entities develops and becomes complex (the shear or vorticity stress, which among other effects brings in new fluid).

In the turbulent jet of this study, at large scales, τ_{mix} is expected to be of the same nature as A. In the PaSR detailed below, a process will play the role of engulfment, governed by an injection timescale τ_{inj}, similar to B.

These findings support the relevance of introducing $(\widetilde{\tau}_{\text{res}}, \tau_{\text{mix}})$ in the turbulent mixing history parameterization, in addition to the local mixture fraction. Since the present work addresses reactive flows, the progress of reaction must be used as a parameter too. This point of view is now explored to propose an SGS modeling strategy for non-premixed turbulent flames.

5.3 FCCT modeling

5.3.1 Modeling strategy

The mass-weighted space filtering operation is defined in Large Eddy Simulation as:

$$\widetilde{Q}(\underline{x}_0, t) = \frac{\int_{\underline{x}} \rho(\underline{x}, t) Q(\underline{x}, t) \mathcal{G}_\Delta(\underline{x} - \underline{x}_0)\mathrm{d}x}{\int_{\underline{x}} \rho(\underline{x}, t)\mathcal{G}_\Delta(\underline{x} - \underline{x}_0)\mathrm{d}x} \,,$$

where $\mathcal{G}_\Delta$ is a filter function used to damp fluctuations at lengths smaller than Δ. Assuming that Q is a unique function of the set of parameters $\underline{\phi}$, $\widetilde{Q}$ may be computed from the joint pdf $p(\underline{\phi}; \underline{x}, t)$:

$$\widetilde{Q}(\underline{x}_0, t) = \int_{\underline{\phi}} Q(\underline{\phi}) p(\underline{\phi}; \underline{x}_0, t)\mathrm{d}\underline{\phi} \,. \quad (5.24)$$

The Flow-Controlled Chemistry Tabulation approach stems from the idea that the residence time $\widetilde{\tau}_{\rm res}(\underline{x},t)$ and mixing timescale $\tau_{\rm mix}(\underline{x},t)$, introduced in Section 5.2, are relevant conditioning variables for the turbulence-chemistry interaction. They are adjoined with the set of parameters $\underline{\widetilde{\phi}} \equiv (\widetilde{Z},\widetilde{Y}_c)$ (mixture fraction and progress of reaction) describing chemistry, to form the conditioning variables $\underline{\psi} \equiv (\underline{\widetilde{\phi}};\widetilde{\tau}_{\rm res},\tau_{\rm mix})$ to express unclosed filtered quantities as:

$$\widetilde{Q} = \widetilde{Q}^{\rm FCCT}(\underline{\psi}) = \widetilde{Q}^{\rm FCCT}(\underline{\widetilde{\phi}};\widetilde{\tau}_{\rm res},\tau_{\rm mix})\,. \tag{5.25}$$

Like in all models based on a reduced parametrization of the variables, the pdf of these variables must be modeled. In presumed pdf methods the pdf is expressed commonly as a function of the first two moments of the composition, here, they are generated in preliminary Monte-Carlo computations of a Partially-Stirred Reactor.

The PaSR simulations model three processes: a mixing process (*i.e.* turbulent mixing), a reaction process (combustion chemistry) and an injection process (engulfment). The joint-$\underline{\phi}$ distributions are monitored and tabulated to form a chemical lookup table. Then, during the run, this table is accessed from the LES flow solver as a lookup table and provides the terms needed to close the filtered equations. One of the key points is to select an injection process that is representative of the flow studied, and reproduce the $(\widetilde{\tau}_{\rm res},\widetilde{Z})$ typical response discussed above. The details of this procedure, sketched in Fig. 5.1, are now presented.

5.3.2 Tabulated chemistry

As in previous simulations of the vitiated air jet-flame considered [Domingo 08], the flame composition is projected onto a two-dimensional manifold [Gicquel 00, van Oijen 01, Nguyen 10], embedding the small-scale balance between chemical reactions and molecular diffusion. The chemistry tabulation spans the whole range of equivalence ratios, from a mixture fraction $Z = 0$ (pure oxidizer) to $Z = 1$ (pure fuel); the stoichiometric mixture fraction is $Z_{\rm st} = 0.177$. A measure of the progress of reaction (or progress variable) Y_c is defined as $Y_c = Y_{\rm CO} + Y_{\rm CO_2}$. This was found to be an effective measure of reaction progress in previous simulations of this configuration presuming beta-function pdfs [Domingo 08]. For each Z value, Y_c varies monotonically from fresh, $Y_{c,0}(Z)$, to burnt gases, $Y_{c,\rm eq}(Z)$. All thermochemical quantities, *i.e.* the temperature T, the species mass fractions Y_i and their rates of change $\dot{\omega}_i$, are tabulated as functions of Z and Y_c. The progress variable has its own rate of change, $\dot{\omega}_{Y_c}$.

The chemical database is built with the detailed GRI 3.0 mechanism, with 53 species [Smith]. For mixture fractions within the range where flame front propagation can be observed ($0.055 \leq Z \leq 0.5$), a set of laminar freely propagating unstrained premixed flamelets is computed with the PREMIX software [Kee 85] and tabulated along the progress variable. Because of potential self-ignition on the lean side, resulting from mixing with vitiated air, the chemical table is prolongated on the oxidizer side by computing the time evolution of chemically homogeneous mixtures with the SENKIN software [Lutz 87]. On the rich side (*i.e.* where premixed flame propagation cannot be observed), a prolongation making use of the equilibrium re-

sponse in proportion of $Y_c/Y_{c,\mathrm{eq}}$ is used. The full table, $Q(Z, Y_c)$, is thus composed of self-igniting responses and premixed flamelets, as in [Godel 09].

It is not the objective of this work to improve that chemistry tabulation specifically, whose shortcomings and limits are well known [Nguyen 10, Bykov 07]. The focus is rather on the procedure to account for SGS effects acting on passive and reactive scalars (Z and Y_c). The method discussed below can be applied to any chemical lookup table grounded on a reduced number of reaction progress variables, or even to any scalars reacting according to a given chemical scheme.

5.3.3 A Partially-Stirred Reactor model for FCCT

Monte-Carlo simulations of a PaSR are performed to mimic the unresolved SGS events. The system is composed of N elements (particles), each of them a sample point in the composition–temperature space situated on the (Z, Y_c)-manifold. Particle k is defined by its properties $\underline{\phi}^{(k)} = (Z^{(k)}, Y_c^{(k)})$, from which all chemical properties $\rho^{(k)}, T^{(k)}, Y_i^{(k)}$ and $\dot{\omega}_{Y_c}^{(k)}$ are obtained from the chemical database. Additionally, an age property, denoted by $a^{(k)}$, is attached to each particle, measuring the time spent in the reactor since its entry; this age will be linked to the flow residence time defined above.

The ensemble average of a quantity Q is denoted by $\overline{Q} = (1/N)\sum_{k=1}^{N} Q^{(k)}$ and its Favre-averaged value:

$$\widetilde{Q} = \frac{\sum_{k=1}^{N} \rho^{(k)} Q^{(k)}}{\sum_{k=1}^{N} \rho^{(k)}} = \frac{\overline{\rho Q}}{\overline{\rho}} \,. \tag{5.26}$$

These averages are meant to be considered as filtered quantities in the LES of reactive flows and the deviation $(Q - \widetilde{Q})$ mimics SGS fluctuations. Also, the average age of the particles in the reactor may be seen as a measure of the residence time obeying Eq. (5.15):

$$\widetilde{\tau}_{\mathrm{res}} \equiv \widetilde{a} \,. \tag{5.27}$$

In the following, the notation a is used for the property of the PaSR particles, while τ_{res} is used for the LES field. This distinction is made because of the specific Z-dependent definition of the latter, see Eq. (5.15).

PaSR formulation

As outlined in Section 5.2.6, at scales in the turbulent inertial range down to the flamelet reference length-scale [Peters 09], the mixing phenomena may be seen as the conjunction of two processes that result in somewhat opposed effects: one tends to reduce the scalar variances, while the other provokes an increase of the local unmixedness, as exterior fluid enters the considered area. In a PaSR, these processes are modeled by so-called mixing and inflow/outflow processes, controlled respectively by a mixing time τ_{mix} (a notation consistent with the former section) and an engulfment time, or injection time τ_{inj}.

On the whole, the discrete PaSR is meant to reproduce the evolution of the turbulence–combustion interaction occurring in the flow, through distributions conditioned by $(\widetilde{Z}, \widetilde{Y}_c, \widetilde{\tau}_{\mathrm{res}}, \tau_{\mathrm{mix}})$. The injection timescale τ_{inj} follows an imposed law that

is designed to reproduce the macroscopic $(\widetilde{Z}, \widetilde{\tau}_{\text{res}})$ properties of the flow evidenced in Section 5.2.6. Thus, τ_{inj} and τ_{mix} are input control parameters of the lookup table construction, while $\widetilde{Z}$, $\widetilde{Y}_c$ and $\widetilde{a}$ are allowed to evolve freely during these simulations. The lookup table, organized as $\widetilde{Q} = \widetilde{Q}(\widetilde{Z}, \widetilde{Y}_c, \widetilde{a} \equiv \widetilde{\tau}_{\text{res}}, \tau_{\text{mix}})$, is progressively built, as explained below.

Unlike in a Lagrange–Euler coupling approach, the particles here are not localized in physical space but evolve in composition space only. The individual particle equations read:

$$\frac{\mathrm{d}\phi^{(k)}}{\mathrm{d}t} = \dot{\omega}_{\phi}^{(k)} + \mathcal{M}_{\phi}^{(k)} + \mathcal{I}_{\phi}^{(k)} , \tag{5.28a}$$

$$\frac{\mathrm{d}a^{(k)}}{\mathrm{d}t} = \dot{\omega}_{a}^{(k)} + \mathcal{M}_{a}^{(k)} + \mathcal{I}_{a}^{(k)} . \tag{5.28b}$$

with $\phi^{(k)} = Z^{(k)}$ or $Y_c^{(k)}$. The interaction between particles is carried by the mixing terms $(\mathcal{M}_{\phi}, \mathcal{M}_a)$, whereas the chemical $(\dot{\omega}_{\phi})$ or age increase $(\dot{\omega}_a)$ and inflow/outflow $(\mathcal{I}_{\phi}, \mathcal{I}_a)$ terms are applied to particles independently from their counterparts. The chemical term is zero for mixture fraction and $\dot{\omega}_{Y_c}(Z, Y_c)$ takes the value of the reaction progress variable chemical source of the chemical database. According to Section (5.2), the age source is $\dot{\omega}_a = 1$. Boundary conditions applied to Eqs. (5.28a) and (5.28b) are given below.

As in Ren *et al.* [Ren 04], Eqs. (5.28) are solved by a time marching scheme of time step Δt, with three fractional steps. Chemical reaction and mixing are solved as continuous processes on time intervals between two integer values of $t/\Delta t$, and a splitting scheme which ensures quadratic accuracy is used [Ren 08]. Δt is chosen small enough, in practice ten times smaller than the smallest τ_{mix} [Ren 04]. The inflow/outflow fractional step occurs at these discrete times.

PaSR micro-mixing

Any mixing model (stochastic or algebraic) could be used in the present approach. Among the numerous options available in the literature, the Euclidian Minimum Spanning Tree (EMST) mixing closure was retained because it demonstrated its precision in transported pdf simulations of jet flames [Xu 00, Cao 05, Wang 08, Merci 06, Stöllinger 10]. Mixing in the PaSR is a variance-decay process parameterized by τ_{mix}. EMST is a pairwise exchange model, local in composition space [Subramaniam 98] and well adapted to non-premixed combustion [Subramaniam 99]. Localness in the composition space ensures that particles in the flow interact with their immediate neighbors in physical space, for example do not mix across the reaction zone without burning.

A subset of the N particles is defined at any given time from their age $a^{(k)}$ by $S_{\mathcal{M}}(t) = \left\{k | h(a^{(k)}, t) > 0\right\}$; only those particles take part to the mixing process. h is a stochastic criterion function, defined in such a way that the distribution of its values is statistically steady, so that the size of the mixing subset $N_{\mathcal{M}} < N$ remains constant on average [Subramaniam 98]. Here, h prescribes a mean $N_{\mathcal{M}}$ equal to $N/2$. The Euclidian minimum spanning tree of $S_{\mathcal{M}}$, uniquely defined, is built. It

binds the $N_{\mathcal{M}}$ mixing particles in $N_{\mathcal{M}}-1$ pairs or edges $(i_{k'}, j_{k'})$, such that the sum of the distances $\sum \left|\underline{\phi}^{(i_{k'})} - \underline{\phi}^{(j_{k'})}\right|$ is minimal. Particle k properties then obey

$$\frac{\mathrm{d}\phi^{(k)}}{\mathrm{d}t} = \mathcal{M}_{\phi}^{(k)} = -\alpha \sum_{k'=1}^{N_{\mathcal{M}}-1} B_{k'} \left[\left(\phi^{(k)} - \phi^{(i_{k'})}\right)\delta_{kj_{k'}} + \left(\phi^{(k)} - \phi^{(j_{k'})}\right)\delta_{ki_{k'}}\right] , \qquad (5.29)$$

where coefficient $B_{k'}$ is an edge weight bounded by unity, lowest for the outer edges of the tree and increasing towards its center. The parameter α is determined at each time step such that the variance function of the system $v = \sum_{k=1}^{N} \left|\underline{\phi}^{(k)} - \overline{\underline{\phi}}\right|^2$ obeys the decay law, with the LES-obtained time scale τ_{mix} (Eq. (5.17)).

In Eq. (5.28b), the mixing term for the age is set to zero, because the age distribution affects neither the particles thermochemical properties, which depend only on ϕ, nor the mixing term $\mathcal{M}_{\phi}$ in Eq. (5.28a), since here the localization of the EMST model is restricted to the (Z, Y_c)-space. Notice that this absence has no impact on the average age $\overline{a}$ retrieved from the PaSR computation.

PaSR boundary conditions: inflow/outflow process

Flow engulfment is mimicked by the injection of particles into the reactor. Every injection is simultaneous to a removal, so as to keep the total number of particles constant (an 'injection' is synonymous with a 'replacement'). Boundary conditions are those of the target flow configuration: pure unburnt oxidizer, $\underline{\phi}_0 \equiv (Z = 0, Y_c = 0)$ and pure unburnt fuel, $\underline{\phi}_1 \equiv (Z = 1, Y_c = 0)$.

Without any injection or replacement, the average age in the reactor increases linearly with time by steps of Δt ($\mathrm{d}\overline{a}/\mathrm{d}t = 1$). With injection of fresh particles of age zero, the age follows the evolution equation:

$$\frac{\mathrm{d}\overline{a}}{\mathrm{d}t} = 1 - \frac{\overline{a}}{\tau_{\mathrm{inj}}} \qquad (5.30)$$

where τ_{inj} is the characteristic injection time; then, $\overline{a}(t) = \tau_{\mathrm{inj}}(1 - \exp(-t/\tau_{\mathrm{inj}}))$ with the asymptotic steady state $\overline{a} = \tau_{\mathrm{inj}}$.

In FCCT, the discrete injection process is controlled by two parameters: (i) p_{inj}, the probability that injection take place and (ii) if it does, the number N_{inj} of particles which are injected (*i.e.* replaced). The steady average age reached by the reactor contents reads[1]

$$\overline{a} = \left(\frac{N}{p_{\mathrm{inj}} N_{\mathrm{inj}}}\right) \Delta t = \tau_{\mathrm{inj}} \, . \qquad (5.31)$$

In practice, for a given τ_{inj}, the number of particles which should be injected each time step if $p_{\mathrm{inj}} = 1$ would be $N_{\mathrm{inj}}^{*} = N\Delta t/\tau_{\mathrm{inj}}$ (Eq. (5.31)). Hence, the determination of p_{inj} and N_{inj} is done as follows: if $N_{\mathrm{inj}}^{*} \geq 1$, p_{inj} is set to 1 and N_{inj} to the integer closest to N_{inj}^{*}; else, $N_{\mathrm{inj}} = 1$ and $p_{\mathrm{inj}} = N_{\mathrm{inj}}^{*}$.

In the target jet flame experiment, fast mixing with burnt gases develops from the burner exit. To mimick this effect, one stoichiometric particle at equilibrium, $\underline{\phi}_{\mathrm{ign}} \equiv$

[1] This is obtained by writing $\overline{a}(t + \Delta t)$ as a function of $\overline{a}(t)$ and searching for the limit when $t \to \infty$.

($Z = Z_{\mathrm{st}}, Y_c = Y_{c,\mathrm{eq}}(Z_{\mathrm{st}})$) is injected at each initialization. Those burnt gases are also needed to ensure burning in the reactor with chemistry tabulated from a single progress variable, since the source of Y_c on the mixing line is not large enough for self-ignition to occur. Because the reactor statistics are cumulated over many composition space trajectories, which rapidly evolve away from this initial point, this was not found to have a profound impact on the lookup table.

Reactor sequences

Reactor sequences are organized to approximate the SGS statistics. The mixing rate that is imposed to the EMST closure needs to be representative of mixing along flow trajectories; typically, the mixing increases right after injection to then decay. Thus the reactor evolution should imitate flow parcel trajectories over which the mixing time is not constant. However, to avoid introducing an additional closure, it was chosen to impose an averaged fixed mixing timescale in EMST. Because of non-linear effects in the integration of mixing and its interaction with reaction, the input value of the model must be adjusted from the LES-obtained τ_{mix}; it was found that $\tau_{\mathrm{mix\ retrieval}} = \alpha_{\mathrm{mix}}\tau_{\mathrm{mix\ LES}}$, with $\alpha_{\mathrm{mix}} = 0.5$, yields satisfactory results and their sensitivity to the α_{mix} parameter will be evaluated in Section 5.4.

The injection process must be designed in a way that enables the reactor contents to reproduce the $\widetilde{Z}$ *vs.* $\widetilde{\tau}_{\mathrm{res}}$ response, in which fuel is mixed with oxidizer, here vitiated air. The reactor sequence starts from a pure fuel condition and oxidizer is injected until it fills the reactor and has replaced all initially present fuel. When considered in composition space, this process is intended to reproduce trajectories originated from both burner inlets. A full sequence captures composition-space mixture evolution from both pure fuel and pure oxidizer, down to mixture featuring the mixture fractions encountered downstream in the simulated domain. Such a reactor sequence is similar to those proposed by Borghi in Euler–Lagrange modeling [Borghi 88]. A single sequence is only one temporal occurrence and needs to be repeated, with a variability coming from a random law in the τ_{inj} definition.

The $\widetilde{Z}$ *vs.* $\widetilde{\tau}_{\mathrm{res}}$ study (Fig. 5.6) brings the necessary information to determine τ_{inj}. The way the reactor's average mixture fraction and age evolve for the simple case of a fixed τ_{inj} value, is first examined. Over one sequence, the reactor's initial stage is set to pure fuel at age zero (coordinates $(0, 1)$ in the $(\widetilde{a}, \widetilde{Z})$ space), and the injected particles are oxidizer, at age zero too (point $(0, 0)$). They are injected as the mixture grows older and homogenizes, so that the reactor's $\overline{Z}$ evolves from 1 to 0, according to:

$$\frac{\mathrm{d}\overline{Z}}{\mathrm{d}t} = -\frac{\overline{Z}}{\tau_{\mathrm{inj}}}\,. \tag{5.32}$$

The computation is stopped when $\overline{Z}$ reaches a threshold value close to zero (10^{-3}), the reactor reset to its initial configuration and the process starts again.

As for the average age $\widetilde{a}$, which is expected to match the flow residence time $\widetilde{\tau}_{\mathrm{res}}$ (Eq. (5.27)), it repeatedly evolves from 0 to values determined by the discrete evolution of τ_{inj}. Typical evolutions of these average parameters are shown in Fig. 5.11a.

For a fixed τ_{inj}, Eqs. (5.30) and (5.32) would lead to a linear trajectory in the $(\overline{a}, \overline{Z})$ space. The trajectory of the reactor averages for this simple constant τ_{inj} case

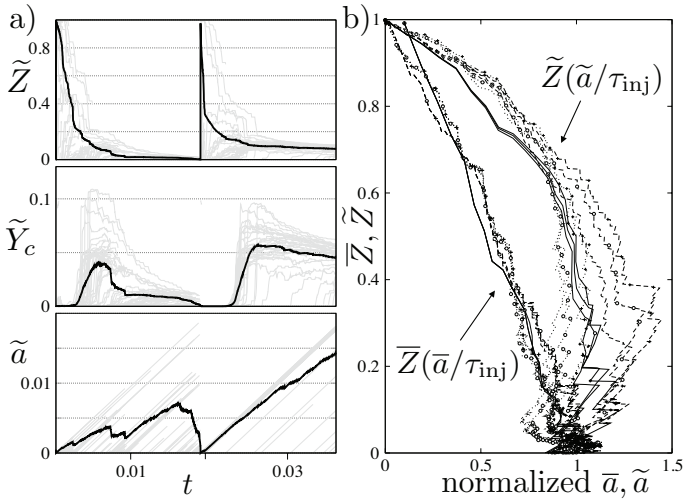

Figure 5.11: a) Time evolution of Favre-averaged reactor quantities (dark lines) and of individual particle properties (gray lines); b) Trajectory samples, in the mixture fraction–residence time space (normalized by $\tau_{\rm inj}$), of the PaSR ensemble-averaged and density-weighted properties for a constant $\tau_{\rm inj}$ case. Solid line: $\tau_{\rm inj} = 10^{-4}$ s; long dashed line: 5.0×10^{-4} s; dashed line: 2.0×10^{-3} s. No symbol: $\tau_{\rm mix} = 1.4 \times 10^{-3}$ s, +: 2.4×10^{-3} s; ○: 7.0×10^{-3} s.

is shown in Fig. 5.11b, where a linear response is indeed observed independently from the mixing timescale, which only affects the variance. The Favre averages, however, depend slighly on $\tau_{\rm mix}$ because of the non-linearity induced by the density-weighting.

It is therefore possible to fully drive the $(\overline{a}, \overline{Z})$ trajectory by determining $\tau_{\rm inj}(t)$ (engulfment time) over the reactor sequence from a stochastic process parameterized with $\widetilde{Z}$, to capture the $(\widetilde{a} = \widetilde{\tau}_{\rm res}, \widetilde{Z})$ seen in Fig. 5.6; details are given in the next paragraph. In practice, various definitions of the injection time may be envisioned, the main point being the selection of one that produces trajectories within the allowed $(\widetilde{\tau}_{\rm res}, \widetilde{Z})$ domain.

The study of Fig. 5.7 has shown that the distinctive structure of the $\widetilde{Z}$ *vs.* $\widetilde{\tau}_{\rm res}$ scatter plot is independent from the $\tau_{\rm mix}$ range. This is consistent with the result just presented (Fig. 5.11), and supports the idea that the choice of $\tau_{\rm mix}$ and $\tau_{\rm inj}$ as the PaSR's control parameters may be done independently. This results from a scale separation in the turbulent mixing process, between the large resolved scales piloting the engulfment process ($\tau_{\rm inj}$) and the molecular micro-mixing ($\tau_{\rm mix}$)[2]. Therefore, the definition of $\tau_{\rm inj}$ was determined independently from $\tau_{\rm mix}$. Several computations of the FCCT PaSR are performed, each at a different $\tau_{\rm mix}$ value.

Injection timescale $\tau_{\rm inj}$ distribution

As illustrated in Fig. 5.12 for the jet under study, the range of $\tau_{\rm inj}$ values ensuring that $\widetilde{a}$ remains below a maximum value as $\widetilde{Z}$ decreases must be narrower at high $\widetilde{Z}$ values than at lower values representative of the oxidizer stream. The limits of this

[2]The canonical micromixing configuration studied in Section 5.2.6 is a case where the scales are not separated; there the mixing and injection times are linked.

range, denoted by $[\tau_{\text{inj}}^{\text{MIN}}, \tau_{\text{inj}}^{\text{MAX}}(\widetilde{Z})]$, are defined as $\tau_{\text{inj}}^{\text{MIN}} = 10^{-4}\,\text{s}$ and

$$\tau_{\text{inj}}^{\text{MAX}}(\widetilde{Z}) = \tau_0 + \frac{1}{2}(\tau_1 - \tau_0)\left(1 + \frac{2}{\pi}\tan^{-1}\left(\frac{Z_{\text{mid}} - \widetilde{Z}}{\Delta Z}\right)\right) \tag{5.33}$$

with $\tau_0 = 3. \times 10^{-3}\,\text{s}$, $\tau_1 = 5. \times 10^{-2}\,\text{s}$, $Z_{\text{mid}} = 0.5$ and $\Delta Z = 10^{-3}$.

To ensure sufficiently high fluctuations of the reactor behavior, the random update of the injection timescale τ_{inj} is done every $\lfloor \tau_{\text{mix}}/\Delta t \rfloor$ time steps, a choice which links this law update frequency with the turbulence level in the reactor.

The injection timescale $\tau_{\text{inj}}(t)$ may be randomly drawn on $[\tau_{\text{inj}}^{\text{MIN}}, \tau_{\text{inj}}^{\text{MAX}}(\widetilde{Z})]$ from either a uniform law or an inverse uniform law, the latter yielding smaller τ_{inj} values than the former, a useful property to correlate the law with the fluid engulfment and related mixture fraction behavior. Indeed, very low mixture fraction are found in the zones where the coflow fluid just entered the mixing area, therefore where the age (or residence time) is still small. Overall in the reactor, small injection times produce average ages tending towards low values (see above analysis). This is why as $\widetilde{Z}$ approaches zero, τ_{inj} must be preferably low to favor small average ages and the inverse uniform law, yielding smaller τ_{inj}, must be favored. As a consequence, the choice between uniform and inverse uniform laws was made as follows: if $\widetilde{Z} \leq 0.2$ the inverse uniform law is chosen with probability $1 - \min(\widetilde{Z}/0.2, \alpha_u)$ and the uniform law with probability $\min(\widetilde{Z}/0.2, \alpha_u)$. If $\widetilde{Z} > 0.2$, the uniform (resp. the inverse uniform) law is chosen with probability α_u (resp. $1 - \alpha_u$). The stochastic parameter α_u is fixed at the start of each reactor sequence, and taken alternatively equal to 0.1 and to 1.

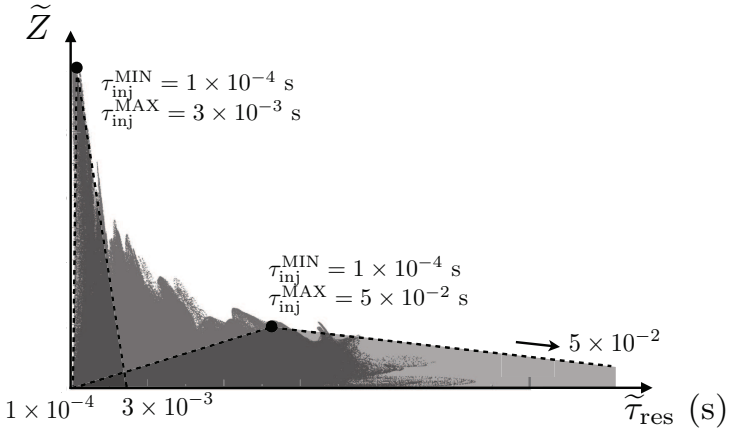

Figure 5.12: Illustration of the determination of the injection timescale variation range as a function of $\widetilde{Z}$.

5.3.4 Lookup table control parameters

For a given mixing timescale τ_{mix}, an FCCT reactor is set up as defined above, and allowed to evolve freely: average values $\widetilde{Z}$, $\widetilde{Y}_c$ and $\widetilde{a}$ are not restricted by any specific constraint. The system output, density-weighted averages of reaction and energy

source terms, temperature and mass fractions, is built along the computation as a function of $\widetilde{Z}$, $\widetilde{Y}_c$ and $\widetilde{a}$, by an approach of accumulation over time. Formally, if the system composition and age temporal development is denoted by $\underline{\widetilde{\phi}}(t), \widetilde{a}(t)$, the output quantities computed on a time interval $[t_0; t_f]$ are defined as

$$\widetilde{Q}(\underline{\widetilde{\phi}}^{\star}, \widetilde{a}^{\star}) = \frac{\displaystyle\int_{t_0}^{t_f} \delta\left(\underline{\widetilde{\phi}}(t) - \underline{\widetilde{\phi}}^{\star}\right) \delta\left(\widetilde{a}(t) - \widetilde{a}^{\star}\right) \overline{\rho Q}(t)\, \mathrm{d}t}{\displaystyle\int_{t_0}^{t_f} \delta\left(\underline{\widetilde{\phi}}(t) - \underline{\widetilde{\phi}}^{\star}\right) \delta\left(\widetilde{a}(t) - \widetilde{a}^{\star}\right) \overline{\rho}(t) \mathrm{d}t}\,, \tag{5.34}$$

where δ is the Dirac function in the composition or age space. It localizes the time integral around the target $(\underline{\widetilde{\phi}}^{\star}, \widetilde{a}^{\star})$, meaning that only the system states at times when the Favre averages $(\widetilde{Z}, \widetilde{Y}_c, \widetilde{a})$ are equal to it contribute to the output average. The relation (5.34) is assumed to correctly define the average result of all τ_{mix}-controlled histories leading to the target point $(\widetilde{Z}^*, \widetilde{Y}_c^*, \widetilde{a}^*)$. The randomness of the system, lying in the injection law and in the intermittency treatment by the EMST model, leads several histories to reach this target point.

In practice, Eq. (5.34) is solved in a discrete and approximate fashion, in two steps. The $(\widetilde{Z}, \widetilde{Y}_c, \widetilde{a})$ space is partitioned into $M_Z \times M_{Y_c} \times M_a$ cells, denoted by the indices (p, q, r): $[\widetilde{Z}_{p-1}; \widetilde{Z}_p] \times [\widetilde{Y}_{c,q-1}; \widetilde{Y}_{c,q}] \times [\widetilde{\tau}_{\text{res},r-1}, \widetilde{\tau}_{\text{res},r}]$. At each timestep, the state of the system is collected and made to contribute to the values of the appropriate table cell. If at a given time the system's $\widetilde{Z}, \widetilde{Y}_c$ and $\widetilde{a}$ fall into cell (p, q, r), the table's average quantity is updated with the current system value

$$\left(\overline{\rho Q}\right)_{p,q,r} \leftarrow \left(n_{p,q,r} \left(\overline{\rho Q}\right)_{p,q,r} + \overline{\rho Q}\right) / (n_{p,q,r} + 1)\,, \tag{5.35}$$

where $n_{p,q,r}$ is the number of times the cell has been reached and updated before. This approach is schematized in Fig. 5.13. The procedure is also carried out for $\overline{\rho}$ alone and for $\overline{\rho Z}$, $\overline{\rho Y}_c$ and $\overline{\rho a}$ themselves. The Favre-averaged quantities are eventually computed as $\widetilde{Q}_{p,q,r} = \left(\overline{\rho Q}\right)_{p,q,r} / \overline{\rho}_{p,q,r}$. Similarly, $\underline{\widetilde{\phi}}_{p,q,r} = (\widetilde{Z}_{p,q,r}, \widetilde{Y}_{c,q,r})$ and $\widetilde{a}_{p,q,r}$ are output; they are within the range of values defined by one cell, but they do not necessarily match the exact value of the center of cell (p, q, r), hence a filtering operation is needed.

A smoothing filter is applied on these $\widetilde{Q}_{p,q,r}$ values, to yield, in any target point $\underline{\widetilde{\phi}}^{\star}, \widetilde{a}^{\star}$,

$$\widetilde{Q}(\underline{\widetilde{\phi}}^{\star}, \widetilde{a}^{\star}) = \frac{1}{w_{\text{sum}}(\underline{\widetilde{\phi}}^{\star}, \widetilde{a}^{\star})} \sum_{p,q,r} n_{p,q,r}\, G_{\underline{\phi}}\left(\underline{\widetilde{\phi}}_{p,q,r} - \underline{\widetilde{\phi}}^{\star}\right) G_a(\widetilde{a}_{p,q,r} - \widetilde{a}^{\star})\, \widetilde{Q}_{p,q,r}\,, \tag{5.36}$$

where the G functions are Gaussian filters in the composition and age spaces, and

$$w_{\text{sum}}(\underline{\widetilde{\phi}}^{\star}, \widetilde{a}^{\star}) = \sum_{p,q,r} n_{p,q,r}\, G_{\underline{\phi}}\left(\underline{\widetilde{\phi}}_{p,q,r} - \underline{\widetilde{\phi}}^{\star}\right) G_a(\widetilde{a}_{p,q,r} - \widetilde{a}^{\star}) \tag{5.37}$$

is a normalizing factor also useful to control the quality of the lookup table, typically $w_{\text{sum}}(\underline{\widetilde{\phi}}, \widetilde{a}) \geq 100$ to ensure that enough events have contributed to the averages. This quantity is stored and it is checked during LES that points accessed in the table satisfy this criterion.

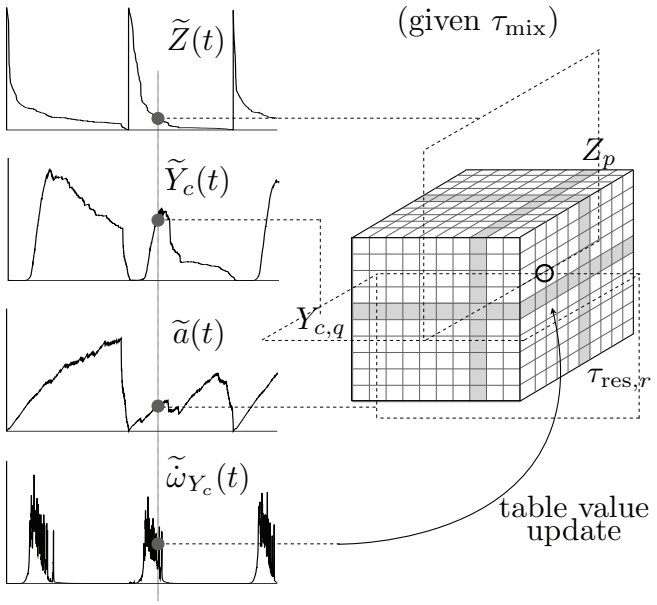

Figure 5.13: Schematic diagram illustrating the lookup table construction procedure (see Eq. (5.35)).

The final output is thus comprised of a set of Favre-averaged quantities on points $(\widetilde{Z}, \widetilde{Y}_c, \widetilde{a})$ of a grid covering the composition and age (residence time) space. A mesh size refined in the regions where high gradients of the output are expected and where the reactor average properties have a high probability of presence, and a filter size equal to the mesh size, have been found to be appropriate.

This approach amounts to a Monte-Carlo integration, and its error therefore decreases slowly, as $n^{-1/2}$ with n the number of time steps. A favorable factor for the computational cost is that a relatively small number of particles is sufficient, because of the accumulation over time of the reactor's response (thus mimicking an overall large number of particles). In the present case, $N = 100$ is convenient; instantaneous distributions carry a satisfactory level of accuracy, and the computation is fast enough to be run over a large number of iterations. The whole procedure is performed on a set of τ_{mix} values, so that the final table is a four-dimensional array of chemical quantities:

$$\widetilde{Q} = \widetilde{Q}(\widetilde{Z}, \widetilde{Y}_c, \widetilde{\tau}_{\mathrm{res}}, \tau_{\mathrm{mix}}) \, . \tag{5.38}$$

It can then be used with multilinear interpolation to evaluate the desired quantities at any value of the four parameters.

5.3.5 Analysis of the FCCT lookup table

The output of the FCCT computation is analyzed in the context of the Cabra experiment [Cabra 05] introduced above. The $\widetilde{Z}$ discretization is refined on the lean and stoichiometric regions; the $\widetilde{Y}_c$ space is normalized at each value of the mixture fraction by $Y_{c,\mathrm{eq}}(Z)$, and refined near the cold mixture line and close to equilibrium. Given the $(\widetilde{\tau}_{\mathrm{res}}, \widetilde{Z})$ structure, which is paramount to the design of the FCCT dynamics, the residence time direction is uniformly discretized conditionally to the mixture

fraction, into 16 points on intervals $[0; \widetilde{\tau}_{\rm res}^{\rm max}(\widetilde{Z})]$. The upper boundary is designed so as to enclose the possible variations of $\widetilde{\tau}_{\rm res}$:

$$\widetilde{\tau}_{\rm res}^{\rm max}(\widetilde{Z}) = \tau_0 + 0.5(\tau_1 - \tau_0)\{1 + \tanh[(\widetilde{Z} - Z_{\rm mid})/\Delta Z]\} \,, \tag{5.39}$$

with $Z_{\rm mid} = 0.35$ and $\Delta Z = 0.1$, evolving smoothly and monotonically from the small value $\tau_1 = 2.5 \times 10^{-3}\,$s in $\widetilde{Z} = 1$ to $\tau_0 = 3.0 \times 10^{-2}\,$s, as the average mixture fraction decreases towards zero. A view of the resulting $(\widetilde{\tau}_{\rm res}, \widetilde{Z})$-grid is shown in Fig. 5.14. As for the mixing timescale dimension, it is discretized into 16 values ranging from $\tau_{\rm mix} = 3.0 \times 10^{-4}\,$s to $\tau_{\rm mix} = 1.6 \times 10^{-2}\,$s.

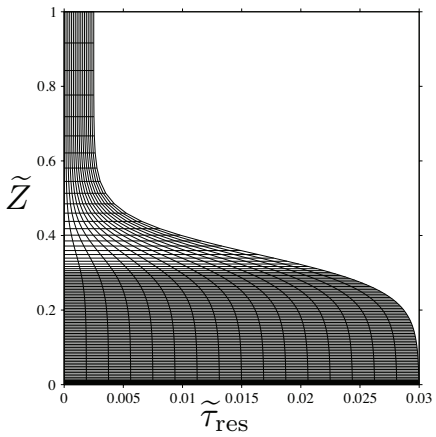

Figure 5.14: Representative FCCT mesh of the residence time – mixture fraction space.

The timestep Δt is set to $10^{-5}\,$s, small enough for the explored range of controlling timescales. The lookup table building is carried out over 3.0×10^7 time steps for each of the $\tau_{\rm mix}$ values.

Output distributions

A distinctive strength of the FCCT tabulation method lies in the spontaneous generation of the composition distributions. Correlations between parameters naturally appear according to the reacting flow properties. As an example, a fine-grained view of the joint (Z, Y_c)-distribution obtained for representative Favre averages $\widetilde{Z} = Z_{\rm st} = 0.177$ (stoichiometric condition) and $\widetilde{Y}_c = 0.5\, Y_{c,{\rm eq}}(Z_{\rm st})$ and the input mixing timescale $\tau_{\rm mix} = 2.5 \times 10^{-3}\,$s and residence timescale $\tau_{\rm res} = 3.0 \times 10^{-3}\,$s, is plotted in Figure 5.15. For this distribution, the unmixednesses–normalized SGS scalar variances, see Eq. (4.29)–are respectively 0.34 and 0.65 for the mixture fraction and the reaction progress variable. It is compared with a distribution which, for the same first and second statistical moments, would be assumed in a presumed pdf approach as equal to the product of two uncorrelated beta-functions. This comparison highlights the clear dependence of the progress of reaction conditional pdf on Z, already discussed for this flame in [Michel 08]; the particles of mixture fraction smaller than 0.3 are all close to the equilibrium, while the richer ones are unburnt. In most presumed pdf approaches, the Z and $Y_c/Y_{c,{\rm eq}}(Z)$ distributions would be assumed to be independent and the SGS correlation between parameters might not be fully reproduced.

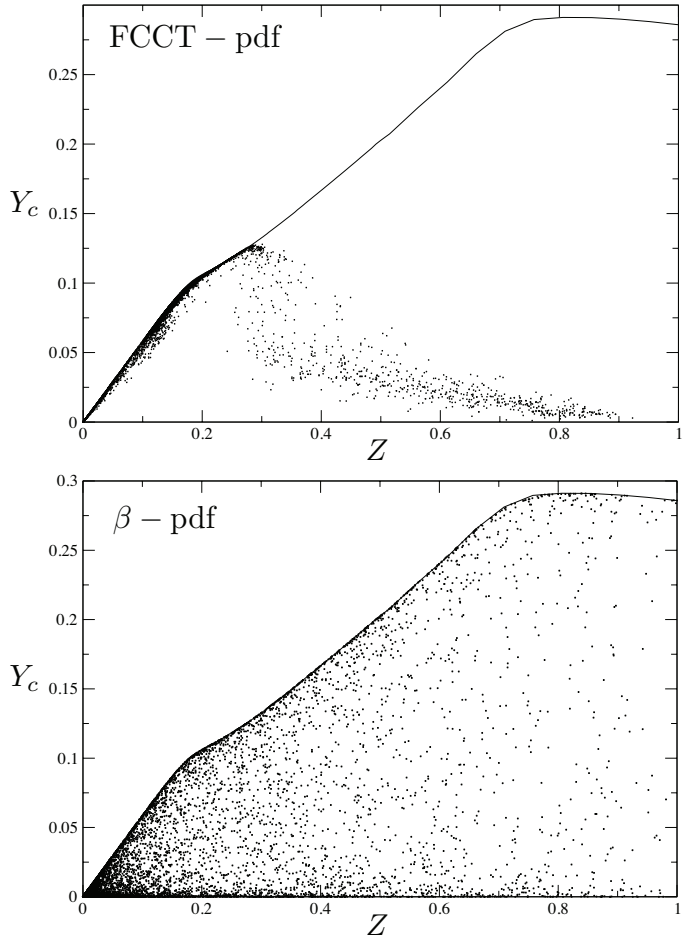

Figure 5.15: Fine-grained visualizations of a joint (Z, Y_c)-distribution as obtained from FCCT, or a product of beta-pdf. Solid line: Y_c at equilibrium.

Average behavior

Following the same principle as what was carried out in Section 5.2.6 from the LES fields, scatter plots of the density-weighted mixture fraction $\widetilde{Z}$, but also progress of reaction $\widetilde{Y}_c$, *vs.* the filtered residence time $\widetilde{\tau}_{\text{res}}$, are sampled along their evolution in the FCCT reactors and shown in Fig. 5.16. The injection (engulfment) process was defined to make the FCCT behavior match that observed in the LES run (see Section 5.3.3), as is shown by the comparison of the scatter plots with the hull then found, which collapse onto each other. These scatters are plotted for several values of τ_{mix}. The mixture fraction plots depend slightly on the mixing timescale: the stronger curvature of the trajectories for larger τ_{mix} may be discerned, as was shown in Fig. 5.11b.

The analysis of the FCCT table allows for illustrating the importance of the interaction resulting from the engulfment and the mixing time scales. Specifically, in addition to the so-called S-curve [Wang 08] response that is representative of a canonical burning diffusive and reactive layer (a decrease of the mixing time is followed by an increase of the burning rate up to quenching occurring because chemistry cannot keep up with fast diffusion), complementary but not antagonistic behaviors are found, which are also observed in real combustion systems.[3]

The $\widetilde{Y}_c$ *vs.* $\widetilde{\tau}_{\text{res}}$ plots possess a specific structure, which illustrates this intricate interaction. The mixing timescales considered here are mostly larger than the chemical timescales, so that mixing imposes its dynamics to the reaction, a situation representative of most combustion systems, except those where very slow combustion is sought. The filtered Y_c are bounded by a maximum value, equal to 0 at the inlet and increasing with the residence time. The steepness of this upper boundary decreases distinctly as τ_{mix} is increased. A higher τ_{mix} imposes a smaller mixing rate, which leads to the slowed average reaction process. This overall decrease of the progress of reaction is also visible in Fig. 5.17, where the time average of the reactor's $\widetilde{Y}_c$ is plotted conditionally to $\widetilde{Z}$. It appears that around stoichiometry, increasing the mixing timescale leads to a mixture burning first more easily, up to a maximum, and then quenching (for a given $\widetilde{Z}$, the conditional mean of $\widetilde{Y}_c$ increases then decreases). When τ_{mix} becomes very large compared to the injection timescale, fuel and oxidizer remain fully segregated over a PaSR sequence and intense burning is indeed not possible.

Output quantities

The influence of $\widetilde{\tau}_{\text{res}}$ and τ_{mix} as parameters to the modeled subgrid scale composition distributions is examined here.

The well-known role of micro-mixing as an enhancer or inhibitor of the reaction may be seen in Fig. 5.18, where the output chemical source term $\widetilde{\dot{\omega}}_{Y_c}$ conditioned to stoichiometric conditions $\widetilde{Z} = Z_{\text{st}}$ has been time-averaged, and plotted as a function of the mixing and residence timescales. For any given τ_{mix}, the reaction rate, seen

[3]Notice, however, that the ignition sequence of the single-progress variable FCCT reactor (flamelet tabulated chemistry) may not capture all the chemical details pertaining to ignition of a turbulent fuel/vitiated-air mixture. The direct integration of the detailed chemical scheme would be necessary for refined description.

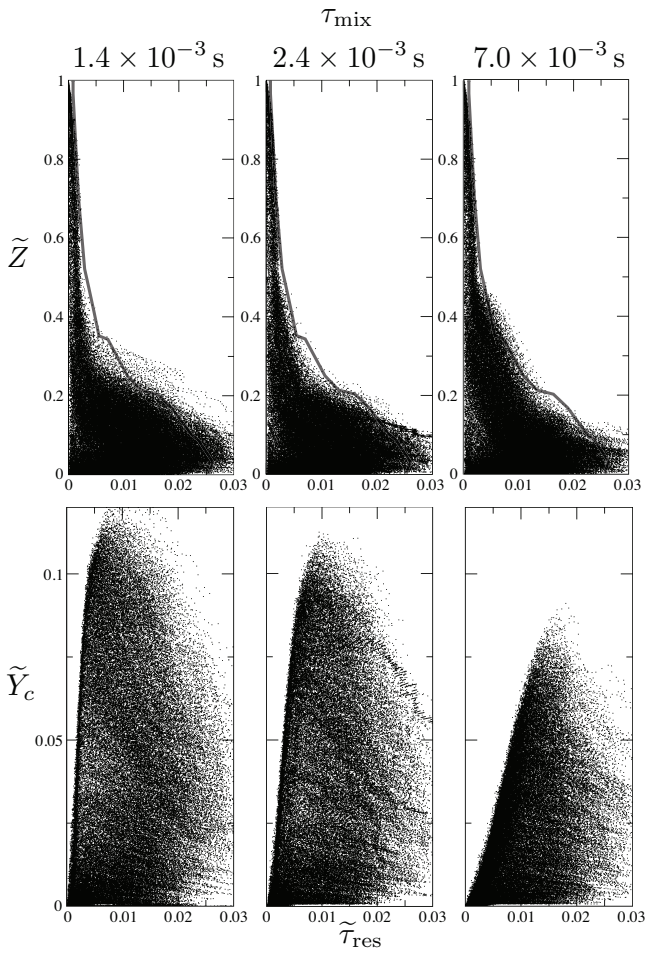

Figure 5.16: Scatter plots of $\widetilde{Z}$ and $\widetilde{Y}_c$ *vs.* $\widetilde{\tau}_{\mathrm{res}}$ sampled along their evolution in the FCCT reactors, for different mixing timescales. The cold LES hull obtained in Fig. 5.6 is shown in gray (top).

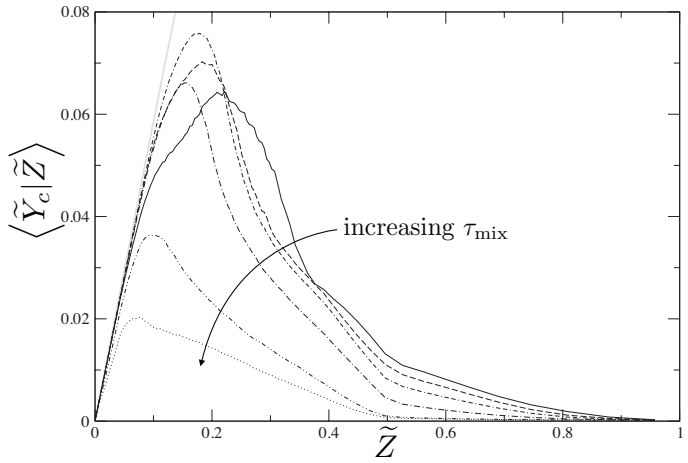

Figure 5.17: Time average of the density-weighted mean progress variable in the FCCT reactor, conditioned by the average mixture fraction. The increasing mixing timescale values are $8.0 \times 10^{-4}, 1.4 \times 10^{-3}, 2.0 \times 10^{-3}, 3.4 \times 10^{-3}, 9. \times 10^{-3}$ and 1.6×10^{-2}s. Gray line: equilibrium.

as a function of the residence time, increases then decreases, as may be expected for the evolution in time of a stoichiometric mixture. This process is much quicker at low τ_{mix} values than at large ones. A high mixing intensity prompts a tall and narrow chemical source term peak; conversely, the reaction proceeds at a slower pace and with lower intensity, in the case of a large mixing timescale.

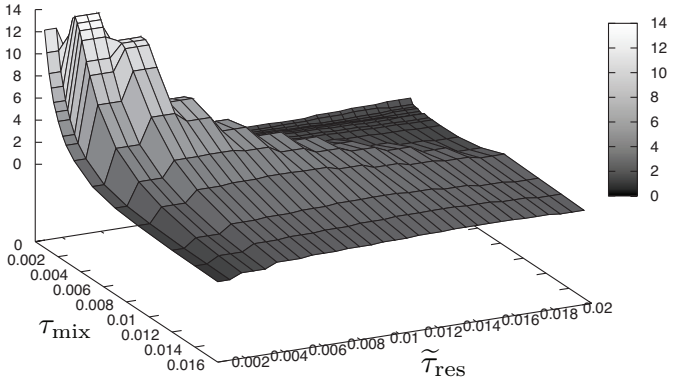

Figure 5.18: Time-averaged output chemical source term $\widetilde{\dot{\omega}}_{Y_c}$ conditioned at stoichiometry, plotted as a function of τ_{mix} and $\widetilde{\tau}_{\text{res}}$.

The FCCT tabulation technique makes the mixture fraction and progress variable variances $v_\phi = \widetilde{\phi^2} - \widetilde{\phi}\widetilde{\phi}$ an output of the system. The study of these variables (or their normalized counterparts, S_Z and S_c) provides much insight on the role of the timescales on the output distributions. These segregations are plotted in Fig. 5.19 as a function of $\widetilde{Z}$, for fixed values of the normalized progress variable and mixing time, and at different residence times. S_Z decreases, at a fixed $\widetilde{Z}$, as the residence time $\widetilde{\tau}_{\text{res}}$ increases (dotted to solid lines), a logical consequence of the variance-decreasing mixing process on a passive scalar. A different behavior characterizes S_c: as $\widetilde{Z}$ goes from 1 to 0, the c segregation peaks; this illustrates the competition of the reaction process, which sees the individual $Y_c^{(k)}$ values increase, against the mixing which tends to homogenize the mixture, helping unburnt particles to reach reactive conditions and pulling burnt particles down towards the average $\widetilde{Y}_c$. The c segregation is maximum in the stoichiometric zone, close to $Z_{\text{st}} = 0.177$. This maximum increases as the residence time increases, reflecting the fact that between two distributions of particles having reached the same $\widetilde{Z}$ and $\widetilde{Y}_c$ averages, the younger one has had a much stronger rate of injection history than the older one, therefore lower variances. Seen from the other point of view, the state of the older distribution could only be reached thanks to a weaker injection-rate history, which allowed more particles to reach their equilibrium state without being replaced – segregations are higher. On these two plots, it may be seen that data is available only for $\widetilde{Z}$ such that $\widetilde{\tau}_{\text{res}} \leq a_{\max}(\widetilde{Z})$.

The mixture fraction segregation is also plotted for fixed average mixture fraction and progress variable in Fig. 5.20, this time as a function of the residence time and for different mixing timescales. While the $\widetilde{Y}_c$-conditioning makes it difficult to really discriminate the role of τ_{mix}, it may still be perceived that the segregations' decrease rate becomes smaller as τ_{mix} take higher values.

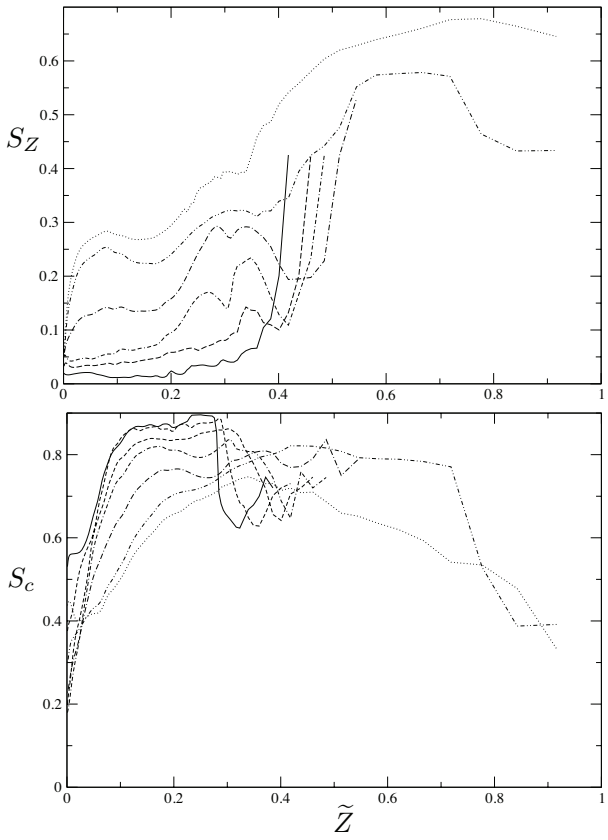

Figure 5.19: Segregations of the mixture fraction and normalized progress variable in the FCCT output distributions as a function of $\widetilde{Z}$, at $\widetilde{Y}_c = 0.5\,Y_{c,\mathrm{eq}}(\widetilde{Z})$ and for residence times ranging from 0.001 (dotted line) to 0.01 s (solid line). The mixing timescale is set to 2.4×10^{-3} s.

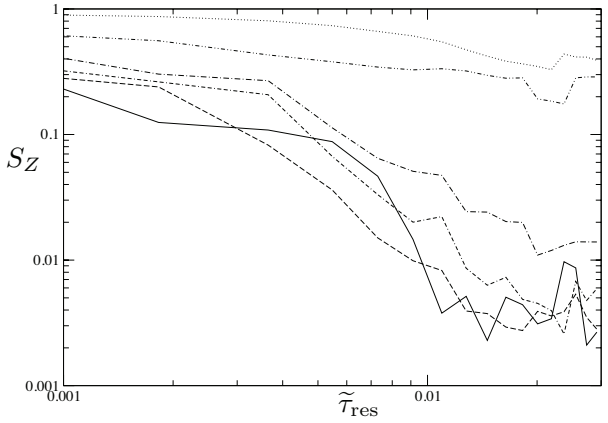

Figure 5.20: Segregations of the mixture fraction in the FCCT output distributions as a function of $\widetilde{\tau}_{\mathrm{res}}$, at $\widetilde{Z} = 0.175$ and $\widetilde{Y}_c = 0.5\,Y_{c,\mathrm{eq}}(\widetilde{Z})$ and for mixing timescales ranging from 0.001 (solid line) to 0.016 s (dotted line).

Finally, filtered chemical quantities which are to be used in the LES, namely the filtered energy source term and mass fractions, are plotted in Fig. 5.21 as functions of the normalized progress variable, for different mixture fractions, and at different residence and mixing times. They are confronted with the quality criterion w_{sum} defined in Eq. (5.37). It is confirmed that values of w_{sum} above 100 indicate smooth and consistent output fields. Where w_{sum} takes lower values, some of the output fields become irregular. They even become strongly spotty, sometimes outright irrelevant if w_{sum} becomes really small. Apart from these cases, it is confirmed that a higher mixing timescale leads to decreased source terms, and that they evolve along the residence time, as increasing then decreasing functions. The behavior of main species, such as CH_4, is not much modified by the timescales; on the contrary, intermediate species see their properties vary along those of the reaction intensity: where the reactions rates are decreased, the production of such species, as *e.g.* OH, is reduced.

5.4 Jet flame LES using FCCT

Large Eddy Simulation of the vitiated-air jet flame [Cabra 05] is now performed, the simulation follows the procedure reported in [Domingo 08], in which the flamelet presumed pdf lookup table has been replaced by the FCCT one. Along with the Navier-Stokes equations in their fully compressible form, Eqs. (5.15) and (5.16) are solved for $\widetilde{\tau}_{\text{res}}$ and $\widetilde{\Theta}$, and relation (5.17) provides τ_{mix}. A usual convection-diffusion equation is solved for the mixture fraction $\widetilde{Z}$; in the Eulerian balance equation for the progress of reaction $\widetilde{Y}_c$, an additional chemical source $\widetilde{\dot{\omega}}_{Y_c} = \widetilde{\dot{\omega}}_{Y_c}(\widetilde{Z}, \widetilde{Y}_c, \widetilde{\tau}_{\text{res}}, \tau_{\text{mix}})$ appears that is read in the lookup table. The thermochemical properties of the flow are also retrieved from the table to ensure energy coupling. The selected numerics and turbulence SGS modeling have been reported above in Section 5.2.4; the 1,900,000-cell mesh is used. The value $\alpha_{\text{mix}} = 0.5$ (Section 5.3.3) is chosen before studying the sensitivity of the results to this parameter.

In the experimental set-up, when starting the burner, autoignition occurs at a position far downstream, then combustion moves upstream and stabilizes between 40 and 50 jet diameters D from the inlet [Cabra 04]. The very first spontaneous self-ignition point is beyond the range of the computation domain. Because of this, and since the initial transient is not the topic of interest here, the initialization of the flame is done, starting from the cold run, by artificially filling a small number of cells with gases at chemical equilibrium ($\widetilde{Y}_c = Y_{c,\text{eq}}(\widetilde{Z})$) on the axis. It has been checked that the distance at which this artificial ignition point is positioned does not impact how and where the flame stabilizes and later keeps a steady position in mean. Figure 5.22 shows that combustion indeed starts in a zone located between 40 and 50 diameters downstream of injection, conform to the experiment.

5.4.1 Comparison with experimental results

To obtain the statistics of the LES computation and compare them with the experimental means, the fields are collected every 100 iterations (or about 2.5×10^{-5} s) and averaged over a 60,000-iteration period, which amounts to about 3.6 τ_{box}, where

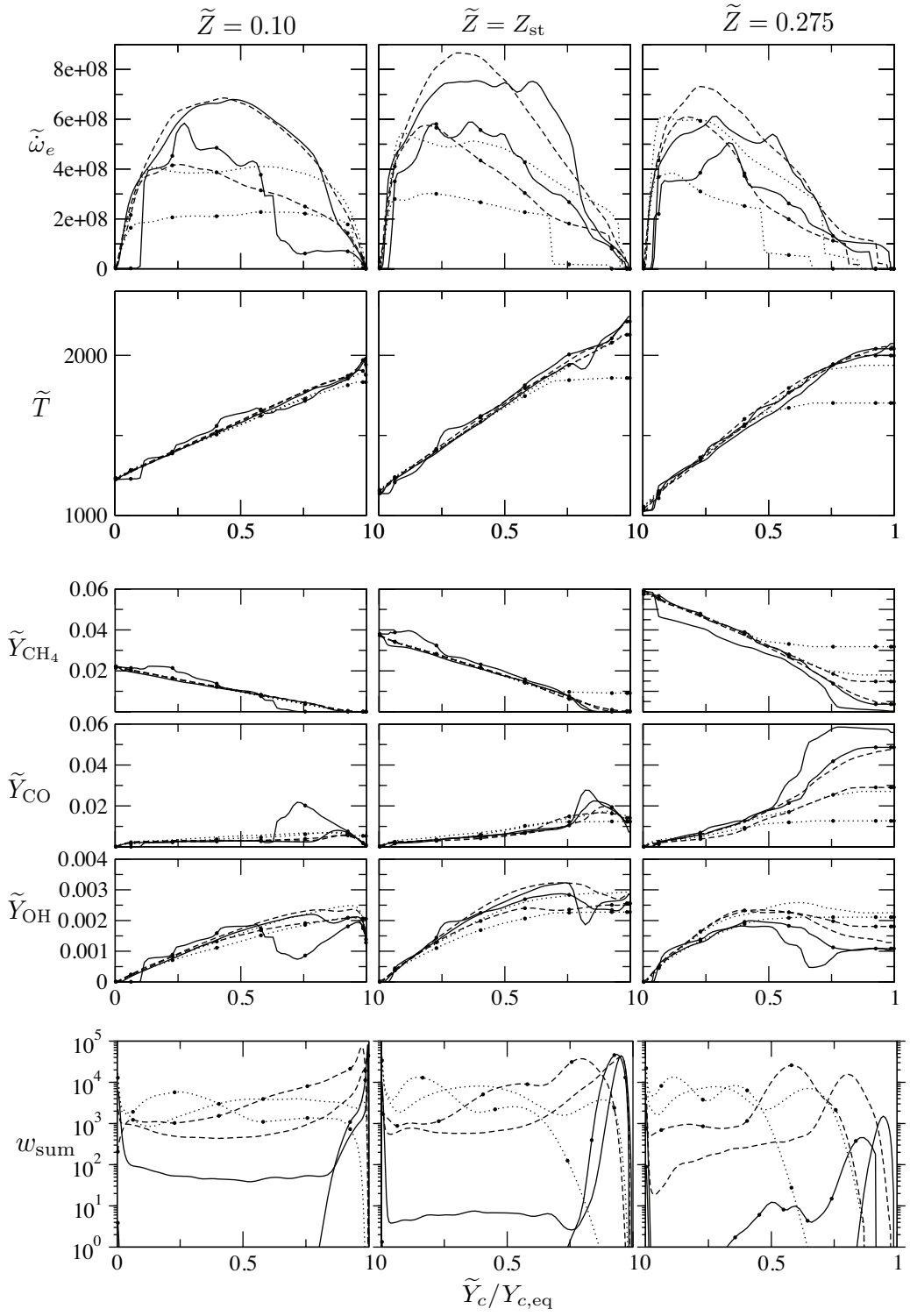

Figure 5.21: Filtered energy source term, temperature and mass fractions output from the FCCT computation, along with $w_{\rm sum}$, as a function of the normalized progress variable and for different mixture fractions. Lines with no symbol: $\tau_{\rm mix} = 1.4 \times 10^{-3}\,{\rm s}$; black circles: $\tau_{\rm mix} = 2.4 \times 10^{-3}\,{\rm s}$. Dotted lines: $\widetilde{\tau}_{\rm res} = 0.002\,{\rm s}$; dashed lines: $\widetilde{\tau}_{\rm res} = 0.005\,{\rm s}$; solid lines: $\widetilde{\tau}_{\rm res} = 0.01\,{\rm s}$.

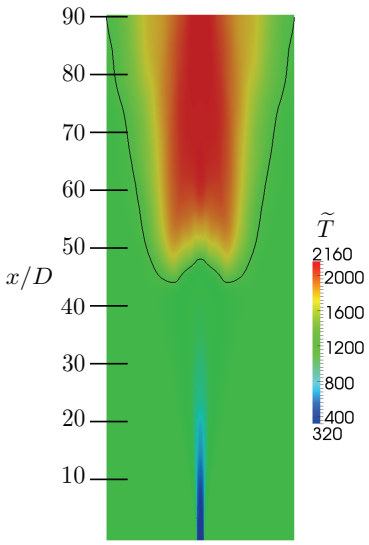

Figure 5.22: 2D view of the averaged temperature field. Line: 1,400 K isoline.

the box time is defined as $\tau_{\text{box}} = 90\,D/u_{\text{jet}}$, with u_{jet} the bulk fuel-jet velocity. This time-averaging duration was found to yield sufficiently converged statistics. In these results, all time-averaged radial profiles have additionally been space-averaged in the azimuthal direction, given the cylindrical symmetry of the flow.

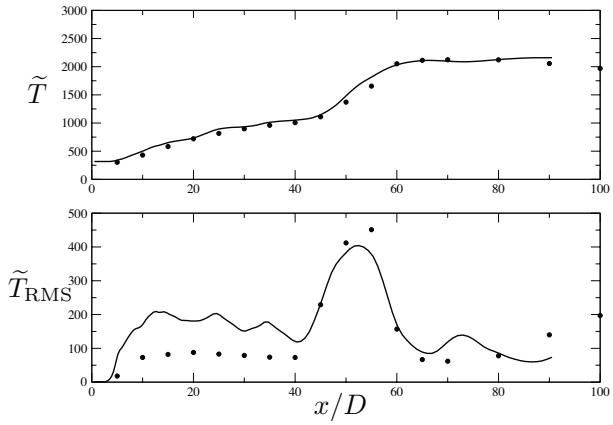

Figure 5.23: Centerline profiles of temperature and temperature fluctuations. Symbols: measurements; lines: LES.

In an initial zone extending down to about 40 D, the temperature follows a mixing trend, from the 320 K jet towards the vitiated coflow temperature of 1,350 K. After reaching the axial position of 40 diameters, the temperature then sees an increase over about 20 jet diameters, up to around 2,200 K, an indicator of the presence of the flame, which is reproduced by the LES (Fig. 5.23). The position of this flame base fluctuates in time, subject to the mixture fraction, residence time and mixing timescale variations. This may be seen on the computed temperature fluctuations whose sharp increase is located where the experimental results position it. Downstream, in the burnt gas at chemical near-equilibrium, the time-averaged temperature conforms to the experimental measurements, remaining constant around 2,200 K. As

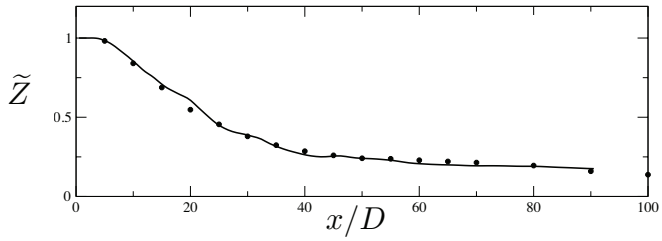

Figure 5.24: Centerline profile of the average mixture fraction. Symbols: measurements; lines: LES.

could be expected from the temperature profiles, which strongly depend on the FCCT lookup table parameters, the mixture fraction decay on the jet axis agrees with measurements (Fig. 5.24).

The radial profiles of $\widetilde{Z}$ and $\widetilde{T}$ at several downstream positions, starting at the flame base ($x = 40\,D$), are given in Fig. 5.25. The mixture fraction profiles show some slight over-prediction of the jet spreading, a consequence of which may be seen on the centerline with the slight underestimation of $\widetilde{Z}$ far from the inlet (Fig. 5.23). Correspondingly, the temperature radial spread exceeds the experimental observations. In the experiment, the flame front reaches more upstream positions slightly away from the axis: at $x = 40\,D, r = 20\,\mathrm{mm}$, the temperature has already started to increase, while on the centerline the mixture is still inert; the LES does predict this bell-shaped flame front.

The radial profiles of the temperature fluctuations are shown in Fig. 5.26. It may be observed that if $\widetilde{T}_{\mathrm{RMS}}$ seems to be over-predicted far downstream on the centerline, its radial profiles in the flame (in particular at $x = 70\,D$) are yet mostly consistent with the experimental findings.

The computational results in terms of the species mass fractions are displayed in Fig. 5.27. The major species' behaviors are closely reproduced in the mixing and flame front regions. In the burnt gas zone, the LES predicts a mixture slightly too lean, with a direct influence on the species mass fractions: non-zero O_2 concentrations and CO_2 levels lower than the experimental results. As far as the minor species are concerned, the behavior in the time-averaged flame front is well captured for H_2, CO, though the peak values are under-predicted. The computed OH increase is too steep compared with the experiment. Farther downstream, the levels of H_2 and CO do not decrease as fast as the measurements. This may owe to the fact that pockets of unburnt gases intermittently manage to go across the flame front and reach positions beyond $x = 60\,D$, burning farther downstream than where the reaction on average takes place. The levels of intermediate species thus remain high.

Overall, comparisons with measurements confirm the prediction capabilities of the proposed SGS modeling. A study of the chemical source term $\widetilde{\dot{\omega}}_{Y_c}$ in the LES computation illustrates how the FCCT formulation accounts for the enhancing role of mixing on the reaction. In Fig. 5.28, a snapshot of the mixture fraction iso-surface at $\widetilde{Z} = Z_{\mathrm{st}}$ is shown at an arbitrary time instant, and colored in several views with different quantities. Displayed on it is the progress variable iso-line $\widetilde{Y}_c = 0.25\,Y_{c,\mathrm{eq}}(Z_{\mathrm{st}})$. The mixing time τ_{mix} is shown (view a), and confronted with iso-surfaces of the Q-criterion, where $Q = 0.5(\widetilde{\Omega}_{ij}\widetilde{\Omega}_{ij} - \widetilde{S}_{ij}\widetilde{S}_{ij})$, $\underline{\underline{\Omega}}$ and $\underline{\underline{S}}$ denoting respectively the

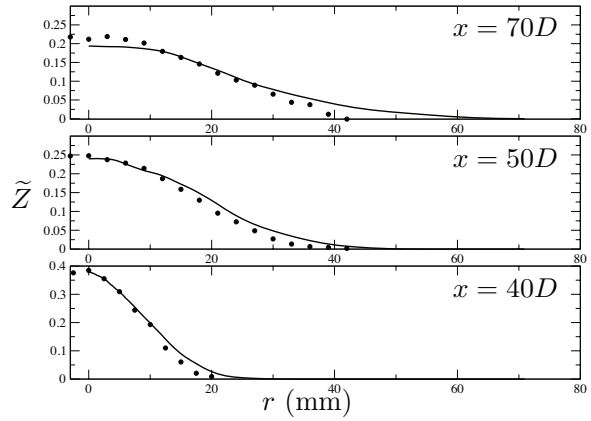

(a) Mixture fraction

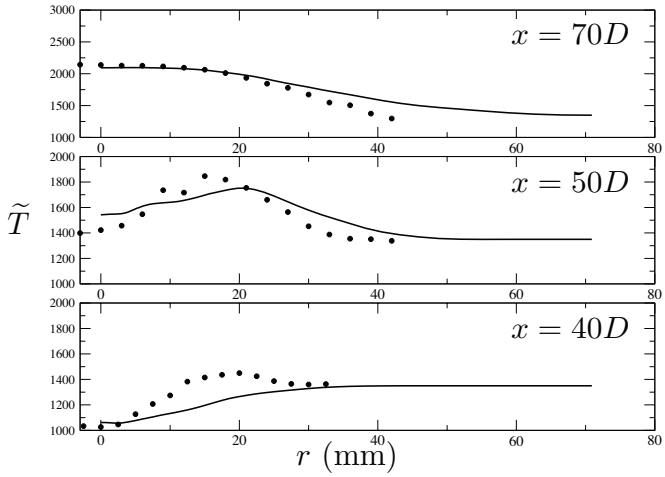

(b) Temperature

Figure 5.25: Radial profiles of the average mixture fraction and temperature at successive downstream positions. Symbols: measurements; lines: LES.

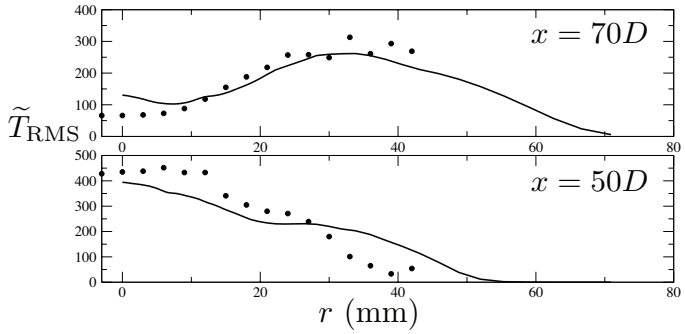

Figure 5.26: Radial profiles of the temperature fluctuations. Symbols: measurements; lines: LES.

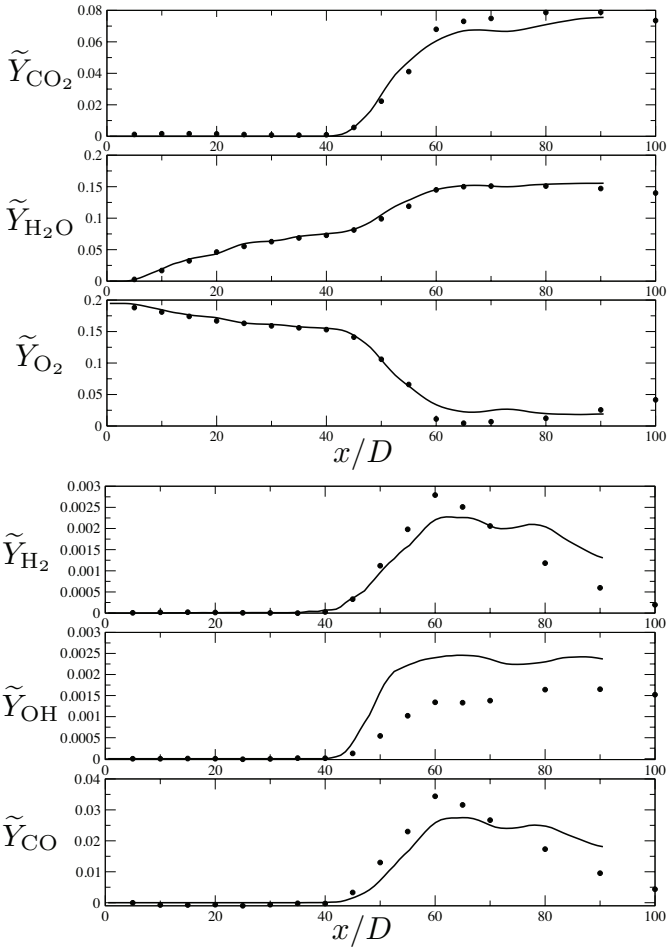

Figure 5.27: Centerline profiles of the average mass fractions of some major and minor species. Symbols: experiments; lines: LES.

antisymmetric and symmetric components of the filtered velocity gradient tensor $\underline{\underline{\nabla}}\,\underline{\widetilde{u}}$ [Dubief 00], which are markers of the turbulent vortical structures (view b). A spot of lower τ_{mix} is visible on the iso-$\widetilde{Y}_c$ line, positioned at the center of an elongated element of the iso-Q surface. At this point, the lower τ_{mix} value signals a history of more intense turbulence, to which the narrow vortex structure has likely contributed. Along the iso-$\widetilde{Y}_c$ line, a clear link between low mixing times and high chemical source terms $\widetilde{\dot{\omega}}_{Y_c}$ (view c) is evidenced. This is consistent with the trend presented in Fig. 5.18. The role of the residence time is here cast aside, since $\widetilde{\tau}_{\text{res}}$ proves to be only weakly varying on the line studied (view d).

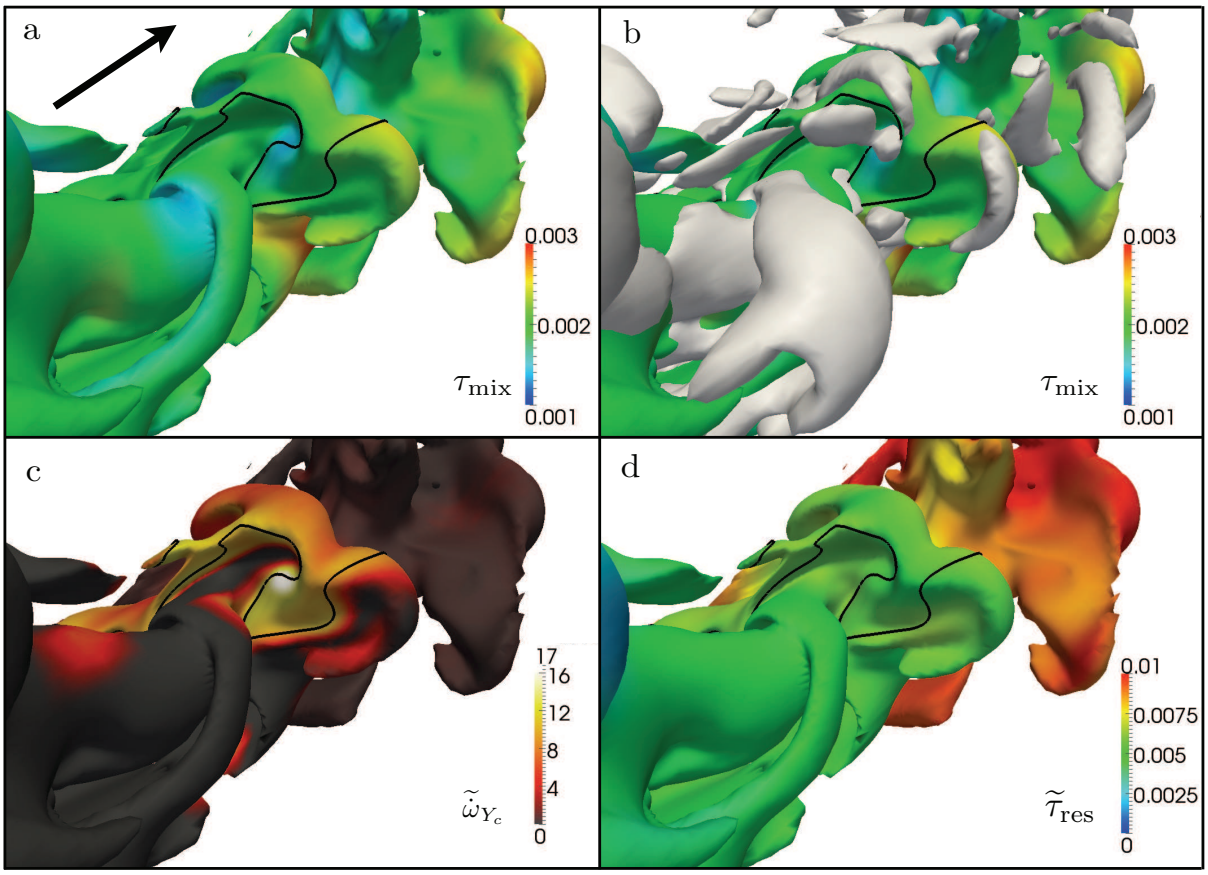

Figure 5.28: Snapshot of the mixture fraction isosurface $\widetilde{Z} = Z_{\text{st}}$, colored with different quantities. Black line: iso-$\widetilde{Y}_c = 0.25\, Y_{c,\text{eq}}(Z_{\text{st}})$. Views *a* and *b*: τ_{mix} (s), with, in view *b*: iso-$Q = 10^6\,\text{s}^{-2}$ in gray; view *c*: progress variable source term (s^{-1}); view *d*: $\widetilde{\tau}_{\text{res}}$ (s). The arrow in view *a* indicates the main flow direction.

5.4.2 Sensitivity to α_{mix}

In the results presented above, the value $\alpha_{\text{mix}} = 0.5$ was found to be optimal. The introduction of this coefficient was made necessary by the constant τ_{mix} assumption. Therefore, it is interesting to study the sensitivity of the computed flame behavior to this parameter.

The centerline profiles of some significant quantities, obtained for different values of the mixing time coefficient are plotted in Fig. 5.29. Unmistakably, it appears that the flame base anchors itself closer and closer to the inlet as α_{mix} is decreased, that is as the EMST-simulated mixing intensity increases. Not shown in this figure but indirectly visible through the steepness of the temperature increase, the chemical source terms become higher as the input τ_{mix} value is decreased, as could be predicted by the source term plot in Fig. 5.18. Thus, the global burning rate becomes higher and enables the flame to stabilize itself closer upstream, towards the high velocity flow regions. Conversely, values of α_{mix} larger than 0.9 lead to a blow-off; the flame leaves the computational domain.

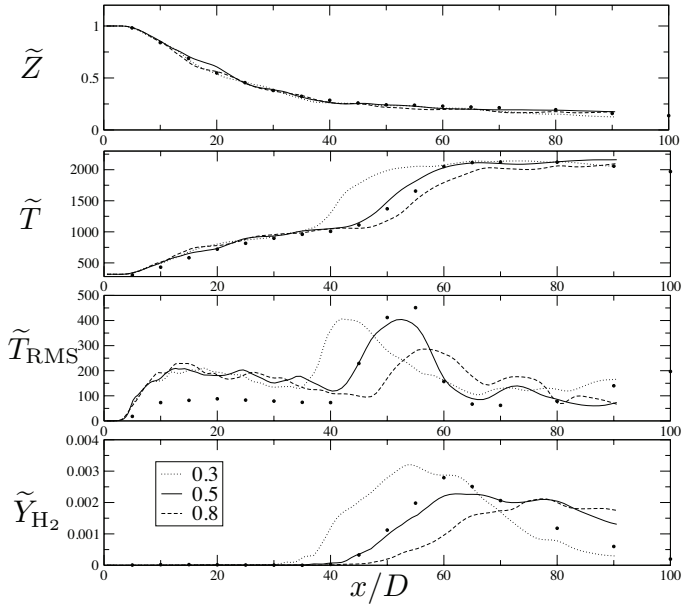

Figure 5.29: Centerline profiles of time-averaged mixture fraction, temperature, temperature fluctuation and H_2 obtained for several values of α_{mix} (see legend box on H_2 graph).

5.4.3 FCCT–LES coupling quality

As discussed earlier, the prediction of the SGS pdf by FCCT from the knowledge of $\widetilde{Z}$, $\widetilde{Y}_c$ and the residence and mixing timescales is an indirect process. In particular, if the injection law in the simulated PaSR has been devised to account for the $(\widetilde{\tau}_{\text{res}}, \widetilde{Z})$ dynamics observed in the non-reacting LES, no result on the filtered progress variable $\widetilde{Y}_c$ has been taken into account in the definition of the reactor. The assumption is that a relevant reproduction of the mixing process on one side, and of the chemical behavior on the other side, leads to a correct prediction of the turbulent combustion dynamics once in the flow simulation. The satisfactory results presented above support this approach, but a more detailed look into the strength of the coupling between the properties transported in the LES and the composition-space-simulated dynamics of FCCT is necessary.

To this end, the most suitable indicator is the quality criterion w_{sum}, which makes

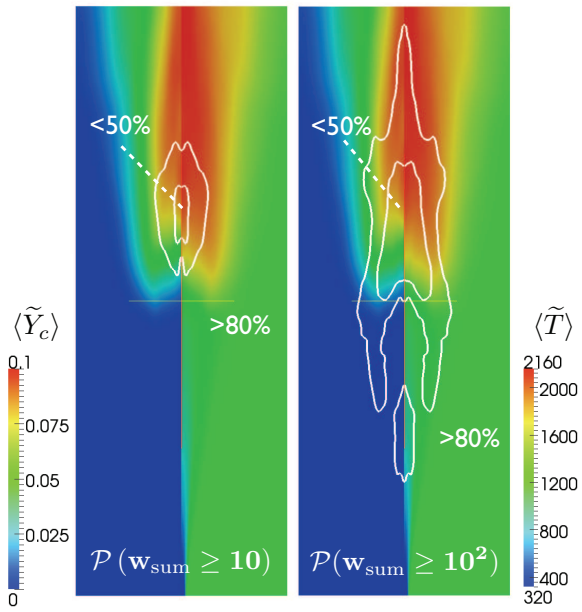

Figure 5.30: Probability maps of the events ($w_{\mathrm{sum}} \geq 10$) and ($w_{\mathrm{sum}} \geq 10^2$), superposed with the time-averaged temperature (left) and progress variable fields (right).

it possible to map, in the flow, the density of occurrences of the local set of parameters $(\widetilde{Z}, \widetilde{Y}_c, \widetilde{\tau}_{\mathrm{res}}, \tau_{\mathrm{mix}})$ in the FCCT-simulated PaSR. The higher this factor, the more stochastic particles have contributed to the fields read in the FCCT table. It was seen in Fig. 5.21 that values of w_{sum} higher than 10^2 indicate very reliable results and that a progressive but systematic degradation of the data starts when w_{sum} drops below about 10. The probability maps of the two events $w_{\mathrm{sum}} \geq 10$ and $w_{\mathrm{sum}} \geq 10^2$ are computed on a time interval of about $2\tau_{\mathrm{box}}$ and plotted in Fig. 5.30. It appears directly that the quality criterion does not always remain above the level of 10 which would be sufficient to fully guarantee the validity of the coupling. The zone where the most frequent degradation of the tabulated fields may be expected is situated in the flame area. This is an unsatisfactory result, however the correctness of the predicted flame behavior presented above calls for a more detailed analysis.

The overall observed departure between the actual filtered flow fields and the simulation result is a complex function of several contributions, which may be symbolically formulated by

$$\mathcal{E}_{\mathrm{total}} = f(\mathcal{E}_{\mathrm{solver}}, \mathcal{E}_{\mathrm{FCCT}}, \mathcal{E}_{\mathrm{PaSR}}, \mathcal{E}_{\mathrm{stat}}) \, .$$

The different terms may be described this way: a) $\mathcal{E}_{\mathrm{solver}}$ is the error introduced by the numerical code, the discretization method and the assumptions in the formulation of the transport equation terms and boundary conditions; it is common to all computations performed with the same code and is not the subject of this work. b) One level below, $\mathcal{E}_{\mathrm{FCCT}}$ is the error introduced by the main hypotheses of the turbulent combustion model; in the present case, the assumption that all unclosed terms may be conditioned by the four parameters $\widetilde{Z}, \widetilde{Y}_c, \widetilde{\tau}_{\mathrm{res}}$ and τ_{mix}. Within the scope restriction implied by this choice, however, an additional source of inaccuracy comes from c) the way the determination of the unclosed fields is formulated: $\mathcal{E}_{\mathrm{PaSR}}$, in the

present case, is the error stemming from the PaSR definition and methodology for computing the chemical table. d) Finally, an ultimate, technical, contribution $\mathcal{E}_{\text{stat}}$ represents the numerical inaccuracy in the computation of the table, *i.e.* the discrepancy between the the actual table and the theoretically fully converged statistics on an infinitely fine grid.

The low levels of w_{sum} obtained in the present computations are related in the first place to $\mathcal{E}_{\text{stat}}$. The statistical origin of the insufficient density of particles contributing to the averages is obvious: a longer generation time for the tables would lead to higher w_{sum} results. Two things must yet be noted: first, the effect of the Monte-Carlo errors is simply an increase of the variance of the output around their expected value. The tabulated terms used in the SiTCom solver are either source terms or mass fractions (see Section 2.1.1). The former are involved in the transport equation of $\widetilde{Y}_c$ and $\widetilde{E}$ which may thus, on the whole, not be affected by these source term fluctations. The latter are used for the computation of temperature, and subsequently of pressure, by solving the filtered counterpart of Eq. (1.18), and the noise with which they are evaluated has indeed an impact on the pressure field, which is patchier than if a presumed pdf method was used. Second, the examination of softer criteria on w_{sum} show that the whole field verifies $\mathcal{P}(w_{\text{sum}} \geq 0.1) = 1$ and $\mathcal{P}(w_{\text{sum}} \geq 5) > 0.5$, so that the interpolated values are never so noisy as to be fully irrelevant. As a conclusion, the overall impact of $\mathcal{E}_{\text{stat}}$ on the computed physics is not very strong.

Still, a simple increase of the table computation time or of its grid fineness will not modify the main structure of the w_{sum} field; the low-value regions will comparably remain the same, despite a general increase in w_{sum}. This originates from the way the PaSR has been formulated, and is therefore related to the term $\mathcal{E}_{\text{PaSR}}$. To analyze this, the LES and FCCT table chemical behaviors are confronted with each other in detail, as shown in Fig. 5.31. From an instantaneous snapshot of the flow, all points with specific $(\widetilde{Y}_c, \tau_{\text{mix}})$ values are picked and plotted in the $(\widetilde{\tau}_{\text{res}}, \widetilde{Z})$ space. They are superposed with $(\widetilde{\tau}_{\text{res}}, \widetilde{Z})$ maps of the w_{sum} criterion obtained in the FCCT table. It is interesting to compare, for each subset, the position of the clouds of LES points with the high-w_{sum} zones. Expectedly, the general trends appear to be similar: for both the LES and FCCT results, higher values of the mean progress variable correspond to points which tend to be older and closer to stoichiometry. Yet there is a clear age shift between the LES points and the zones of highest w_{sum}, visible in particular for $\widetilde{Y}_c/Y_{c,\text{eq}} = 0.5$. The point cloud is located in zones of w_{sum} around 10, although for these $(\widetilde{Y}_c, \tau_{\text{mix}})$ points some areas are well populated, with w_{sum} above 10^4. In all cases, the average residence time of the points is larger than the zone where w_{sum} is optimal. It means that the reaction in the FCCT reactor starts faster than it does in the LES where the FCCT table is used. This observation confirms the need for an improvement of the reactor formulation, in such a way that the chemical response to the modeled mixing process in the FCCT reactor matches that of the reacting flow simulated in the LES using FCCT.

As complex as this retroactive coupling may appear to be, there is room for improvement: the mixing law has been given a very simple formulation: the reactor mixing time τ_{mix} is taken constant, but in actuality the flow particles, during their trajectories, are not submitted to constant-intensity mixing; as Figs. 5.3 and 5.7 suggest, the instantaneous mixing timescale is very small close to the inlet, in the

rich zones where no burning is possible, and decreases as the particles reach the flammable regions. Imposing in the reactor a variable mixing time in the PaSR would therefore lead to a slower burning, thus to a better match with the LES behavior. This appears to be the most obvious direction to take for an improvement of the method. A formalism such as that developed in Section 5.2.3, to access details of the τ^*_{mix} history, may prove useful.

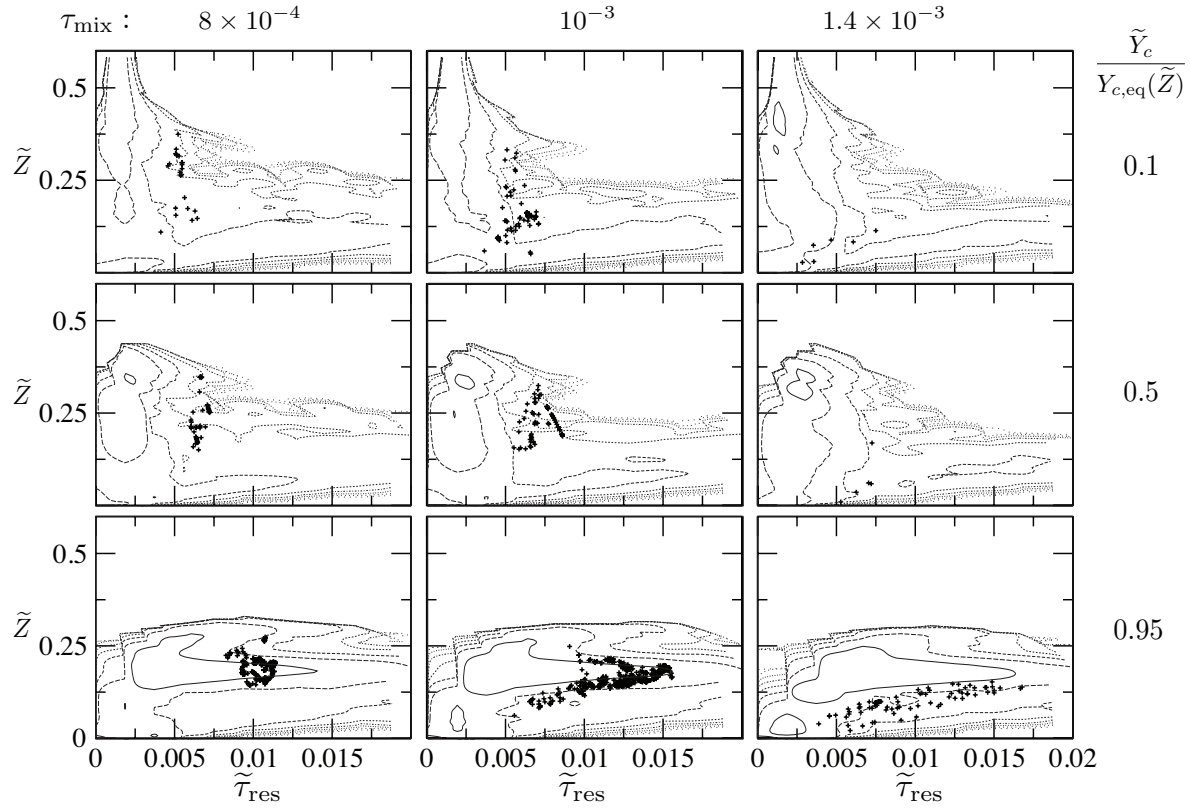

Figure 5.31: Superposition of LES points (symbols) of fixed $\widetilde{Y}_c/Y_{c,\text{eq}}$ and τ_{mix} properties with FCCT-output w_{sum} maps in the $(\widetilde{\tau}_{\text{res}}, \widetilde{Z})$ space: the isolines delimit regularly-spaced powers of 10; full line: 10^4; — — —: 10^3; – – –: 10^2; etc., decreasing with lighter line style.

As a conclusion, in spite of some imperfect results in the quality check, which call for improvements in the PaSR formulation, the FCCT conditioning hypothesis seems comforted by the satisfactory comparison between the computational and experimental statistics. Further tests should prove fruitful, but this study demonstrates to some extent the pertinency of using timescales – which describe the average history of the flow – as conditioning parameters of the unclosed chemical terms.

5.5 Summary

A novel chemistry tabulation approach for LES has been presented that is based on properties of the flow history. It is formulated through probability density functions

which are not presumed, but generated in Monte-Carlo simulations of a Partially-Stirred Reactor that models three processes: turbulent mixing, chemical reaction and inflow/outflow (engulfment). The result is a lookup table accessed from the flow solver with the following input parameters: a residence time and a mixing timescale, which describe the flow mixing history, and the transported filtered chemical parameters.

It has been tested in the LES of a laboratory lifted jet flame in a vitiated air co-flow, experimentally investigated by Cabra *et al.* [Cabra 05], with flamelet chemistry described through a mixture fraction and a progress variable. The simulation reproduces satisfactorily the properties of the lifted turbulent flame.

The Flow-Controlled Chemistry Tabulation (FCCT) method requires collecting information on the mixture fraction response *vs.* residence time. To initiate the simulation, this response can derive from a preliminary cold flow LES (or even RANS) of the burner. After using FCCT, a first solution including heat release is available providing a new mixture fraction/residence time response, useful to optimize the FCCT lookup table. This process can be repeated with an overall rapid convergence expected, since the mixing field is mainly sensitive to global heat release.

The method offers the possibility of tabulating chemistry without presuming the intercorrelations between the thermochemical variables in the SGS statistics. Possible future applications are multiple inlet burners in the presence of recirculating, non-constant enthalpy, burnt gases [Wang 10b], which may be difficult to handle with presumed pdfs. In the next chapter, a preliminary work is conducted to evaluate how FCCT could be implemented in a three-fluid turbulent combustion problem.

Chapter 6

Prospects for the RANS computation of a three-fluid turbulent combustion problem

The initial objective of the FCCT development is a prospective application to multiple-fluid, variable-enthalpy problems. The REOXAL burner is a configuration that meets these criteria and is a challenging object for the improvement of turbulent combustion modeling. Already simulated in a RANS framework by the Air Liquide research center's modeling team, it came as a natural candidate for an FCCT application. In this chapter, the prospects and challenges posed by such an undertaking are explored.

A discussion on the parameterization of the configuration is given in a first section: mixing must be described by two variables. Through the study of mixture fraction and enthalpy fields, the complex flow mixing patterns are then examined in a second section. The study leads to a modification of the FCCT residence time introduced in Chapter 5 and the design of a possible PaSR network that would account for the observed recirculation patterns.

Contents

6.1 Mixing and chemistry parameterization of the REOXAL configuration

6.1.1 Description of the mixing

The configuration considered in this note is a confined combustion chamber into which three fluids issue:

- Natural gas, later referred to as the fuel stream, denoted by F;
- Oxygen gas, later referred to as oxidizer, denoted by Ox;
- Recirculating burnt products, referred to as the External Gas Recirculation (EGR) stream.

The EGR fluid is a mixture of the main oxidizer and fuel inlet streams, in close to stoichiometric proportions, which has lost enthalpy during its recirculation; the problem is therefore non-adiabatic. The description of the mixing between the three fluids requires more than a single mixture fraction Z, which is sufficient only in adiabatic conditions.

Two possible parameterizations

A two-mixture-fraction parameterization of the fluid may be adopted, involving two passive scalars Z_1 and Z_2, with inlet conditions distinct from each other: Z_1, the fuel mixture fraction, is the elemental mass fraction of the fuel stream in the flow, and Z_2, the secondary mixture fraction, that of the EGR stream in the flow. Their inlet conditions are defined in Table 6.1. The elemental mass fraction of the oxidizer stream may be obtained from the other two as $1 - Z_1 - Z_2$.

	Z_1	Z_2	Z	h	ζ	z	Y_c
F	1	0	1	h^0_{F}	0	1	1
Ox	0	0	0	h^0_{Ox}	0	0	0
EGR	0	1	Z_{EGR}	h_{EGR}	1	-	$Y_{c,\mathrm{eq}}(Z_{\mathrm{EGR}})$

Table 6.1: Inlet conditions of the parameter scalars.

A different description of the mixture, involving the enthalpy h, may be chosen: indeed, the lower enthalpy of the EGR stream compared with the fresh F and Ox fluids mixed in similar proportions makes h a relevant tracer of the EGR mass fraction in the flow. The parameterization may involve the standard two-inlet mixture fraction $Z = (\varphi - \varphi_{\mathrm{Ox}})/(\varphi_{\mathrm{F}} - \varphi_{\mathrm{Ox}})$, which tracks the proportion of fluid originating from the fuel stream, and h. Here h refers to total enthalpy, which obeys Eq. (1.15). In the recirculating gases, Z is equal to Z_{EGR}, the bulk mixture fraction of the burner (close to Z_{st} in the present conditions) and $h = h_{\mathrm{EGR}}$, a value lower than $Z_{\mathrm{EGR}}h^0_{\mathrm{F}} + (1 - Z_{\mathrm{EGR}})h^0_{\mathrm{Ox}}$, the adiabatic mixture enthalpy in same proportions. This departure makes the transported h non-linearly related to Z and therefore a carrier of additional information. The inlet conditions are summarized in Table 6.1.

Equivalence

Enthalpy, under adiabatic, viscous-free conditions and if external forces $\underline{f}$ are absent, behaves like a passive scalar.

Therefore, the result on passive scalars enunciated in Section 1.4.1 may be invoked. The two formulations (Z_1, Z_2) and (Z, h) may actually be unified provided that the flow *inside* the chamber is assumed adiabatic (this is in no contradiction with the fact that the EGR has lost enthalpy compared to the adiabatic mixture, in same proportions, of inlet Ox and F, and that as a whole the problem is not enthalpy-conserved) and that the conditions above are satisfied, as is now detailed.

In the chamber, enthalpy losses are due to either radiation or heat exchange at the walls. Since velocities are high in the flame zone and upstream, radiation may be considered negligible, and the main physical hypothesis may be formulated as follows: no enthalpy loss occurs except in the burnt gases. Thus, the adiabatic assumption is valid in the reaction and upstream mixing zones.

Where h is considered a passive scalar, the (Z, h) parameter couple is linearly related to the two mixture fractions (Z_1, Z_2). Any conserved property Q may be obtained from its values in the three inlet streams $Q^0_{\rm F}$, $Q^0_{\rm Ox}$, and $Q_{\rm EGR}$ as

$$Q = Z_1 Q^0_{\rm F} + Z_2 Q_{\rm EGR} + (1 - Z_1 - Z_2) Q^0_{\rm Ox} \,. \tag{6.1}$$

Applied to Z and h, this relation leads to the following linear system:

$$\begin{aligned} Z &= Z_1 + Z_2 Z_{\rm EGR} && (6.2)\\ h &= Z_1 h^0_{\rm F} + Z_2 h^0_{\rm EGR} + (1 - Z_1 - Z_2) h^0_{\rm Ox} && (6.3) \end{aligned}$$

It is useful to introduce intermediary scalars providing a different angle of description of the mixing proportions within the fluid: ζ is the mass fraction of the EGR stream within the mixture as opposed to fluid coming from the Ox or F inlets, and z is the proportion of F within this portion of fluid that comes from the Ox and F inlets. An illustrative schematic is provided in Fig. 6.1, and their values at the inlets given in Table 6.1. With this definition, any conserved property Q may be obtained, in the flow, from its limit values as:

$$Q = \zeta Q^0_{\rm EGR} + (1 - \zeta) \left(z Q^0_{\rm F} + (1 - z) Q^0_{\rm Ox} \right) \,. \tag{6.4}$$

The relations between (ζ, z) and the two sets (Z, h) and (Z_1, Z_2) are obtained as follows:

- Choosing Q equal to Z and to h, Eq. (6.4) leads to a system that, once inverted, yields the following set of equations:

$$\begin{aligned} \zeta(Z,h) &= \frac{Z h^0_{\rm F} + (1-Z) h^0_{\rm Ox} - h}{Z_{\rm EGR} h^0_{\rm F} + (1 - Z_{\rm EGR}) h^0_{\rm Ox} - h_{\rm EGR}} \\ z(Z,h) &= \frac{Z - \zeta Z_{\rm EGR}}{1 - \zeta} \\ &= \frac{h - h^0_{\rm Ox} - \frac{h - h_{\rm EGR}}{Z - Z_{\rm EGR}} Z}{h^0_{\rm F} - h^0_{\rm Ox} - \frac{h - h_{\rm EGR}}{Z - Z_{\rm EGR}}} \end{aligned} \tag{6.5}$$

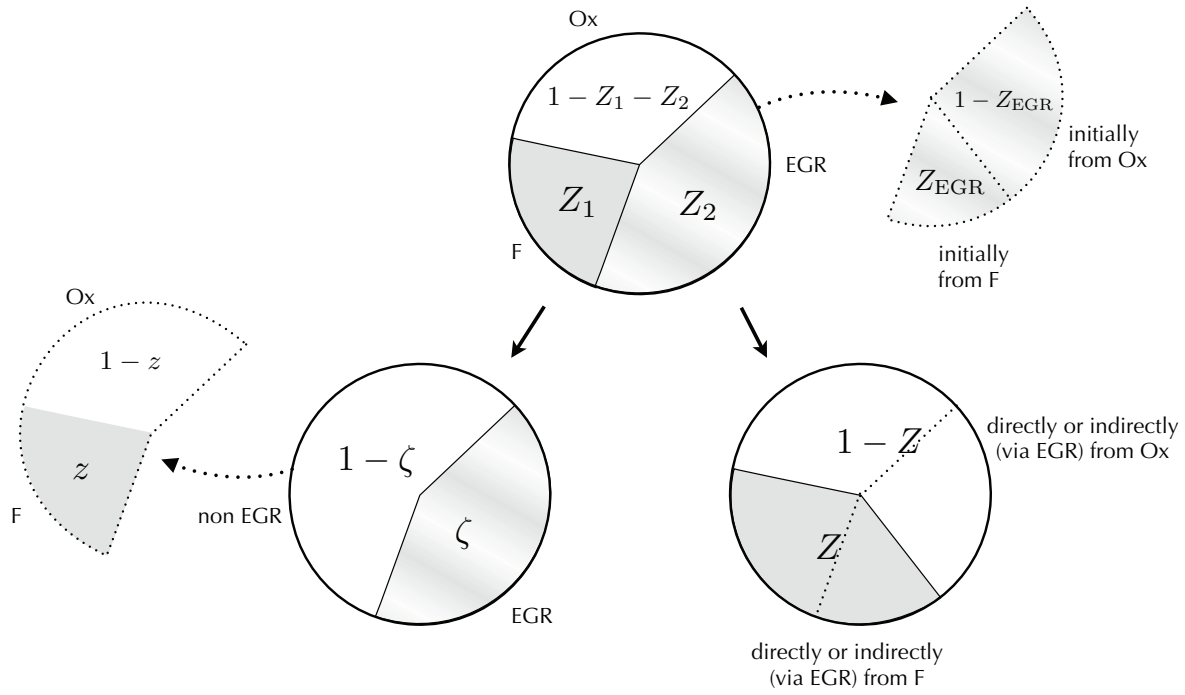

Figure 6.1: Schematic illustrating the different set of parameters describing the mixture. A full circle represents the state of a fluid particle, and the angular sectors the diverse proportions from the inlets.

- The set of Eqs. (6.1) and (6.4), true for any Q, implies that

$$Z_1 = (1 - \zeta)z \,, \quad Z_2 = \zeta \,. \tag{6.6}$$

It must be noted that z is not a passive scalar, since it is defined as a fraction and displays a singular behavior when ζ nears zero. The last two sets of equations, if merged, lead to System (6.3) relating Z_1 and Z_2 with Z and h. However, the formulation involving ζ and z – Eqs. (6.4) and (6.5) – is most useful to parameterize the chemical database, since it directly links the flow properties to those of the pure fuel and oxidizer streams, as is presented in the next section.

6.1.2 Chemical database

On top of the two parameters describing the mixture, a progress variable Y_c is introduced to account for the chemical reaction, forming a three-parameter (Z, h, Y_c or Z_1, Z_2, Y_c) description of the chemistry. As in the FPI formalism, it is defined as a convenient linear combination of certain mass fractions, *e.g.* $Y_c = Y_{\mathrm{CO}} + Y_{\mathrm{CO_2}}$, varying monotonously along the reaction from fresh reactants to burnt products.

The reference chemical database which is to be generated must provide unfiltered chemical fields in the form:

$$T(Z, h, Y_c), \quad \dot{\omega}_{Y_c}(Z, h, Y_c), \quad Y_i(Z, h, Y_c), \quad \ldots$$

using in the following the (Z, h) description for the mixing. Chemistry tabulation is done as discussed in Section 4.2.3, for example through laminar flamelet computations.

Whatever the favored approach, the reactant mixture (set, for example, as the fresh gas condition for a premixed flamelet or as the initial gas composition for a PSR) is a mixture of the three inlet fluids, characterized by $Z \in [0; 1]$ and $h \in [h_{\min}; h_{\max}]$, where $h_{\min|\max} = \min|\max(h^0_{\mathrm{F}}, h^0_{\mathrm{Ox}}, h_{\mathrm{EGR}})$. The species composition is obtained from (Z, h) through:

$$Y_i(Z, h) = \zeta Y_{i,\mathrm{EGR}} + (1 - \zeta)\left(zY^0_{i,\mathrm{F}} + (1 - z)Y^0_{i,\mathrm{Ox}}\right) , \tag{6.7}$$

where ζ and z are obtained from Z and h via System (6.5).

6.2 Reactor configuration and timescales computation

In this study, the REOXAL burner was simulated with the RANS approach, using the commercial software FLUENT®. All computations presented here were performed in conditions which the modeling team at Air Liquide had already used, with other combustion models, and from which they had obtained meaningful results. Following the methodology used for the jet flame, the study starts with exploratory runs performed in cold flow conditions: the combustion model was switched off. The main modeling task is to analyze the mixing parameters $\widetilde{Z}$ and $\widetilde{h}$ structure *vs.* the residence time $\widetilde{\tau}_{\mathrm{res}}$ so as to design injection laws for a PaSR which would reproduce the observed flow behavior.

6.2.1 Flow topology

The present burner is composed of five inlet streams, as illustrated in Fig. 6.2. Fuel

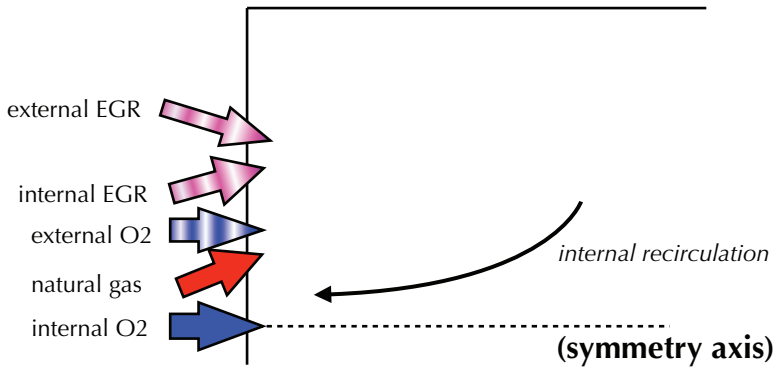

Figure 6.2: Schematic of the inlet streams. Full coloring: straight injection; streaked coloring: swirled injection.

issues through four circularly positioned nozzles at the chamber bottom. Oxidizer is brought in through two inlets: a jet nozzle positioned on the axis (internal O_2),

and a circular swirl injector surrounding the fuel inlet points (external O_2). The REOXAL burner is completed by two streams of warm recirculating gases (EGR) injected through circular swirling nozzles.

The burner is 90 °-periodic in the azimuthal angle direction. In the following, all views of the computed fields in the burner are presented on two planes, one on a fuel inlet, the other a bisector between two of them, see Fig. 6.3.

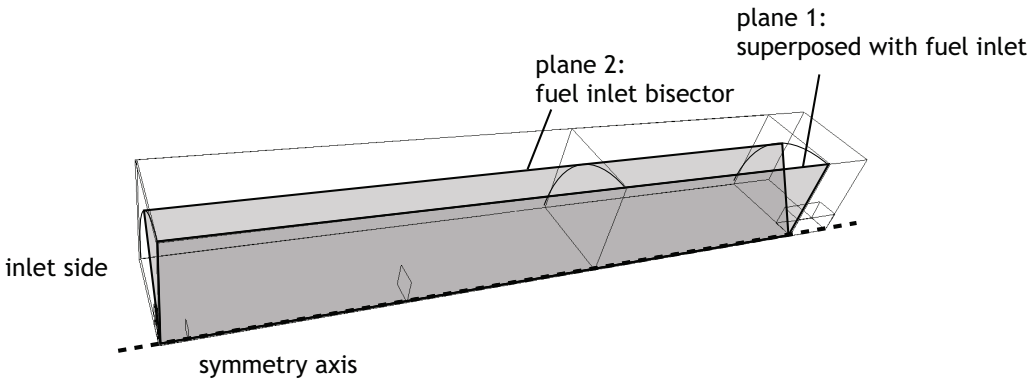

Figure 6.3: Outline of the computational domain and display planes.

A study of the velocity field reveals two recirculation zones. The first one, expected like in all confined chambers where the momentum injection is performed close to the symmetry axis, is a toroidal "dead zone" at the chamber bottom, near the enclosing walls. The second one, whose role in the mixing behavior will be emphasized by this study, is caused by the swirling pattern of the gas injection and creates a movement of fluid from the center of the chamber in the upstream direction and towards the symmetry axis. These two zones are visible in Fig. 6.4, where the negative axial velocity areas have been highlighted.

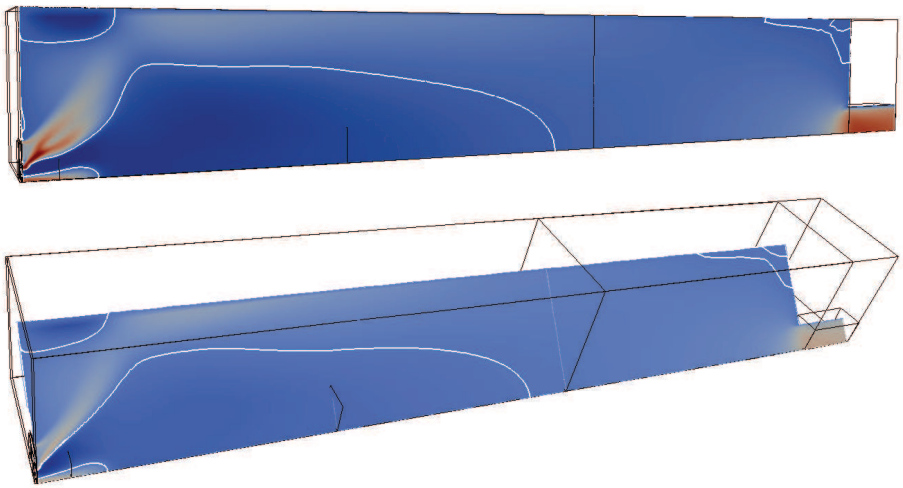

Figure 6.4: Average axial velocity field: zero-isoline shown in white.

The two mixing-describing scalars $\widetilde{Z}$ and $\widetilde{h}$ are plotted in Figs. 6.5 and 6.6. A scatter plot of their computed values across the full flow region is displayed and

analyzed in Fig. 6.7: the points are enclosed within a convex, triangular structure whose vertices correspond to the three inlet streams compositions. It may be noted that the EGR inlet point is below the Ox–F mixing line, confirming that the enthalpy of the EGR stream is lower than that of the adiabatic mixture of Ox and F in similar proportions.

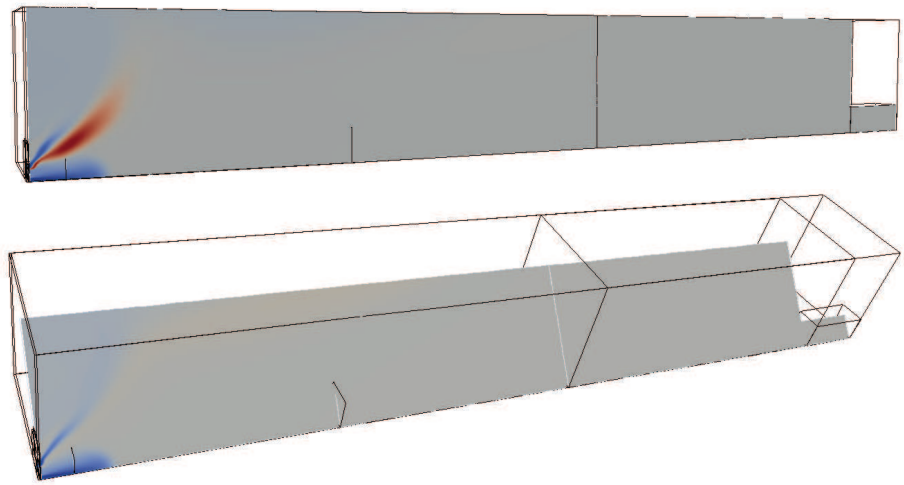

Figure 6.5: Average mixture fraction $\widetilde{Z}$ field.

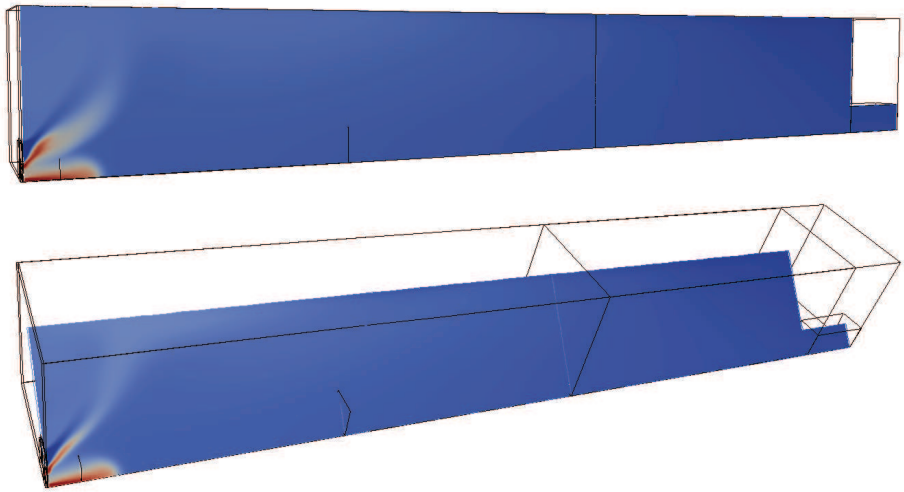

Figure 6.6: Average enthalpy $\widetilde{h}$ field.

Already some remarks on the mixing structure can be made from Fig. 6.7. The Ox–F and Ox–EGR mixing lines are populated; not the third edge of the triangle, the F–EGR mixing line. This indicates that no direct mixing between the EGR and the fuel streams occurs in the flow, and is easily corroborated by a look at the burner geometry: the fuel pipes are separated from the EGR injection by the stream of external O_2. Moreover, a denser pattern may be observed along a straight line that connects the oxidizer point and a point indicated by an asterisk in Fig. 6.7. The latter corresponds to a mixture in stoichiometric proportions and an enthalpy higher than

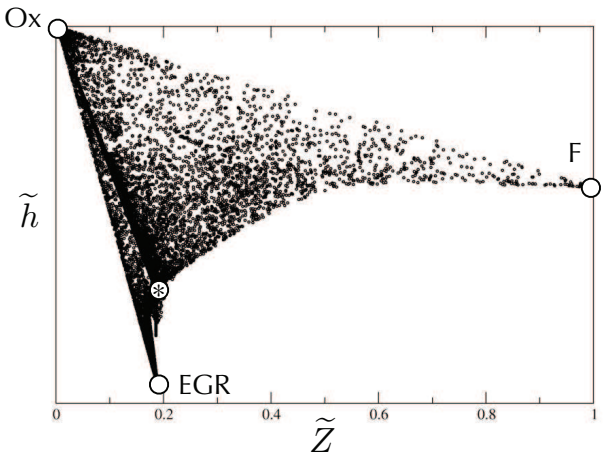

Figure 6.7: Scatter plot of the average mixture fraction $\widetilde{Z}$ values in the flow *vs.* enthalpy $\widetilde{h}$. Asterisk: point corresponding to the tip of the internal recirculation zone.

the EGR. A study of the flow reveals these are the properties of the fluid where the internal recirculation zone mentioned above reaches the injection zone, between the internal O_2 and the fuel injectors. The role of this recirculation zone in the mixing pattern in the flame region turns out to be pivotal and is further examined in the coming sections, thanks to the use of the residence time.

6.2.2 "Standard" residence time

In order to develop the FCCT modeling of the present problem, a first computation of the residence time $\widetilde{\tau}_{\text{res}}$ is performed in the RANS solver. This is done as prescribed in Section 5.2.5, through the resolution of a convective–diffusive equation of source term ρ. For the moment no specific restriction on the source term is imposed, and the inlet values are set to zero, so that $\widetilde{\tau}_{\text{res}}$ is literally the average time spent by the fluid particles in the chamber starting from their injection. With these settings, the residence time is referred to as "standard". A snapshot of its field is shown in Fig. 6.8. Its structure reveals the different injection velocities; along inlet streams of high velocities, the residence time increase needs longer distances and is therefore smaller than in the slower injection zones. Despite the highly diffusive character of the RANS simulations, the occurrence of recirculation is faintly visible in the zones where $\widetilde{\tau}_{\text{res}}$ increases in upstream directions, as highlighted in Fig. 6.8.

Structure of the mixing

In a fashion similar to the study of the simple jet configuration (Section 5.2.5), the mixing behavior of the flow is plotted *vs.* the residence time. Here, as mentioned earlier, mixing is described by a set of two parameters, Z and h, so that the plot must now be three-dimensional. As was done earlier with a $(\widetilde{\tau}_{\text{res}}, \widetilde{Z})$ scatter plot, a $(\widetilde{\tau}_{\text{res}}, \widetilde{Z}, \widetilde{h})$ scatter plot is thus built, expanding the previous $(\widetilde{Z}, \widetilde{h})$ plot, Fig. 6.7, along the $\widetilde{\tau}_{\text{res}}$ direction. This is presented in Fig. 6.9.

Inspected with the information brought by the residence time, the mixing patterns

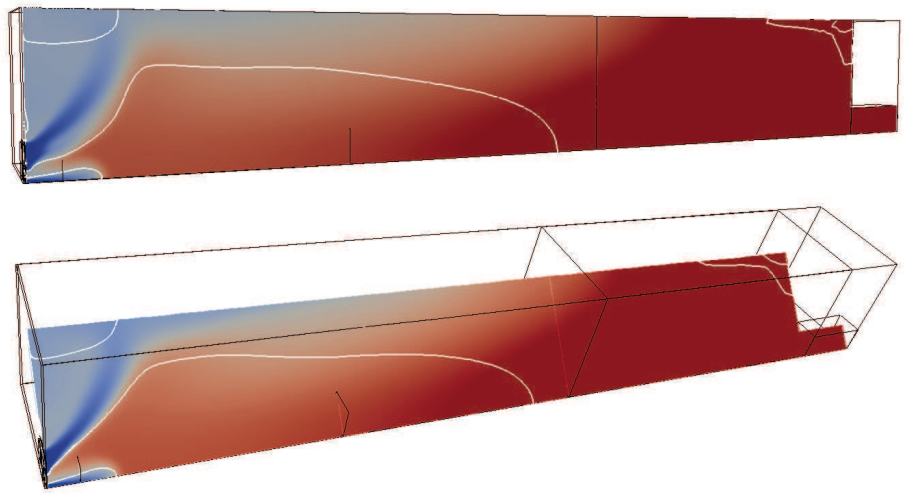

Figure 6.8: Average field of the standard residence time. Zero axial velocity isoline is shown in white.

appear with more clarity than in previous Fig. 6.7. At a first glance, two observations can be made: first, the earliest mixing takes place on the Ox–F and Ox–EGR lines (looking at the $\widetilde{\tau}_{\text{res}} = 0$ plane); second, the mixture is all but fully homogenized when $\widetilde{\tau}_{\text{res}}$ reaches the value τ^*_{res} indicated on the plot in Fig. 6.9, and its properties $(\widetilde{Z}^*, \widetilde{h}^*)$ remain thereafter approximately constant. The long streak of points corresponds to flow parcels mixing with each other and growing older without significant evolution of their properties. A slow decrease of the enthalpy $\widetilde{h}$ along time (as the residence time increases) is actually visible, corresponding to heat losses at the walls. At any rate, the role of the internal recirculation zone – denoted from here on by IGR (Internal Gas Recirculation) – may now be examined by considering the $\widetilde{\tau}_{\text{res}} \in [0 : \tau^*_{\text{res}}]$ interval.

The triangle formed by the $(\widetilde{Z}, \widetilde{h})$ scatter is now extruded in the τ_{res} direction, into an approximate tetrahedron of vertices Ox, F, EGR and the new point IGR $\equiv (Z^*, h^*, \tau^*_{\text{res}})$. As a completing point of view, the three-dimensional scatter is plotted in Fig. 6.10 as intersections with constant-$\widetilde{\tau}_{\text{res}}$ planes. The scatter repartition is not uniform, but rather displays the following structures:

- (1) and (1)' the two already mentioned lines, markers of a very quick mixing between Ox and F, and between Ox and EGR.
- (2) a dense, elongated cluster of points along the Ox–IGR line indicates a distinctive mixing pattern between the two streams, one issuing from the central O_2, the other coming in the reverse direction from the inside of the chamber. It corresponds to the dense line mentioned in the analysis of the 2D scatter plot (Fig. 6.7).
- (3) a group of points is spread mainly on the triangle F–Ox–IGR, but at positions near from the Ox–EGR–IGR plane, fills the inside of the zone separating the two planes.
- (4) the triangle joining the Ox, EGR and IGR vertices is filled with points, in a shape separate from structure (2). It corresponds to a mixing between the Ox–EGR line mentioned in (1) and the internal recirculation IGR.

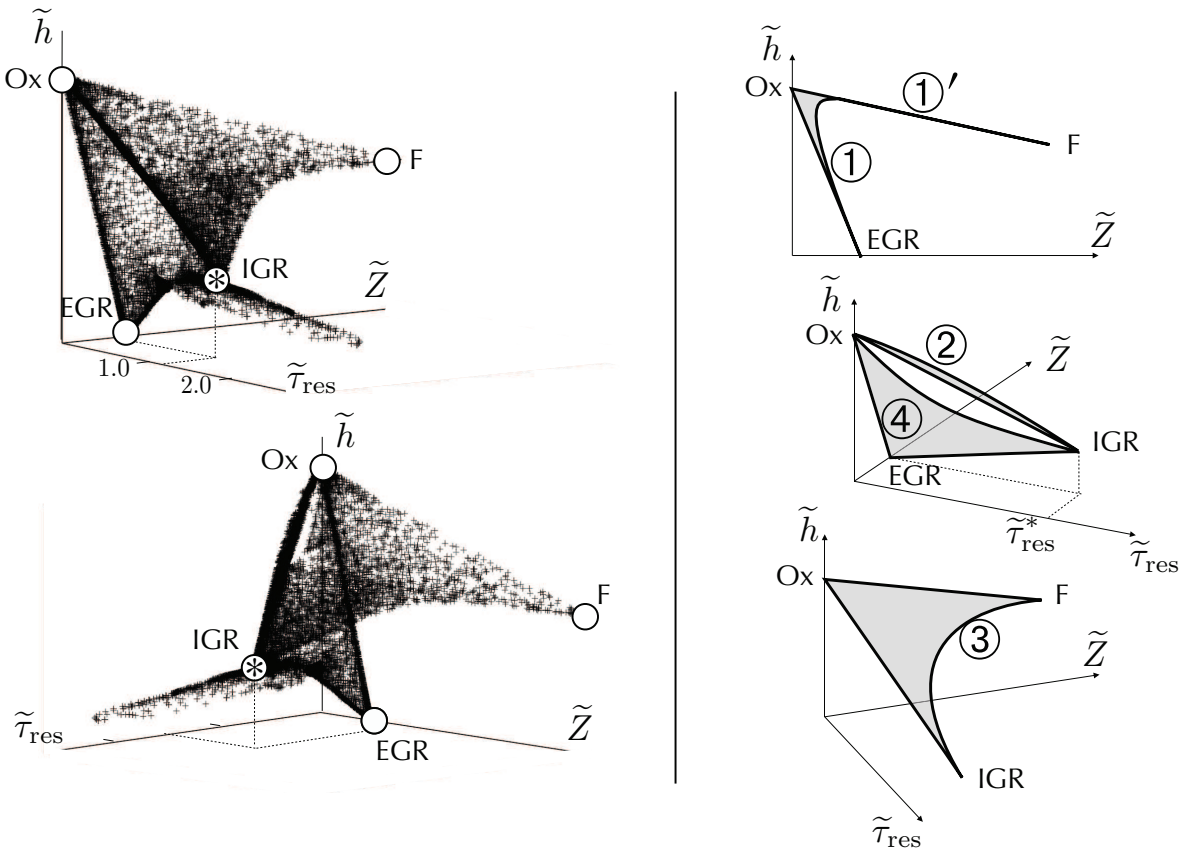

Figure 6.9: Scatter plot of the resolved $(\widetilde{Z}, \widetilde{h})$ *vs.* the resolved residence time $\widetilde{\tau}_{\mathrm{res}}$ in its standard version, *left:* 3D views, *right:* schematized features.

This structure is complex and the difficulty to describe it matches the complexity of the flow itself close to the injectors. Yet unclear is the exact way in which mixings (3) and (4) occur, which could appear more clearly if more insight were had into how the Ox–EGR–IGR triangle is filled, and into how points streaking from the F vertex blend into the latter.

Basis of the FCCT formulation

However, from the results just obtained, the framework of the PaSR formulation that should be involved in an FCCT table computation can already be outlined.

Four limit conditions must be used: the expected burner inlet conditions Ox, F and EGR, and the additional IGR which, it was seen, plays the role of a limit point in the mixing pattern although it is not a physical inlet of the burner, but is rather due to the flow geometry. To be considered a valid inlet, useable in the PaSR model as an input condition, one condition must be satisfied: it should be a homogeneous fluid of known composition. One may quite safely assume this is the case here, because the IGR point is the result of a long recirculation history, in a zone where it is verified that the average fluctuations are very weak, and therefore has had the time to become homogeneous.

Still, the presence of this fourth "boundary condition" fluid, the internal recircu-

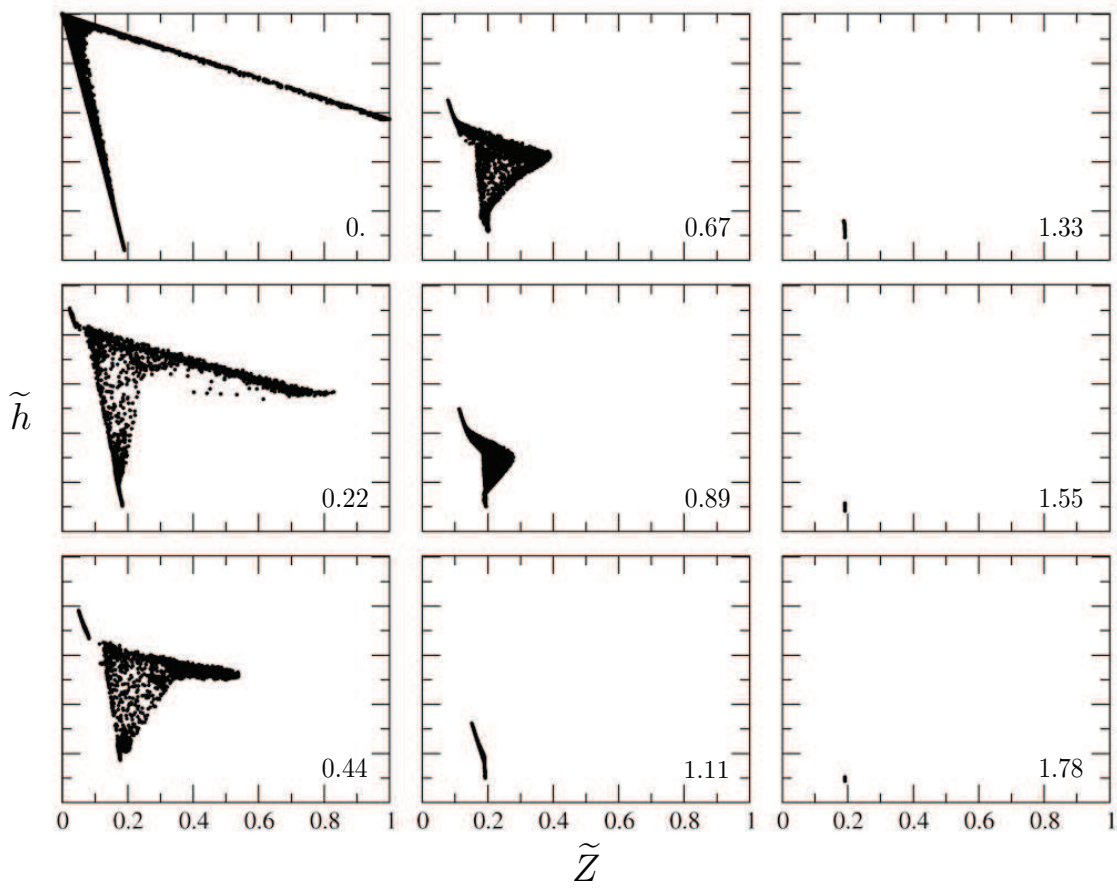

Figure 6.10: Scatter plot of the resolved $(\widetilde{Z}, \widetilde{h})$ *vs.* the resolved residence time $\widetilde{\tau}_{\text{res}}$ in its standard version, plotted on constant $\widetilde{\tau}_{\text{res}}$ slices, whose values are indicated in seconds.

lating gases, is not a seamless addition to the reference situation, studied earlier, of the fuel jet in an oxidizer co-flow. Actually, the age of the IGR, τ^*_{res}, is non-zero and this creates a practical difficulty in the exploitation of the $(\widetilde{Z}, \widetilde{h}, \widetilde{\tau}_{\text{res}})$ scatter plot, as explained here.

The mixing structure of a set of two streams 1 and 2 with zero-age limit conditions ($\tau_{\text{res},1} = \tau_{\text{res},2} = 0$) and mixture-describing properties $Q_1 < Q_2$ is always shaped, in the $(\widetilde{\tau}_{\text{res}}, \widetilde{Q})$ space, as in Fig. 6.11(a): the scatter plot is bounded on the lower $\widetilde{\tau}_{\text{res}}$ side by the straight line 1–2, and on the higher $\widetilde{\tau}_{\text{res}}$ side, by a curve $\mathcal{C}$. The characteristic width of the shape in the $\widetilde{\tau}_{\text{res}}$ direction is denoted by $\Delta\tau_{\text{res}}$. This was true in the jet situation, and, adapted in three dimensions, it would be true for the three-inlet conditions studied here if no internal recirculation took place.

In the event of one or more boundary conditions of non-zero age, the scatter plot limit on the lower $\widetilde{\tau}_{\text{res}}$ side is still the line or plane joining the inlet points, which corresponds to an infinitely fast mixing between their respective streams (see the study of mixing *vs.* aging in Section 5.2.5), but is just not the $\widetilde{\tau}_{\text{res}} = 0$ axis as previously. Compared with the all zero-age inlets situation, the width $\Delta\tau_{\text{res}}$ is unchanged, as illustrated in Fig. 6.11(b). Yet it is the *departure* from the infinitely

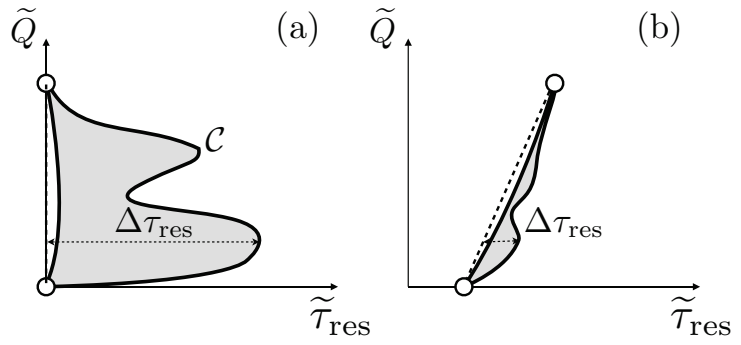

Figure 6.11: Schematic description of the mixing patterns seen in the $(\widetilde{Q}, \widetilde{\tau}_{\mathrm{res}})$ space, where Q is a generic mixture-describing quantity. (a) all zero-age inlet conditions; (b) non-zero age inlet. Dash line: infinitely fast mixing line.

fast mixing line that must be captured to design the τ_{inj} law. And, in practice, attempting to design τ_{inj} laws appropriate for reproducing the $(\widetilde{\tau}_{\mathrm{res}}, \widetilde{Q})$ pattern (see Section 5.3.3) becomes difficult if $\Delta\tau_{\mathrm{res}} \ll \max_{i\neq j}|\tau_{\mathrm{res},i} - \tau_{\mathrm{res},j}|$, i, j standing for the possible inlet conditions. In this case, the age variations due to aging are small compared with those due to the reduction of the large-scale age gradients, possibly becoming impossible to capture in a strongly diffusive simulation: the numerical error on the residence time field may be of the order of the shift induced by the aging process. Put differently, this may arise when the source term (one), in the residence time equation (5.15), becomes negligible in comparison with the diffusion terms, a condition coming down to:

$$\max\left(\frac{u\,\widetilde{\tau}_{\mathrm{res}}}{L}, \frac{\mathcal{D}_{\mathrm{eff}}}{L^2}\,\widetilde{\tau}_{\mathrm{res}}\right) \gg 1\,, \tag{6.8}$$

where u, L and $\mathcal{D}_{\mathrm{eff}}$ are characteristic velocity and length of the zone of interest, and a measure of the computational diffusivity, a sum of the molecular, turbulent and artificial diffusivities.

In the scatter plot of the present case, obtained in RANS, this problem is encountered. In Fig. 6.9, it is visible that almost all points seem to approximately snap on the faces of the Ox–F–EGR–IGR tetrahedron, with a characteristic $\Delta\tau_{\mathrm{res}} \simeq 0.03\,\mathrm{s}$, while the IGR residence time τ^*_{res} is of the order of 2 s. The error level linked to the numerical scheme and due to the large variation range of the residence time in the mixing region hides its variations caused by the aging source term, the ones that must be captured.

To summarize, the internal recirculation, leading old fluid to mix in the zone of interest with freshly injected matter, hinders an accurate capture of the departure of the $(\widetilde{\tau}_{\mathrm{res}}, \widetilde{Z}, \widetilde{h})$ from the instantaneous mixing behavior. A strategy to address this problem is described in the next section.

6.2.3 Dealing with the internal recirculation

The objective is to emulate a situation where the four problem inlets – here, the only stream not verifying it being the internal recirculation – would be of age zero.

This can only be achieved by modifying the transport equation of $\widetilde{\tau}_{\text{res}}$ outside the zone of interest, which is successfully done as detailed in the first paragraph. The mixing structure can then finally be studied with sufficient accuracy and the results and implications in terms of FCCT formulation are subsequently examined.

Relaxation of the residence time to zero

The FCCT table data are, strictly speaking, only required in the zone where the burning and the mixing history leading to it occur. Out of it, the key phenomena are independent of the turbulence-chemistry interaction; in particular in the burnt gases, downstream of this interest zone, the controlling phenomena are rather inert mixing, as well as, if they are activated in the simulation, radiation and energy loss at the walls, and a simplified description of the unclosed terms may be used.

Therefore, liberty is taken to modify the equation for the residence time outside the zone of interest. In order to force the residence time to be zero as the IGR reaches the zone where it comes in contact with the inlet streams, the source term in Eq. (5.15) (ρ) is replaced on a domain $\mathcal{S}_{\text{recirc.}}$ by a relaxation term towards zero:

$$\overline{\rho}\widetilde{S}_{\tau_{\text{res}}} = -\overline{\rho}\frac{\widetilde{\tau}_{\text{res}}}{T_{\text{relax}}} \,. \tag{6.9}$$

Several attempts in fixing T_{relax} were necessary and the extent of the recirculation domain $\mathcal{S}_{\text{recirc.}}$ was defined as the points for which $\widetilde{Z}$ and $\widetilde{h}$ were each between conveniently chosen intervals.

With these settings, the standard transport equation for the residence time, with $\widetilde{\rho}$ as the source term, is still fully verified in the zone of interest[1]. Everything happens, within its boundaries, as if there were four physical inlets, of age zero and of determined mixture-describing properties $(\widetilde{Z}, \widetilde{h})$.

Defined this way, the residence time is referred to as "relaxed", its notation unchanged. Unless explicitly mentioned, it is this definition which is used in the following.

Results

The resulting scatter plot of the mixture fraction and enthalpy *vs.* the relaxed residence time is shown in Fig. 6.12. As was the purpose of the modification in τ_{res}'s definition, the structures linked to the aging are much more visible than previously.

First of all, the four limit points are all located on the zero-age plane, and any point found with $\widetilde{\tau}_{\text{res}} > 0$ corresponds to a flow parcel which has aged as it was formed by the mixing of the streams coming from the inlets, be they physical (Ox, F, EGR) or emulated as such (IGR).

Expectedly too, the variation amplitude in the $\widetilde{\tau}_{\text{res}}$ direction has drastically dropped: the majority of points, forming the main structure as described in detail below, have a residence time between 0 and $\Delta\tau_{\text{res}} \simeq 0.035\,\text{s}$. This $\widetilde{\tau}_{\text{res}}$ variation, exclusively due to the aging from an initial zero value, was already discernible on the former plot,

[1]Keeping in mind that the use of the FCCT data will be restricted to this zone. Elsewhere in the flow, invoking a more simple closure will be possible, with for example an equilibrium hypothesis.

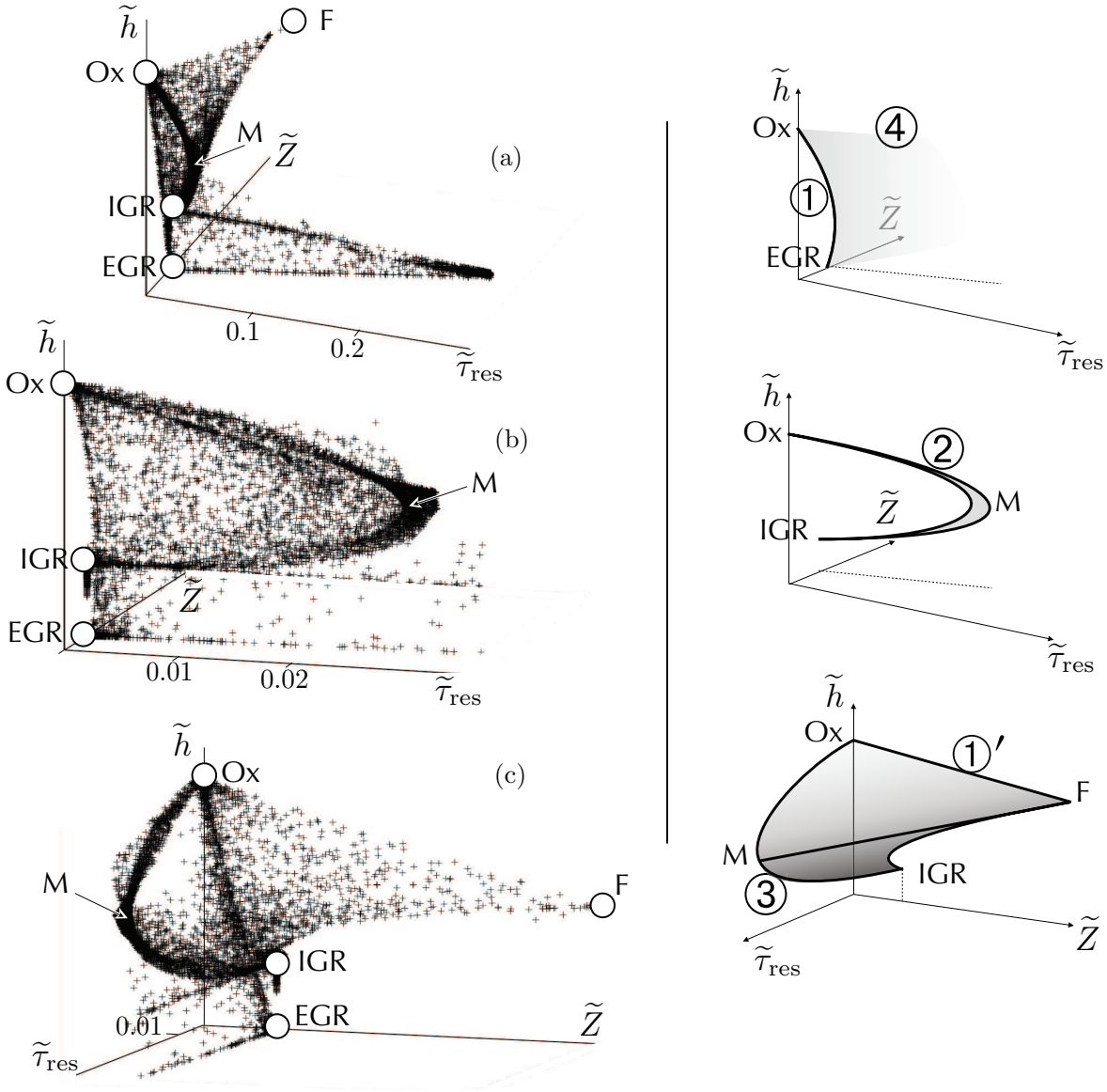

Figure 6.12: Features of the scatter plot of the resolved $(\widetilde{Z}, \widetilde{h})$ *vs.* the resolved residence time $\widetilde{\tau}_{\mathrm{res}}$, in its "relaxed" definition, Eq. (6.9).

but only unreliably, since it was eclipsed by the mixing between non-zero, large age properties (the order of up to 2 s).

The remaining points form a structure which is the trace of the former streak of points, seen in view (a) of Fig. 6.12; they correspond to the zone of the flow where the relaxation source term is used. With the relaxed residence time, the maximum age reached is 0.3 s; it is visible that some mixing occurs between these points and some from the main structure, but it occurs outside the critical region where the turbulence-reaction interaction must be described, downstream of the flame.

The main structure is seen in view (b) of Fig. 6.12. The study conducted in Section 6.2.2 may be refined. Structures that appeared as thick straight lines in Fig. 6.9 because of the poor resolution due to the non-zero age inlet values are now

more clearly identifiable; they will provide quantitative information about the rates at which the engulfment of different parts of the flow into each other occurs, and therefrom about how to define the τ_{inj} law in the FCCT reactor.

- the mixing between Ox and EGR, which was one of the straight lines (1) with the standard definition of the residence time, is now visibly spread as a structure bounded in the low $\widetilde{\tau}_{\text{res}}$ by a parabola-like curve, of apex at $\widetilde{\tau}_{\text{res}} \simeq 0.002\,\text{s}$. The structure blends itself with other point structures as $\widetilde{\tau}_{\text{res}}$ increases.
- a coherent set of points links the Ox and the IGR limit points, forming a parabola-like streak, of apex about 0.03 s (identified by 'M' on the graph) and with a $\widetilde{\tau}_{\text{res}}$ thickness about 0.003 s. This corresponds to structure (2).
- the blending of F into the rest of the flow may be seen this way: part of it mixes instantly with the external O_2 stream (points are seen on the Ox–F line previously denoted by (1)', embedded in the $\widetilde{\tau}_{\text{res}} = 0$ plane); this pattern appears unchanged by the definition of the relaxed τ_{res}. But it is only a part of a larger engulfment pattern of F into the mixture formed by Ox and IGR; seen in Fig. 6.12, the points spread on a manifold from F to the Ox–IGR parabola (2), along two asymptotes: on the low $\widetilde{\tau}_{\text{res}}$ side, the plane F–Ox–M, and on the other side, the IGR–M branch of the parabola. A parabola-like bounding curve links points F and IGR, with an apex at $\widetilde{\tau}_{\text{res}} \simeq 0.012\,\text{s}$. This is still identified as pattern (3).
- the remaining points, matching the previously introduced pattern (4), are linking the Ox–EGR faster mixing limit (1) with the bulk of the F–Ox–IGR points as they approach parabola (2).

The study of this plot allows for establishing a schematic representation of the engulfment pattern in the region of interest, presented in Fig. 6.13.

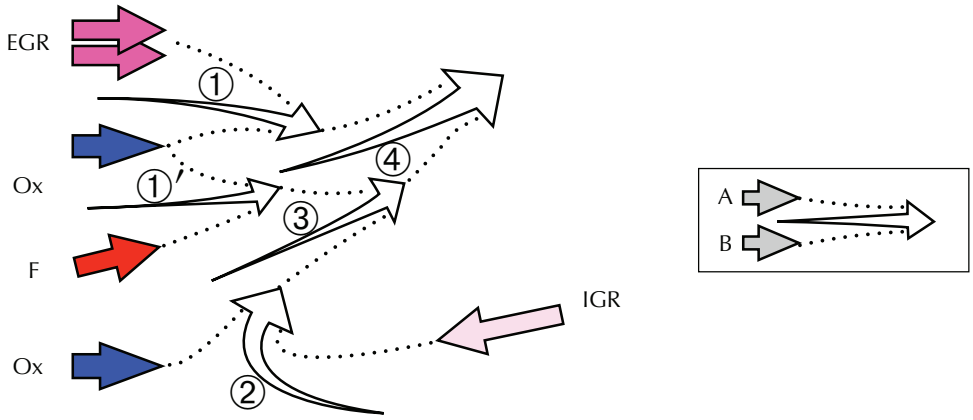

Figure 6.13: Schematic description of the engulfment process as interpreted from the $(\widetilde{Z}, \widetilde{h}, \widetilde{\tau}_{\text{res}})$ scatter plot of Fig. 6.12. Illustrating example in the legend box: stream A mixes with stream B.

Now that the patterns describing the mixing between the different inlet streams have been highlighted, the settings of the PaSR to be implemented in an FCCT

computation may be defined. Given the complexity of the flow, the simple one-reactor two-inlet model used in the jet flame configuration will prove insufficient, as explained in the section below.

FCCT: multiple-PaSR modeling

The first difference with the jet flame case, already pointed out, is the larger number of limit points, four instead of two.

It would be possible to design a four-inlet PaSR. However, it also appears that using a single reactor cannot reproduce the engulfment patterns seen in the flow by the study of the $(\widetilde{Z}, \widetilde{h}, \widetilde{\tau}_{\text{res}})$ behavior. Considering the fuel and EGR streams enables to understand why: as illustrated in Fig. 6.13, F fluid particles get in contact with EGR fluid particles not earlier than at stage (4). This occurs only after F first mixed with the external O_2 stream (1)', itself mixing (3) with the Ox–IGR stream (2); and after EGR mixed with O_2 (1). In a single reactor approach, it is impossible to put into contact two mixtures that are all not in the pure boundary conditions. Thus, fresh F could be injected into an Ox–EGR mixture, or pure EGR into a F–Ox–IGR mixture; it would be impossible to render the complex mixing history just described.

Instead, a network of inter-connected PaSR could accomplish this task. Let us consider the reactor configuration presented in Fig. 6.14, which is designed so as to closely match the pattern schematized in Fig. 6.13. The reactor numbering matches that of the engulfment patterns distinguished in the schematized flow.

Actually putting into practice and validating this model has not been completed. Because of that, and although it is the simplest structure that may be considered given the complexity of the flow, it can only be meant as a sketch of an actual procedure to finally obtain an FCCT table $\widetilde{\phi}(\widetilde{Z}, \widetilde{h}, \widetilde{Y}_c, \widetilde{\tau}_{\text{res}}, \tau_{\text{mix}})$.

Still, before any practical validation, some properties that should be assigned to the injection between the reactors can be foreseen here. Some are just working hypotheses – unverified – about the optimal settings:

- The reactor whose joint (Z, h, Y_c)-distribution should be used to build the output is reactor (4). With an appropriate repartition of the injections, the content of any of the upstream reactors can be directly transferred into this reactor, since it is positioned at the output of the network.
- Each reactor (k) is piloted by its own micro-mixing, injection and reaction processes, with laws which could be designed for the mixing time $\tau_{\text{mix},(k)}$ and injection time $\tau_{\text{inj},(k)}$. Setting individual levels of τ_{mix} for each reactor would actually match the different intensities of turbulent mixing occurring in the flow. Yet, for simplicity reasons, a uniform, constant law of τ_{mix} could also be set, as was done in the jet flame case, and the non-linearity induced by the interaction of mixing with reaction could be compensated by a constant α_{mix} (see Section 5.3.3). As was said earlier, accounting for more realistic mixing time histories is one of the main prospects of improvement of the method, which promises a more rigorous coupling between the flow and the PaSR modeling.

Other settings may be strictly deduced from the information provided by the $(\widetilde{Z}, \widetilde{h}, \widetilde{\tau}_{\text{res}})$ scatter plot. Some examples are given:

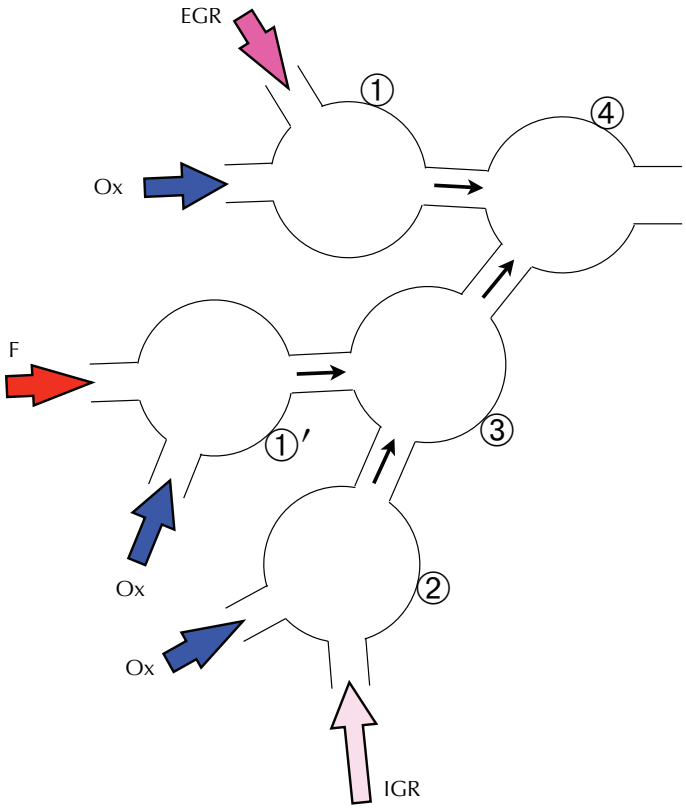

Figure 6.14: Proposed structure of a PaSR network that would reproduce the engulfment pattern schematized in Fig. 6.13.

- The shape of the curve bounding the set of points (1) on the low $\widetilde{\tau}_{\text{res}}$ side, which can be parameterized as

$$\left\{ \begin{array}{rcl} (\widetilde{Z},\widetilde{h}) & = & (1-x)(Z_{\text{Ox}},h_{\text{Ox}}) + x\,(Z_{\text{EGR}},h_{\text{EGR}}) \\ \widetilde{\tau}_{\text{res}} & = & 4\,\tau_{(1)}x(1-x) \end{array} \right. , \quad x \in [0:1] \qquad (6.10)$$

  with $\tau_{(1)} \simeq 0.002\,\text{s}$ (see the description of structure (1) with the relaxed residence time definition), imposes that the injection rate be bounded by a maximum value. In terms of the injection timescale $\tau_{\text{inj},(1)}$, it should not cross a minimum value, such a condition may be derived as depending on parameter x and on what fluid is injected:

$$\text{Ox injection}: \quad \tau^{\text{MIN}}_{\text{inj},(1)}(x) = 4\tau_{(1)}x(2-3x) \qquad (6.11)$$

$$\text{EGR injection}: \quad \tau^{\text{MIN}}_{\text{inj},(1)}(x) = 4\tau_{(1)}(1-x)(3x-1)\,. \qquad (6.12)$$

- Similar properties may be deduced on the mixing in other reactors. In (1)', the injection must be considered virtually instantaneous and the contents of the reactor quickly injected forward into reactor (3). In (2), the compact shape on the scatter plot indicates that the interval $[\tau^{\text{MIN}}_{\text{inj},(1)}, \tau^{\text{MAX}}_{\text{inj},(1)}]$ must be narrow. In (3), the fluid particles from (1)' should be injected only if the contents coming from (2) correspond to the branch IGR–M of the parabola (2) linking IGR and Ox, that is if they are comprised dominantly of IGR.

6.3 Conclusions and prospects

In this chapter, the possibility of applying Flow-Controlled Chemistry Tabulation to a three-fluid problem, namely the simulation of an Air Liquide REOXAL burner, has been assessed. A discussion on mixing parameterization was held. One specificity of the configuration is the presence of an internal recirculation current, that leads to four, rather than only three, limit conditions in the mixing patterns. The definition of the residence time was modified to make the structure of the flow in the mixing–residence time space more discernible. When it comes to modeling, the simple one-reactor approach considered in Chapter 5 turns out to be insufficient and a complex reactor network must be built.

The method followed in this chapter to study the mixing patterns in a non-reactive context could be systematized and extended to other three-fluid configurations with internal recirculation. However a large number of unknown remains to reach a completely operational FCCT table: interesting further work would be to study the turbulence intensity patterns through the instantaneous and trajectory-averaged mixing times, to determine, even with simple assumptions, mixing and injection timescales for each reactor of the network. A first FCCT table for REOXAL could be generated, and the flame structure obtained in a simulation be examined to assess the potential of the method for such a complex flow.

Conclusions

In this PhD work, two aspects of the numerical turbulent combustion activity have been addressed: with the SAFIR flame simulation, a technically complex case aiming at the numerical simulation of a multi-physics problem has been built; with FCCT, a theoretical framework meant to extend the reach of turbulent combustion modeling capabilities has been developed and validated to a two-fluid problem.

The simulation of one configuration of the SAFIR experiment is, to date, the first LES of a spray flame with tabulated detailed chemistry, and the first to reach such a spatial resolution. It called for the development of a number of numerical tools (Chapter 2): a Lagrangian droplet evaporation model, a particle-aware load-balancing approach, a numerical dispersed-phase statistics retrieval method, as well as flexible particle injection algorithms; for the design of simulation strategies addressing liquid spray issues (Chapter 3); and for the application of turbulent combustion models to this novel spray flame case (Chapter 4). Using the YALES2 solver enabled to reach high resolution in both the treatment of the dispersed phase, with a direct particle simulation of the spray, and of the gaseous phase, with a 215-million-cell grid. There is room for improvement, as detailed in the conclusions of Chapters 3 and 4, in particular because the spray injection had to be strongly adapted to reach realistic flame structures. Direct numerical simulation of the injection zone very close to the nozzle could provide valuable information on the turbulence properties and be used for improving the subgrid-scale spray–gas coupling. As far as turbulent combustion modeling is concerned, it was seen that none of the two scaling laws used for the variances enables a full capture of the flame structure: either the lift-off height is recovered (linear, "gradient" model) or the flame front structure is correctly predicted (quadratic, "mixing" model). It should be possible to assess variances through balance equations, although modeling of some of their terms, in this two-phase context, does not appear to be obvious. Else, other turbulent combustion modeling frameworks, requiring no input of variances, could be invoked, such as those based on thickened or filtered flamelets [Colin 00, Fiorina 10]. At any rate, the results call for an extension of the present simulation case to other dilution levels and other co-flow velocities, in particular to attempt at recovering the various flame types studied experimentally on the SAFIR bench.

FCCT is a novel approach to describe turbulent non-premixed combustion, through timescales linked to the fluid particle trajectories and the characterization of the turbulence–chemistry interaction. Applied to the two-fluid reference case of the Cabra *et al.* jet flame, it led to statistics comparing very satisfactorily with the experimental results. Yet the model will benefit from further work on some points: in particular, it is necessary to collect more information on the mixing time history

patterns. A possibility is to make use of the detailed tracking method presented in Section 5.2.3; alternatively, a refined Euler–Lagrange computation could be run with YALES2 to collect individual particular histories and have input for improved PaSR modeling. A study on the effect of the mixing model on the FCCT results would be interesting: here EMST was used but other models such as IEM or modified Curl models could be tested. Other improvements could come from including 'age' in the localization space for such models as EMST; a DNS study would provide the basis for assessing whether and how this should be implemented. In particular, the variation of directional weighting in the EMST mixing space could be the object of an interesting sensitivity study. Age, or the residence time, could also prove a relevant conditioning variable for turbulent combustion models such as MMC.

Chapter 6 shows that the extension of FCCT to more complex configurations is not straightforward. However, with work conducted on both the SAFIR simulation and the FCCT approach, the latter could be a possible modeling framework to eventually tackle the spray flame problem. It would be valid as much in the case addressed here where no dilution effects are observed, as in the more complex case where, stabilized father downstream, the flame is diluted by the recirculating burnt gases.

As more advanced technological solutions are developed to address ever stronger environmental challenges, the way REOXAL was for the flexibility needed in the context of boiler revamping, simulated problems will grow in complexity. Two directions are being taken as a response. On the one hand, increased computational capacities, with faster and more numerous processors – and the software solutions that can take advantage of these evolutions – enable to increase spatial resolution and/or the physical duration of the resolved problem; the present work on the SAFIR flame simulation belongs to this train of high-resolution computations. On the other hand, the development of approaches that can both account for complex phenomena and retain a reasonable computational cost (both in terms of number of processors and of process memory) is necessary, for all actors may not quickly be able to dispose of extended computational resources; the development of FCCT belongs to this second category of solutions. At any rate, the two approaches respond to each other, as the former high-resolution simulations enable to explore scales at which information is often useful for developing the latter modeling solutions.

Appendix A

Particle size distributions

A.1 Link between number and volume distributions

The classical inlet particle diameter distributions are given in two categories: number distributions (subscript 0) and volume distributions (subscript 3). All of them are functions of D the diameter, and verify, if denoted by f,

$$\int_0^\infty f_k(D)\mathrm{d}D = 1\,. \tag{A.1}$$

However they do not describe the same properties. The corresponding cumulative distributions (cdf), denoted by F, and defined as

$$F_k(D) = \int_0^D f_k(\delta)\mathrm{d}\delta \qquad \Longleftrightarrow \qquad f_k(D) = F_k'(D)\,, \tag{A.2}$$

characterize:

- $F_0(D)$ the ratio between the number of droplets of diameter $\leq D$ and the total number of droplets
- $F_3(D)$ the volume ratio occupied by the droplets of diameter $\leq D$.

The definitions imply that, if the number distribution f_0 is known, the volume cdf verifies

$$F_3(D) = \frac{\int_0^D \delta^3 f_0(\delta)\mathrm{d}\delta}{\int_0^\infty \delta^3 f_0(\delta)\mathrm{d}\delta} \tag{A.3}$$

so that

$$f_3(D) = \frac{D^3 f_0(D)}{\int_0^\infty \delta^3 f_0(\delta)\mathrm{d}\delta} \tag{A.4}$$

In the other way, Eq. (A.4) gives us that f_0 is proportional to f_3; the constant is necessarily determined from the condition $\int f_0 = 1$:

$$f_0(D) = \frac{f_3(D)/D^3}{\int_0^\infty f_3(\delta)/\delta^3\mathrm{d}\delta}\,. \tag{A.5}$$

A.2 Normal and log-normal distributions

A.2.1 Definition

Normal distribution. It is a classical definition, used here as an intuitive number distribution:

$$f_0(D) = \frac{1}{\sqrt{2\pi}\sigma} \exp\left(-\frac{1}{2}\left(\frac{D-\mu}{\sigma}\right)^2\right) . \tag{A.6}$$

Log-normal distribution. In this distribution, $\ln D$ follows a normal random law

$$f_0(D) = \frac{1}{D\sigma'\sqrt{2\pi}} \exp\left(-\frac{1}{2}\left(\frac{\ln(D/D^*)}{\sigma'}\right)^2\right) . \tag{A.7}$$

The parameters may be named as follows: D^* is such that $\mu' = \ln D^*$ is the log-mean diameter, that is the mean of the random variable $\ln D$; while σ' is the standard deviation of $\ln D$.

A.2.2 Properties and alternative parameterization

The mean and standard deviation of the random variable D, respectively denoted by M and S, verify:

$$\left\{ \begin{array}{rcl} M & = & D^*\sqrt{e^{\sigma'^2}} \\ S & = & D^*\sqrt{e^{\sigma'^2}(e^{\sigma'^2}-1)} \end{array} \right. \tag{A.8}$$

The inverse of this system reads

$$\left\{ \begin{array}{rcl} D^* & = & \dfrac{M}{\sqrt{1+(S/M)^2}} \\ \sigma' & = & \sqrt{\ln\left(1+(S/M)^2\right)} \end{array} \right. \tag{A.9}$$

and M and S can therefore also be input as parameters to define the log-normal distribution.

A.2.3 Generation of normal and log-normal distributions

If u_1 and u_2 are two independent variables following uniform laws on $[0;1]$, then the random variable

$$x = \mu + \sigma\sqrt{-2\ln u_1}\cos(2\pi u_2) \tag{A.10}$$

follows a normal law of mean μ and standard deviation σ. $y = \exp x$ with conveniently defined mean and standard deviations provides the desired log-normal distribution.

A.3 The Rosin–Rammler distribution

A.3.1 Definition

It is defined, in Babinsky & Sojka [Babinsky 02] as well as in Wikipedia (Weibull distribution), from its volume distribution

$$F_3(D) = 1 - e^{-(D/\lambda)^k} \tag{A.11}$$

$$f_3(D) = \frac{k}{\lambda}\left(\frac{D}{\lambda}\right)^{k-1} e^{-(D/\lambda)^k}\,, \tag{A.12}$$

(implying that Eq. (11) in [Babinsky 02] is actually f_3 not f_0) where λ is the mean particle size, and k a measure of the particle size spread.

Let us determine f_0. Introducing first the denominator integral

$$\begin{aligned}
I &= \int_0^\infty f_3(\delta)/\delta^3 \mathrm{d}\delta \\
&= \frac{k}{\lambda^k}\int_0^\infty \delta^{k-4} e^{-(\delta/\lambda)^k}\mathrm{d}\delta \\
&= \{\text{variable change } u = \delta/\lambda, \mathrm{d}\delta = \lambda \mathrm{d}u\} \\
&= \frac{k}{\lambda^3}\int_0^\infty u^{k-4} e^{-u^k}\mathrm{d}u \\
&= \{\text{variable change } x = u^k, \mathrm{d}u = \mathrm{d}x/(ku^{k-1})\} \\
&= \frac{1}{\lambda^3}\int_0^\infty x^{-3/k} e^{-x}\mathrm{d}x \\
&= \frac{1}{\lambda^3}\,\Gamma\left(-\frac{3}{k}+1\right)
\end{aligned}$$

Plugging this into Eq. (A.5) leads, for the number pdf, to the expression:

$$\begin{aligned}
f_0(D) &= \frac{D^{-3}k\lambda^{-k}D^{k-1}e^{-(D/\lambda)^k}}{I} \\
&= \frac{1}{\Gamma(-3/k+1)}\frac{k}{\lambda}\left(\frac{D}{\lambda}\right)^{k-4} e^{-(D/\lambda)^k}
\end{aligned}$$

In turn, the number cdf reads:

$$\begin{aligned}
F_0(D) &= \frac{1}{\Gamma(-3/k+1)}\frac{k}{\lambda^{k-3}}\int_0^D \delta^{k-4} e^{-(\delta/\lambda)^k}\mathrm{d}\delta \\
&= \{\text{variable change } u = (\delta/\lambda)^k, \mathrm{d}\delta = (\lambda^k/k)\delta^{1-k}\mathrm{d}u\} \\
&= \frac{\lambda^3}{\Gamma(-3/k+1)}\int_0^{(D/\lambda)^k} \delta^{-3} e^{-u}\mathrm{d}u \\
&= \frac{1}{\Gamma(-3/k+1)}\int_0^{(D/\lambda)^k} u^{-3/k} e^{-u}\mathrm{d}u
\end{aligned}$$

A.3.2 Properties

While λ is the mean of the f_3 distribution, the arithmetic mean diameter d_{10} is equal to

$$d_{10} = \int_0^\infty f_0(\delta)\delta \mathrm{d}\delta = \lambda \, \frac{\Gamma(-2/k+1)}{\Gamma(-3/k+1)} \, . \tag{A.13}$$

A.3.3 Simulation of a Rosin–Rammler distribution

The volume distribution f_3 may easily be simulated thanks to the remark that if u is a random variable uniform on $[0;1]$, then the random variable $\lambda(-\ln(u))^{1/k}$ is Rosin–Rammler distributed with parameters λ and k. Indeed, if $v = \lambda(-\ln(u))^{1/k}$, then $u = \exp(-(v/\lambda)^k)$, which has the desired cumulative distribution $(1 - F_3)$.

The simulation of a variable of law f_0 is not as straightforward. It actually follows a modified Gamma distribution. Introducing the lower gamma function

$$\gamma(s;x) = \int_0^x u^{s-1}e^{-u}\mathrm{d}u \, ,$$

the expression for F_0 may be reformulated

$$F_0(D) = \frac{\gamma\left(-3/k+1;(D/\lambda)^k\right)}{\Gamma(-3/k+1)} \, . \tag{A.14}$$

Property : if Y is a random variable on $[0;\infty)$ whose cdf is $F(y)$, and if $g : [0 : \infty) \to [0 : \infty)$ is an increasing function (thus bijective), then $X = g^{-1}(Y)$ follows the law of cdf $F \circ g$ (and therefore of pdf $g' \times f \circ g$).

Here is an algorithm to simulate f_0 (see Wikipedia, incomplete Gamma function). One defines δ as the fractional part of $-3/k + 1$, so that

$$\delta = 1 - \frac{3}{k} - \left\lfloor 1 - \frac{3}{k} \right\rfloor \, .$$

1. draw a, b, c three independent uniform variables on $]0 : 1]$
2. define $\begin{cases} \xi = b^{1/\delta} & \eta = c\,\xi^{\delta-1} \quad \text{if } a \le e/(e+\delta) \\ \xi = 1 - \ln b & \eta = c\,e^{-\xi} \quad \text{else} \end{cases}$
3. if $\eta \le \xi^{\delta-1}e^{-\xi}$ then choose ξ and exit. Else loop again from 1.

The result of this loop is ξ which follows $\Gamma(\delta, 1)$. Take

$$Y = \xi - \sum_{i=1}^{\lfloor 1-3/k \rfloor} \ln U_i \sim \gamma(-3/k+1) \tag{A.15}$$

where the U_i are independent uniform variables on $(0;1]$. The final variable is then obtained by

$$D = \lambda Y^{1/k} \sim f_0 \, . \tag{A.16}$$

A.4 The Nukiyama–Tanasawa distribution

A.4.1 Definition

It is defined from its number distribution

$$f_0(D) = K_D D^p e^{-(D/\lambda)^q} \tag{A.17}$$

where K_D is a normalizing constant equal to

$$K_D = \frac{q}{\lambda^{p+1}\Gamma(\frac{p+1}{q})} .$$

Its cumulative distribution may then be expressed as

$$F_0(D) = \frac{\gamma\left(\frac{p+1}{q}; (D/\lambda)^q\right)}{\Gamma(\frac{p+1}{q})} . \tag{A.18}$$

A.4.2 Simulation of a Nukiyama–Tanasawa distribution

It may be performed in a similar way to the Rosin–Rammler distribution, as was remarked by González-Tello *et al.* [González-Tello 08]. Therefore, the generation of these distributions is merged. Three parameters are used: λ, p and q, with Rosin–Rammler a specific case where $p = q - 4$.

A.5 Discrete distributions

A.5.1 Unweighted

The diameter may take a finite number n of values, $D_1 < \cdots < D_n$, each with (number) probability $p_i, i = 1, \ldots, n$. The relation

$$\sum_{i=1}^{n} p_i = 1$$

is verified. The number probability may formally written

$$f_0(D) = \sum_{i=1}^{n} p_i \delta(D - D_i) . \tag{A.19}$$

From this data, the cdf is a discontinuous function, defined by

$$F_0(D) = \begin{cases} 0 & \text{if } D < D_1 \\ \sum_{i=1}^{k} p_i & \text{if } D_k \leq D < D_{k+1} \\ 1 & \text{if } D \geq D_n \end{cases} \tag{A.20}$$

A.5.2 Weighted

In YALES2, an array of weights correlated with the diameters may be supplied. They are defined as $w_i, i = 1, \ldots, n$ and respectively applied to the weight of each category of particles. At this point the physical number of particles must be differentiated from the computational number of them.

The physical distribution is not modified, thus the p_i must be given unchanged. The physical number of particles of diameter D_i is denoted by N_i and its average verifies $\langle N_i \rangle = p_i \sum N_i = p_i N$. If the computational number of particles is in turn denoted by N_i^* and defined as $N_i^* = N_i / w_i$, the following relation holds:

$$\langle N_i^* \rangle = \frac{p_i}{w_i} N \tag{A.21}$$

so that class $\#i$ of weighted particles is given a probability p_i/w_i instead of p_i for the matching unweighted particles.

Now looking at the computational probability of each class, needed for generating the weighted distribution, one introduces the total number of computational particles $N^* = \sum N_i^*$. The computational probability of class $\#i$ is

$$p_i^* = \frac{\langle N_i^* \rangle}{N^*} = \frac{p_i / w_i}{\sum_{i=1}^{n} p_i / w_i} \,. \tag{A.22}$$

Thus, the same procedure as the unweighted case is used, except the particles diameters are drawn with the probabilities p_i^* and individually weighted with w_i.

A.6 Histogram distribution

Exactly the same procedure may be carried out, except once it is determined that class $\#i$ is the result of the draw, the output variable must be uniformly drawn on an interval $[D_i; D_{i+1}]$.

Appendix B

On tabulated source terms

This appendix aims at illustrating that the tabulation of chemical quantities by the resolution of archetypal problems, as described in Section 4.2.3, leads, in the parameter space, to specific behaviors and do not collapse on each other. It shows in particular that a temperature source term $T^{\mathrm{PF}}(Z, Y_c)$ obtained from an unstrained laminar premixed flamelet resolution is different from that obtained from an auto-ignition computation, $T^{\mathrm{AI}}(Z, Y_c)$. The former must therefore not be used to create a turbulent auto-ignition table, and vice versa.

B.1 Laminar premixed flamelets and homogeneous reactors, native equations

The laminar flame equations read, in space coordinates and with convenient assumptions and notations:

$$\rho\frac{\partial Y_m}{\partial t} + \rho\underline{u}\cdot\underline{\nabla}Y_m = \underline{\nabla}\cdot(\rho D\underline{\nabla}Y_m) + \dot{\omega}_m \tag{B.1}$$

$$\rho\frac{\partial T}{\partial t} + \rho\underline{u}\cdot\underline{\nabla}T = \frac{1}{c_P}\underline{\nabla}\cdot(\lambda\underline{\nabla}T) + \dot{\omega}_T \tag{B.2}$$

where

$$\dot{\omega}_T = -\frac{1}{c_P}\sum_m h^0_{f,i}\dot{\omega}_m\,.$$

Writing them in 1D and assuming stationarity leads to the laminar premixed flamelet equations:

$$\rho_0 S_L\frac{\partial Y_m}{\partial x} = \frac{\partial}{\partial x}\left(\rho D\frac{\partial Y_m}{\partial x}\right) + \dot{\omega}_m \tag{B.3}$$

$$\rho_0 S_L\frac{\partial T}{\partial x} = \frac{1}{c_P}\frac{\partial}{\partial x}\left(\lambda\frac{\partial T}{\partial x}\right) + \dot{\omega}_T \tag{B.4}$$

since $\rho u = \rho_0 S_L$ is a constant.

The homogeneous reactor equations are much simpler:

$$\rho\frac{\partial Y_m}{\partial t} = \dot{\omega}_m \tag{B.5}$$

$$\rho\frac{\partial T}{\partial t} = \dot{\omega}_T\,. \tag{B.6}$$

The purpose of this appendix is to quantify the difference between the source terms $\dot{\omega}_m$ and $\dot{\omega}_T$ when expressed as functions of the tabulating parameters Z, Y_c. From here on they are differentiated by the notation $^{\mathrm{PF}}$ for premixed flame and $^{\mathrm{AI}}$ for auto-ignition. For simplicity reasons the mixture fraction is fixed in the following: the initial states of both the premixed flame (fresh gas limit condition) and the auto-ignition problem (initial condition) are identical.

B.2 Rewriting in the progress of reaction space

A progress of reaction Y_c is defined as a linear combination of the species mass fractions, and therefore verifies

$$\frac{\partial Y_c}{\partial x} = \frac{1}{\rho_0 S_L}\left(\frac{\partial}{\partial x}\left(\rho D\frac{\partial Y_c}{\partial x}\right) + \dot{\omega}_c^{\mathrm{PF}}\right) \tag{B.7}$$

within the premixed flame context, and

$$\frac{\partial Y_c}{\partial t} = \dot{\omega}_c^{\mathrm{AI}} \tag{B.8}$$

for the auto-ignition problem.

The following discussion is carried out only for the temperature equation, but can equivalently be applied to the species components. The temperature equations are rewritten in the Y_c space. For the premixed flame, it becomes

$$\frac{\partial T}{\partial Y_c}\dot{\omega}_c^{\mathrm{PF}} = \frac{\lambda}{c_P}\left(\frac{\partial Y_c}{\partial x}\right)^2\frac{\partial^2 T}{\partial Y_c^2} + \dot{\omega}_T^{\mathrm{PF}}$$

so that introducing the scalar dissipation rate of Y_c

$$\chi_{Y_c} = \frac{\lambda}{c_P}\left(\frac{\partial Y_c}{\partial x}\right)^2 \tag{B.9}$$

leads to

$$\frac{\partial T}{\partial Y_c}\dot{\omega}_c^{\mathrm{PF}} = \chi_{Y_c}\frac{\partial^2 T}{\partial Y_c^2} + \dot{\omega}_T^{\mathrm{PF}}\,. \tag{B.10}$$

In turn, the auto-ignition equation reads

$$\frac{\partial T}{\partial Y_c}\dot{\omega}_c^{\mathrm{AI}} = \dot{\omega}_T^{\mathrm{AI}}\,. \tag{B.11}$$

B.3 Consequences on modeling

The laws of thermodynamics state that there is a unique equilibrium temperature for a given initial state. This applies to the two cases of a premixed flame and a homogeneous reactor. Consequently, the temperature increase ΔT in a flame with a cold gas mixture of given temperature T_0 and equivalence ratio ϕ

$$\Delta T = \int_{Y_c^0}^{Y_c^{\mathrm{eq}}} \frac{\dot{\omega}_T^{\mathrm{PF}} + \chi_{Y_c} \dfrac{\partial^2 T}{\partial Y_c^2}}{\dot{\omega}_c^{\mathrm{PF}}} \, \mathrm{d}Y_c \tag{B.12}$$

is equal to the temperature increase of this same gas burning in a homogeneous reactor

$$\Delta T = \int_{Y_c^0}^{Y_c^{\mathrm{eq}}} \frac{\dot{\omega}_T^{\mathrm{AI}}}{\dot{\omega}_c^{\mathrm{AI}}} \, \mathrm{d}Y_c \, . \tag{B.13}$$

Now let us consider a model in which a temperature is determined through this equation

$$\frac{\partial T}{\partial Y_c} \dot{\omega}_c = \mathcal{M} + \dot{\omega}_T \tag{B.14}$$

where $\mathcal{M}$ is a term modeling diffusion and other phenomena. The temperature increase reads similarly

$$\Delta T = \int_{Y_c^0}^{Y_c^{\mathrm{eq}}} \frac{\dot{\omega}_T + \mathcal{M}}{\dot{\omega}_c} \, \mathrm{d}Y_c \, . \tag{B.15}$$

If the source terms are taken from a laminar premixed flamelet table (meaning in the above equation $\dot{\omega}_T \leftarrow \dot{\omega}_T^{\mathrm{PF}}$ and $\dot{\omega}_c \leftarrow \dot{\omega}_c^{\mathrm{PF}}$), the difference in temperature increase between this model and the expected temperature difference ΔT^{PF} will read

$$\Delta T^{\mathcal{M},\mathrm{PF}} - \Delta T = T_b^{\mathcal{M},\mathrm{PF}} - T_b = \int_{Y_c^0}^{Y_c^{\mathrm{eq}}} \frac{\mathcal{M} - \chi_{Y_c} \dfrac{\partial^2 T}{\partial Y_c^2}}{\dot{\omega}_c^{\mathrm{PF}}} \, \mathrm{d}Y_c \, . \tag{B.16}$$

More specifically, if the premixed flame source terms are plugged into a 0D reactor model (for which $\mathcal{M} = 0$), the temperature difference reads

$$T_b^{\mathrm{0D,PF}} - T_b = \int_{Y_c^0}^{Y_c^{\mathrm{eq}}} -\frac{\chi_{Y_c} \dfrac{\partial^2 T}{\partial Y_c^2}}{\dot{\omega}_c^{\mathrm{PF}}} \, \mathrm{d}Y_c \, . \tag{B.17}$$

Appendix C

Generic formalism for multi-dimensional interpolation

All values obtained from the turbulent chemistry tables (PCM or FCCT) are computed by multilinear interpolation. In the present case, the dimension is four (mixture fraction, progress variable, residence time and mixing time) but a generic algorithm is present in the code, enabling any dimension and paving the way to configurations requiring more parameters.

C.1 Mathematical expression

Denoting the dimension by N_d, let a point $\underline{x}$ of coordinates $x^{(1)}, x^{(2)}, \ldots, x^{(N_d)}$ be considered. These coordinates are positioned on the discrete grid in such a way that there exist integers $k_1, k_2, \ldots, k_{N_d}$ for which

$$\forall i \in [1, N_d], \quad x_{k_i}^{(i)} \leq x^{(i)} \leq x_{k_i+1}^{(i)} \, ,$$

the $^{(i)}$ denoting the coordinates in the i-th dimension. Point $\underline{x}$ is positioned inside the hypercube defined by the indices k_i.

Values of the quantity ϕ at the hypercube's corners are known, there are 2^{N_d} of them, and they are denoted by

$$\phi_{k_1+\sigma_1, k_2+\sigma_2, \ldots, k_{N_d}+\sigma_{N_d}} = \phi(x_{k_1+\sigma_1}^{(1)}, x_{k_2+\sigma_2}^{(2)}, \ldots, x_{k_{N_d}+\sigma_{N_d}}^{(N_d)})$$

where the σ_i are equal to either 0 or 1. If $\sigma_i = 0$, the hypercube corner considered is on the "left" of $\underline{x}$ in the dimension i, if $\sigma_i = 1$, it is on the "right" of $\underline{x}$. Let the set of all combinations of N_d 0's or 1's be denoted by ς (of size 2^{N_d}, consistently). Then the values at the corners may be written

$$\phi_{k_1, k_2, \ldots, k_{N_d}, \underline{\sigma}}, \quad \underline{\sigma} \in \varsigma \, .$$

The sought result is the value of ϕ in $\underline{x}$, which may be formulated as

$$\phi(\underline{x}) = \sum_{\underline{\sigma} \in \varsigma} \alpha_{\underline{\sigma}}(\underline{x}) \, \phi_{k_1, k_2, \ldots, k_{N_d}, \underline{\sigma}} \, .$$

In the multilinear framework, the coefficients $\alpha_{\underline{\sigma}}$ are equal to

$$\alpha_{\underline{\sigma}}(\underline{x}) = \prod_{i=1}^{N_d} \begin{cases} 1 - \dfrac{x^{(i)} - x_{k_i}^{(i)}}{x_{k_i+1}^{(i)} - x_{k_i}^{(i)}} & \text{if } \sigma_i = 0 \\ \dfrac{x^{(i)} - x_{k_i}^{(i)}}{x_{k_i+1}^{(i)} - x_{k_i}^{(i)}} & \text{if } \sigma_i = 1 \end{cases} ,$$

also expressed by the generic formulation

$$\alpha_{\underline{\sigma}}(\underline{x}) = \prod_{i=1}^{N_d} (-1)^{\sigma_i} \frac{x_{k_i+\sigma_i}^{(i)} - x^{(i)}}{x_{k_i+1}^{(i)} - x_{k_i}^{(i)}} .$$

These coefficients verify

$$\forall \underline{x}, \qquad \sum_{\underline{\sigma} \in \varsigma} \alpha_{\underline{\sigma}}(\underline{x}) = 1 .$$

C.2 Code implementation

Here is how this is implemented in the FCCT table generation code. In the header file `FCCT/com_FCCT.f`, integer variables `*_linint` are defined:

`ndim_linint`	the table dimension N_d
`power2_linint`	must be equal to 2^{N_d}, this is checked in initialization routine `build_linint_basecoords`
`basecoords_linint`	array of dimensions (`power2_linint,ndim_linint`) contains all possible vectors of 0's and 1's of this size (corresponds to the set ς)

An initialization routine `build_linint_basecoords` is first called which initializes the 0-1-vectors `basecoords_linint` (they are actually the writing of all integers between 0 and $2^{N_d} - 1$ in the binary base).

Then, when an interpolation is necessary, a call is made to routine `INTERPOL`, which takes as input parameters, on top of the three `ndim`, `power2` and `basecoords` introduced above:

`nfields`	the number of fields
`X`	the coordinates of vector $\underline{x}$
`Xleft`	the coordinates of the "lower left" corner of the hypercube $\underline{x}_{k_1,k_2,\ldots,k_{N_d}}$
`Xright`	the coordinates of the "upper right" corner of the hypercube $\underline{x}_{k_1+1,k_2+1,\ldots,k_{N_d}+1}$
`values`	the values $\phi_{k_1,k_2,\ldots,k_{N_d},\underline{\sigma}}$ for the `nfields` different fields, in an order consistent with that used in `basecoords`

and returns an array `output` of `nfields` values computed from the equations written above.

Appendix D

One-dimensional residence-time jet model

A simplified steady one-dimensional formulation of the jet properties may be derived, following classical results on the entrainment by Ricou & Spalding [Ricou 61] and subsequent works [Lee 03, Enjalbert 09]. Based on self-similarity observations, axial velocity and scalar profiles are assumed to be Gaussian in the radial direction, of half-width $b(x)$. In a constant-density configuration (ρ_0 the density of the inlet fluid is equal to ρ_∞, that of the environment), the time-averaged fields are denoted by $\langle u\rangle(x)$ and $\langle \tau_{\rm res}\rangle(x)$, omitting the radial $r/b(x)$ dependency.

The evolution equations are based on mass and momentum flux balances on thin transverse sets. The momentum flux is conserved, which leads to $\pi b^2\langle u\rangle^2 = \pi(D/2)^2 u_0^2$, where u_0 is the bulk jet velocity. The mass flux conservation equation is written thanks to an entrainment hypothesis, which states that the rate of incorporation of environment fluid by the jet, as it develops, is proportional to its centerline axial velocity, so that

$$\frac{{\rm d}(\pi b^2\langle u\rangle)}{{\rm d}x} = 2\alpha\pi b\langle u\rangle \tag{D.1}$$

with α the entrainment constant, measured at 0.056 [Ricou 61]. This set of equations leads to the well-known results of a linear spreading: $b \sim 2\alpha x$ and a decreasing velocity as $\langle u\rangle \sim u_0 D/(4\alpha x)$.

As far as the scalars are concerned, similar balance equations may be written, with an adjustment on the rate of spreading: the scalar half-width increases as $2\lambda\alpha x$, with λ which was found of the order of 1.19. In the case of the residence time, a source term is inserted in the rhs:

$$\frac{{\rm d}(\pi b^2\langle u\rangle\langle \tau_{\rm res}\rangle)}{{\rm d}x} = \pi b^2 \,. \tag{D.2}$$

Building on the results on the half-width and velocity, this leads to

$$\frac{{\rm d}\langle \tau_{\rm res}\rangle}{{\rm d}x} = \frac{4\lambda\alpha x^2}{u_0} \,, \tag{D.3}$$

hence to

$$\langle \tau_{\rm res}\rangle \sim \frac{4\lambda\alpha}{(3u_0 D)x^2} \,. \tag{D.4}$$

In the present case, the density is not uniform, the cold fuel injected in the center is of density $\rho_0 = 0.947\,\mathrm{kg.m^{-3}}$ while for the warm coflow, $\rho_\infty = 0.2432\,\mathrm{kg.m^{-3}}$. This may be tackled by retaining the present formulation, considering $\rho = \rho_\infty$ everywhere, and assuming only that the inlet diameter is modified to $D^* = \sqrt{\rho_0/\rho_\infty}D$ [Ricou 61], thus preserving the initial mass and momentum flow rates. This leads to the final result

$$\langle\widetilde{\tau}_{\mathrm{res}}\rangle \sim \frac{4\lambda\alpha}{3u_0 D}\sqrt{\frac{\rho_\infty}{\rho_0}}x^2\,. \tag{D.5}$$

Bibliography

[Apte 03a] S.V. Apte, M. Gorokhovski & P. Moin. *LES of atomizing spray with stochastic modeling of secondary breakup.* International Journal of Multiphase Flow, vol. 29, pages 1503–1522, 2003.

[Apte 03b] S.V. Apte, K. Mahesh, P. Moin & J.C. Oefelein. *Large-eddy simulation of swirling particle-laden flows in a coaxial-jet combustor.* International Journal of Multiphase Flow, vol. 29, pages 1311–1331, 2003.

[Apte 08] S.V. Apte, K. Mahesh & T. Lundgren. *Accounting for finite-size effects in simulations of disperse particle-laden flows.* International Journal of Multiphase Flow, vol. 34, pages 260–271, 2008.

[Apte 09a] S.V. Apte, K. Mahesh, M. Gorokhovski & P. Moin. *Stochastic modeling of atomizing spray in a complex swirl injector using large eddy simulation.* Proceedings of the Combustion Institute, vol. 32, pages 2257–2266, 2009.

[Apte 09b] S.V. Apte, K. Mahesh & P. Moin. *Large-eddy simulation of evaporating spray in a coaxial combustor.* Proceedings of the Combustion Institute, vol. 32, pages 2247–2256, 2009.

[Ashgriz 11] N. Ashgriz. Handbook of atomization and sprays. Springer, 2011.

[Babinsky 02] E. Babinsky & P.E. Sojka. *Modeling drop size distributions.* Progress in Energy and Combustion Science, vol. 28, pages 303–329, 2002.

[Bailly 03] C. Bailly & G. Comte-Bellot. Turbulence. CNRS Editions, 2003.

[Barths 98] H. Barths, N. Peters, N. Brehm, A. Mack, M. Pfitzner & V. Smiljanovski. *Simulation of Pollutant Formation in a Gas-Turbine Combustor Using Unsteady Flamelets.* Twenty-Seventh Symposium (International) on Combustion, pages 1841–1847, 1998.

[Bilger 04] R. Bilger. *Marker fields for turbulent premixed combustion.* Combustion and Flame, vol. 138, pages 188–194, 2004.

[Bini 07] M. Bini & W.P. Jones. *Particle acceleration in turbulent flows: A class of nonlinear stochastic models for intermittency.* Physics of Fluids, page 035104, 2007.

[Bini 08] M. Bini & W.P. Jones. *Large-eddy simulation of particle-laden turbulent flows.* Journal of Fluid Mechanics, vol. 614, pages 207–252, 2008.

[Bini 09] M. Bini & W.P. Jones. *Large Eddy Simulation of an evaporating acetone spray.* International Journal of Heat and Fluid Flow, vol. 30, pages 471–480, 2009.

[Boileau 07] M. Boileau. *Simulation aux grandes échelles de l'allumage diphasique des foyers aéronautiques.* PhD thesis, Institut National Polytechnique de Toulouse, 2007.

[Boileau 08a] M. Boileau, M. Pascaud, E. Riber, B. Cuenot, L. Gicquel, T. Poinsot & M. Cazalens. *Investigation of Two-Fluid Methods for Large Eddy Simulation of Spray Combustion in Gas Turbines.* Flow, Turbulence and Combustion, vol. 80, pages 291–321, 2008.

[Boileau 08b] M. Boileau, G. Staffelbach, B. Cuenot, T. Poinsot & C. Bérat. *LES of an ignition sequence in a gas turbine engine.* Combustion and Flame, vol. 154, pages 2–22, 2008.

[Boivin 98] M. Boivin, O. Simonin & K.D. Squires. *Direct numerical simulation of turbulence modulation by particles in isotropic turbulence.* Journal of Fluid Mechanics, vol. 375, pages 235–263, 1998.

[Boivin 00] M. Boivin, O. Simonin & K.D. Squires. *On the prediction of gas–solid flows with two-way coupling using large eddy simulation.* Physics of Fluids, vol. 12, no. 8, pages 2080–2090, 2000.

[Borghi 88] R. Borghi. *Turbulent combustion modeling.* Progress in Energy and Combustion Science, vol. 14, no. 4, pages 245–292, 1988.

[Boulanger 02] J. Boulanger & L. Vervisch. *Diffusion Edge-Flame: Approximation of the Flame Tip Damköhler Number.* Combustion and Flame, vol. 130, pages 1–14, 2002.

[Bray 66] K. Bray. *The challenge of turbulent combustion.* Twenty-Sixth Symposium (International) on Combustion, vol. 1, pages 1–26, 1966.

[Bushe 99] W.K. Bushe & H. Steiner. *Conditional moment closure for large eddy simulation of nonpremixed turbulent reacting flows.* Physics of Fluids, vol. 11, no. 7, pages 1896–1906, 1999.

[Bykov 07] V. Bykov & U. Maas. *The extension of the ILDM concept to reaction–diffusion manifolds.* Combustion Theory and Modelling, vol. 11, no. 6, pages 839–862, 2007.

[Cabra 04] R. Cabra. *Turbulent jet flame into a vitiated coflow.* Technical Report CR-2004-212887, NASA Glenn Research Center, March 2004.

[Cabra 05] R. Cabra, J.Y. Chen, R.W. Dibble, A.N. Karpetis & R.S. Barlow. *Lifted methane-air jet flames in a vitiated coflow.* Combustion and Flame, vol. 143, pages 491–506, 2005.

[Cao 05] R.R. Cao, S.B. Pope & A.R. Masri. *Turbulent lifted flames in a vitiated coflow investigated using joint PDF calculations.* Combustion and Flame, vol. 142, pages 438–453, 2005.

[Cessou 10] A. Cessou, D. Honoré & G. Cléon. *SAFIR – Simulation Avancée des Foyers Industriels avec Recycle. Phase 3, rapport final.* Rapport technique, CORIA CNRS UMR 6614, Université et INSA de Rouen, 2010.

[Cha 01] C.M. Cha, G. Kosály & H. Pitsch. *Modeling extinction and reignition in turbulent nonpremixed combustion using a doubly-conditional moment closure approach.* Physics of Fluids, vol. 13, page 3824, 2001.

[Cieutat 09] D. Cieutat, I. Sanchez-Molinero, R. Tsiava, P. Recourt, N. Aimard & C. Prébendé. *The Oxy-combustion burner development for the CO_2 pilot at Lacq.* Energy Procedia, vol. 1, pages 519–526, 2009.

[Cleary 09a] M.J. Cleary & A.Y. Klimenko. *A Generalised Multiple Mapping Conditioning Approach for Turbulent Combustion.* Flow, Turbulence and Combustion, vol. 82, pages 477–491, 2009.

[Cleary 09b] M.J. Cleary, A.Y. Klimenko, J. Janicka & M. Pfitzner. *A sparse-Lagrangian multiple mapping conditioning model for turbulent diffusion flames.* Proceedings of the Combustion Institute, vol. 32, pages 1499–1507, 2009.

[Coelho 01] P.J. Coelho & N. Peters. *Unsteady Modelling of a Piloted Methane/Air Jet Flame Based on the Eulerian Particle Flamelet Model.* Combustion and Flame, vol. 124, pages 444–465, 2001.

[Colin 00] O. Colin, F. Ducros, D. Veynante & T. Poinsot. *A thickened flame model for large eddy simulations of turbulent premixed combustion.* Physics of Fluids, vol. 12, page 1843, 2000.

[Cook 04] A.W. Cook & W.H. Cabot. *A high-wavenumber viscosity for high-resolution numerical methods.* Journal of Computational Physics, vol. 195, no. 2, pages 594–601, 2004.

[Correa 95] S.M. Correa. *A Direct Comparison of Pair-Exchange and IEM Models in Premixed Combustion.* Combustion and Flame, vol. 103, pages 194–206, 1995.

[Crowe 96] C.T. Crowe, T.R. Troutt & J.N. Chung. *Numerical models for two-phase turbulent flows.* Annu. Rev. Fluid Mech., vol. 28, no. 1, pages 11–43, 1996.

[Crowe 98] C.T. Crowe, M. Sommerfeld & Y. Tsuji. Multiphase flows with droplets and particles. CRC, 1998.

[Darabiha 92] N. Darabiha. *Transient behaviour of laminar counterflow-hydrogen-air diffusion flames with complex chemistry.* Combustion Science and Technology, vol. 86, no. 1–6, pages 163–181, 1992.

[de Chaisemartin 09] S. de Chaisemartin. *Modèles eulériens et simulation numérique de la dispersion turbulente de brouillards qui s'évaporent.* PhD thesis, Ecole Centrale Paris, March 2009.

[Delhaye 08] S. Delhaye, L.M.T. Somers, J.A. van Oijen & L.P.H de Goey. *Incorporating unsteady flow-effects in flamelet-generated manifolds.* Combustion and Flame, vol. 155, pages 133–144, 2008.

[Desjardins 08] O. Desjardins, V. Moureau & H. Pitsch. *An accurate conservation level set/ghost fluid method for simulating turbulent atomisation.* Journal of Computational Physics, vol. 227, pages 8395–8416, 2008.

[Domingo 05a] P. Domingo, L. Vervisch, S. Payet & R. Hauguel. *DNS of a premixed turbulent V flame and LES of a ducted flame using a FSD-PDF subgrid scale closure with FPI-tabulated chemistry.* Combustion and Flame, vol. 143, pages 566–586, 2005.

[Domingo 05b] P. Domingo, L. Vervisch & J. Reveillon. *DNS analysis of partially premixed combustion in spray and gaseous turbulent flame-bases stabilized in hot air.* Combustion and Flame, vol. 140, no. 3, pages 172–195, 2005.

[Domingo 08] P. Domingo, L. Vervisch & D. Veynante. *Large-eddy simulation of a lifted methane jet flame in a vitiated coflow.* Combustion and Flame, vol. 152, pages 415–432, 2008.

[Dopazo 74] C. Dopazo & E.E. O'Brien. *An approach to the autoignition of a turbulent mixture.* Acta Astronautica, vol. 1, no. 9-10, pages 1239–1266, 1974.

[Dopazo 79] C. Dopazo. *Relaxation of initial probability density functions in the turbulent convection of scalar fields.* Physics of Fluids, vol. 22, no. 1, page 20, 1979.

[Dubief 00] Y. Dubief & F. Delcayre. *On coherent-vortex identification in turbulence.* Journal of Turbulence, vol. 1, pages 1–22, 2000.

[Ducros 00] F. Ducros, F. Laporte, T. Souleres, V. Guinot, P. Moinat & B. Caruelle. *High-order fluxes for conservative skew-symmetric-like schemes in structured meshes : Application to compressible flows.* Journal of Computational Physics, vol. 161, pages 114–139, 2000.

[Dufour 05] G. Dufour. *Modélisation multi-fluide eulérienne pour les écoulements diphasiques à inclusions dispersées*. PhD thesis, Université Toulouse III, December 2005.

[Duplat 10] J. Duplat, C. Innocenti & E. Villermaux. *A Non-Sequential Turbulent Mixing Process*. Physics of Fluids, vol. 22, no. 035104, 2010.

[Enjalbert 09] N. Enjalbert, D. Galley & L. Pierrot. *An entrainment model for the turbulent jet in a coflow*. Comptes Rendus Mecanique, vol. 337, pages 639–644, 2009.

[Enjalbert 11] N. Enjalbert, P. Domingo & L. Vervisch. *Mixing time-history effects in Large Eddy Simulation of non-premixed turbulent flames: Flow-Controlled Chemistry Tabulation*. Combustion and Flame, no. doi:10.1016/j.combustflame.2011.06.005, 2011.

[Fessler 94] J.R. Fessler, J.D. Kulick & J.K. Eaton. *Preferential concentration of heavy particles in turbulent channel flow*. Physics of Fluids, vol. 6, pages 3742–3749, 1994.

[Février 05] P. Février, O. Simonin & K.D. Squires. *Partitioning of particle velocities in gas–solid turbulent flows into a continuous field and a spatially uncorrelated random distribution: theoretical formalism and numerical study*. Journal of Fluid Mechanics, vol. 533, pages 1–46, 2005.

[Finkenrath 11] M. Finkenrath. *Cost and Performance of Carbon Dioxide Capture from Power Generation*. Working paper, International Energy Agency, 2011.

[Fiorina 05] B. Fiorina, O. Gicquel, L. Vervisch, S. Carpentier & N. Darabiha. *Approximating the chemical structure of partially premixed and diffusion counterflow flames using FPI flamelet tabulation*. Combustion and Flame, vol. 140, pages 147–160, 2005.

[Fiorina 10] B. Fiorina, R. Vicquelin, P. Auzillon, N. Darabiha, O. Gicquel & D. Veynante. *A filtered tabulated chemistry model for LES of premixed combustion*. Combustion and Flame, vol. 157, pages 465–475, 2010.

[Fukagata 00] K. Fukagata. *Large eddy simulation of particulate turbulent channel flows*. PhD thesis, Kungliga Tekniska Högskolan, February 2000.

[Galpin 08] J. Galpin, A. Naudin, L. Vervisch, C. Angelberger, O. Colin & P. Domingo. *Large-eddy simulation of a fuel-lean premixed turbulent swirl-burner*. Combustion and Flame, vol. 155, pages 247–266, 2008.

[Garmory 11] A. Garmory & E. Mastorakos. *Capturing localised extinction in Sandia Flame F with LES–CMC*. Proceedings of the Combustion Institute, vol. 33, no. 1, pages 1673–1680, 2011.

[Germano 91a] M. Germano, U. Piomelli, P. Moin & W.H. Cabot. *A dynamic subgrid-scale eddy viscosity model*. Physics of Fluids A: Fluid Dynamics, vol. 3, page 1760, 1991.

[Germano 91b] M. Germano, U. Piomelli, P. Moin & W.H. Cabot. *Erratum: A dynamic subgrid-scale eddy viscosity model*. Physics of Fluids A: Fluid Dynamics, vol. 3, no. 12, page 3128, 1991.

[Ghirelli 04] F. Ghirelli & B. Leckner. *Transport equation for the local residence time of a fluid*. Chemical Engineering Science, vol. 59, pages 513–523, 2004.

[Gicquel 99] O. Gicquel, D. Thévenin, M. Hilka & N. Darabiha. *Direct numerical simulation of turbulent premixed flames using intrinsic low-dimensional manifolds*. Combustion Theory and Modelling, vol. 3, pages 479–502, 1999.

[Gicquel 00] O. Gicquel, N. Darabiha & D. Thévenin. *Laminar Premixed Hydrogen/Air Counterflow Flame Simulations Using Flame Prolongation of ILDM with Differential Diffusion.* Proceedings of the Combustion Institute, vol. 28, pages 1901–1908, 2000.

[Gkagkas 07] K. Gkagkas & R.P. Lindstedt. *Transported PDF modelling with detailed chemistry of pre- and auto-ignition in CH_4/air mixtures.* Proceedings of the Combustion Institute, vol. 31, no. 1, pages 1559–1566, 2007.

[Godel 09] G. Godel, P. Domingo & L. Vervisch. *Tabulation of NO_x chemistry for Large-Eddy Simulation of non-premixed turbulent flames.* Proceedings of the Combustion Institute, vol. 32, pages 1555–1561, 2009.

[González-Tello 08] P. González-Tello, F. Camacho, J.M. Vicaria & P.A. González. *A modified Nukiyama–Tanasawa distribution function and a Rosin–Rammler model for the particle-size-distribution analysis.* Powder Technology, vol. 186, pages 278–281, 2008.

[Gordon 07] R.L. Gordon, A.R. Masri, S.B. Pope & G.M. Goldin. *Transport budgets in turbulent lifted flames of methane autoigniting in a vitiated co-flow.* Combustion and Flame, vol. 151, no. 3, pages 495–511, 2007.

[Grout 07] R.W. Grout. *An age extended progress variable for conditioning reaction rates.* Physics of Fluids, vol. 19, no. 105107, 2007.

[Gutheil 98] E. Gutheil & W.A. Sirignano. *Counterflow Spray Combustion Modeling Including Detailed Transport and Detailed Chemistry.* Combustion and Flame, vol. 113, no. 2, page 92, 1998.

[Ham 03] F. Ham, S.V. Apte, G. Iaccarino, X. Wu, M. Herrmann, G. Constantinescu, K. Mahesh & P. Moin. *Unstructured LES of reacting multiphase flows in realistic gas turbine combustors.* In Proceedings of the Summer Program. Center for Turbulence Research, 2003.

[Han 01] D. Han & M.G. Mungal. *Direct measurement of entrainment in reacting/nonreacting turbulent jets.* Combustion and Flame, vol. 124, no. 3, pages 370–386, 2001.

[Haworth 09] D.C. Haworth. *Progress in probability density function methods for turbulent reacting flows.* Progress in Energy and Combustion Science, 2009.

[Hollmann 98] C. Hollmann & E. Gutheil. *Flamelet-Modeling of Turbulent Spray Diffusion Flames Based on a Laminar Spray Flame Library.* Combustion Science and Technology, vol. 135, pages 175–192, 1998.

[Hubbard 75] G.L. Hubbard, V.E. Denny & A.F. Mills. *Droplet evaporation: effects of transients and variable properties.* International Journal of Heat and Mass Transfer, vol. 18, no. 9, pages 1003–1008, 1975.

[Ihme 08] M. Ihme & H. Pitsch. *Prediction of extinction and reignition in nonpremixed turbulent flames using a flamelet/progress variable model 1. A priori study and presumed PDF closure.* Combustion and Flame, vol. 155, pages 70–89, 2008.

[Ihme 10] M. Ihme & Y.C. See. *Prediction of autoignition in a lifted methane/air flame using an unsteady flamelet/progress variable model.* Combustion and Flame, vol. 157, no. 10, pages 1850–1862, 2010.

[Im 99] H.G. Im, J.H. Chen & J.Y. Chen. *Chemical response of methane/air diffusion flames to unsteady strain rate.* Combustion and Flame, vol. 118, no. 1–2, pages 204–212, 1999.

[Jaberi 99] F.A. Jaberi, P.J. Colucci, S. James, P. Givi & S.B. Pope. *Filtered mass density function for large-eddy simulation of turbulent reacting flows.* Journal of Fluid Mechanics, vol. 401, pages 85–121, 1999.

[Jones 88] W.P. Jones & R.P. Lindstedt. *Global reaction schemes for hydrocarbon combustion.* Combustion and Flame, vol. 73, no. 3, pages 233–249, 1988.

[Jones 10a] W.P. Jones & C. Lettieri. *Large eddy simulation of spray atomization with stochastic modeling of breakup.* Physics of Fluids, vol. 22, no. 115106, 2010.

[Jones 10b] W.P. Jones, S. Lyra & A.J. Marquis. *Large Eddy Simulation of a droplet laden turbulent mixing layer.* International Journal of Heat and Fluid Flow, vol. 31, pages 93–100, 2010.

[Jones 10c] W.P. Jones, S. Lyra & A.J. Marquis. *Large Eddy Simulation of evaporating kerosene and acetone sprays.* International Journal of Heat and Mass Transfer, vol. 53, pages 2491–2505, 2010.

[Jones 10d] W.P. Jones & V.N. Prasad. *Large Eddy Simulation of the Sandia Flame Series (D–F) using the Eulerian stochastic field method.* Combustion and Flame, vol. 157, pages 1621–1636, 2010.

[Jones 11] W.P. Jones, S. Lyra & S. Navarro-Martinez. *Large Eddy Simulation of a swirl stabilized spray flame.* Proceedings of the Combustion Institute, vol. 33, pages 2153–2160, 2011.

[Kanniche 10] M. Kanniche, R. Gros-Bonnivard, P. Jaud, J. Valle-Marcos, J.-M. Amann & C. Bouallou. *Pre-combustion, post-combustion and oxy-combustion in thermal power plant for CO_2 capture.* Applied Thermal Engineering, vol. 30, pages 53–62, 2010.

[Karypis 95] G. Karypis & V. Kumar. *METIS – Unstructured Graph Partitioning and Sparse Matrix Ordering System, Version 2.0.* Rapport technique, 1995.

[Kee 85] R.J. Kee, J.F. Gracer, M.D. Smooke & Miller J.A. *PREMIX: A FORTRAN program for modeling steady laminar one-dimensional premixed flames.* Rapport technique SAND85-8240, SANDIA National Laboratories, 1985.

[Klein 03] M. Klein, A. Sadiki & J. Janicka. *A digital filter based generation of inflow data for spatially developing direct numerical or large eddy simulations.* Journal of Computational Physics, vol. 186, pages 652–665, 2003.

[Klimenko 99] A.Y. Klimenko & R. Bilger. *Conditional moment closure for turbulent combustion.* Progress in Energy and Combustion Science, vol. 25, pages 595–687, 1999.

[Klimenko 03] A.Y. Klimenko & S.B. Pope. *The modeling of turbulent reactive flows based on multiple mapping conditioning.* Physics of Fluids, vol. 15, no. 7, pages 1907–1925, 2003.

[Klimenko 07] A.Y. Klimenko. *On simulating scalar transport by mixing between Lagrangian particles.* Physics of Fluids, vol. 19, no. 031702, 2007.

[Klimenko 09] A.Y. Klimenko. *Lagrangian particles with mixing. II. Sparse-Lagrangian methods in application for turbulent reacting flows.* Physics of Fluids, vol. 21, no. 065102, 2009.

[Kolaitis 06] D.I. Kolaitis & M.A. Founti. *A tabulated chemistry approach for numerical modeling of diesel spray evaporation in a "stabilized cool flame" environment.* Combustion and Flame, vol. 145, pages 259–271, 2006.

[Koornneef 12] J. Koornneef, A. Ramírez, W. Turkenburg & A. Faaij. *The environmental impact and risk assessment of CO_2 capture, transport and storage – An evaluation of the knowledge base.* Progress in Energy and Combustion Science, vol. 38, pages 62–86, 2012.

[Kraushaar 11] M. Kraushaar, V. Moureau, N. Lamarque & L. Gicquel. *A family of Runge-Kutta schemes with incorporated tunable diffusion.* Journal of Computational Physics, vol. to be submitted, 2011.

[Kronenburg 04] A. Kronenburg. *Double conditioning of reactive scalar transport equations in turbulent nonpremixed flames.* Physics of Fluids, vol. 16, page 2640, 2004.

[Kronenburg 08] A. Kronenburg & M.J. Cleary. *Multiple mapping conditioning for flames with partial premixing.* Combustion and Flame, vol. 155, no. 1–2, pages 215–231, 2008.

[Kuo 86] K.K. Kuo. Principles of combustion. John Wiley, 1986.

[Lacaze 09] G. Lacaze, E. Richardson & T. Poinsot. *Large eddy simulation of spark ignition in a turbulent methane jet.* Combustion and Flame, vol. 156, pages 1993–2009, 2009.

[Lasheras 00] J.C. Lasheras & E.J. Hopfinger. *Liquid Jet Instability and Atomization in a Coaxial Gas Stream.* Annu. Rev. Fluid Mech., vol. 32, pages 275–308, 2000.

[Leboissetier 05] A. Leboissetier, N. Okong'o & J. Bellan. *Consistent large-eddy simulation of a temporal mixing layer laden with evaporating drops. Part 2. A posteriori analysis.* Journal of Fluid Mechanics, vol. 523, pages 37–78, 2005.

[Lecocq 10] G. Lecocq. *Approches hybrides combinant chimie complexe, description statistique et densié de surface de flamme pour la simulation aux grandes échelles de l'auto-inflammation, l'allumage par bougie et la flamme de prémélange dans les moteurs à allumage commandé.* PhD thesis, Institut National des Sciences Appliquées de Rouen, March 2010.

[Lee 03] J. Lee & V. Chu. Turbulent jets and plumes – a Lagrangian approach. Kluwer Academic Publishers, Boston, 2003.

[Lefebvre 89a] A.H. Lefebvre. Atomization and sprays. CRC, 1989.

[Lefebvre 89b] A.H. Lefebvre. *Properties of sprays.* Particles & Particle Systems Characterization, vol. 6, pages 176–186, 1989.

[Leplat 11] N. Leplat, P. Dagaut, C. Togbé & J. Vandooren. *Numerical and experimental study of ethanol combustion and oxidation in laminar premiex flames and in jet-stirred reactor.* Combustion and Flame, vol. 158, pages 705–725, 2011.

[Li 07] J. Li, A. Kazakov, M. Chaos & F. Dryer. *Chemical Kinetics of Ethanol Oxidation.* In Fifth US Combustion Meeting, page C26, March 2007.

[Lodato 08a] G. Lodato. *Conditions aux Limites Tridimensionnelles pour la Simulation Directe et aux Grandes Échelles des Écoulements Turbulents. Modélisation de Sous-Maille pour la Turbulence en Région de Proche Paroi.* PhD thesis, Institut National des Sciences Appliquées de Rouen, December 2008.

[Lodato 08b] G. Lodato, P. Domingo & L. Vervisch. *Three-dimensional boundary conditions for Direct and Large-Eddy Simulation of compressible viscous flows.* Journal of Computational Physics, 2008.

[Lundgren 67] T. Lundgren. *Distribution Functions in the Statistical Theory of Turbulence.* Physics of Fluids, vol. 10, no. 5, pages 969–975, 1967.

[Lutz 87] A.E. Lutz, R.J. Kee & Miller J.A. *SENKIN: A FORTRAN program for predicting homogeneous gas phase chemical kinetics with sensitiviy analysis.* Rapport technique SAND87-8248, SANDIA National Laboratories, 1987.

[Maas 92] U. Maas & S.B. Pope. *Simplifying chemical kinetics: intrinsic low-dimensional manifolds in composition space.* Combustion and Flame, vol. 88, pages 239–264, 1992.

[Marinov 99] N.M. Marinov. *A Detailed Chemical Kinetic Model for High Temperature Ethanol Oxidation.* Chemical Kinetics, no. 31, pages 183–220, 1999.

[Mastorakos 98] E. Mastorakos & R. Bilger. *Second-order conditional moment closure for the autoignition of turbulent flows.* Physics of Fluids, vol. 10, no. 6, pages 1246–1248, 1998.

[Ménard 07] T. Ménard, S. Tanguy & A. Berlemont. *Coupling level set/VOF/ghost fluid methods: Validation and application to 3D simulation of the primary break-up of a liquid jet.* International Journal of Multiphase Flow, vol. 33, no. 5, pages 510–524, 2007.

[Merci 06] B. Merci, D. Roekaerts & B. Naud. *Study of the performance of three micromixing models in transported scalar PDF simulations of a piloted jet diffusion flame ("Delft Flame III").* Combustion and Flame, vol. 144, pages 476–493, 2006.

[Meunier 03] P. Meunier & E. Villermaux. *How vortices mix.* Journal of Fluid Mechanics, vol. 476, pages 213–222, 2003.

[Meyer 09] D.W. Meyer & P. Jenny. *Micromixing models for turbulent flows.* Journal of Computational Physics, vol. 228, pages 1275–1293, 2009.

[Michel 08] J.-B. Michel, O. Colin & D. Veynante. *Modeling ignition and chemical structure of partially premixed turbulent flames using tabulated chemistry.* Combustion and Flame, vol. 152, pages 80–99, 2008.

[Moin 02] P. Moin. *Advances in Large Eddy Simulation methodology for complex flows.* International Journal of Heat and Fluid Flow, vol. 23, no. 5, pages 710–720, 2002.

[Mortensen 09] M. Mortensen & R. Bilger. *Derivation of the conditional moment closure equations for spray combustion.* Combustion and Flame, vol. 156, pages 62–72, 2009.

[Moureau 11a] V. Moureau, P. Domingo & L. Vervisch. *Design of a massively parallel CFD code for complex geometries.* Comptes Rendus Mécanique, vol. 339, no. 2–3, pages 141–148, 2011.

[Moureau 11b] V. Moureau, P. Domingo & L. Vervisch. *From Large-Eddy Simulation to Direct Numerical Simulation of a lean premixed swirl flame: Filtered laminar flame-PDF modeling.* Combustion and Flame, vol. 158, pages 1340–1357, 2011.

[Naudin 08] A. Naudin. *Simulation des grandes échelles de la combustion turbulente avec chimie détaillé tabulée.* PhD thesis, Institut National des Sciences Appliquées de Rouen, November 2008.

[Nauman 81] E. B. Nauman. *Residence time distributions and micromixing.* Chemical Engineering Communications, vol. 8, pages 53–131, 1981.

[Navarro-Martinez 05] S. Navarro-Martinez, A. Kronenburg & F. Di Mare. *Conditional Moment Closure for Large Eddy Simulations.* Flow, Turbulence and Combustion, vol. 75, pages 245–274, 2005.

[Navarro-Martinez 09] S. Navarro-Martinez & A. Kronenburg. *LES–CMC simulations of a lifted methane flame.* Proceedings of the Combustion Institute, vol. 32, no. 1, pages 1509–1516, 2009.

[Nguyen 10] P.-D. Nguyen, L. Vervisch, V. Subramanian & P. Domingo. *Multidimensional flamelet-generated manifolds for partially premixed combustion.* Combustion and Flame, vol. 157, pages 43–61, 2010.

[Nicolaides 87] R. Nicolaides. *Deflation of conjugate gradients with applications to boundary value problems.* SIAM J. Num. Anal., vol. 24, no. 2, pages 355–365, 1987.

[Nicoud 99] F. Nicoud & F. Ducros. *Subgrid-Scale Stress Modelling Based on the Square of the Velocity Gradient Tensor.* Flow, Turbulence and Combustion, vol. 62, pages 183–200, 1999.

[Okong'o 04] N. Okong'o & J. Bellan. *Consistent large-eddy simulation of a temporal mixing layer laden with evaporating drops. Part 1. Direct numerical simulation, formulation and a priori analysis.* Journal of Fluid Mechanics, vol. 499, pages 1–47, 2004.

[Pera 06] C. Pera, J. Reveillon, L. Vervisch & P. Domingo. *Modeling subgrid scale mixture fraction variance in LES of evaporating spray.* Combustion and Flame, vol. 146, no. 4, pages 635–648, 2006.

[Peters 09] N. Peters. *Multiscale combustion and turbulence.* Proceedings of the Combustion Institute, 2009.

[Philips 65] H. Philips. *Flame in a buoyant methane layer.* 10th Symp. (Int.) on Combustion, vol. 10, page 329, 1965.

[Pitsch 98] H. Pitsch, M. Chen & N. Peters. *Unsteady Flamelet Modeling of Turbulent Hydrogen–Air Diffusion Flames.* Twenty-Seventh Symposium (International) on Combustion, pages 1057–1064, 1998.

[Pitsch 00] H. Pitsch & H. Steiner. *Scalar Mixing and Dissipation Rate in Large-Eddy Simulations of Non-Premixed Turbulent Combustion.* Proceedings of the Combustion Institute, vol. 28, pages 41–49, 2000.

[Poinsot 92] T. Poinsot & S.K. Lele. *Boundary conditions for direct simulations of compressible viscous flows.* Journal of Computational Physics, vol. 101, no. 1, pages 104–129, 1992.

[Poinsot 05] T. Poinsot & D. Veynante. Theoretical and numerical combustion. RT Edwards, Inc., 2005.

[Pope 85] S.B. Pope. *PDF methods for turbulent reactive flows.* Progress in Energy and Combustion Science, vol. 11, pages 119–192, 1985.

[Pope 04] S.B. Pope. *Ten questions concerning the large-eddy simulation of turbulent flows.* New Journal of Physics, vol. 6, page 35, 2004.

[Pozorski 09] J. Pozorski & S.V. Apte. *Filtered particle tracking in isotropic turbulence and stochastic modeling of subgrid-scale dispersion.* International Journal of Multiphase Flow, vol. 35, pages 118–128, 2009.

[Raman 06] V. Raman, H. Pitsch & R.O. Fox. *Eulerian transported probability density function sub-filter model for large-eddy simulations of turbulent combustion.* Combustion Theory and Modelling, vol. 10, no. 3, pages 439–458, 2006.

[Ranz 52] W.E. Ranz & W.R. Marshal. *Evaporation from drops.* Chemical Engineering Progress, vol. 48, no. 3, pages 141–146, 1952.

[Reitz 82] R.D. Reitz & F.V. Bracco. *Mechanism of atomization in a liquid jet.* Physics of Fluids, vol. 25, no. 10, pages 1730–1742, 1982.

[Ren 04] Z. Ren & S.B. Pope. *An investigation of the performance of turbulent mixing models.* Combustion and Flame, vol. 136, pages 208–216, 2004.

[Ren 08] Z. Ren & S.B. Pope. *Second-order splitting schemes for a class of reactive systems.* Journal of Computational Physics, vol. 227, pages 8165–8176, 2008.

[Reveillon 00] J. Reveillon & L. Vervisch. *Spray Vaporization in Nonpremixed Turbulent Combustion Modeling: A Single Droplet Model.* Combustion and Flame, vol. 121, pages 75–90, 2000.

[Reveillon 07] J. Reveillon & F.-X. Demoulin. *Effects of the preferential segregation of droplets on evaporatioin and turbulent mixing.* Journal of Fluid Mechanics, vol. 583, pages 273–302, 2007.

[Ricou 61] F. Ricou & D. Spalding. *Measurements of entrainment by axisymmetric turbulent jets.* Journal of Fluid Mechanics, pages 21–32, 1961.

[Sabel'nikov 05] V. Sabel'nikov & O. Soulard. *Rapidly decorrelating velocity-field model as a tool for solving one-point Fokker–Planck equations for probability density functions of turbulent reactive scalars.* Physical Review E, vol. 016301, 2005.

[Sanjosé 11] M. Sanjosé, J.M. Senoner, F. Jaegle, B. Cuenot, M. Moreau & T. Poinsot. *Fuel injection model for Euler–Euler and Euler–Lagrange large-eddy simulation of an evaporating spray inside an aeronautical combustor.* International Journal of Multiphase Flow, vol. doi:10.1016/j.ijmultiphaseflow.2011.01.008, 2011.

[Sazhin 06] S.S. Sazhin. *Advanced models of fuel droplet heating and evaporation.* Progress in Energy and Combustion Science, vol. 32, pages 162–214, 2006.

[Schiller 35] L. Schiller & B. Naumann. *A drag coefficient correlation.* VDI Zeitung, vol. 77, pages 318–320, 1935.

[Sheikhi 05] M.R.H. Sheikhi, T.G. Drozda, P. Givi, F.A. Jaberi & S.B. Pope. *Large eddy simulation of a turbulent nonpremixed piloted methane jet flame (Sandia Flame D).* Proceedings of the Combustion Institute, vol. 30, pages 549–556, 2005.

[Shetty 10] D.A. Shetty, A.J. Chandy & S.H. Frankel. *A new fractal interaction by echange with the mean mixing model for large eddy simulation/filtered mass density function applied to a multiscalar three-stream turbulent jet.* Physics of Fluids, page 025102, 2010.

[Sirignano 10] W.A. Sirignano. Fluid dynamics and transport of droplets and sprays, second edition. Cambridge University Press, 2010.

[Smagorinsky 63] J. Smagorinsky. *General circulation experiments with the primitive equations.* Monthly Weather Review, vol. 91, no. 3, pages 99–164, 1963.

[Smith] G.P. Smith, D.M. Golden & M. Frenklach. `http://www.me.berkeley.edu/gri-mech/`.

[Stöllinger 10] M. Stöllinger & S. Heinz. *Evaluation of scalar mixing and time scale models in PDF simulations of a turbulent premixed flame.* Combustion and Flame, pages 1671–1685, 2010.

[Subramaniam 98] S. Subramaniam & S.B. Pope. *A Mixing Model for Turbulent Reacting Flows based on Euclidian Minimum Spanning Trees.* Combustion and Flame, vol. 115, pages 487–514, 1998.

[Subramaniam 99] S. Subramaniam & S.B. Pope. *Comparison of Mixing Model Performance for Nonpremixed Turbulent Reactive Flow.* Combustion and Flame, vol. 117, pages 732–754, 1999.

[Subramanian 10a] V. Subramanian. *Numerical Simulation of Forced Ignition Using LES Coupled with a Tabulated Detailed Chemistry Approach.* PhD thesis, Institut National des Sciences Appliquées de Rouen, January 2010.

[Subramanian 10b] V. Subramanian, P. Domingo & L. Vervisch. *Large-Eddy Simulation of forced ignition of an annular bluff-body burner.* Combustion and Flame, vol. 157, no. 3, pages 579–601, 2010.

[Tatsumi 95] S. Tatsumi, L. Martinelli & A. Jameson. *Flux-limited schemes for the compressible Navier–Stokes equations.* AIAA Journal, vol. 33, no. 2, pages 252–261, 1995.

[Triantafyllidis 09] A. Triantafyllidis, E. Mastorakos & R.L.G.M. Eggels. *Large Eddy Simulation of forced ignition of a non-premixed bluff-body methane flame with Conditional Moment Closure.* Combustion and Flame, vol. 156, pages 2328–2345, 2009.

[Valino 98] L. Valino. *A field Monte Carlo formulation for calculating the probability density function of a single scalar in a turbulent flow.* Flow, Turbulence and Combustion, vol. 60, no. 2, pages 157–172, 1998.

[Van der Vorst] H.A. Van der Vorst. *Parallel iterative solution methods for linear systems arising from discretized PDE's.* Special Course on Parallel Computing in CFD, pages 1–39.

[van Oijen 00] J.A. van Oijen & L.P.H de Goey. *Modelling of Premixed Laminar Flames Using Flamelet-Generated Manifolds.* Combustion Science and Technology, vol. 161, pages 113–137, 2000.

[van Oijen 01] J.A. van Oijen, F.A. Lammers & L.P.H de Goey. *Modeling of Complex Premixed Burner Systems by Using Flamelet-Generated Manifolds.* Combustion and Flame, vol. 127, pages 2124–2134, 2001.

[Vantieghem 11] S. Vantieghem. *Numerical simulations of quasi-static magnetohydrodynamics using an unstructured finite volume solver: development and applications.* PhD thesis, Université Libre de Bruxelles, January 2011.

[Vasilyev 98] O.V. Vasilyev, T.S. Lund & P. Moin. *A General Class of Commutative Filters for LES in Complex Geometries.* Journal of Computational Physics, vol. 146, pages 105–123, 1998.

[Vervisch 92] L. Vervisch. *Study and modeling of finite rate chemistry effects in turbulent non-premixed flames.* Annual Research Briefs, Center for Turbulent Research, vol. 94, pages 411–431, 1992.

[Vervisch 98] L. Vervisch & T. Poinsot. *Direct Numerical Simulation of Non-Premixed Turbulent Flames.* Annu. Rev. Fluid Mech., vol. 30, pages 655–91, 1998.

[Vervisch 04] L. Vervisch, R. Hauguel, P. Domingo & M. Rullaud. *Three facets of turbulent combustion modelling: DNS of premixed V-flame, LES of lifted nonpremixed flame and RANS of jet-flame.* Journal of Turbulence, vol. 5, no. 4, pages 1–36, 2004.

[Vervisch 10] L. Vervisch, P. Domingo, G. Lodato & D. Veynante. *Scalar energy fluctuations in Large-Eddy Simulation of turbulent flames: Statistical budgets and mesh quality criterion.* Combustion and Flame, vol. 157, no. 4, pages 778–789, 2010.

[Veynante 02] D. Veynante & L. Vervisch. *Turbulent Combustion Modeling.* Progress in Energy and Combustion Science, vol. 28, no. 3, pages 193–266, 2002.

[Veynante 06] D. Veynante & R. Knikker. *Comparison between LES results and experimental data in reacting flows.* Journal of Turbulence, vol. 7, page 35, 2006.

[Vicquelin 09] R. Vicquelin. *Tabulation de la cinétique chimique pour la modélisation et la simulation de la combustion turbulente.* PhD thesis, Ecole Centrale Paris, June 2009.

[Villermaux 99] E. Villermaux & C. Innocenti. *On the geometry of turbulent mixing.* Journal of Fluid Mechanics, vol. 393, pages 123–147, 1999.

[Wall 00] C. Wall, B.J. Boersma & P. Moin. *An evaluation of the assumed beta probability density function subgrid-scale model for Large Eddy Simulation of non-premixed turbulent combustion with heat release.* Physics of Fluids, vol. 12, no. 10, pages 2522–2529, 2000.

[Wang 08] H. Wang & S.B. Pope. *Lagrangian investigation of local extinction, re-ignition and auto-ignition in turbulent flames.* Combustion Theory and Modelling, vol. 12, no. 5, pages 857–882, 2008.

[Wang 10a] B. Wang. *Inter-phase interaction in a turbulent, vertical channel flow laden with heavy particles. Part I: Numerical methods and particle dispersion properties.* International Journal of Heat and Mass Transfer, vol. 53, pages 2506–2521, 2010.

[Wang 10b] K. Wang, G. Ribert, P. Domingo & L. Vervisch. *Self-similar behavior and chemistry tabulation of burnt-gases diluted premixed flamelets including heat loss.* Combustion Theory and Modelling, vol. 14, no. 4, pages 541–570, 2010.

[Wilke 50] C.R. Wilke. *A viscosity equation for gas mixtures.* Journal of Chemical Physics, vol. 18, pages 517–519, 1950.

[Williams 58] F. Williams. *Spray combustion and atomization.* Physics of Fluids, vol. 1, pages 541–545, 1958.

[Xu 00] J. Xu & S.B. Pope. *PDF Calculations of Turbulent Nonpremixed Flames with Local Extinction.* Combustion and Flame, vol. 123, pages 281–307, 2000.

[Yaldizli 10] M. Yaldizli, K. Mehravaran & F.A. Jaberi. *Large-eddy simulations of turbulent methane jet flames with filtered mass density function.* International Journal of Heat and Mass Transfer, vol. 53, pages 2551–2562, 2010.

[Yamashita 96] H. Yamashita, M. Shimada & T. Takeno. *A numerical study on flame stability at the transition point of jet diffusion flames.* Twenty-Sixth Symposium (International) on Combustion, vol. 26, no. 1, pages 27–34, 1996.

[Yoshikawa 10] I. Yoshikawa. *Développement d'un modèle de flamme épaissie dynamique pour la simulation aux grandes échelles de flammes turbulentes prémélangées.* PhD thesis, Ecole Centrale Paris, June 2010.

[Yuu 01] S. Yuu, T. Ueno & T. Umekage. *Numerical simulation of the high Reynolds number slit nozzle gas–particle jet using subgrid-scale coupling large eddy simulation.* Chemical Engineering Science, vol. 56, pages 4293–4307, 2001.